



HAL
open science

Experimental study of turbulent sediment transport processes

Hélder Guta

► **To cite this version:**

Hélder Guta. Experimental study of turbulent sediment transport processes. Applied geology. Université Grenoble Alpes [2020-..], 2022. English. NNT : 2022GRALU018 . tel-04602858

HAL Id: tel-04602858

<https://theses.hal.science/tel-04602858>

Submitted on 6 Jun 2024

HAL is a multi-disciplinary open access archive for the deposit and dissemination of scientific research documents, whether they are published or not. The documents may come from teaching and research institutions in France or abroad, or from public or private research centers.

L'archive ouverte pluridisciplinaire **HAL**, est destinée au dépôt et à la diffusion de documents scientifiques de niveau recherche, publiés ou non, émanant des établissements d'enseignement et de recherche français ou étrangers, des laboratoires publics ou privés.

THÈSE

Pour obtenir le grade de

DOCTEUR DE L'UNIVERSITÉ GRENOBLE ALPES

Spécialité : Sciences de la Terre et de l'Univers et de
l'Environnement

Arrêté ministériel : 25 mai 2016

Présentée par

Hélder GUTA

Thèse dirigée par **David HURTHER**
et codirigée par **Julien CHAUCHAT**

préparée au sein du **Laboratoire des Écoulements
Géophysiques et Industriels (LEGI)**
dans l'**École Doctorale Sciences de la Terre de l'Environnement
et des Planètes (STEP)**

Étude expérimentale des processus turbulents de transport sédimentaire

Experimental study of turbulent sediment transport processes

Thèse soutenue publiquement le **3 juin 2022**,
devant le jury composé de :

Pr Koen BLANCKAERT

Professeur, Vienna University of Technology, Rapporteur

Dr Benoît CAMENEN

Directeur de Recherche, INRAE, Rapporteur

Pr Olivier EIFF

Professeur, Karlsruhe Institute of Technology, Président

Pr Philippe SÉCHET

Maître De Conférence, LEGI-UGA, Examineur

Dr Magali JODEAU

Ingénieur-Chercheur, EDF-Lab. d'Hydraulique St-Venant, Examinatrice

Dr Matthieu de LINARES

Ingénieur conseil, Artelia Eau & Environnement, Membre invité

Dr David HURTHER

Directeur de Recherche, LEGI-CNRS, Directeur de thèse

Pr Julien CHAUCHAT

Maître De Conférence, LEGI-UGA, Co-directeur de thèse



Abstract

Modelling intense sediment transport caused by high bed shear stress is of primary engineering and environmental interest. Such conditions are encountered typically during river floods and coastal storms, which have a major impact on short to long-term river morphology and coastal shoreline evolutions. The law of the wall and the Rouse equation are found to describe reasonably well the velocity and concentration distributions, respectively. However, the parameters in these equations may present significant variability. Determining these parameters requires high-resolution data over a wide range of flow conditions, including in the dense high concentration near-wall region. In this Thesis, a new experimental dataset of co-located velocity and sediment concentration profile measurements. Two (PMMA) particle diameters are used, $dp=3\text{mm}$ and $dp=1\text{mm}$, covering a wide range of suspension numbers $0.4 < w_s/u_* < 1.3$ and Shields numbers $0.35 < \theta < 1.2$. First, parametrizations for improved description of the solid-load as result of velocity and concentration are provided. The results indicate that at high sediment concentration, the velocity profile may not be strictly logarithmic, such that the adopted κ values represent a global trend, rather than the local flow feature. A parametrization of the depth-averaged ratio of sediment and momentum diffusivity, the β -factor, based on the present experimental results is proposed, allowing to extend literature models to a wider range of suspension numbers ($0.1 < w_s/u_* < 1.5$). The bulk flow resistance, parametrized by the friction factor does not display discernible differences from the reference clear-water flows, indicating a negligible effect of sediment motion, in the upper plane bed regime. With the larger particle experiments ($dp=3\text{mm}$), it is shown that inside the bed-load layer, turbulent momentum mixing is highly reduced, compared to the corresponding clear-water flow. This change in flow structure should be taken into account in the turbulent mixing length model, affecting both the law of the wall and the Rouse formulation. As result, a modified analytical solution that includes the bed-load effects for the concentration profile was derived. Further investigations show that the turbulent kinetic energy balance is also heavily affected by the presence of a thick bed-load layer. In such conditions, the peak production region is heavily upshifted, inducing an increased energy diffusion towards the bed. It is suggested that this downward transport may feed the bed-load transport. Based on the Quadrant Threshold Method, it is confirmed that the referred transport of turbulent energy is realized by the turbulent coherent flow structures, as well as the turbulent transport of momentum $u'w'$ and of sediments $c'w'$.

Keywords: sediment transport, suspension, ACVP, bed-load effects, turbulent kinetic energy

Résumé

La modélisation du transport intense de sédiments causé par une forte contrainte de cisaillement du lit est d'un intérêt primordial pour l'ingénierie et l'environnement. De telles conditions sont rencontrées typiquement pendant les crues des rivières et les tempêtes côtières, qui ont un impact majeur sur la morphologie des rivières à court et à long terme et sur l'évolution du littoral. La loi de la paroi et l'équation de Rouse décrivent raisonnablement bien les distributions de vitesse et de concentration de sédiments, respectivement. Cependant, les paramètres de ces équations peuvent présenter une variabilité importante. La détermination de ces paramètres nécessite des données à haute résolution sur une large gamme de conditions d'écoulement, y compris dans la région dense à forte concentration près de la paroi. Dans cette thèse, un nouveau jeu de données de mesures de profils de vitesse et de concentration de sédiments co-localisés. Deux diamètres de particules (PMMA) sont utilisés, $dp=3\text{mm}$ et $dp=1\text{mm}$, couvrant une large gamme de nombres de suspension $0.4 < w_s/u_* < 1.3$ et de nombres de Shields $0.35 < \theta < 1.2$. Tout d'abord, ces paramètres qui permettent une meilleure description de la charge solide défini comme produit intégré en profondeur de la vitesse et de la concentration sont étudiés. Les résultats indiquent qu'à forte concentration de sédiments, le profil de vitesse peut ne pas être strictement logarithmique, de sorte que les valeurs de la constante κ de von Karman adoptées représentent une tendance globale, plutôt que la caractéristique locale de l'écoulement. Une paramétrisation du rapport moyen en profondeur de la diffusivité des sédiments et de la quantité de mouvement, le facteur β , basée sur les présents résultats expérimentaux est proposée, permettant d'étendre les modèles de la littérature à une gamme plus large de nombres de suspension ($0.1 < w_s/u_* < 1.5$). La résistance globale à l'écoulement, paramétrée par le facteur de friction, ne présente pas de différences discernables par rapport aux écoulements en eau claire, indiquant un effet négligeable du mouvement des sédiments, en l'absence de formes fond. Avec les expériences de particules plus grandes ($dp=3\text{mm}$), il est montré qu'à l'intérieur de la couche de charriage, le mélange turbulent de la quantité de mouvement est fortement réduit, comparé à l'écoulement correspondant en eau claire. Ce changement dans la structure de l'écoulement doit être pris en compte dans le modèle de longueur de mélange turbulent, affectant à la fois la loi de la paroi et la formulation de Rouse. En conséquence, une solution analytique modifiée qui inclut les effets du transport par charriage pour le profil de concentration a été dérivée. Les analyses montrent que l'équilibre de l'énergie cinétique turbulente k est également fortement affecté par la présence d'une épaisse couche de charriage. Dans de telles conditions, la région de production maximale est fortement décalée vers le haut, ce qui induit une diffusion d'énergie accrue vers le lit. Il est suggéré que ce transport vers le bas peut alimenter le transport par charriage. Sur la base de la méthode des quadrants, il est confirmé que ce transport d'énergie turbulente kw' est réalisé par les structures turbulentes cohérentes, ainsi que le transport turbulent de la quantité de mouvement $u'w'$ et des sédiments $c'w'$.

Mots clés: Transport des sédiments, suspension, ACVP, effets du charriage, énergie cinétique turbulente

Acknowledgements

I start by expressing my profound gratitude to my PhD advisors, David Hurther and Julien Chauchat, for giving me the opportunity to do experimental research on a topic that fascinates me. I enjoyed the freedom to explore different directions and follow my intuition, with the necessary guidance from them. I have learnt a lot from their comments, advices and from our numerous discussions.

I thank Olivier Eiff, Magali Jodeau, Matthieu de Linares for accepting to be part of the jury and the reviewers in particular, Benoît Camenen and Koen Blanckaert, for reviewing my manuscript.

I would like to thank the colleagues in LEGI, from the different services, especially Lafiyatou Emeriaud, who had the patience to seek for 6 hosting agreements in a short time, necessary for my visa, due the complex setup of the funding scheme. Special thanks also to Stéphane Pioz-Marchand, who provided much support on the experimental facility, throughout the entire work. I am grateful for the time and experience shared with the fellow PhD students, as well as other researchers.

I am grateful to Eric Barthélemy, my Hydraulics professor in Ense3, for further sparking my interest in Hydraulics and introducing me to the topic of flood modelling, sediment transport and river morphology. Special thanks to Philippe Séchet, whose teaching during my Master's were captivating, and to whom I have repeatedly presented my work, i.e., for my Master's internship defense, then during the doctorate as the referee of the Thesis committee and member of the PhD defense jury. I acknowledge Guillaume Fromant for introducing me to the experimental facility during the Master's internship and for integrating my Thesis committee.

The Project ANR SHEET-FLOW, granted by Agence Nationale de la Recherche (ANR), has funded the experiments and an essential part of this Thesis. The remaining financial support was granted through a Doctoral Scholarship by the French Ministry of Foreign Affairs. I express therefore my sincere gratitude to both institutions.

I thank my family in Mozambique, who supported me when I decided to leave a stable job to seek further training in Hydraulics, and kept the same support throughout the doctorate. I acknowledge the friends in Grenoble, with whom I have shared many great moments in the past three years, particularly, Alex, Thabi, Pedro and Mariana. Finally yet importantly, I have no words to express my appreciation for my wife Pauline and my son Pierre, born during the second year of the Ph.D. They are both my greatest source of joy.

Table of contents

Table of contents.....	i
1. Introduction.....	1
1.1. Context	1
1.2. Sediment transport and large-scale river morphology	3
1.3. State of the art.....	4
1.3.1. Momentum equations of water-sediment mixture	4
1.3.2. Turbulent kinetic energy (TKE) equations of water-sediment mixture.....	7
1.3.3. Suspended sediment concentration equation	9
1.3.4. Intense sediment transport: physical description of the phenomena.....	10
1.3.5. Sediment transport in turbulent rough open-channel flows	12
1.3.6. Velocity and concentration measurements in open-channel flows	13
1.4. PhD objectives and organisation	15
2. Experimental and methodological considerations.....	18
2.1. Experimental setup	18
2.2. Experimental protocol and flow conditions	20
2.2.1. Sediment feeding system	20
2.2.2. Experimental procedure	21
2.3. Instrumentation and data processing	25
2.3.1. Principle of velocity and concentration measurements with ACVP	25
2.3.2. ACVP calibration.....	28
2.3.3. Turbulence measurement resolution	31
2.3.4. Doppler noise reduction in turbulence measurements	32
3. Mean profiles and modelling parameters.....	35
3.1. Flow structure: bed-load and suspension layers.....	35
3.2. Mean profiles.....	36
3.2.1. Velocity, concentration and Reynolds shear stress	36
3.2.2. Eddy viscosity, mean solid flux and repartition bed-load/suspended-load..	40
3.3. Modelling parameters.....	44
3.3.1. von Karman parameter κ	44
3.3.2. β -factor	47
3.3.3. Flow resistance: friction factor	50

3.4.	Conclusions	54
4.	Bedload effects on turbulent suspension properties in large particle sediment-laden flows ($dp=3mm$)	56
4.1.	Introduction	56
4.2.	Turbulent mixing length and eddy viscosity	57
4.3.	Velocity distribution.....	59
4.4.	Concentration distribution.....	61
4.5.	Discussion	63
4.6.	Conclusions	64
5.	TKE Budget in Sediment-laden flows.....	67
5.1.	Introduction	67
5.2.	Second order moments and turbulence spectra	68
5.3.	TKE budget	71
5.4.	Discussion	74
5.4.1.	Effect of bed-load on the TKE budget.....	74
5.4.2.	Energy repartition	76
5.4.3.	Turbulence-particle interactions	77
5.4.4.	Turbulence modelling: $k - \epsilon$ model closures.....	79
5.5.	Conclusions	83
6.	Coherent Flow Structures Dynamics	85
6.1.	Introduction	85
6.2.	Quadrant Threshold Method	87
6.3.	Ejections and sweeps: fractional contributions, time fractions and periods.....	89
6.4.	Connection between Bursting motions and TKE transport.....	92
6.5.	Correlation between turbulent suspension and coherent structures	94
6.6.	Discussion and conclusions.....	98
7.	Conclusions and perspectives	101
7.1.	Conclusions	101
7.2.	Perspectives	103
A.	Additional experimental considerations	106
A.1.	Repeatability of the experiments	106
A.2.	Additional experimental runs.....	107
B.	Mixing length for $dp1$	109

C. Pick-up functions and reference concentration	110
D. A simple total solid flux based on the TKE budget results	112
E. Constants of $k - \varepsilon$ model	113
References	I
List of Figures	IX

1. Introduction

In this chapter, introductory considerations related to sediment transport in rivers are presented. The problems related to sediment transport will be presented in terms of the main engineering and environmental applications. The challenges related to the modelling of large-scale morphological evolution in rivers will be briefly described, before the state of the art on turbulent sediment-laden flows is presented. The goals and scope of the present research will be presented in the last section of the chapter.

1.1. Context

Sediment transport is a phenomenon of great engineering and environmental importance. It consists in the carrying of particles by the water flow when the flow becomes energetic enough. If the amount of sediment entering a given river or channel reach, is superior to the maximum solid-load that can be transported by the flow (transport capacity), part of sediments will be deposited along the reach. Inversely, if the amount of sediments entering the considered reach is inferior to its transport capacity, the river will erode its bed and banks. This is quantified by a continuity equation of the sediment mass, the Exner equation (Eq. (1-3)) relating the spatial gradients of sediment fluxes to the time evolution of the bed level. Under equilibrium conditions, no appreciable deposition or erosion occurs (Vanoni 2006). Although important modifications occur over short periods (days - months), mainly during floods, a river in equilibrium keeps its morphological features roughly unchanged over extended periods (years-decades-centuries). Several examples of problems in which sediment transport is of primary importance are briefly described below:

- Accelerated degradation and aggradation: although they may occur with low or high intensity due to natural causes, accelerated erosion or deposition are often linked to human activity, and occur generally much faster than those due to natural/geological causes (Vanoni 2006). Examples are river works (straightening, constriction, construction of dams, etc.), changing of land use in the catchment such as urbanization, excessive deforestation, etc. Overall, any drastic change in sediment and runoff production as well modifications of channel geometry will have important consequences on the river morphology. Furthermore, increased local erosion will often induce downstream deposition because only a minor portion of all transported material reach the oceans because the gravity induced flow forcing generally decreases in a river with proximity to the ocean.
- Reservoir sedimentation and management strategies: sediment accumulation reduces storage capacity and efficiency, clog outlet works and in severe sedimentation cause problems in hydropower intake works, treating safety of hydraulic machines. It was not the case before the 1950s, but currently the design of dams must imperatively consider the aspects related to reservoir sedimentation (Hager et al. 2020). Efforts should be done to anticipate the evolution of dead volume of the reservoir due to accumulation of sediments. Strategies for prevention and mitigation measures against reservoir sedimentation should

be envisaged, since the design stage when possible. Schleiss et al. (2016) have recently presented the state-of-art on these strategies. One frequent sediment management alternative consists of flushing operations, which has its own environmental consequences. Modelling turbidity currents in reservoirs (Jodeau et al. 2018) as well as downstream sediment dynamics due to flushing (Antoine et al. 2020) are becoming rapidly important in reservoir management.

- Downstream long-term impacts of dams: the presence of dams reduce the amount of larger sediments downstream the dam. Since the stream is not fed with large sediments, it may progressively degrade in order to reach a new equilibrium. The second effect of the dam is the change of hydrologic regime (Vanoni 2006), often consisting in reduced peak discharges that may induce deposition. The net result will depend on the combination of both factors. For example, Ronco et al. (2010) concluded that the net effects of the Kariba (largest reservoir storage capacity in the world) and Cahora Bassa (third largest hydroelectric power plant in Africa) dams on the lower Zambezi river were pronounced in the first decades after the construction, and that its equilibrium seems to be recovered decades later.
- Scour around bridge piers: erosion around piers may occur due to local scour (local modification of the flow pattern) and general (non-local) effects. The bed level in river reach suffering excessive erosion may lower several meters and endanger the stability of bridge foundations. A study by (Taricska 2014) indicated that in the USA 50% of bridge collapses were due to scouring and flooding. Chanson (2004) points the example Mount Isa railway bridges in Australia in which several bridges failed due to erosion of pier foundations in early 1960s. Famous examples in France are the collapses of Wilson bridge (Tours) in 1978 (Figure 1-1) and the Saint-Etienne bridge (Reunion) in 2007 (Boujia 2018). According to Cerema (2019), the former was due to general scour, whilst the latter was result a of local scour.



Figure 1-1. Collapse of Wilson Bridge (Tours, France) in 1978 due to general scour; source: Cerema (2019)

1.2. Sediment transport and large-scale river morphology

From the previous section, it can be deduced that one of the primary applications of sediment transport computations in rivers and channels is the prediction of their morphological evolutions. An example of a simple 1D system of equations appropriate for large-scale ($O(10-1000\text{km})$) morphological evolution in rivers is given below (Graf and Altinakar 1998, García 2008):

$$\frac{\partial h}{\partial t} + U \frac{\partial h}{\partial x} + h \frac{\partial U}{\partial x} = 0 \quad (1-1)$$

$$\frac{1}{g} \frac{\partial U}{\partial t} + \frac{U}{g} \frac{\partial U}{\partial x} + \frac{\partial h}{\partial x} + \frac{\partial z}{\partial x} + S_f = 0 \quad (1-2)$$

$$(1 - p) \frac{\partial \eta}{\partial t} + \frac{\partial q_s}{\partial x} = 0 \quad (1-3)$$

h is the flow depth, U is the depth-averaged velocity, S_f is the energy slope, p is the porosity of the sediments of the bed, η is the vertical bed elevation, $q_s = \int_0^h \bar{c}\bar{u} dz = CUh$ is the total volumetric solid-load per meter width, including the bed-load and suspended load (see 1.3.4), representing the solid transport capacity at the given river reach. In numerical simulations, Eq. (1-3) is often employed adopting a bed-load function and introducing a net entrainment function, representing the net balance between erosion and deposition fluxes.

Because the tendency of a given river reach to degrade, aggrade or remain in equilibrium is directly related to the transport capacity, accurately quantifying q_s is of primary importance to predict the morphological evolution of rivers. The simplest numerical solution for solving river morphodynamics system of equations consists in solving the Saint-Venant equations for U and h , keeping the bed elevation constant during the time step Δt . Then, the Exner equation will provide the variation of the bed elevation after a given time step. This new elevation is then used to determine the new hydrodynamic conditions and the procedure is iterated (Cunge et al. 1980). This corresponds to an implicit coupling between the Saint-Venant equations and the Exner equation (Graf and Altinakar 1998). It becomes clear that the first step for large-scale prediction of morphological evolution is to have a robust hydrodynamic model, able to determine accurately the hydraulic variables in unsteady flow conditions, which poses its own challenges. The prediction of sediment transport capacity q_s has progressed in the last decades, with important contributions such as the simple models of Engelund and Hansen (1967), Ackers and White (1973) and van Rijn 1984 that perform better than most of the existing models (van Rijn 1993, Graf and Altinakar 1998). Nevertheless, accurate prediction of sediment load as product of velocity and concentration, is still considered as a scientific challenge even in idealized prismatic channels (non-evolving geometry in the streamwise direction) under steady flow over a plane bed (Lyn 2008). One of the main reasons lies in the limited understanding of small-scale processes, such as the turbulence-particle and particle-particle interactions, that may or not affect the open-channel flow as a turbulent shear boundary layer, depending on the flow and particle characteristics. This framework becomes even more complex when dealing with natural river systems. One well-known problem is the reduction of transport capacity due to the progressive accumulation of larger particles over smaller ones, which are entrained under lower bed shear stress. This leads to a coarser protective layer on the surface, which inhibits the transport of smaller particle beneath it, until a strong event with ability

to carry the large particles occurs. This phenomenon is termed *armor*ing (Graf 1984), and occurs when the bed material is non-uniform, mainly in gravel-bed streams (Parker 2008). One way of accounting for it, is the introduction of hiding functions (Egiazaroff 1965, Parker et al. 1982), when determining the threshold of movement. Additionally, the hiding factor has been introduced directly in several formulations of bed-load models (Einstein 1950, Wu et al. 2000). An aspect related to the previous point is the modelling of non-uniform sediment distribution. For this problem, one classical solution is to define around five grain classes, and solve the problem for each grain class separately (Graf and Altinakar 1998). The total load will be the sum of the transported sediments in each class. van Rijn (1993) referred that this procedure is recommended when $d_{90}/d_{50} \geq 5$, and that the correction factor should be applied for each grain class, to account for non-uniformity of sediment distribution.

It should be stressed that the difficulties in developing large-scale models for practical applications is not linked only with the theoretical limitations in describing the processes referred above. Data availability is also a major problem in the field of sediment transport. For example, bed-load measurements are very rare because they are technically difficult to perform, and even the established trap sampling techniques (Bed-load Transport Meter Arnhem, Helley Smith Sampler, Delft Nile Sampler) present large deficiencies and uncertainties (van Rijn 1993). Suspended-load is often obtained by bottle and trap samplers (bottle sampler, USP-61, Delft bottle) or using turbidity measurements, but the latter it is limited to relatively low concentration. Generally, reliable measurements are necessary to develop solid-load rating curves and to calibrate or validate model results.

From the discussion above, it can be deduced that reliable predictions of large-scale morphological evolution in rivers requires accurate description of the hydrodynamics and coupled solid-load. Several factors make it difficult to predict hydraulic variables accurately, notably the complex geometry of rivers, with pools and other macro-roughness elements that make them distinct from the simplified prismatic channels of uniform roughness and slope. On the other hand, the determination of q_s in rivers poses challenges that go beyond the adequacy of a given model for transport capacity estimations, for example, non-uniformity of sediments size, lack of reliable data on solid-load/concentration and bed elevation for calibration, etc. Having established the connexion between the large-scale and small-scale sediment processes, we will focus on the latter as the subject of the present research.

1.3. State of the art

1.3.1. Momentum equations of water-sediment mixture

Given that the velocity measurements performed in the present study are those of water-sediment mixture with no fluid-particle phase distinction, the governing equations are those based on the Boussinesq approximation. The sediment presence is considered through density stratification via the sediment concentration gradients inducing local buoyancy forces. The momentum and TKE equations can be derived from the Navier-Stokes equations, which can be written as:

$$\frac{\partial u_i}{\partial t} + u_j \frac{\partial u_i}{\partial x_j} = \frac{\rho_m}{\rho} g_i - \frac{1}{\rho} \frac{\partial p}{\partial x_i} + \nu_m \frac{\partial^2 u_i}{\partial x_j \partial x_j} \quad (1-4)$$

where t is the time, g_i is gravitational acceleration in direction i , ν_m is the mixture kinematic viscosity, p is the pressure, u_i and u_j are the mixture velocities in directions x_i and x_j , respectively. In addition, $\rho_m = \rho_0 + (\rho_s - \rho_0)\bar{c}$ is the local mixture density, ρ_s and ρ_0 are the sediment and fluid densities, respectively. A reference density of the mixture ρ similar to the fluid is often adopted. If a fluid parcel is displaced from lower to higher vertical level, it has a tendency to move downwards under the action of gravity, whilst it tends to move upwards due to buoyancy, when displaced downwards. Hence, the typical sediment transport problem, where mixture density decreases with vertical distance from the bed is a stably stratified flow (Monin and Yaglom 1971). Herein, the equations will be derived for the streamwise component, before generalizing for all directions. The streamwise, spanwise and vertical velocities are defined by the coordinates $x_1 = x$, $x_2 = y$ and $x_3 = z$, respectively; it implies that $u_1 = u$, $u_2 = v$ and $u_3 = w$. Applying the Reynolds convention $u_i = \bar{u}_i + u'_i$ in the Navier-Stokes equations, the total equation for the streamwise velocity component is given as follows:

$$\begin{aligned} \frac{\partial(\bar{u} + u')}{\partial t} + (\bar{u} + u') \frac{\partial(\bar{u} + u')}{\partial x} + (\bar{v} + v') \frac{\partial(\bar{u} + u')}{\partial y} + (\bar{w} + w') \frac{\partial(\bar{u} + u')}{\partial z} \\ = \frac{(\bar{\rho} + \rho')}{\rho} g_x - \frac{1}{\rho} \frac{\partial(\bar{p} + p')}{\partial x} + \nu_m \left(\frac{\partial^2(\bar{u} + u')}{\partial x^2} + \frac{\partial^2(\bar{u} + u')}{\partial y^2} + \frac{\partial^2(\bar{u} + u')}{\partial z^2} \right) \end{aligned} \quad (1-5)$$

In this steady uniform flow the following simplifications are valid $\bar{v} = \bar{w} = \partial/\partial x = \partial/\partial y = 0$. The total equation becomes:

$$\frac{\partial(\bar{u} + u')}{\partial t} + w' \frac{\partial(\bar{u})}{\partial z} + w' \frac{\partial(u')}{\partial z} = \frac{(\bar{\rho} + \rho')}{\rho_m} g_x - \frac{1}{\rho} \frac{\partial(\bar{p} + p')}{\partial x} + \nu_m \left(\frac{\partial^2(\bar{u} + u')}{\partial z^2} \right) \quad (1-6)$$

If we take the mean of Eq. (1-6), recalling that $\bar{v}' = \bar{w}' = 0$, it holds the well-known Reynolds-Averaged-Navier-Stokes Equations (RANS). They are shown in terms of x and z directions, the only relevant momentum equations in 2D open-channel flows:

$$\frac{\partial(\bar{u})}{\partial t} + \frac{\partial(\overline{u'w'})}{\partial z} = \frac{\bar{\rho}}{\rho_m} g_x + \nu_m \left(\frac{\partial^2(\bar{u})}{\partial z^2} \right) \quad (1-7)$$

$$\frac{\partial(\bar{w})}{\partial t} + \frac{\partial(\overline{w'w'})}{\partial z} = \frac{\bar{\rho}}{\rho_m} g_z - \frac{1}{\rho} \frac{\partial(\bar{p})}{\partial z} + \nu_m \left(\frac{\partial^2(\bar{w})}{\partial z^2} \right) \quad (1-8)$$

Further simplifications due to flow steadiness and uniformity implies that $\partial/\partial t = \partial\bar{p}/\partial x = 0$. Multiplying the equations by ρ , taking the dynamic viscosity as $\mu = \nu\rho$ and $g_x = g\sin(\theta)$ and $g_z = g\cos(\theta)$ we obtain the following equations in the streamwise direction x and bed-normal w :

$$\frac{\partial(-\rho\overline{u'w'})}{\partial z} = -\mu \frac{\partial^2\bar{u}}{\partial z^2} - \rho g \sin \theta \quad (1-9)$$

The gravity term in the streamwise equation is negligibly affected in presence of sediments, such that the streamwise velocity is described by a similar equation in both CW and SL, except that the sediments may affect the term $-\rho u'w'$. Eq. (1-9) shows that the distribution of the streamwise velocity \bar{u} in uniform flows can be determined if $-\overline{u'w'}$ is known. This corresponds to the

turbulence closure problem, which should be solved employing turbulence models (Bradshaw 1971). Most of the turbulence models used for calculating open-channel flows employ the eddy-viscosity concept, which is based on the assumption that the turbulent stresses are proportional to the mean velocity gradients, in analogy to the viscous stresses in laminar flow. The Reynolds shear stress is then given by:

$$-\rho \overline{u'w'} = \epsilon_m \rho \frac{d\bar{u}}{dz} \quad (1-10)$$

where ϵ_m is the eddy viscosity, also known as momentum diffusivity or eddy diffusion coefficient, with units in m^2s^{-1} . The eddy viscosity can be regarded as the product of a velocity scale and a length scale. Thus, its specification can be expected to be in terms of the former or the latter. (Rodi 1993). Turbulence models exist in terms of algebraic specification of eddy viscosity, usually through a length scale (zero-equation models, for example the mixing length), differential specification through a velocity or length scale, often velocity through k (one-equation models), and differential specification through both scales (two-equation models, such as $k - \epsilon$, $k - \omega$, etc.). The difference in algebraic and differential specification is that the former does not include effects of history and transport. This implies that it assumes a local equilibrium, in which the eddy viscosity is only affected by local conditions (Lyn 2008). The mixing length and the $k - \epsilon$ will be discussed in chapters 4 and 5, respectively. Nevertheless, it can already be stated that the streamwise velocity distribution is classically described by the log-law, given by:

$$u = \frac{u_*}{\kappa} \ln \frac{z}{z_0} \quad (1-11)$$

where u is the streamwise velocity, u_* is the friction velocity, κ is the von Karman constant, z is the vertical distance from the bed, z_0 is the point from zero velocity. This equation was first proposed by Prandtl (1925), who employed the mixing length model. The assumptions and limitations of the model, which is employed also in the derivation of sediment suspension equations, will be further discussed in chapter 4.

We can show the theoretical evidence that in uniform open-channel flows, the Reynolds shear stress (and the total stress) is linearly distributed over the flow depth. We can re-write Eq. (1-9) as:

$$-\frac{d}{dz} \left[\mu \frac{d\bar{u}}{dz} + (-\rho \overline{u'w'}) \right] = \frac{\tau_0}{H_f} \quad (1-12)$$

where the terms inside the brackets correspond to the total shear stress τ , including its viscous τ_v (the first term inside the brackets) and the turbulent τ_{xz} parts (the second term), such that $\tau = \tau_v + \tau_{xz}$. On the right-hand side, H_f is the flow depth and τ_0 is the bed shear stress. By performing a balance between the gravity force and the friction forces in uniform flow, the bed shear stress can be expressed as $\tau_0 = \rho g H_f \sin \theta$. The streamwise momentum equation becomes:

$$-\frac{d\tau}{dz} = \rho g \sin \theta = \frac{\tau_0}{H_f} \quad (1-13)$$

Integrating, it yields:

$$\tau = -\frac{\tau_0}{H_f} \int_{H_f}^z dz = -\frac{\tau_0}{H_f} (z - H_f) = \tau_0 \left(1 - \frac{z}{H_f} \right) \quad (1-14)$$

Eq. (1-14) shows that in uniform open-channel flows the total shear stress increases linearly from zero at the free surface ($z=H_f$) to maximum values in the near-bed region ($z=0$). Because the viscous effects are negligible except in the near-bed region, the distribution of the total shear stress and its turbulent component (Reynolds shear stress) remains rather similar throughout most of the flow depth.

1.3.2. Turbulent kinetic energy (TKE) equations of water-sediment mixture

The subtraction of the mean momentum equation from the total equations holds the momentum equation of the velocity fluctuations:

$$\frac{\partial(u')}{\partial t} + w' \frac{\partial(\bar{u})}{\partial z} + w' \frac{\partial(u')}{\partial z} - \frac{\partial(\overline{u'w'})}{\partial z} = \frac{\rho'}{\rho} g_x - \frac{1}{\rho} \frac{\partial(p')}{\partial x} + \nu_m \left(\frac{\partial^2(u')}{\partial x^2} + \frac{\partial^2(u')}{\partial y^2} + \frac{\partial^2(u')}{\partial z^2} \right) \quad (1-15)$$

The complete viscous term has been reintroduced in the last term on the right-hand side to illustrate the complete term of viscous dissipation. It is important because it is associated with the mean dissipation rate, as it will be shown below. If we multiply the turbulent momentum equation by the velocity fluctuation and perform the averaging, we obtain the equation of the streamwise component of TKE ($1/2\overline{u'^2}$). This becomes clear if we recall the following relationship:

$$\overline{u' \frac{\partial u'}{\partial t}} = \frac{\partial}{\partial t} \left(\overline{\frac{1}{2} u'^2} \right) \quad (1-16)$$

An important algebraic manipulation concerns the last term, which gives rise to two different terms, including the viscous dissipation rate. The demonstration will be made only for the term containing $\partial/\partial z$. From the product of the second order derivative, we can write:

$$\overline{u' \left(\frac{\partial^2 u'}{\partial z^2} \right)} = \nu_m \left(\overline{u' \frac{\partial^2 u'}{\partial z^2}} + 2 \frac{\partial \overline{u'}}{\partial z} \frac{\partial \overline{u'}}{\partial z} + \overline{u' \frac{\partial^2 u'}{\partial z^2}} \right) \quad (1-17)$$

that leads to:

$$\nu_m \left(\overline{u' \frac{\partial^2 u'}{\partial z^2}} \right) = \nu_m \left(\frac{\partial^2 (\overline{1/2 u'^2})}{\partial z^2} - \frac{\partial \overline{u'}}{\partial z} \frac{\partial \overline{u'}}{\partial z} \right) \quad (1-18)$$

Further details on the derivation of the TKE equation in stratified flows following the described method can be found in the literature (Monin and Yaglom 1971, Kundu and Cohen, 1990, Guo and Julien, 2001). The equations for the turbulent kinetic energy associated with each velocity component are given as follows:

$$\begin{aligned} \overline{u' \frac{\partial(u')}{\partial t}} + \overline{u'w' \frac{\partial \bar{u}}{\partial z}} + \frac{\partial \overline{(w'u'u')}}{\partial z} - \overline{u' \frac{\partial(\overline{u'w'})}{\partial z}} \\ = \overline{u' \frac{\rho'}{\rho_m} g_x} - \overline{u' \frac{1}{\rho} \frac{\partial(p')}{\partial x}} + \nu_m \left(\overline{u' \frac{\partial^2(u')}{\partial x^2}} + \overline{u' \frac{\partial^2(u')}{\partial y^2}} + \overline{u' \frac{\partial^2(u')}{\partial z^2}} \right) \end{aligned} \quad (1-19)$$

Applying the same procedure for the other velocity components, we can give the equation of turbulent kinetic energy for each direction as follows:

$$\begin{aligned}
& \frac{\partial}{\partial t} \left(\frac{1}{2} \overline{u_i'^2} \right) + \overline{u'w'} \frac{\partial \bar{u}}{\partial z} + \frac{\partial \overline{(w'u'u')}}{\partial z} & (1-20) \\
& = 0 - \frac{1}{\rho} \frac{\partial \overline{(p'u')}}{\partial x} - \frac{1}{\rho} \overline{p'} \frac{\partial \overline{(u')}}{\partial x} + v_m \left(\frac{\partial^2 \overline{(u'u')}}{\partial x^2} + \frac{\partial^2 \overline{(u'u')}}{\partial y^2} + \frac{\partial^2 \overline{(u'u')}}{\partial z^2} \right) \\
& - v_m \left(\frac{\partial \overline{u'} \partial \overline{u'}}{\partial x \partial x} + \frac{\partial \overline{u'} \partial \overline{u'}}{\partial y \partial y} + \frac{\partial \overline{u'} \partial \overline{u'}}{\partial z \partial z} \right)
\end{aligned}$$

$$\begin{aligned}
& \frac{\partial}{\partial t} \left(\frac{1}{2} \overline{v_i'^2} \right) + \frac{\partial \overline{(w'v'v')}}{\partial z} & (1-21) \\
& = 0 - \frac{1}{\rho} \frac{\partial \overline{(p'v')}}{\partial y} - \frac{1}{\rho} \overline{p'} \frac{\partial \overline{(v')}}{\partial y} + v_m \left(\frac{\partial^2 \overline{(v'v')}}{\partial x^2} + \frac{\partial^2 \overline{(v'v')}}{\partial y^2} + \frac{\partial^2 \overline{(v'v')}}{\partial z^2} \right) \\
& - v_m \left(\frac{\partial \overline{v'} \partial \overline{v'}}{\partial x \partial x} + \frac{\partial \overline{v'} \partial \overline{v'}}{\partial y \partial y} + \frac{\partial \overline{v'} \partial \overline{v'}}{\partial z \partial z} \right)
\end{aligned}$$

$$\begin{aligned}
& \frac{\partial}{\partial t} \left(\frac{1}{2} \overline{w_i'^2} \right) + \frac{\partial \overline{(w'w'w')}}{\partial z} & (1-22) \\
& = -(s-1) \overline{w'c'} g - \frac{1}{\rho} \frac{\partial \overline{(p'w')}}{\partial z} - \frac{1}{\rho} \overline{p'} \frac{\partial \overline{(w')}}{\partial z} + v_m \left(\frac{\partial^2 \overline{(w'w')}}{\partial x^2} + \frac{\partial^2 \overline{(w'w')}}{\partial y^2} + \frac{\partial^2 \overline{(w'w')}}{\partial z^2} \right) \\
& - v_m \left(\frac{\partial \overline{w'} \partial \overline{w'}}{\partial x \partial x} + \frac{\partial \overline{w'} \partial \overline{w'}}{\partial y \partial y} + \frac{\partial \overline{w'} \partial \overline{w'}}{\partial z \partial z} \right)
\end{aligned}$$

The first term on the left-hand side is the kinetic energy evolution of each velocity component of the TKE. The second term, the deformation work by turbulent stresses, represents the kinetic energy of the mean flow that is lost to the agency that generates the stress. Since turbulence stresses perform the deformation work, the agency that benefits from this loss of mean kinetic energy of the mean flow is the turbulent kinetic energy (Tennekes and Lumley 1972). Therefore, this term is the turbulent energy production. The third term is the turbulent energy diffusion by transport. The fourth term is the buoyancy or sediment suspension due to density fluctuations. It was derived as follows:

$$\frac{\overline{w'\rho'}}{\rho} g_z = \frac{\rho_s - \rho_0}{\rho} \overline{w'c'} g = -(s-1) \overline{w'c'} g \quad (1-23)$$

where $g_z = -g \cos(\theta) = -g$, for $\theta \ll 1$. Since the concentration field is homogeneous in x direction, the net turbulent solid fluxes are $\overline{u'c'} = \overline{v'c'} = 0$. The net turbulent solid flux $\overline{w'c'}$ is positive, and in equilibrium suspension, it is balanced by the downward settling flux $w_s \bar{c}$, as will be demonstrated in section 4.4, when deriving the equation for sediment concentration). A very important theoretical result is that $\overline{w'c'}$ only appears in the turbulent kinetic energy equation, and not in the mean kinetic energy equation. This indicates that turbulence governs the suspension of particles, rather than the mean flow. The fifth term is the pressure strain. The sixth term is energy diffusion by pressure fluctuations. The seventh term corresponds to the viscous transport of energy. The eighth term is the viscous dissipation. In this wall bounded shear flow, the turbulent kinetic energy is produced in the x direction, through the second term on the left-hand side. Other components ($1/2 \overline{v'^2}$ and $1/2 \overline{w'^2}$) get the energy by transfer performed by non-linear pressure-velocity interactions (Tennekes and Lumley 1972). It is also noteworthy that the effect of density fluctuations appear in the vertical equation of kinetic energy. Since it represents an energy loss, it

suggests that sediment transport may directly reduce the intensity of vertical velocity fluctuations. Summing the equations for each direction, we retrieve the mean TKE equation:

$$\frac{\partial k}{\partial t} = -\overline{u'w'} \frac{\partial \bar{u}}{\partial z} - (s-1)\overline{w'c'}g - \frac{\partial}{\partial z} \left(\overline{kw'} + \frac{1}{\rho} \overline{p'w'} - v_m \frac{\partial k}{\partial z} \right) - \varepsilon \quad (1-24)$$

Note that the pressure strain terms vanish in the equation of k due to continuity. The terms in parenthesis correspond to the sum of transport terms. Because the accuracy of $\overline{w'c'}$ in inertial conditions (velocity fluctuations of particles cannot be approximated to those of the fluid) is questionable, this term is replaced by $w_s \bar{c}$, that is measured with greater confidence. Without the measurement of transverse velocity, two common approximations for the turbulent diffusion term in 2D mean flows are $\overline{v'^2 w'} = 0.5(\overline{u'^2 w'} + \overline{w'^3})$ as given by Raupach (1981) or $\overline{v'^2 w'} = \overline{w'^3}$ as proposed by Nezu and Nakagawa (1993). Herein, the first approximation was considered, leading to:

$$F_k = \overline{kw'} = 3/4(\overline{u'^2 w'} + \overline{w'^3}) \quad (1-25)$$

In homogeneous turbulence, the mean dissipation rate is determined from Kolmogorov second hypothesis as:

$$\varepsilon = \left(\frac{E_u(k_u) \kappa_u^{5/3}}{C_1} \right)^{3/2} \quad (1-26)$$

where $E_u(u)$ is the one-dimensional energy spectra, k_u is the wave number, C_1 is a constant with a value of 0.5 (Monin and Yaglom, 1975, Pope, 2000). Obtaining $E_u(k_u)$ directly from measurements is very difficult. Instead, the spectra is measured in terms of frequency, $F_{11}(f)$, from the temporal velocity fluctuations u' . One can then apply Taylor's hypothesis of frozen turbulence (Townsend, 1976) to obtain the wave number one-dimensional spectra, as:

$$E_u(k_u) = \frac{\bar{u}}{2\pi} F_{11}(f) \text{ with } \kappa_u = \frac{2\pi f}{\bar{u}} \quad (1-27)$$

Thus, the local mean dissipation rate based on velocity fluctuations is given by:

$$\varepsilon = \frac{2\pi}{\bar{u}} \left(\frac{F_{11}(f) f^{5/3}}{C_1} \right)^{3/2} \quad (1-28)$$

If Eq. (1-24) is integrated along the vertical direction z , production is balanced by viscous dissipation and sediment suspension term. One crucial question in the stratified flow theory concerns the repartition of energy between these terms. This aspect will be discussed later in chapter 5.

1.3.3. Suspended sediment concentration equation

The sediment concentration can be obtained from the mass conservation equation, for the solid phase. For 2D flows, the latter is expressed by the following advection-diffusion equation:

$$\frac{\partial c}{\partial t} + \left(\bar{u} \frac{\partial \bar{c}}{\partial x} + \bar{w} \frac{\partial \bar{c}}{\partial z} \right) = \nu \left(\frac{\partial^2 \bar{c}}{\partial x^2} + \frac{\partial^2 \bar{c}}{\partial z^2} \right) - \left(\frac{\partial \overline{u'c'}}{\partial x} + \frac{\partial \overline{w'c'}}{\partial z} \right) \quad (1-29)$$

where the first and second terms on the left-hand side represent the local rate of change of sediment concentration and the advection of concentration, respectively. The first and second terms on the right-hand side are the molecular and turbulent diffusion of concentration, respectively. The molecular diffusion is negligible compared to turbulent mixing. In addition, in steady uniform flow, $\partial/\partial t = \partial/\partial x = 0$. Therefore, following Rouse (1938), the equation for suspended sediment distribution can be obtained from the equilibrium between the upward ($\overline{c'w'} = \epsilon_s d\bar{c}/dz$) and downward ($w_s \bar{c}$) sediment fluxes:

$$w_s \bar{c} + \epsilon_s \frac{\partial \bar{c}}{\partial z} = 0 \quad (1-30)$$

Rearranging, and taking $\epsilon_s = \beta \epsilon_{ms}$ one can write:

$$\int_{C_a}^c \frac{d\bar{c}}{\bar{c}} = -w_s \int_a^z \frac{dz}{\beta \epsilon_{ms}} \quad (1-31)$$

To obtain the concentration profile, Eq.(1-32) is usually integrated using the parabolic eddy-viscosity (as will be demonstrated later in chapter 4) $\epsilon_{ms} = \kappa_s u_* z (1 - z/H_f)$, which yields the so-called Rouse equation:

$$\frac{\bar{c}}{C_a} = \left(\frac{H_f - z}{z} \frac{a}{H_f - a} \right)^{\frac{w_s}{\beta \kappa_s u_*}} \quad (1-32)$$

where C_a is a reference concentration at a vertical elevation $z=a$ at the top of the bed-load layer (beginning of suspended-load), w_s is the settling velocity, β is the inverse of Schmidt number. It is traditionally taken as $a \approx 0.05H_f$ or $a \approx 2d_p$ (García 2008). The exponent $Z_R = w_s/(\beta \kappa_s u_*)$ is often referred to as the Rouse number. The Rouse profile is valid in the suspension layer.

1.3.4. Intense sediment transport: physical description of the phenomena

Sediment transport occurs in different modes, namely bed-load, suspended load and wash-load. In the first mode, particles move near the bed, by saltation, rolling and sliding, whereas in the second mode flow turbulence is the main driver of particle motion. The third mode is restricted to very fine particles transported at low concentrations as tracers, with negligible effects on hydrodynamics, and will not be treated in the present study. The Shields number θ is the most used dimensionless parameter to characterize the intensity of sediment transport. It represents the ratio between the bed shear force and its submerged weight:

$$\theta = \frac{\tau_0}{(\gamma_s - \gamma)d_p} \quad (1-33)$$

where τ_0 is the bed shear stress, d_p is the particle diameter, γ_s and γ are the specific weight of particle and water, respectively. The ratio between the shear/friction velocity (u_*) and the settling velocity (w_s), also termed suspension number (w_s/u_*), indicates the importance of suspended load. These different modes of transport generally co-exist, but the intensity or dominance of each mode is often evaluated using these dimensionless numbers. Naturally, the threshold conditions for occurrence of bed-load and suspended-load are commonly reported based on θ and w_s/u_* . The Shields diagram establishes the condition of incipient motion, through the identification of the critical Shields number θ_c . It was found that it depends on the Reynolds particle number $R_p = u_* d_{50}/\nu$ (ν is the kinematic viscosity). The value for sand and gravel particles is around $\theta_c \approx 0.03 - 0.05$. This delineation can only be performed approximatively, since the definition of the incipient condition itself is subjective, based on visual observations (Graf 1984). With increasing Shields number θ , compared to the critical value θ_c , the solid-transport becomes more intense and the physical processes may differ from the low intensity bed-load transport. Generally, at low values of θ , bedforms (ripples or dunes) develop and the transport will occur primarily as bed-load. As the bed shear stress increases, bedforms are washed out and particles are transported both as bed-load and suspended-load. This high Shields regime without bed forms is termed upper plane bed or sheet-flow regime (García 2008). In this regime, an important fraction of transport occurs in the high concentration region, the sheet-flow/bed-load layer. Furthermore, the solid transport processes are reported to differ from the low Shields number regime (Wilson 1987, 1989). This is further discussed in chapter 4.

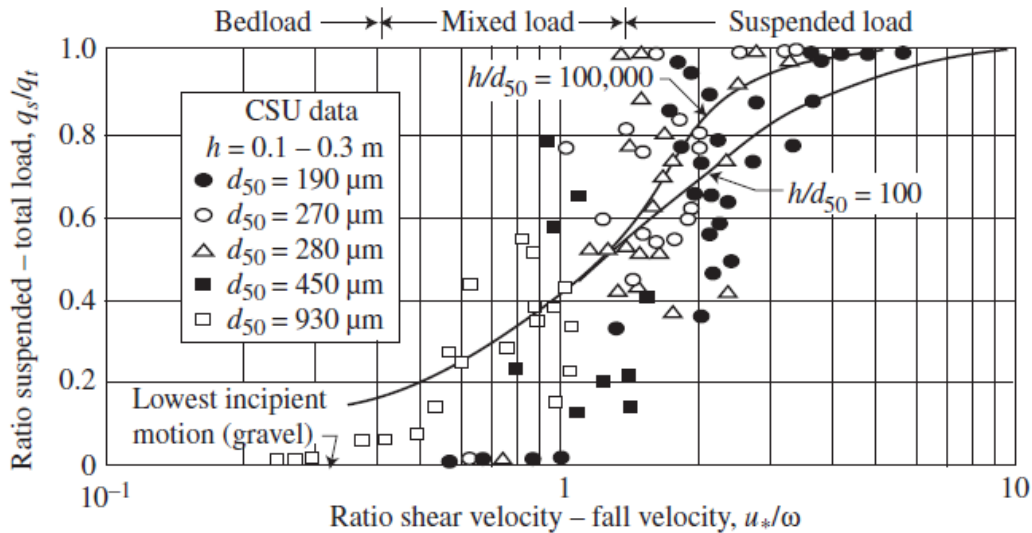


Figure 1-2. Proportion of suspended-load on the total solid-load versus the ratio u_*/w_s (adapted from Julien 2018).

1.3.5. Sediment transport in turbulent rough open-channel flows

As seen previously, the solid-load (per meter of width) can be determined by depth-averaging the product of flow velocity and concentration over the flow depth. Therefore, it is crucial to accurately describing the flow and concentration fields. We will consider the flow over plane bed. This should be recognized as a great simplification of real systems, although the high bed shear conditions studied herein are associated with a prevalence of the upper flow regime, in which the dunes are washed out. The equations to describe the flow velocity and concentration in a steady turbulent flow are known. They are the log-law (Eq. (1-11)) and the Rouse profile (Eq. (1-32)). Both equations are based on the linear mixing length model proposed by Prandtl. However, the modifications of the turbulent boundary layer in intense sediment-laden flow conditions implies greater efforts in the parametrization of these equations.

A key assumption is that the sediment and the fluid have the same streamwise velocities, but they are distinct in the vertical direction due to gravitational particle settling (Garcia 2008). It is well recognized that in the bed-load layer, particle-particle (granular) interactions are important in the transfer of momentum, whereas in the dilute suspension turbulence-particle interactions are the dominant transport mechanism. Therefore, depending on the flow conditions and solid transport regime (concentration), the referred processes will have more or less impact on the overall flow structure. As result, some parameters in these equations may present significant variability. Concerning the velocity prediction, there is still debate on the universality of the value of the von Karman constant κ . Its reduction in sediment-laden flows has been reported in early studies (Vanoni 1946) and more recently based on experimental (Dey 2014, Revil-Baudard et al. 2015, 2016) and numerical evidence (Cheng et al. 2018). However, Coleman (1981) and Graf and Cellino (2002) argued that the universal value ($\kappa \approx 0.4$) provides good results, if the wake coefficient due to free-surface flow effects is properly evaluated. The universality of this parameter was further supported recently by (Garcia 2008). Another challenge concerns the concentration profile prediction. Although the Rouse profile is a physically based model, it is often required to tune the β -factor, which describes the ratio between particle and momentum diffusivities (Cellino & Graf 1999).

Figure 1-3 is a schematic representation of smooth and rough flows in open channel flows. It should be mentioned that even in clear-water, the description of turbulent flows in rough open-channels might be challenging. Differently from smooth flows that have been much studied, the understanding of turbulent processes in rough flows is less developed. This include some basic questions such as the appropriate origin level in presence of a roughness canopy, or a more fundamental aspect such as the turbulence production close to rough surfaces. The former question has implications on the parametrization of the log-law, particularly z_0 . The latter is related to the bursting phenomena, known to be at the origin of turbulence production, as result of instabilities of the viscous sublayer, that lead to the collapse of low speed streaks and violent ejections of parcels of slow moving fluid into the main flow region. In fully rough flows, the viscous sublayer is suppressed, but sweeps and ejections are still important in shear production, suggesting that different turbulent processes occur in smooth and rough flows Nezu and Nakagawa (1993). More details on this aspect will be discussed in chapter 6.

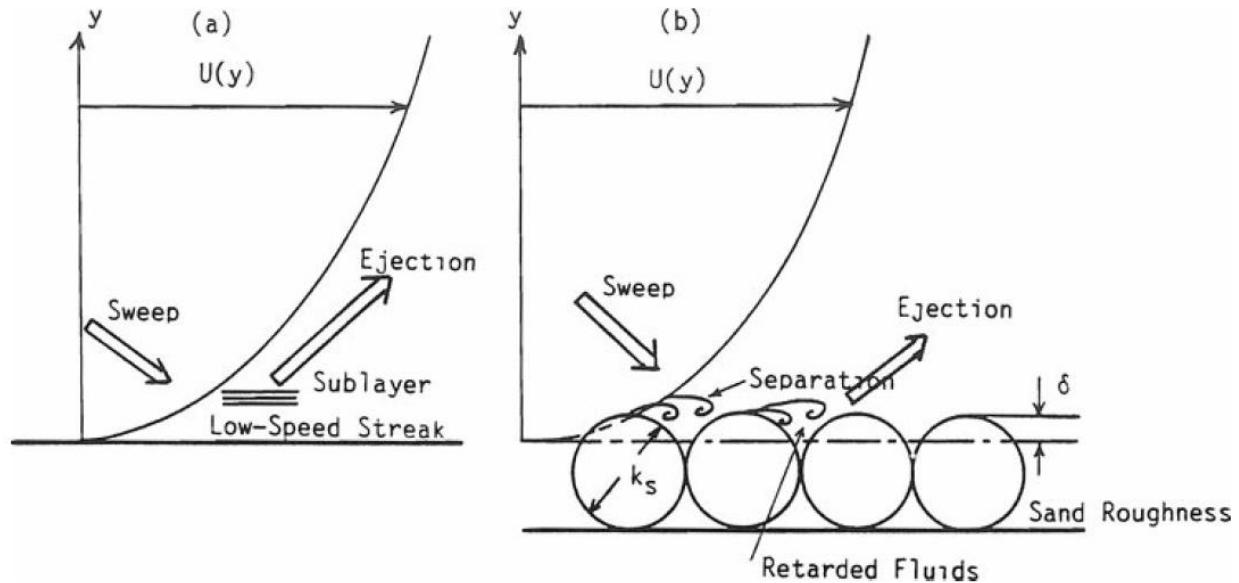


Figure 1-3. Scheme of turbulent flow over smooth (a) and rough (b) beds (from Nezu and Nakagawa 1993)

1.3.6. Velocity and concentration measurements in open-channel flows

A non-exhaustive summary of the experimental works in high Reynolds number open-channel flows is given here. The cited studies concern mainly suspension open-channel flows (dominated by suspended-load), but reference is also made to studies addressing velocity and concentration fields in flows with bed-load and sheet-flow layers.

Detailed experimental studies on suspended-load distribution in flumes started with the classical work of Vanoni (1946). Shortly after, Brooks (1954), Barton and Lin (1955) and Einstein and Chien (1955) provided further information on velocity and concentration distribution in sediment-laden open-channel flows. In these studies, the particles were added gradually, and they concerned mostly starved-bed conditions, with only few runs near capacity. Generally, they did not consist of equilibrium bed experiments (bed constituted of particles at rest). The flow measurements concerned only the mean streamwise velocity with a Pitot-tube and the concentration profiles were often comprised of sparse measurements points, obtained with suction techniques. Nevertheless, these early studies provided very important information on the log-law (Eq. (1-11)) and the Rouse profile (Eq. (1-32)). They identified already the potential effects of sediments on the velocity distribution. Furthermore, they were crucial in the validation of the Rouse equation. In order to verify the basic assumptions of the Rousean formulation, Coleman (1970) presented the profiles of the sediment diffusivity, based on both field and flume data. He provided experimental quantitative evidence of the near parabolic distribution of sediment diffusivity, as one of the most important assumptions taken in the Rouse profile.

To further advance the understanding of the solid transport processes in energetic conditions, improvements in the measurements capabilities and the associated spatio-temporal resolution, were essential. Lyn (1986) was among the first to present datasets of velocity and concentration measurements both below capacity and in equilibrium beds. In these equilibrium bed experiments, the bed was covered by a layer of natural sand of approximately $20-30d_p$. Laser Doppler

Velocimetry (LDV) system and a suction method were applied to measure profiles of two velocity components and concentration, respectively. Information on some turbulence quantities, such as the Reynolds stresses were provided. In the highest concentration experiments, the reliability of the measurements for $z/H_f < 0.2$ was no longer guaranteed. No measurements below $z/H_f = 0.1$ were reported. The measurement system was considered as not suitable for velocity measurements inside the bed-load layer. Sumer et al. (1996) used a Pitot tube and conductivity concentration meter to measure the streamwise velocity component and concentration, respectively, in the very challenging sheet-flow regime. They were able to estimate the flow velocity over the entire boundary layer, including the bed-load layer, only for the experiments with large plastic particles ($d_p = 2.5$ and 3 mm). Only few of their experiments had a free surface, most of them having a lid as the upper flow boundary (duct flow). Furthermore, the free-surface experiments were significantly less energetic than the duct flows. Other experimental studies in intense bed-load regime were done by Wilson (1987) and Nnadi and Wilson (1997), in pressurized flows.

Flow measurements using acoustic systems became a common practice by river monitoring agencies. The devices employed in large-scale measurements campaign are the Acoustic Doppler Current Profilers (ADCP). These are composed of several monostatic (emitter = receiver) divergent beams, and are adapted for measuring flow velocities over flow depth $h > 0.5$ m. Nevertheless, they are not suitable for turbulence measurements. The divergent beams do not allow obtaining more than one velocity component in the same sampling volume, and the resolution (temporal-spatial) is not adapted to describe the high frequency velocity fluctuations of the small turbulent eddies. For this purpose, Acoustic Doppler Velocity (ADV) and Acoustic Doppler Velocity Profilers (ADVP) have been applied intensively. The difference between ADVs and ADVPs is that the former perform turbulence measurements at single position whereas the latter provide profiles over a given vertical range of multi-component velocity field. Some systems provide co-located two (2C) or three (3C) velocity component measurements depending on the number of acoustic transducer used as transmitter and / or receiver. For ADVPs, the vertical profiling range varies from several cm to about 30 cm dependent on the system sensor and hardware characteristics (see section 2.3.4 for further details). These systems (mainly ADVs) have become a standard measurement technology for mean flow and turbulence estimations in open-channel flows.

ADVPs can also be used for measuring solid fluxes when sediment concentration profiling based on Acoustic Backscattering System technology is integrated into the system. One of the first systems was designed by Shen and Lemmin (1997) as the Acoustic Sediment Flux Profiler (ASFP) providing simultaneously velocity and suspended sediment concentration measurements, in the same insonified sampling volume. With this ASFP system, the first large dataset of high resolution flow and concentration measurements were presented by Cellino and Graf (1999) and Graf and Cellino (2002) in sediment-laden uniform and steady open-channel flows. They measured turbulent particle flux profiles limited to the suspension layer, combined with suction sampling techniques for the mean concentration profiles, to provide unique sediment and momentum diffusivity profiles and their depth-averaged ratio as the β -factor (inverse turbulent Schmidt number in Eq. (1-32)). They have reported turbulence characteristics over a wide range of hydraulic conditions with high Reynolds number ($Re \approx 2 - 3 \times 10^5$), in fully suspension dominated sediment-laden flows ($w_s/u_* \approx 0.2 - 0.5$). Revil-Baudard et al. (2015, 2016) performed detailed measurements with another ADVP system developed by Hurther et al. (2011) as the Acoustic Concentration and Velocity Profiler system (ACVP). They focused on properties of sheet flows over mobile granular beds (*i.e.* under capacity conditions) by presenting mean profiles of streamwise velocity, sediment

concentration and sediment flux, as well as some of the main turbulence quantities, namely, the Reynolds stresses, turbulent mixing length, momentum and sediment diffusivities, turbulent Schmidt number as well as coherent flow structure quantities such as quadrant threshold distributions (addressed in Chapter 6). The high performance electronic and software designs of this ACVP system allowed significant improvements in terms of spatial and temporal measurement resolution (1.5mm and up to 100Hz instead of 6mm and 25Hz) and data inversion methodologies (Bricault 2006). This offered the, at time unique, ability to explore sediment flux profiles not only in the dilute suspension layer but it could be extended into the bed-load layer. This measurement performances opened new perspectives in process oriented sediment transport research in a variety of river (Naqshband et al. 2014, Fromant et al. 2018, Chauchat et al. 2022) and coastal wave-driven flows (Hurther and Thorne 2011, Chassagneux and Hurther 2014, van der Zanden et al. 2018, van der A et al. 2017). Important limitations in the study of Revil-Baudard et al. (2015, 2016) were linked to the experimental protocol and facility performance inducing short experiment duration (120 s) for each run. These limitations imposed a repetition of many runs with an ensemble average procedure over the runs in order to get low statistical bias errors in the measured mean turbulent quantities. Because of this time demanding experimental protocol, the range of studied hydraulic and sediment transport parameters was very narrow. Blanckaert et al. (2017) used an ADV technology developed by Lemmin and Rolland (1997) to focus on velocity profile measurement inside the bed-load layer. The hydraulic conditions varied from no motion to intense transport with plane bed with high Reynolds number ($Re > 3 \times 10^5$). They concluded that in the bedload layer, the measured ADV velocities correspond to sediment velocities further confirming the ability of ADV systems to provide reliable measurements in dense bed-load layers.

1.4. PhD objectives and organisation

The first goal of the present doctoral research was to create a new dataset suitable for the analysis of fine-scale sediment transport processes. For this purpose, a new sediment-feeding unit was installed on the LEGI tilting flume, assuring a well-controlled injection of the solid-load. The ACVP technology was used as the main measurement technology in addition to other more standard flow measurement systems. This offered collection of co-located, simultaneous and time-resolved measurements of velocity components (2C), and particle concentration, both inside the bed-load and suspended-load layers, with a limited flow intrusion and perturbation. This represents a departure from virtually all previously acquired sediment-laden flows datasets.

The second main objective consisted in investigating the role of sediments on the modification of the open-channel flow structure and properties, by comparing the sediment-laden (SL) measurements to their reference clear-water (CW), performed under the exact same conditions, without any modification in the experimental setup. This is a requirement for improving our modelling capabilities. We focus on high bed-shear stress regimes ($\theta \geq 0.4$) with suspension numbers values of the order of $w_s/u_* \approx 0.4 - 1.3$. The transitional range ($0.8 < w_s/u_* < 1.3$) in which bed-load and suspended-load may have both important contributions haven been rarely investigated in details before despite their frequent occurrence in natural sediment-laden flows.

In the chapter 2, the experimental and methodological considerations are presented. This includes the procedures for the experiments and data processing. Results are presented from chapter 3 on, which reports the global features of the sediment-laden flows, as well as important modelling parameters. In the following chapter 4, we focus on the effects of the bed-load on the suspension

properties, due to the development of a thick bed-load layer. It concerns only the experiments with the larger particles ($d_p=3\text{mm}$). Further details on the turbulent flow features are analysed in the following chapters. In chapter 5, the turbulent kinetic energy budget is analysed, whilst the dynamics of coherent flow structures are investigated in chapter 6. Summary of the main results, conclusions and perspectives are given in chapter 7.

2. Experimental and methodological considerations

In this chapter, information about the experiments and data processing methodology is presented. It includes the description of the experimental facility, the procedure of the experiments, the studied flow conditions, as well as some considerations regarding the data processing, particularly, the calibration of the system for solid-load measurements, the bed detection method and the noise correction.

2.1. Experimental setup

The experiments were carried out at the LEGI/ENSE3 tilting flume. The flume is 10 m long and 0.35 m wide (see Figure 2-1 and Figure 2-2). The particles are made of Poly-Methyl MethAcrylate (PMMA) with a density $\rho_s = 1192 \text{ kg/m}^3$. The median diameters are $dp=1\text{mm}$ (dp1) and $dp=3\text{mm}$ (dp3). The measured settling velocity for dp3 in still water is $w_s = 5.6 \text{ cm/s}$, with an uncertainty of less than 17% estimated experimentally in Revil-Baudard (2015). The measured w_s (for dp3) is about 45% lower than predicted by standard formulas in the literature, notably Wu and Wang (2006) and Camenen (2007). Given that dp1 corresponds to the same type of particles (same manufacturer with same manufacturing procedure) but with a smaller diameter, w_s for dp1 was estimated by the referred formulas, applying the same reduction factor of 1.45. This leads to a $w_s \approx 2.2 \text{ cm/s}$, with assumed uncertainty of about 17%, as for dp3. The fixed bed is covered by glued PMMA particles, with $dp=3\text{mm}$.

From the depth-averaged flow quantities presented in Table 2-1 and Table 2-2, the flow may be characterized as highly turbulent ($Re = 4UR_h/\nu \gg 2000$, R_h is the hydraulic radius and ν is the kinematic viscosity), hydraulically rough (roughness Reynolds number: $Re_* = u_*k_s/\nu > 70$, with the following approximation for the roughness height $k_s \approx d_p$) and subcritical (Froude number: $Fr = U/\sqrt{gH_f} < 1$). To enhance the full development of the turbulent boundary layer, a honeycomb at the flume inlet, followed by a macro-roughness bed surface extended over about 50 cm are used. The sediment injection point is located 5.50 m upstream the measurement section for reaching fully developed sediment transport conditions in the flow transverse and vertical directions.

The water discharge Q and the slope S_0 control the flow conditions. The discharge is measured by a triangular weir installed in a chamber downstream the flume and the flow rate can be adjusted through a regulating valve upstream the flume inlet. The slope can be adjusted by modifying the vertical level at a regulation point located 5.6 m downstream the pivotal point. At the regulation point, a submillimetric scale allows to set the height difference Δh for the desired flume bed slope S_0 , such that $S_0 = \Delta h/5.6$.

The measurement section was deliberately placed far enough from the channel inlet so that the turbulent boundary layer was fully developed in the measurement section. Nevertheless, a minimum distance from the outlet was also respected (about 3m upstream), to avoid the region of

high flow sensitivity to the flume outlet conditions. This region is usually associated with flow non-uniformities contrary to the aimed uniform flow conditions. The bottom level at the outlet can be adjusted to control the outlet water level. The influence of the outlet flow conditions was determined by measuring the backwater profile (not shown here), corresponding to different outlet water levels. Simple 1D-flow simulations complemented and confirmed the experimental tests. The measurement section with well-established uniform flows was found at 3 m from the flume outlet and about 7 m from the inlet.

The normal open-channel flow depth for the desired flow conditions were predicted using the Manning-Strickler equation (Chow 1959, Henderson 1966). Generally, a relatively good agreement (relative differences less than 10%) between the predicted and measured flow conditions was confirmed. An exception was the hydraulic regime with the smaller energy slopes. In these configurations, deviations from the predicted conditions were noticeable. We attribute these deviations to the higher sensitivity of the flow to the bed irregularities when the mean bed slope S_0 becomes too low.

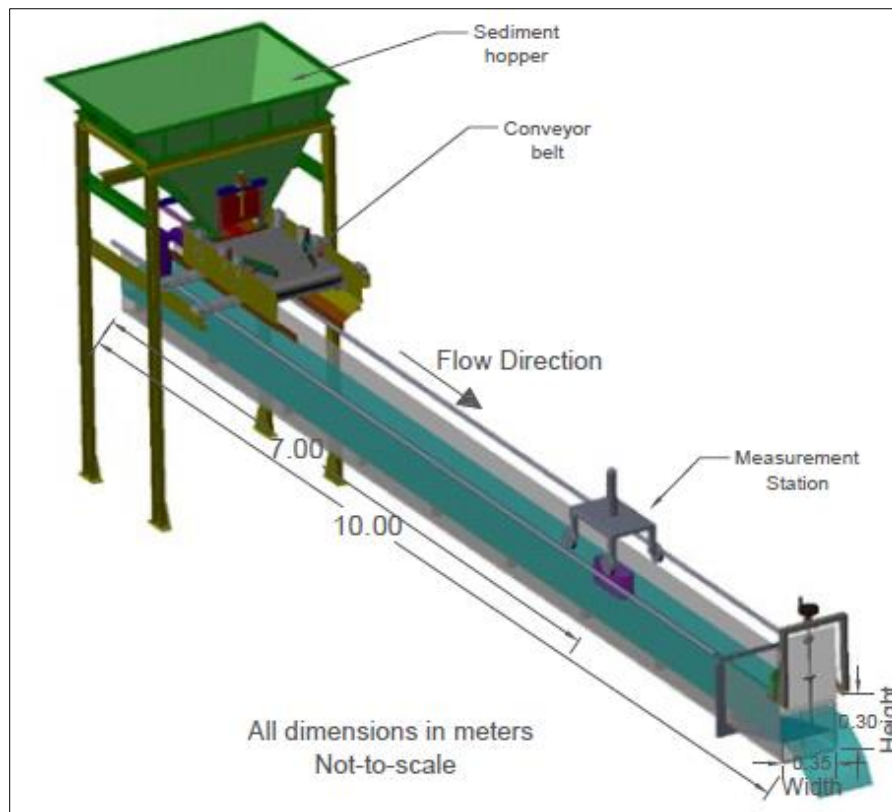


Figure 2-1. Sketch of experimental set up

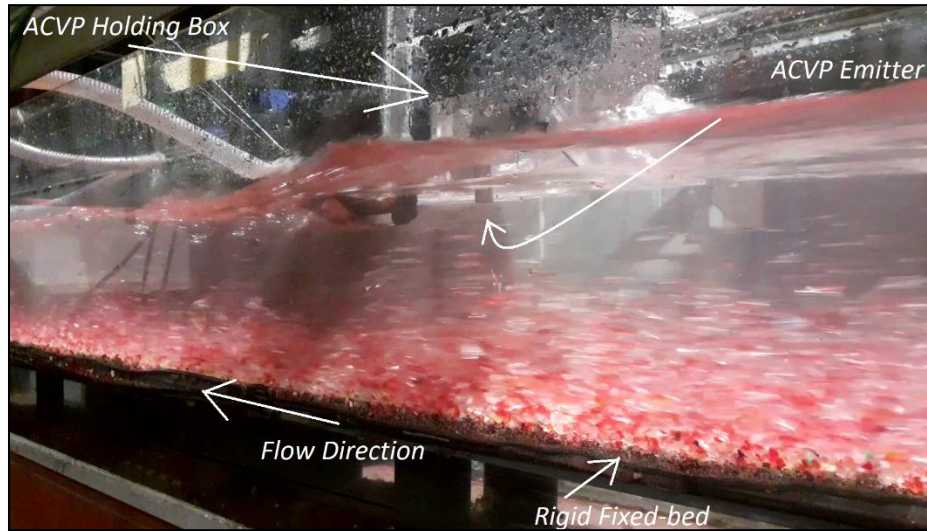


Figure 2-2. Photo of the flume during a sediment-laden experimental run ($d_p=3\text{mm}$)

2.2. Experimental protocol and flow conditions

In this subsection, details concerning the experimental protocol are provided. The experimental protocol and most procedures were defined before the first measurement campaign with the large particles d_p3 . Hence, in the descriptions that will follow, often reference will be made to the calibration and verifications carried out with d_p3 .

2.2.1. Sediment feeding system

A sediment feeder is used for continuously injecting a pre-determined solid-load flux into the flow. The solid-load injection is controlled by two parameters, the outlet vane of the sediment container defining the amount of sediments deposited on a conveyor belt and the speed of the conveyor belt injecting the sediment layer into the open-channel flow. The speed of the conveyor belt is set by the electric supply voltage of its step motor. A calibration relation was established between electric voltage - speed - injected solid-load time rate. After determining a relationship of conveyor belt voltage - speed, a relationship voltage - q_{injected} was obtained independently. The injected solid-load was defined as the (packed) volume of sediment collected in a bucket divided by the corresponding time interval of filling. Since the graduated bucket has a maximum capacity of 12 litres, it limited the duration of the tests to 40 to 240 s, depending on the conveyor belt speed. The referred durations are lower than the experimental runs (300 s), but the high stability in the functioning of feeding unit allows it to be representative of the injected mean solid-load flux over much longer durations. Regarding the uncertainties in estimating q_{injected} , the potential error in the measurement of the volume and the corresponding filling time were estimated as 0.5 l (constant for all measurements) and 1 s (increasing 2% for each decimal unit of voltage). The resulting uncertainties for the injected solid-load flux remained below 10%. As the used particles are similar to the one used in previous experiments (Revil-Baudard et al. 2015, Fromant et al. 2018), the same porosity of the packed bed ($p = 45\%$) is used. This imply a packed-bed volumetric concentration of 0.55. Figure 2-3 displays the relationship between supply voltage and injected solid-load for a given set of controlling parameters applied for d_p3 . It is observed that the solid discharge varies

linearly with the velocity, thus, one can set the tension according to the desired solid-load. The obtained calibration curve is valid for a given set of geometrical parameters of the sediment container output vanne, specifically the opening of vertical gate ($h_t=10.0$ mm) and the horizontal output section (fixed by the position of the horizontal output plate, $h_h=78.8$ mm) using wet sediments. Similar curves were determined for $dp1$.

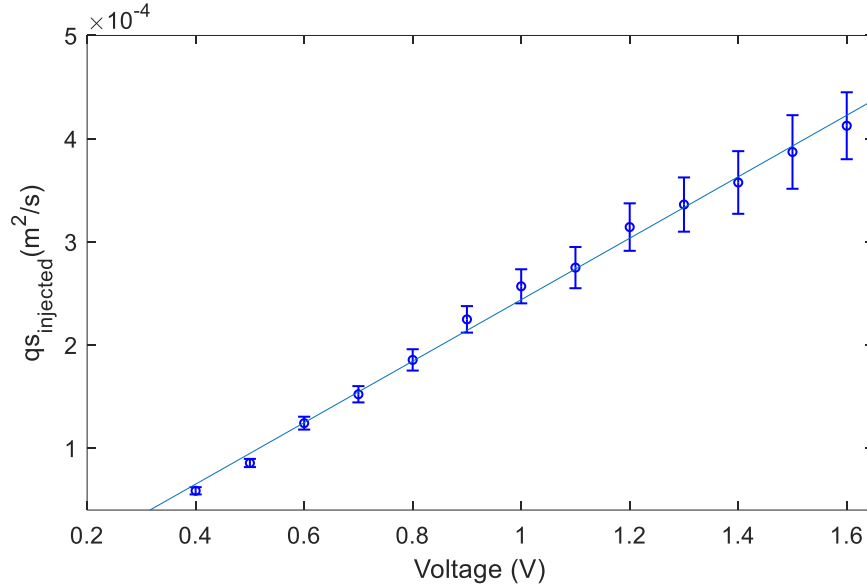


Figure 2-3. Calibration of solid-load (with $dp=3\text{mm}$) as function of voltage on the conveyor belt system. The uncertainties in each measured are represented independently, with a minimum of 5% (for Voltage = 0.4 V) and a maximum of 9% (for Voltage = 1.5 V).

The sediment injection conditions are different for $dp3$ and $dp1$. With the larger particles, the sediments were injected wet, whereas for small particles they were injected dry in order to avoid particle cohesion affecting injection control and stability. The larger particles were injected wet because of the limited total sediment quantity available and the too long time required for drying them in between the different runs. The recovered sediments at the flume output had to be re-injected in the hopper, and differences in humidity between the newly recovered sediments and the remaining dry sediments could have affected injection stability. Consequently, all 3mm sediments in the hopper were systematically watered and mixed before the experiments. This also implied that the calibration of the sediment feeding system were carried out with wet sediments for $dp3$ and dry sediments for $dp1$.

2.2.2. Experimental procedure

The measurements were carried out in sequences that started with a clear-water (CW) run, followed by one, two or three sediment-laden (SL) runs, with different sediment concentration (i.e. different qS_{injected} values). This ensured that all runs were performed in the exact same flow configuration and setup (i.e. without shutting down the flow nor the measuring systems between the CW and SL runs), with only the addition of sediments. The position of the fixed rigid bed (the zero vertical level) for all sediment-laden runs is identified based on the corresponding clear-water runs, because it is easier to detect it without a moving sediment layer covering the bed. Note that this is justified in the present conditions, given that there is no permanent deposition (no particles

at rest over the fixed rigid bed), even in capacity conditions. Once the CW run was completed, the feeding unit was turned on, beginning the injection of the sediments. Before starting the recording for the sediment-laden runs, a delay was necessary for the flow to return to stationary conditions. This time varied depending on the hydraulic and transport regimes, ranging between 60 – 90 s. It was estimated experimentally by analysing the time necessary for reaching a constant net sediment transport rate, from the ACVP measurements.

The sediment-laden open-channel flow study of Hurther and Lemmin (2003) carried out in a similar hydrodynamic regime has shown that a run duration of 180s was sufficient to obtain statistically converged measurements of mean Reynolds stresses, particle fluxes but also of their conditional statistics obtained from quadrant threshold methods. However, in order to further reduce the statistical bias error in the measured mean quantities, several open-channel turbulence studies (spectral analysis, third-order moments, etc.) used time durations of 300 s (Dey and Das 2012) or 600 s (Hurther and Lemmin 2001, Blanckaert and Lemmin 2006, Hurther, et al. 2007). Based on these considerations, the present collected datasets for each experiments have the duration of 300 s. The adequacy of this duration for turbulence analysis was verified in clear water flows by comparing the measured turbulent mean flow quantities obtained with 300s, including those in the TKE budget (*i.e.* up to third order velocity moments), with those obtained with a duration of 600s. The analysis was performed at the preparatory stage of the first measurement campaign, for the flow with the highest Reynolds number ($Re=2.9 \times 10^5$). Differences of the order of $O(1\%)$ were found even for the high order velocity moments. Hence, a 300s long duration was considered as sufficient and more appropriate from an experimental point of view.

As can be seen in Table 2-1 and Table 2-2, three flow conditions for each particle diameter were studied. For each flow condition, one clear-water and three sediment transport regimes, from lower concentration to saturation, are studied. The injected solid-load in saturation was defined experimentally as the beginning of sediment deposition at the bed (from visual observation). It corresponds to the condition for which significant increase in the injected solid-load would lead to continuous deposition of sediments on the bed. Since the convergence to full transport capacity is relatively subjective, the degree of saturation is to some extent uncertain (Lyn 1986). Hence, the saturated cases correspond to conditions near full-capacity regime. The injected solid-load Q_s^{inj} for the two regimes below capacity was determined from target values of mean volumetric concentration, given as the ratio between the injected solid-load and the flow discharge, such that $Q_s^{inj} = C^{inj} \times Q$. The defined mean volumetric concentrations are approximately $C^{inj} \approx 6 \times 10^{-4}$ and 2×10^{-3} , for the lower (LOW) and the intermediate (MED) solid-load cases, respectively. It was desired that the same values of mean concentration below capacity regimes were similar for all forcing conditions.

Three runs for each solid transport condition were acquired to confirm the repeatability of the results, leading to 9 solid-load runs for each hydraulic regime. This led to a total of 27 runs of sediment-laden flows for each particle diameter, hence, 54 SL for the two particle diameters. Table 2-1 and Table 2-2 show 87 runs discussed in the present report, from 103 runs acquired. The additional 16 runs not discussed herein are redundant. In the Appendix A, 12 out of these 16 redundant runs will be briefly presented. They correspond to capacity conditions, with $\theta \approx 0.35$ and $\theta \approx 0.5$ (with dp_3).

Table 2-1. Flow conditions and hydraulic parameters, for PMMA with $d_{50} = 3$ mm (d_{p3}): Note: u_* : friction velocity; θ : Shields number; S : suspension number (w_s/u_*); Q : flow discharge; S_0 : Slope of the channel; U : bulk mean velocity; H_f : water depth; Re : bulk Reynolds number; Re_* : Reynolds roughness number: bulk Reynolds number; Fr : Froude number; q_s : measured solid-load per unit width; \bar{C} : measured depth-averaged volumetric concentration;

Runs	u_* (m/s)	θ (-)	S (-)	Q (m ³ /s)	S_0 (-)	U (m/s)	H_f (m)	Re (-)	Fr (-)	Re_* (-)	q_s (m ² /s)	\bar{C}
P3S03D4_CW	0.047	0.39	1.2	0.032	0.0023	0.62	0.150	2.0x10 ⁵	0.51	141	-	-
P3S03D5_CW	0.043	0.32	1.3	0.032	0.0023	0.61	0.150	2.0x10 ⁵	0.50	128	-	-
P3S03D6_CW	0.043	0.33	1.3	0.032	0.0023	0.60	0.151	2.0x10 ⁵	0.50	129	-	-
P3S03D7_CW	0.042	0.31	1.3	0.032	0.0023	0.61	0.151	2.0x10 ⁵	0.50	126	-	-
P3S03D8_CW	0.042	0.31	1.3	0.032	0.0023	0.62	0.149	2.0x10 ⁵	0.51	126	-	-
P3S03D9_CW	0.043	0.33	1.3	0.032	0.0023	0.62	0.149	2.0x10 ⁵	0.51	130	-	-
P3S03D10_CW	0.045	0.36	1.2	0.032	0.0023	0.61	0.151	2.0x10 ⁵	0.50	135	-	-
P3S03D11_CW	0.043	0.33	1.3	0.032	0.0023	0.62	0.149	2.0x10 ⁵	0.51	130	-	-
P3S03D4_LOW	0.048	0.41	1.2	0.032	0.0023	0.62	0.150	2.0x10 ⁵	0.51	144	6.6x10 ⁻⁵	1.2x10 ⁻³
P3S03D5_LOW	0.043	0.32	1.3	0.032	0.0023	0.60	0.155	2.0x10 ⁵	0.48	128	7.2x10 ⁻⁵	1.3x10 ⁻³
P3S03D6_LOW	0.043	0.32	1.3	0.032	0.0023	0.60	0.155	2.0x10 ⁵	0.48	128	6.5x10 ⁻⁵	1.2x10 ⁻³
P3S03D4_MED	0.048	0.41	1.2	0.032	0.0023	0.62	0.150	2.0x10 ⁵	0.51	144	1.3x10 ⁻⁴	2.4x10 ⁻³
P3S03D7_MED	0.042	0.31	1.3	0.032	0.0023	0.60	0.155	2.0x10 ⁵	0.48	126	1.5x10 ⁻⁴	2.6x10 ⁻³
P3S03D8_MED	0.042	0.31	1.3	0.032	0.0023	0.61	0.153	2.0x10 ⁵	0.49	126	1.5x10 ⁻⁴	2.6x10 ⁻³
P3S03D9_SAT	0.044	0.34	1.3	0.032	0.0023	0.63	0.148	2.0x10 ⁵	0.52	131	2.5x10 ⁻⁴	4.3x10 ⁻³
P3S03D10_SAT	0.046	0.37	1.2	0.032	0.0023	0.62	0.151	2.0x10 ⁵	0.51	137	2.5x10 ⁻⁴	4.2x10 ⁻³
P3S03D11_SAT	0.043	0.33	1.3	0.032	0.0023	0.62	0.150	2.0x10 ⁵	0.51	130	2.4x10 ⁻⁴	3.8x10 ⁻³
P3S05D1_CW	0.048	0.41	1.2	0.041	0.0040	0.77	0.151	2.5x10 ⁵	0.63	144	-	-
P3S05D2_CW	0.050	0.44	1.1	0.041	0.0040	0.76	0.152	2.5x10 ⁵	0.62	150	-	-
P3S05D3_CW	0.054	0.52	1.0	0.041	0.0040	0.77	0.150	2.5x10 ⁵	0.64	162	-	-
P3S05D4_CW	0.055	0.54	1.0	0.041	0.0040	0.77	0.149	2.5x10 ⁵	0.64	165	-	-
P3S05D5_CW	0.055	0.54	1.0	0.041	0.0040	0.77	0.151	2.5x10 ⁵	0.63	166	-	-
P3S05D8_CW	0.054	0.51	1.0	0.041	0.0040	0.77	0.151	2.5x10 ⁵	0.63	161	-	-
P3S05D1_LOW	0.048	0.41	1.2	0.041	0.0040	0.77	0.150	2.5x10 ⁵	0.64	145	6.6x10 ⁻⁵	8.1x10 ⁻⁴
P3S05D2_LOW	0.047	0.39	1.2	0.041	0.0040	0.77	0.149	2.5x10 ⁵	0.64	141	6.5x10 ⁻⁵	8.0x10 ⁻⁴
P3S05D8_LOW	0.054	0.51	1.0	0.041	0.0040	0.76	0.152	2.5x10 ⁵	0.62	161	8.2x10 ⁻⁵	1.0x10 ⁻³
P3S05D1_MED	0.048	0.41	1.2	0.041	0.0040	0.78	0.149	2.5x10 ⁵	0.64	145	2.1x10 ⁻⁴	2.7x10 ⁻³
P3S05D2_MED	0.051	0.46	1.1	0.041	0.0040	0.77	0.151	2.5x10 ⁵	0.63	152	2.1x10 ⁻⁴	2.7x10 ⁻³
P3S05D8_MED	0.054	0.51	1.0	0.041	0.0040	0.77	0.150	2.5x10 ⁵	0.63	161	2.3x10 ⁻⁴	3.0x10 ⁻³
P3S05D3_SAT	0.054	0.52	1.0	0.041	0.0040	0.76	0.153	2.5x10 ⁵	0.62	162	3.9x10 ⁻⁴	4.6x10 ⁻³
P3S05D4_SAT	0.055	0.54	1.0	0.041	0.0040	0.75	0.154	2.5x10 ⁵	0.61	166	3.9x10 ⁻⁴	4.7x10 ⁻³
P3S05D5_SAT	0.055	0.54	1.0	0.041	0.0040	0.74	0.156	2.5x10 ⁵	0.60	166	4.4x10 ⁻⁴	5.3x10 ⁻³
P3S08D2_CW	0.070	0.87	0.8	0.048	0.0061	0.87	0.157	2.9x10 ⁵	0.70	210	-	-
P3S08D3_CW	0.078	1.08	0.7	0.048	0.0061	0.87	0.157	2.9x10 ⁵	0.70	234	-	-
P3S08D5_CW	0.068	0.82	0.8	0.048	0.0061	0.87	0.157	2.9x10 ⁵	0.70	204	-	-
P3S08D7_CW	0.071	0.89	0.8	0.048	0.0061	0.87	0.158	2.9x10 ⁵	0.70	212	-	-
P3S08D8_CW	0.071	0.90	0.8	0.048	0.0061	0.88	0.156	2.9x10 ⁵	0.71	214	-	-
P3S08D9_CW	0.074	0.98	0.8	0.048	0.0061	0.88	0.156	2.9x10 ⁵	0.71	223	-	-
P3S08D3_LOW	0.078	1.08	0.7	0.048	0.0061	0.89	0.155	2.9x10 ⁵	0.72	234	8.5x10 ⁻⁵	7.5x10 ⁻⁴
P3S08D7_LOW	0.071	0.89	0.8	0.048	0.0061	0.87	0.158	2.9x10 ⁵	0.70	212	1.0x10 ⁻⁴	9.6x10 ⁻⁴
P3S08D9_LOW	0.073	0.95	0.8	0.048	0.0061	0.88	0.157	2.9x10 ⁵	0.71	220	1.0x10 ⁻⁴	9.3x10 ⁻⁴
P3S08D2_MED	0.065	0.75	0.9	0.048	0.0061	0.89	0.154	2.9x10 ⁵	0.73	196	3.0x10 ⁻⁴	3.0x10 ⁻³
P3S08D8_MED	0.063	0.71	0.9	0.048	0.0061	0.89	0.154	2.9x10 ⁵	0.72	190	3.1x10 ⁻⁴	3.0x10 ⁻³

P3S08D9_MED	0.071	0.88	0.8	0.048	0.0061	0.89	0.155	2.9×10^5	0.72	212	3.3×10^{-4}	2.9×10^{-3}
P3S08D2_SAT	0.067	0.79	0.8	0.048	0.0061	0.89	0.154	2.9×10^5	0.73	201	1.0×10^{-3}	1.0×10^{-2}
P3S08D3_SAT	0.065	0.74	0.9	0.048	0.0061	0.88	0.155	2.9×10^5	0.72	194	9.5×10^{-4}	9.2×10^{-3}
P3S08D5_SAT	0.061	0.66	0.9	0.048	0.0061	0.88	0.156	2.9×10^5	0.71	183	9.4×10^{-4}	8.7×10^{-3}

Table 2-2. Flow conditions and hydraulic parameters, for PMMA with $d_{50} = 1$ mm (d_{p1})

Runs	u_* (m/s)	θ (-)	S (-)	Q (m ³ /s)	S_o (-)	U (m/s)	H_f (m)	Re (-)	Fr (-)	Re_* (-)	q_s (m ² /s)	\bar{C}
P1S04D1_CW	0.033	0.6	0.6	0.019	0.0007	0.40	0.134	1.2×10^5	0.35	99	-	-
P1S04D2_CW	0.033	0.6	0.6	0.019	0.0007	0.40	0.134	1.2×10^5	0.35	98	-	-
P1S04D3_CW	0.031	0.5	0.6	0.019	0.0007	0.40	0.134	1.2×10^5	0.35	92	-	-
P1S04D1_LOW	0.030	0.5	0.7	0.019	0.0007	0.40	0.134	1.2×10^5	0.35	90	2.8×10^{-5}	7.6×10^{-4}
P1S04D2_LOW	0.031	0.5	0.6	0.019	0.0007	0.40	0.134	1.2×10^5	0.35	92	2.1×10^{-5}	6.1×10^{-4}
P1S04D3_LOW	0.030	0.5	0.7	0.019	0.0007	0.39	0.134	1.2×10^5	0.34	89	3.2×10^{-5}	1.1×10^{-3}
P1S04D1_MED	0.031	0.5	0.6	0.019	0.0007	0.40	0.134	1.2×10^5	0.35	92	4.8×10^{-5}	1.0×10^{-3}
P1S04D2_MED	0.030	0.5	0.7	0.019	0.0007	0.40	0.134	1.2×10^5	0.35	90	6.0×10^{-5}	1.0×10^{-3}
P1S04D3_MED	0.030	0.5	0.7	0.019	0.0007	0.39	0.135	1.2×10^5	0.34	91	6.3×10^{-5}	1.1×10^{-3}
P1S04D1_SAT	0.032	0.5	0.6	0.019	0.0007	0.40	0.134	1.2×10^5	0.35	95	5.8×10^{-5}	3.2×10^{-3}
P1S04D2_SAT	0.030	0.5	0.7	0.019	0.0007	0.40	0.134	1.2×10^5	0.35	90	6.4×10^{-5}	4.0×10^{-3}
P1S04D3_SAT	0.028	0.4	0.7	0.019	0.0007	0.39	0.134	1.2×10^5	0.34	85	5.9×10^{-5}	3.7×10^{-3}
P1S06D2_CW	0.041	0.9	0.5	0.026	0.0016	0.55	0.134	1.7×10^5	0.48	123	-	-
P1S06D3_CW	0.035	0.6	0.6	0.026	0.0016	0.54	0.135	1.7×10^5	0.47	104	-	-
P1S06D4_CW	0.038	0.8	0.5	0.026	0.0016	0.55	0.134	1.7×10^5	0.48	113	-	-
P1S06D5_CW	0.037	0.7	0.5	0.026	0.0016	0.54	0.137	1.7×10^5	0.46	110	-	-
P1S06D2_LOW	0.043	1.0	0.5	0.026	0.0016	0.54	0.135	1.7×10^5	0.47	129	3.3×10^{-5}	1.0×10^{-3}
P1S06D3_LOW	0.037	0.7	0.5	0.026	0.0016	0.55	0.134	1.7×10^5	0.48	110	4.2×10^{-5}	1.0×10^{-3}
P1S06D4_LOW	0.038	0.8	0.5	0.026	0.0016	0.55	0.134	1.7×10^5	0.48	113	5.3×10^{-5}	1.1×10^{-3}
P1S06D2_MED	0.043	1.0	0.5	0.026	0.0016	0.55	0.134	1.7×10^5	0.48	128	1.3×10^{-4}	2.7×10^{-3}
P1S06D3_MED	0.043	1.0	0.5	0.026	0.0016	0.55	0.134	1.7×10^5	0.48	128	1.5×10^{-4}	2.7×10^{-3}
P1S06D5_MED	0.037	0.7	0.5	0.026	0.0016	0.54	0.136	1.7×10^5	0.47	110	8.8×10^{-5}	1.8×10^{-3}
P1S06D2_SAT	0.045	1.1	0.4	0.026	0.0016	0.53	0.138	1.7×10^5	0.46	135	1.3×10^{-4}	2.6×10^{-3}
P1S06D3_SAT	0.043	1.0	0.5	0.026	0.0016	0.55	0.133	1.7×10^5	0.48	129	1.3×10^{-4}	3.4×10^{-3}
P1S06D5_SAT	0.043	1.0	0.5	0.026	0.0016	0.54	0.136	1.7×10^5	0.47	128	1.1×10^{-4}	1.7×10^{-3}
P1S10D1_CW	0.041	0.9	0.5	0.032	0.0023	0.64	0.146	2.0×10^5	0.53	124	-	-
P1S10D2_CW	0.044	1.0	0.5	0.032	0.0023	0.64	0.144	2.0×10^5	0.54	131	-	-
P1S10D4_CW	0.048	1.2	0.4	0.032	0.0023	0.65	0.143	2.0×10^5	0.55	144	-	-
P1S10D5_CW	0.045	1.1	0.4	0.032	0.0023	0.65	0.143	2.0×10^5	0.55	134	-	-
P1S10D7_CW	0.047	1.2	0.4	0.032	0.0023	0.65	0.142	2.0×10^5	0.55	142	-	-
P1S10D8_CW	0.041	0.9	0.5	0.032	0.0023	0.68	0.136	2.0×10^5	0.59	123	-	-
P1S10D1_LOW	0.045	1.1	0.4	0.032	0.0023	0.64	0.146	2.0×10^5	0.53	136	5.8×10^{-5}	9.8×10^{-4}
P1S10D2_LOW	0.050	1.3	0.4	0.032	0.0023	0.64	0.145	2.0×10^5	0.54	150	6.4×10^{-5}	1.3×10^{-3}
P1S10D4_LOW	0.051	1.4	0.4	0.032	0.0023	0.65	0.143	2.0×10^5	0.55	152	5.9×10^{-5}	1.4×10^{-3}
P1S10D1_MED	0.045	1.1	0.4	0.032	0.0023	0.63	0.146	2.0×10^5	0.53	135	1.4×10^{-4}	1.6×10^{-3}
P1S10D2_MED	0.049	1.2	0.4	0.032	0.0023	0.64	0.145	2.0×10^5	0.54	146	1.5×10^{-4}	2.1×10^{-3}
P1S10D4_MED	0.052	1.5	0.4	0.032	0.0023	0.65	0.143	2.0×10^5	0.55	157	9.8×10^{-5}	2.2×10^{-3}
P1S10D5_SAT	0.042	0.9	0.5	0.032	0.0023	0.65	0.143	2.0×10^5	0.55	126	2.2×10^{-4}	3.5×10^{-3}
P1S10D7_SAT	0.049	1.2	0.4	0.032	0.0023	0.65	0.143	2.0×10^5	0.55	146	1.7×10^{-4}	1.9×10^{-3}
P1S10D8_SAT	0.047	1.2	0.4	0.032	0.0023	0.68	0.136	2.0×10^5	0.59	140	1.7×10^{-4}	2.5×10^{-3}

2.3. Instrumentation and data processing

2.3.1. Principle of velocity and concentration measurements with ACVP

The Acoustic Concentration and Velocity Profiler (ACVP) technology, combining ADVP (Acoustic Doppler Velocity Profiler) with ABS (Acoustic Backscattering Systems) technologies in a single instrumentation (Hurther et al. 2011), is used herein for the measurements. It provides co-located profiles along the bed-normal direction of streamwise and wall-normal velocity components, particle volumetric concentration and particle flux across both the dense bed-load and dilute suspension layers (Revil-Baudard et al. 2015, 2016, Fromant et al. 2018, 2019). Following the statistical convergence criteria proposed in Thorne and Hurther (2014) for incoherent particle scattering theory, the sampling frequency in the present study is set to 100 Hz and 5 Hz for velocity and concentration, respectively. The operating acoustic frequency of 1MHz, with a pulse duration of $2\mu\text{s}$ leads to a vertical resolution of $\Delta z = 1.5$ mm. Further details on the employed temporal resolution for velocity and concentration measurements will be presented in the following points. To minimise the flow intrusiveness, the ACVP sensors are placed into a vacuum box, with its lower end slightly below the free-surface level (see Figure 2-2). Because the box disturbs locally the free-surface, the profiles presented herein are restricted to the lower 60% of the flow depth.

Velocity measurements based on the Doppler effect consist in the estimation of the Doppler frequency shift to retrieve the velocity of the acoustic scattering targets. In clear-water flows, the targets are micro air-bubbles with negligible inertial lag compared to fluid parcels. In sediment-laden flows, the targets are both the air-bubbles and the solid particles. Consequently, the measured velocity is associated to a water-sediment mixture velocity. The corresponding Doppler frequency shift is the difference between the received frequency f_r and the emitted carrier frequency f_0 : $f_D = f_r - f_0$. This frequency relates to the velocity of a target as $f_D = f_0 v_R / c$, where $v_R = \vec{v} \cdot (\vec{e}_s - \vec{e}_r)$ is the radial velocity. For monostatic configuration, the radial velocity component is the vector sum of the target velocity projected on the same emitting and receiving directions. For a bistatic case (the present configuration), the emitting and receiving directions are different which induces that v_R corresponds to the target velocity projected on the bisector of the emitting and receiving directions. As detailed by Blanckaert et al. (2006), in bistatic configuration the Doppler frequency becomes $f_D = f_0 / c (v_e + v_r)$. If we take the typical configuration of the ACVP systems (see Figure 2-4), in which the emitting and local receiving directions are separated by an angle α , and having $v_e = v_z$ and $v_r = v_H \sin(\alpha) + v_z \cos(\alpha)$, the Doppler frequency will be given as:

$$f_D^+ = [u \sin(\alpha) + w(1 + \cos(\alpha))] \quad (2-1)$$

Note that if only one Doppler frequency is known, we cannot obtain explicitly u and w . For this reason, a second receiver is used with the same angle α but oriented on the opposite direction compared to the first one. The Doppler frequency for this second bistatic system is:

$$f_D^- = \frac{f_0}{c} (-u \sin(\alpha) + w(1 + \cos(\alpha))) \quad (2-2)$$

From these Equations (2-3) and (2-4), one can retrieve the streamwise and vertical velocities, u and w , respectively:

$$u = \frac{c}{2f_0 \sin \alpha} (f_d^+ - f_d^-) \quad (2-3)$$

$$w = \frac{c}{2f_0(1 + \cos \alpha)} (f_d^+ + f_d^-) \quad (2-4)$$

Each local estimate of the Doppler frequencies (hence of velocities u and w) is obtained with a pulse-pair algorithm after averaging over a given number (N_{pp}) of consecutive pairs of echoes to limit the Doppler noise contribution in the quasi-instantaneous velocities. For typical flow applications, N_{pp} varies between 8 and 64 resulting in a final acquisition frequency of $f_{acq} = PRF/N_{pp}$, where PRF is the pulse repetition frequency. Herein, we have defined $PRF = 1600$ Hz and $N_{pp} = 16$, leading to a temporal resolution of 100 Hz. The high PRF value is necessary to track the coherent Doppler phase evolution between two consecutive pulses. This differs from the estimation of concentration based on the backscattered acoustic intensity, which requires temporal incoherent backscattering echoes as statistically independent intensity realizations. This can only be ensured for PRF values smaller than about 20 Hz as was shown by Thorne and Hurther (2014) in similar turbulent flow conditions. This explains the difference between the velocity and concentration time resolutions.

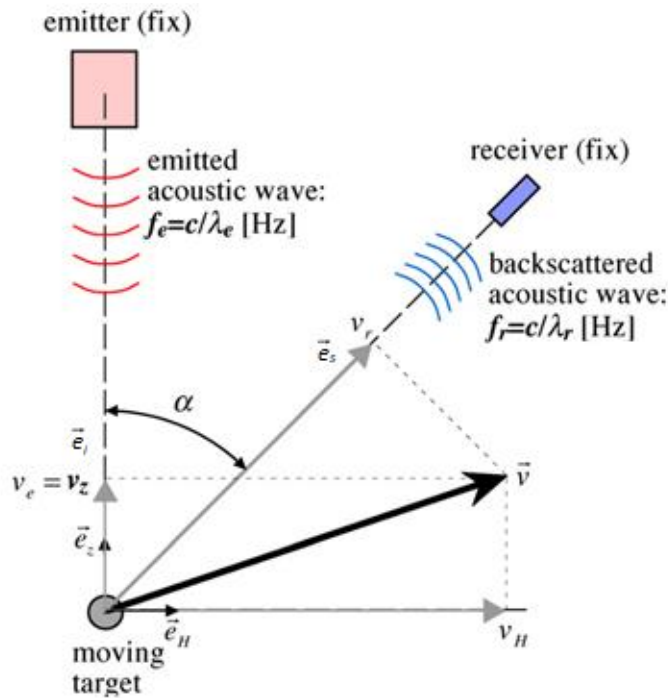


Figure 2-4. Configuration of typical ADV systems. Adapted from Blanckaert and Lemmin (2006)

The sediment concentration estimation is based on a statistical model of the recorded squared voltage (intensity). It is derived from semi-theoretical and experimental determinations of the acoustical backscattering and attenuation properties and it is valid under incoherent scattering conditions, which implies that the time should be long enough for the individual consecutive samples to be statistically independent. This explains the lower resolution adapted for concentration measurements, as mentioned previously. Under incoherent scattering conditions, the density probability function of the intensity realizations follow a Rayleigh distribution. The mean squared

voltage signal V_{rms}^2 proportional to the echo intensity I , as the sum of the echo intensity of all individual particles contained in the measurement volume, is given by the following equation (Thorne and Hanes 2002, Hurther et al. 2011):

$$V_{rms}^2 = I = A_j A_s C \exp^{-4\alpha r} \quad (2-5)$$

where the term A_j includes the system dependent parameters along the profile. The term A_s is the particle scattering term, C is the mass concentration and $\alpha = \alpha_w + \alpha_s$ is the attenuation constant (α_w from water absorption and α_s from sediment viscous absorption and scattering). For noncohesive sediments insonified at megahertz, the sediment scattering component dominates the viscous induced attenuation (Thorne and Hanes 2002). Under such conditions, one can consider only the sediment attenuation as $\alpha_s = \frac{1}{r} \int_0^r \zeta_s M dr$. If we replace this term in the previous equation, the mean squared voltage signal can be written as:

$$I = K A_j A_s C \exp\left(-4 \int_0^r \zeta_s C dr\right) \quad (2-6)$$

where K is an adjusted calibration constant best fitting the known injected solid-loads for all SL experiments and for a given particle diameter (see the next subsection). The high vertical resolution (1.5 mm) of the ACVP allows the discretization of the attenuation integral in Eq. (2-6) with a low order scheme (Hurther et al. 2011) in order to extract explicitly the vertical profile of C .

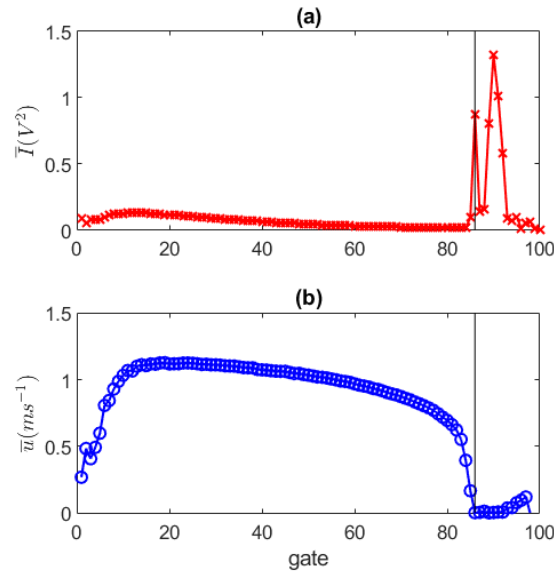


Figure 2-5. Example of bed detection based on mean profile echo intensity I (a) and mean streamwise velocity (b); for P1S08D5_CW. The convergence to zero velocity coincides with the sudden increase of the backscattered intensity at gate number 86, identified by the vertical solid line.

As mentioned above, the present experimental protocol allows defining the same origin of the bed normal axis z for the sediment-laden and their clear-water runs, because each run is performed without any modification in the experimental setup. One example of the bed detection with the run P3S08D05_CW is shown in Figure 2-5. The mean profiles of echo intensity and streamwise

velocity agree rather well on the location of sudden increase of the backscattered echo intensity and the location of zero-velocity, respectively. This position is defined as the origin of the z-axis. Since the bed consists of a rough surface (one layer of glued dp3 particles), an uncertainty remains concerning the exact position over a vertical thickness of about 3mm corresponding to the roughness canopy. Regardless of the difficulty in the interpretation of the zero-level in a rough canopy, we considered that it is clearly an advantage to study the CW and SL runs with a well-defined identical bed reference.

2.3.2. ACVP calibration

The mean sediment flux is estimated over the 300s long time interval $T=t_1-t_0$ of the experimental run:

$$q_s = \frac{1}{T} \int_{t_0}^{t_1} \int_{z_b}^{H_f} u(z, t) c(z, t) dz dt \quad (2-7)$$

Two calibration constants K (see Eq. (2-6)) were determined for the two studied particle diameters dp1 and dp3. Figure 2-6 displays the comparison between the fitted solid-loads measured from ACVP and the injected ones. In Figure 2-6, the alignment of the points with the solid line shows a good agreement of the fitted ACVP measurements with the injected solid-load. This is valid over the wide range of studied sediment transport regimes. The relative error (determined using Eq. 5) over all 27 studied SL runs is shown in Figure 2-7. Its mean value and the standard deviation are represented by the solid line and dashed line, respectively, estimated as:

$$E(\%) = \frac{(q_{S_{ACVP}} - q_{S_{injected}})}{q_{S_{injected}}} \quad (2-8)$$

The relative errors remain generally below 30%, with few exceptions. A larger dispersion is observed for dp1. The mean and standard deviation values are approximately $E_{qs}(\%) = -4.7 \pm 10$ and $E_{qs}(\%) = -10 \pm 22$, for dp3 and dp1, respectively. The negative sign indicates that the ACVP measurements are globally lower than the injected values. However, the general trend suggests a good agreement with the observed solid-load. It must be noted that discrepancies between the injected load and the measured load can also result from non-homogeneous particle concentration over the flow section. Suspended sediments concentration could be influenced by the presence of secondary currents in the present high aspect ratio open-channel flow.

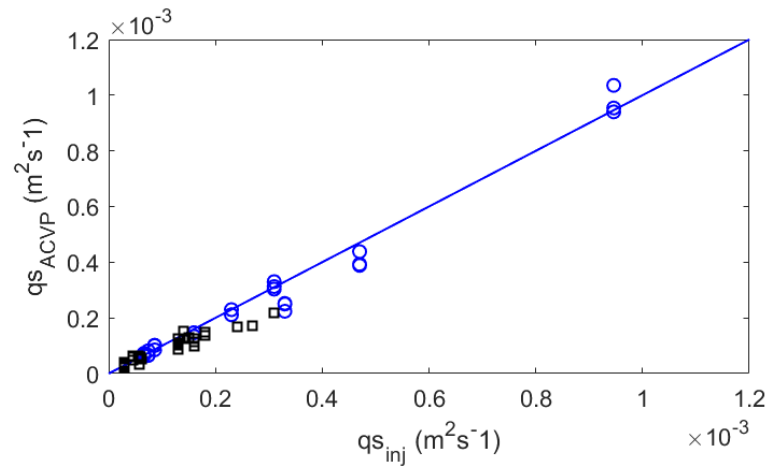


Figure 2-6. Comparison $q_{S_{ACVP}}$ versus $q_{S_{injected}}$ Solid line is $X=Y$; for d_{p3} (blue, circle) and for d_{p1} (black, square).

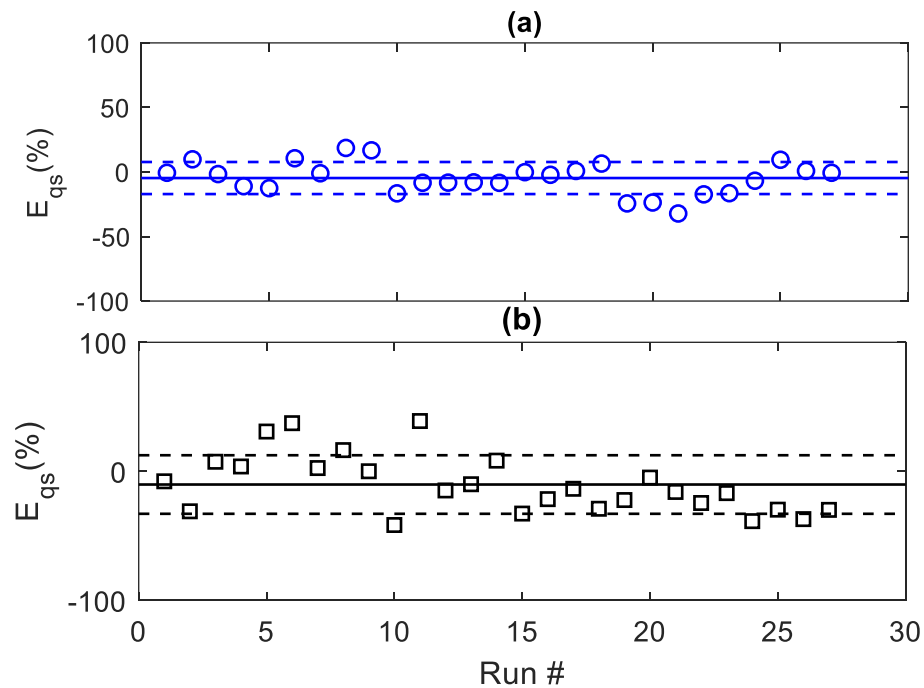


Figure 2-7. Relative error of the solid-load measurements (in percentage); for d_{p3} (blue, circle) and d_{p1} (black, square) solid line is the mean value; dashed lines are the standard deviations.

In the bottom panels of Figure 2-8 and Figure 2-9 it is shown the time evolution of the accumulated volume of transported sediments over the entire duration of the run, for the hydraulic condition S08 and S10 (the other flow conditions are presented in the Appendix A). The time evolution of the measured flow depth is also included for each run (top panel), only to highlight the flow steadiness. The three repeated runs for each transport regime are shown.

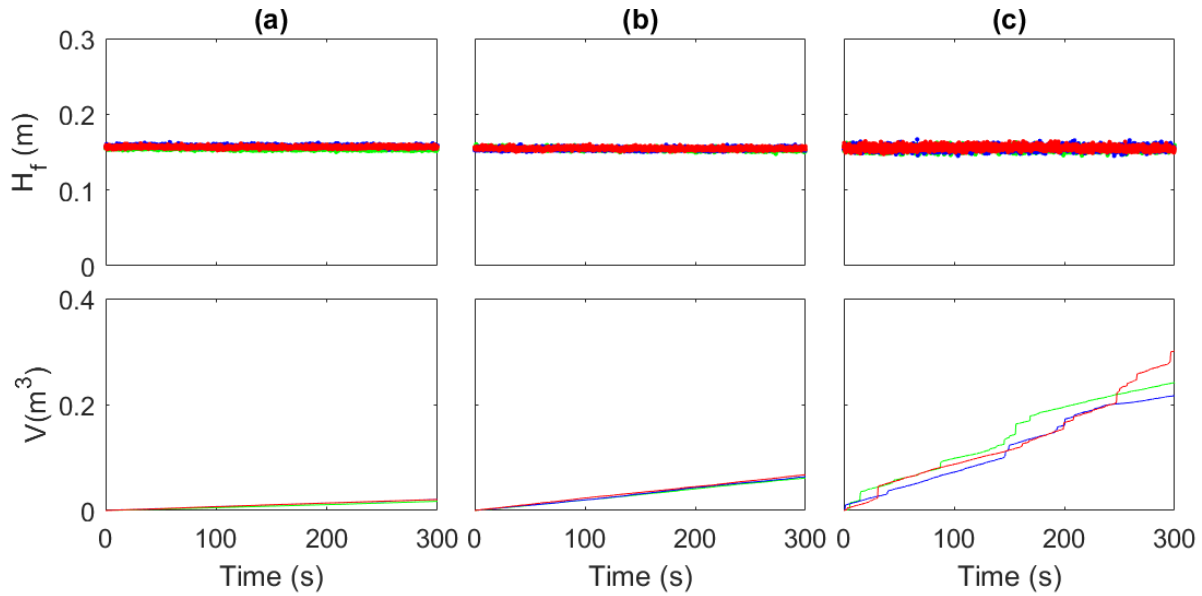


Figure 2-8. Time evolution of flow depth and cumulative volume of transported sediments for dp3 (S08); for lower (LOW), intermediate (MED) and saturation (SAT) conditions.

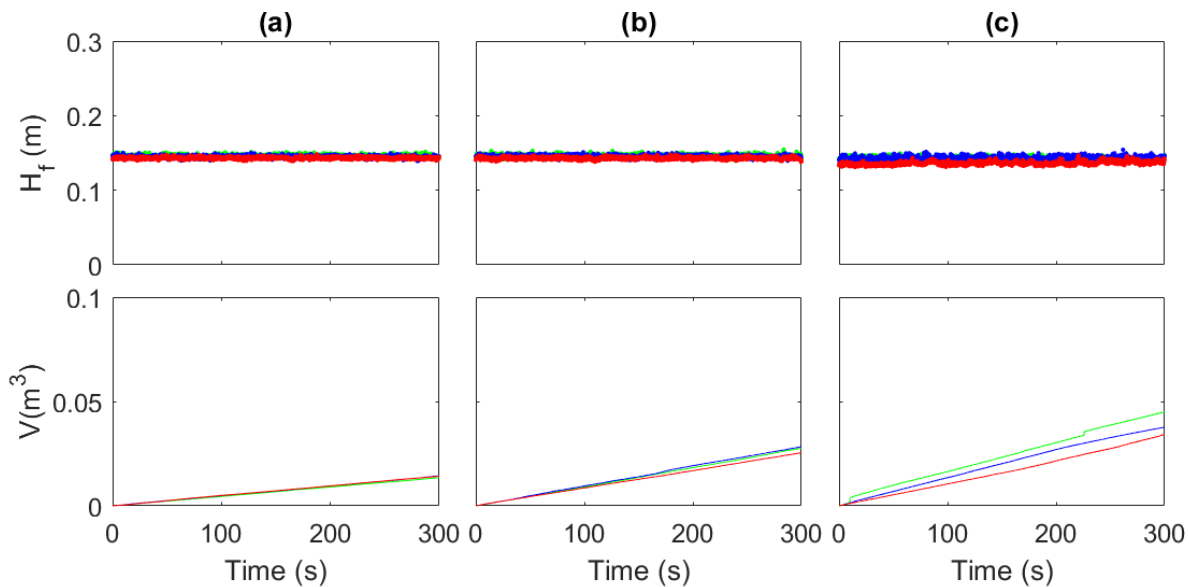


Figure 2-9. Time evolution of flow depth and cumulative volume of transported sediments for dp1 (S10); for lower (LOW), intermediate (MED) and saturation (SAT) conditions.

In most cases, they are almost superimposed, suggesting that they evolve very similarly over time. In terms of accumulated volume, the linear trend of the measured transported sediment volume confirms that the runs of sediment-laden flows are well established in terms of sediment transport rate. The bumps observed for the cases of full-capacity regimes are supposed to be associated with the intermittent deposition of particles in the bed and occurrence of clusters of high concentration in the near-bed region. The repeatability over the different runs of the mean profile measurements will be shown and discussed in chapter 3.

2.3.3. Turbulence measurement resolution

Two main aspects determine the measurement sampling frequency f of the ACVP required for turbulence resolved measurements. The first is f_{max} , as the highest frequency associated with the smallest turbulent flow scale, the second, is the instrument dependent measurement noise as the Doppler noise which was shown to be the main noise source of turbulent velocity measurements in acoustic pulse coherent Doppler system (Garbini et al. 1982, Voulgaris and Trowbridge 1998, Hurther and Lemmin 2001, Blanckaert and Lemmin 2006). The first aspect is discussed in the present section; the second aspect is addressed in the following section.

The Nyquist-Shannon sampling theorem imposes that the sampling frequency f_{acq} satisfies the condition $f_{acq} > 2f_{max}$. In highly turbulent open-channel flows, Nezu and Nakagawa (1993) showed on the basis of turbulent velocity spectra measurements that $f_{max} \approx k_u L_x$ and must reach at least a value of 100 Hz in order to resolve the turbulence spectra up to the Kolmogorov scale. Considering that $k_u = 2\pi f/U$ with U as the flow discharge velocity and that $L_x \approx 0.5H_f$ (Fig. 4.16 in Nezu and Nakagawa 1993), f_{max} becomes:

$$f_{max} \approx \frac{100U}{2\pi L_x} \approx \frac{100U}{\pi H_f} \quad (2-9)$$

In our hydrodynamic open-channel flow conditions $f_{max} \approx 80 - 200\text{Hz}$, from the less to the most energetic flow of lowest to highest bulk Reynolds number value, respectively. With the present sampling frequency of 100Hz, the highest resolved frequency is the Nyquist frequency $f_N = 100/2 = 50$ Hz, indicating that a significant range of high frequencies associated with turbulence microscales cannot be resolved. Furthermore, as will be seen in the following section, Doppler noise can reduce this theoretical Nyquist frequency to lower values dependent of the vertical measurement position. This assertion can be further confirmed by estimations of the Kolmogorov length scales timescales $t_K = (\nu/\varepsilon)^{1/2}$ and the associated Kolmogorov frequency as $f_K = 1/t_K$. The approximate mean dissipation rate valid for turbulent open-channel flows can be estimated from the parametrization proposed by Nezu and Nakagawa (1993):

$$\frac{-\varepsilon H_f}{u_*^3} = E_1 \left(\frac{z}{H_f} \right)^{-0.5} \exp(-3z/H_f) \quad (2-10)$$

where E_1 is a constant with a value of 9.1. Applying this equation at a relative flow depth $H_f \approx 0.15$, it is seen that the Kolmogorov frequency in our conditions, is roughly $f_K \approx 55 - 190$ Hz, increasing from the less to the most turbulent regime, respectively. Note the good agreement of this spectral range with the previous method to estimate the range of f_{max} values. The Kolmogorov length scale $(\nu^3/\varepsilon)^{1/4}$, estimated at the same relative depth, increases from about $7.3 \times 10^{-5}\text{m}$ to $1.3 \times 10^{-4}\text{m}$ from the most to the less energetic flow, persistently remaining below the maximum available spatial resolution ($\Delta z \approx 1.5 \times 10^{-3}\text{m}$). From these considerations, it is confirmed that ACVP measurements do not resolve turbulent microscales of the order of the Kolmogorov flow scales. Efforts should then be to resolve the Taylor microscales, associated with the inertial subrange of the turbulent velocity spectra. The local Taylor microscale is defined as:

$$\lambda = u_{rms} \sqrt{\frac{15\nu}{\varepsilon}} \quad (2-11)$$

where u_{rms} is the local streamwise turbulent intensity. The associated Taylor timescale is then $t_\lambda = \lambda/u_{rms}$. In our flow conditions, the resulting range of Taylor scales becomes $\lambda \approx 2.8 \times 10^{-3} - 4.2 \times 10^{-3}$ m and $f_\lambda \approx 14 - 50$ Hz, increasing from less to most turbulent flow regime. Note that these approximations are valid for a relative flow depth of $z/H=0.15$, such that below this level the Taylor microscales are even smaller (of the order of $O(1\text{mm})$), and the inertial subrange of the turbulence spectra is poorly resolved. However, above this level, the present analysis indicates that the inertial subrange is partially resolved and that the mean TKE dissipation rate can be measured with the ACVP technology.

2.3.4. Doppler noise reduction in turbulence measurements

The presence of Doppler noise in the time fluctuating velocity signals measured with acoustic pulse-coherent Doppler velocimetry, is known to affect strongly measurements of mean Reynolds normal stress and TKE dissipation rate. Several Doppler noise reduction methods are proposed in the literature, two of them were tested here. The first is the method proposed by Garbini et al. (1982) is based on a cross correlation of the velocity time signal measured at two consecutive points in the profile. The second consists in the evaluation of the noise floor levels in the high-frequency range of the raw turbulence spectra and the subsequent removal of the corresponding noise spectra under the assumption of a white noise characteristic. The white noise level is evaluated at high frequencies in the turbulence spectra (see Figure 2-10) where it reaches a constant magnitude with frequency (Hurther and Lemmin 2001). By removing this white noise spectrum from the raw turbulence spectrum, only the spectral region below the one over which the noise spectra has been evaluated, can be used as a noise free turbulence spectrum. On the contrary, the cross-correlation method of Garbini et al. (1982) removes kinetic energy associated with velocity fluctuations that are statistically independent between two consecutive points in the profile. This means that energy originating from noise but also kinetic energy from turbulent isotropic eddies of size smaller than the separation distance between two consecutive points (i.e. 1.5 mm) are removed from the raw velocity signal. Therefore, although none of the two corrections methods provides fully resolved turbulence spectra over the entire measurement bandwidth, they both significantly improve the spectra by reducing the Doppler noise contribution over the low frequency part of the inertial subrange. This can be seen in Figure 2-10 in which the convergence to the Kolmogorov $-5/3$ slope of the raw spectrum is barely noticeable whereas the corrected spectra obtained with the two methods allow to identify the inertial subranges. The comparison of the two correction methods indicates that they provide very similar results. This is further confirmed in Figure 2-11, that shows the normalized turbulence intensities obtained from the integral over the entire frequency bandwidth of the turbulence spectra. It is seen that the noise affects the longitudinal velocity much more significantly than vertical component. This ADV geometry induced behaviour has been well described by Hurther and Lemmin (2001). The TKE dissipation rate has been estimated with the two correction methods, and the differences were as negligible as those observed for the two corrected streamwise turbulence intensities Figure 2-11 (about few percents). Hence, the results presented later will be based on the white noise correction method.

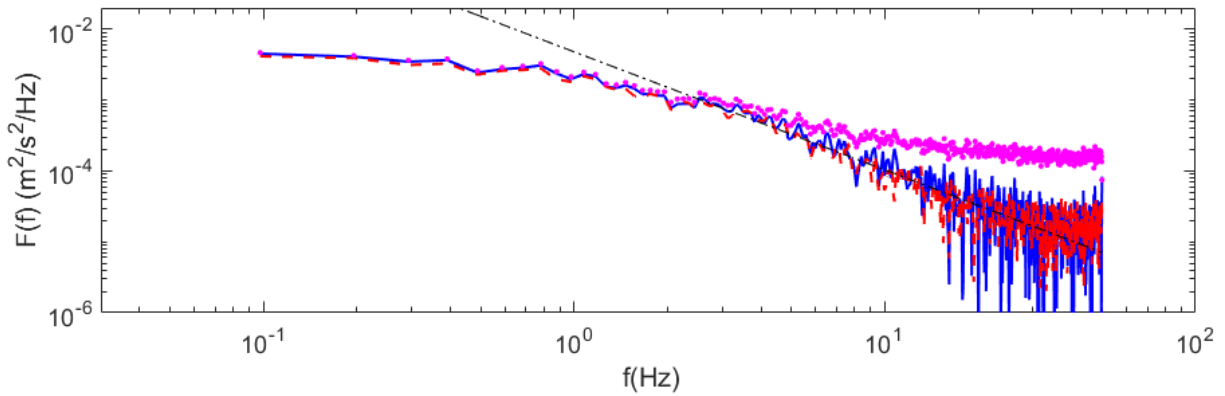


Figure 2-10. Comparison of noise correction methods applied for the signal of u' ; uncorrected(.), spectra based noise (-), Garbini method (-); for P3S08D5_CW. Black line represents the $-5/3$ slope; the white noise level was determined at $f \approx 25$ Hz.

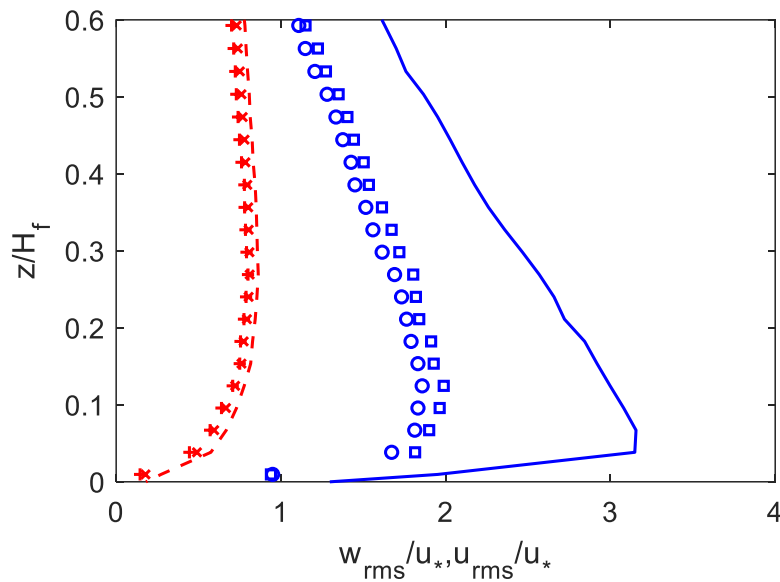


Figure 2-11. Normalized turbulence intensities; uncorrected (u' (-) and w' (--)), spectra based correction (u' (\square) and w' (+)) Garbini method (u' (o) and w' (x)); for P3S08D5_CW

3. Mean profiles and modelling parameters

In this chapter, results are presented in terms of mean profiles of streamwise velocity, concentration and Reynolds shear stress. Based on these measurements, several hydrodynamic and solid (particle) transport quantities can be deduced such as the profiles of eddy viscosity and solid particle fluxes. Important modelling parameters obtained from the presented profiles are discussed, specifically, the von Karman parameter value κ , the β -factor, and the friction factor f . All profiles correspond to results in individual experimental runs. This averaging procedure was preferred because all sediment-laden runs have their separate reference clear-water runs performed under the exact same flow and setup conditions. Nevertheless, the low variability of the measurements over the repeated runs was highlighted in sections 2.3.2 and 3.2.1 as well as in Table 4-1. The impact of the two studied particle sizes on the flow structure is only briefly described. The detailed analysis and specific results are presented in the following chapters.

3.1. Flow structure: bed-load and suspension layers

At low suspension numbers $w_s/u_* < 0.8$, the transported solid-load is dominated by suspension, as mentioned in section 1.3. Moreover, for the experiments with smaller particle diameter (dp1) the roughness height k_s is likely to be as important or even larger than the bed-load layer, since the particles covering the bed surface are three times larger than the transported particles. The roughness height in sediment-laden flows can be approximated as $k_s \approx 2 - 3d_p$ (Engelund and Hansen 1967, Raudkivi 1998, Revil-baudard 2015). This is a rough approximation, because k_s depends on the hydraulic and solid transport regime (Camenen et al. 2006). This approximation can be compared to the bed-load layer thickness based on the formulation proposed by van Rijn (1984a), based on particle saltation height analysis:

$$\delta = 0.3d_{50}D_*^{0.7} \left(\frac{\theta}{\theta_{cr}} - 1 \right)^{0.5} \quad (3-1)$$

with

$$D_* = d_{50} \left[\frac{(s-1)g}{v^2} \right]^{1/3} \quad (3-2)$$

where $s = \rho_s/\rho$ and $d_{50} = 1$ and 3 mm for dp1 and dp3, respectively. With the increasing flow intensities for each particle diameter, we obtain $\delta/d_p \approx 1.6, 2.3, 2.6$ and $\delta/d_p \approx 8, 10, 13$, for dp1 and dp3 experiments, respectively. The bed-load thickness was normalized by the $d_p = 3$ mm that corresponds to the diameter of particles glued on the fixed bed, even for the dp1 experiments. This result suggests that the bed-load thickness for dp1 has the same magnitude as the roughness height; hence, it is rather small compared to dp3. In these cases, the common approximation for the reference level of the suspension layer as $a = \delta = 0.05H_f$ (Cellino and Graf 1999) seems to be

well justified. However, this assumption fails in presence of thick bed-load layers (intense bed-load with large particles or in presence of bedforms such as dunes), that may represent a non-negligible portion of the flow depth. This aspect will be discussed in detail in chapter 4. Nevertheless, this simple analysis suggests that the vertical flow structure in the dp1 and dp3 experiments is different.

3.2. Mean profiles

3.2.1. Velocity, concentration and Reynolds shear stress

Measurements of velocity, concentration and Reynolds shear stress profiles are crucial quantities in the experimental study of turbulent sediment-laden flows, since they allow determining all the quantities and parameters of interest, such as, the bed shear stress, bed friction velocity, mean solid flux, eddy viscosity and sediment diffusivity. In addition to the individual velocity fluctuations (u' and w'), signals of velocity, concentration and Reynolds shear stress are used for studying the effects of sediments on the different terms of the momentum and TKE budgets but also on the dynamics of turbulent flow eddies such as coherent flow structures, which will be addressed in later chapters.

In Figure 3-1 and Figure 3-2, mean profiles of velocity, concentration and Reynolds shear stress are shown, for saturated (upper row), moderate (second row), low (third row) and clear-water (bottom) particle load conditions, corresponding to dp3 and dp1, respectively. These figures include all runs of sediment-laden flows. For the sake of clarity, only three clear-water runs are included for each hydraulic condition, even when more runs were acquired (see Table 2-2). The similar profiles of the three repeated runs for the same solid-load regime confirm the high degree of experiment repeatability. Some variability is seen with the two hydraulic regimes with highest flow intensities, for dp1. Indeed, in these flow regimes, the profiles of the three repeated runs display some differences. Even when differences in the measured profiles occurred in terms of absolute values, the trends of the discussed quantities are the same.

Figure 3-1a and Figure 3-2a show the mean streamwise velocity \bar{u} profiles versus the flow-depth normalized distance z/H_f from the bed. For all conditions, the mean velocity profiles show the gradual increase in the hydrodynamic forcing with no clear evidence of effects of particle-load on the shape and magnitude of the velocity profiles in absolute values. For this purpose, they were analysed in detail, by comparing the velocities in CW and SL performed under nearly the same conditions. This was done in sections 3.3.1 and 4.3.

The time-averaged concentration \bar{c} profiles shown in Figure 3-1b and Figure 3-2b confirm the increase in injected particle load from the lower to the upper panels. Moreover, for a given solid-load regime (SAT, MED or LOW), the differences in the vertical distribution of particle concentration with hydraulic forcing condition can be analysed. It can also be seen that the vertical extension of the concentration profile increases with flow velocity (hydrodynamic forcing). This is often described in terms of w_s/u_* , that decreases as the flow becomes more energetic. Therefore, the concentration profiles confirm that less particles are transported in suspension as w_s/u_* increases. The corresponding concentration profile for the high suspension number value exhibits higher vertical gradients suggesting less turbulent particle mixing.

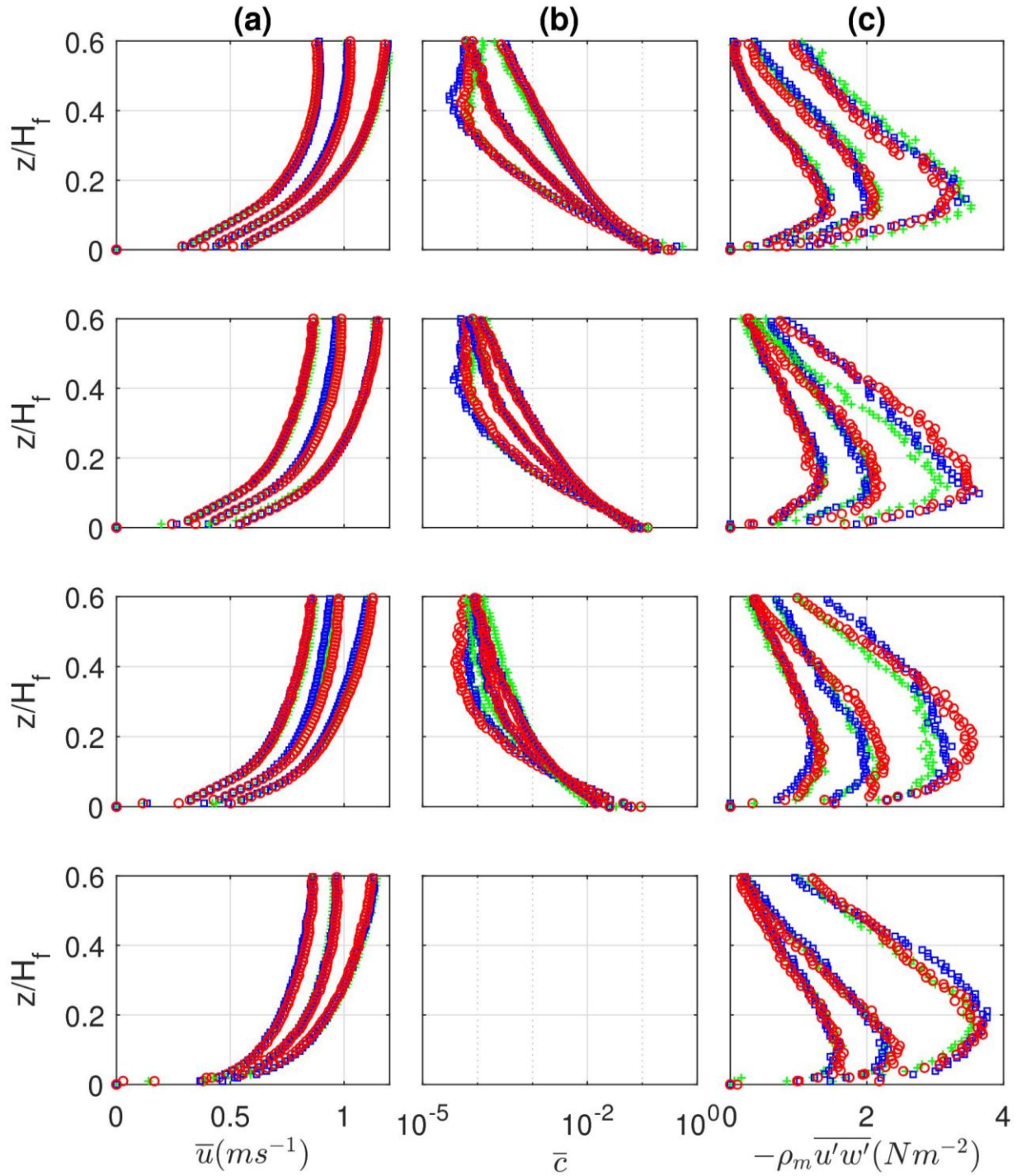


Figure 3-1. Mean velocity (a), concentration (b) and Reynolds shear stress (c) profiles for dp3; for the three repeated sediment-laden runs (o, □ and +); with increasing concentration from clear-water (bottom row) to saturation (top row); the three hydrodynamic forcing are distinguished by the magnitude of the measured profiles.

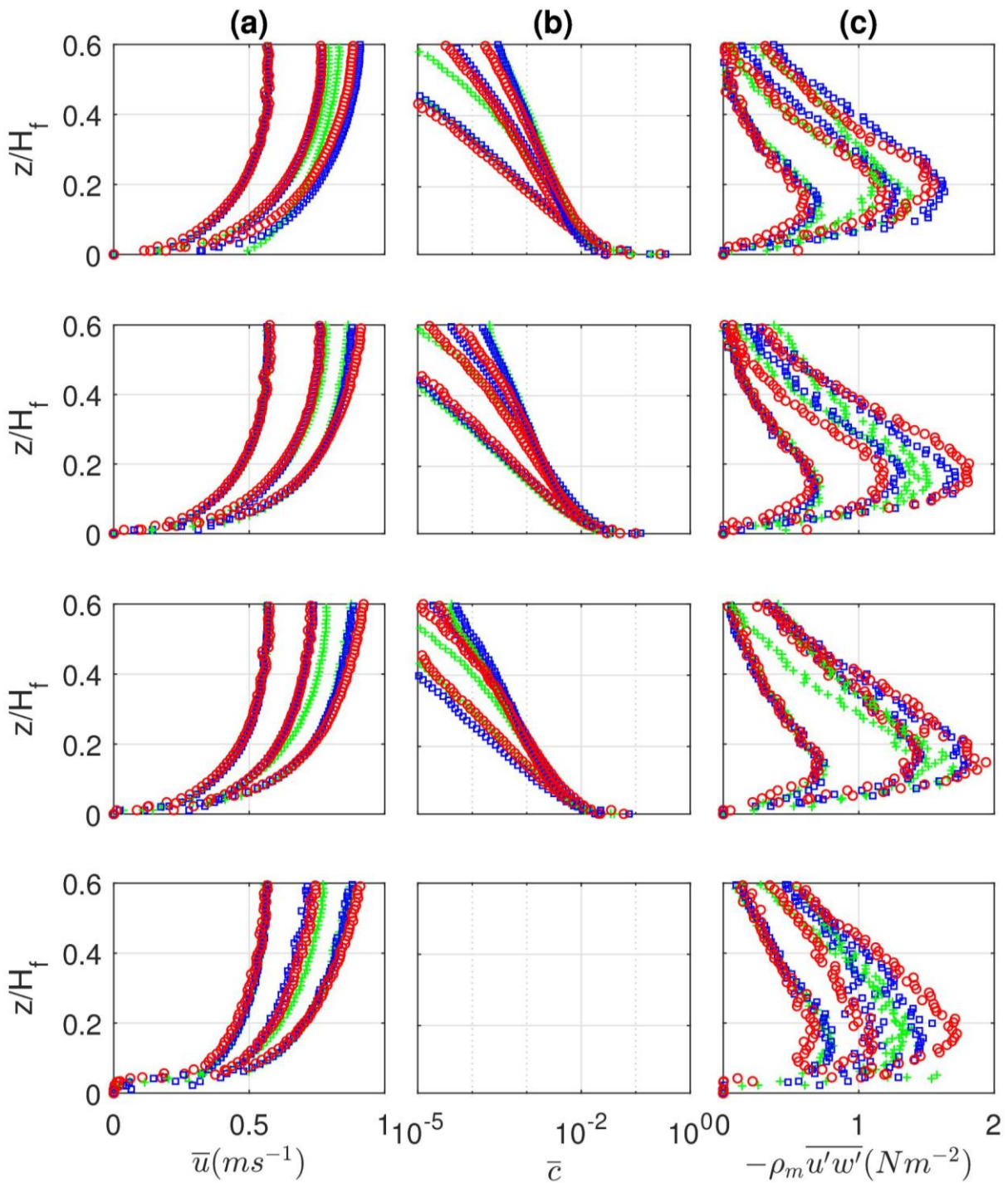


Figure 3-2. Mean velocity (a), concentration (b) and Reynolds shear stress (c) profiles for dp1; with increasing concentration from clear-water (bottom row) to saturation (top row); for the three repeated sediment-laden runs (o, \square and +); with increasing concentration from clear-water (bottom row) to saturation (top row); the three hydrodynamic forcing are distinguished by the magnitude of the measured profiles.

The profiles of Reynolds shear stress $-\rho_m \overline{u'w'}$ (where $\rho_m = (1 - \bar{c})\rho_f + \bar{c}\rho_p$ is the mixture density) are shown in Figure 3-1c and Figure 3-2c. All flow conditions show a linear profile for $z/H_f > 0.2$, although small deviations are observed, particularly in full capacity. This behaviour reveals the high degree of flow uniformity in streamwise direction (Kironoto and Graf 1994, Dey 2014). The bed friction velocity is estimated from the linear extrapolation of these profiles to the flow bed position ($z=0$) with an uncertainty in u_* of about 10%. It can be seen that the bed shear stress of the most energetic flow regime is approximately twice that of the less energetic one, both in dp3 and dp1. Despite minor differences in profile shapes and maxima location inside the inner flow region ($z/H_f < 0.2$), the values of bed friction velocity do not vary more than 20% between CW and SL flows and with no clear trends. Please note that secondary currents due to side wall and bottom wall induced boundary layer interactions as well as flow perturbations due to the ACVP holding box may affect the vertical distribution of the shear-stress profiles in the upper flow region for $z/H_f > 0.6$. For this reason, all observations are restricted to the flow region $z/H_f \leq 0.6$.

The bed shear stress values, based on the extrapolation of the measured Reynolds shear stress profiles were compared to estimations based on momentum balance incorporating the sidewall correction method of Vanoni and Brooks (Vanoni 2006). Although the direct measurements of the Reynolds shear stress is the most representative of the total shear stress exerted by the uniform open-channel flow (Nezu and Rodi 1986), this analysis allows to compare the present experiments with others from the literature in which the referred methodology was applied. As shown in Figure 3-3, it was found that the bed shear stress based on the sidewall correction τ_{corr} is about 50% larger than the measured ones. This result was independent of the solid-load conditions. Therefore, the Shields numbers reported in the present study correspond to values majored by a factor 1.5, if they would be compared to the studies that applied the referred sidewall correction methodology, such as Sumer et al. (1996), Camenen et al. (2006) and Recking et al. (2008). This result further supports that we are in the upper plane bed regime, since the minimum values of Shields number $\theta \approx 0.35$ (based on the extrapolation of the Reynolds shear stress) correspond to $\theta_{corr} \approx 0.5$, based on the side-wall correction. At these values of θ , bedforms are fully washed out and the upper plane bed stage also called the sheet-flow regime is established. The maximum values observed herein were $\theta \approx 1.2$, corresponding to $\theta_{corr} \approx 1.8$. This shows that very energetic sediment transport conditions were reached in the present study. Laboratory sheet-flow studies in open channel flows rarely reached such conditions. For example, in the well-known sheet flow experiments of Sumer et al. (1996), the maximum Shields number in open channel experiments was $\theta \approx 1.1$. All experiments with higher values were duct flows, without a free surface.

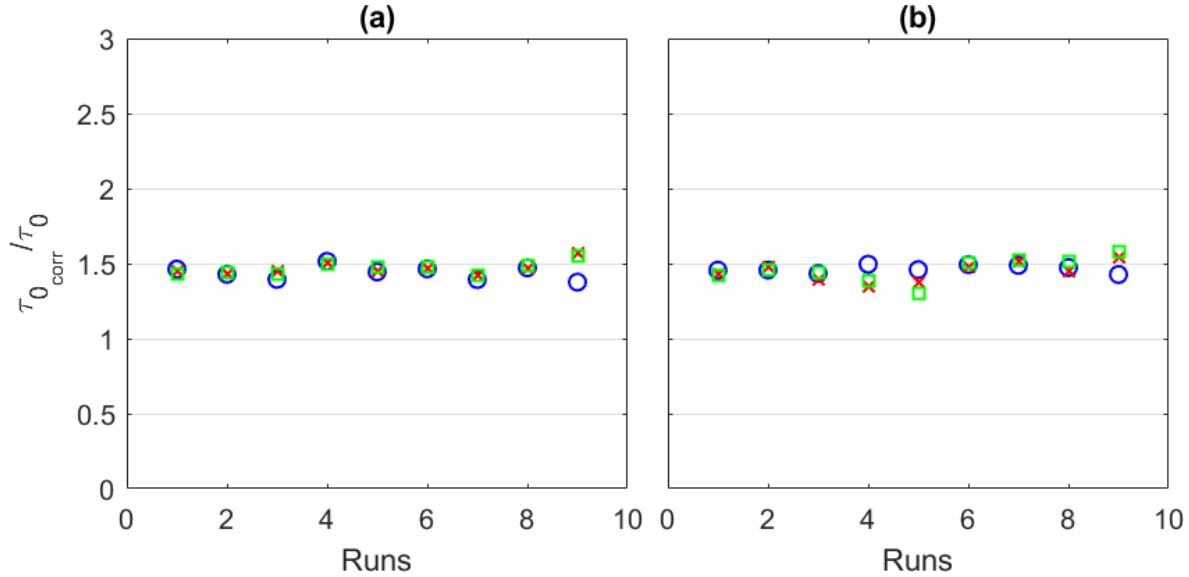


Figure 3-3. Ratio of bed-shear stress with sidewall correction and the measured one (extrapolation of the Reynolds shear stress to the bed) for dp1 (a) and dp3 (b); (o) SAT, (x) MED and (\square) LOW; including all 27 SL runs for each particle diameter.

3.2.2. Eddy viscosity, mean solid flux and repartition bed-load/suspended-load

Based on the high degree of experiment repeatability seen in the previous section, the studied quantities will be presented for only one out of the three repeated CW runs from this point forward, considering that the others display similar behaviour. In this section, some hydrodynamic and solid transport quantities determined from the mean profiles presented in the previous section are presented, namely, the eddy viscosity, mean solid flux and vertical cumulative solid transport. From the latter quantity, the repartition between bed-load and suspended-load is evaluated, taking the approximation of the bed-load layer height δ used in section 3.1.

Figure 3-4a and Figure 3-5a show the (turbulent) eddy viscosity profiles, defined as $\epsilon_{ms} = \overline{u'w'}/(d\bar{u}/dz)$, for dp3 and dp1, respectively. The concentration increases from the bottom panels (lower concentration) upwards (saturation). In both figures, ϵ_{ms} increases with flow depth, before reaching a nearly constant values from $z/H_f \approx 0.3$. From this vertical level, considerable scatter is observed, due to the smaller velocity gradient values. A particular trend is observed for dp3, where ϵ_{ms} remains nearly constant in the near-bed region. This trend is observed in all solid-load regimes but it becomes more pronounced in capacity conditions, indicating a modification of the nearbed flow structure with increasing solid-load. Note that this is true only for dp3, since even in capacity conditions, the eddy viscosity profiles for dp1 increase with z without a near-bed region of constant value.

Figure 3-4b and Figure 3-5b show the profiles of sediment flux density $\pi(z) = \bar{u}(z) \times \bar{c}(z)$ in streamwise direction. As expected, the most energetic flow conditions (red circle symbol) in capacity conditions (upper panels) carries more particles due to higher bed shear stresses and flow velocities. This is not only true close to the bed but also far from the bed, in the outer flow region where suspension transport occurs.

In order to quantify directly the relative contribution of bed-load and suspended-load as a function of hydraulic forcing and solid-load, Figure 3-4c and Figure 3-5c represent the cumulative sediment flux $\Pi(z)$ in streamwise direction (normalized by the total solid flux):

$$\Pi(z) = \int_0^z \pi(z) dz \quad (3-3)$$

From the capacity conditions (upper panels), it can be seen in both figures that the less energetic flow (highest suspension number w_s/u_* , represented by the green cross symbol curve) carries more particles close to the bed as bed-load than in the more dilute region as suspended-load. With the estimations of bed-load thickness provided in section 3.1, it is found that (only in capacity conditions) the proportion bed-load/suspended-load is approximately 80/20, 85/15 and 90/10% for dp3, against 25/75, 30/70 and 70/30% for dp1. These simple estimations further support that in regimes with lower suspension numbers $w_s/u_* < 0.6$ (the two most energetic regimes for dp1) suspended-load dominates. Although it displays higher suspension, the observed repartition for less energetic flow regime with dp1 approaches that of the most energetic hydraulic regime with dp3. This seems consistent with their close values of suspension number, $w_s/u_* \approx 0.65$ for the former and $w_s/u_* \approx 0.8$ for dp1. On the other hand, the most energetic regime with dp1 corresponds nearly to the same hydrodynamic forcing as the less intense regime with dp3. Yet, due to different particle sizes, the former is strongly dominated by bed-load, whilst the latter approaches typical high suspension flows. Note that at lower sediment concentration, the proportion of suspension is generally greater. This is well noticed in both set of experiments, but the empirical definition of bed-load layer thickness (section 3.1) is no longer valid because of the flows are not under (full transport) capacity conditions. Nevertheless, as it was established that the classical approximation of $\delta = 0.05H_f$ holds for dp1, it could be applied for the lower concentration regime (LOW), for the purpose of comparison. The sediment transport repartition values are 16/84, 23/77 and 40/60%. Hence, the modification in the repartition seems to be much more pronounced for the regime with higher proportion of bed-load. The two suspension dominated regimes also display the same trend, but is less pronounced. As mentioned previously, the approximation of the bed-load thickness valid for dp1 is not justified for dp3, even below capacity. Given the particularity of the dataset with dp3, namely with the large particle size and the presence of a thick bed-load layer, the dp3 results will be analysed separately in detail in chapter 4.

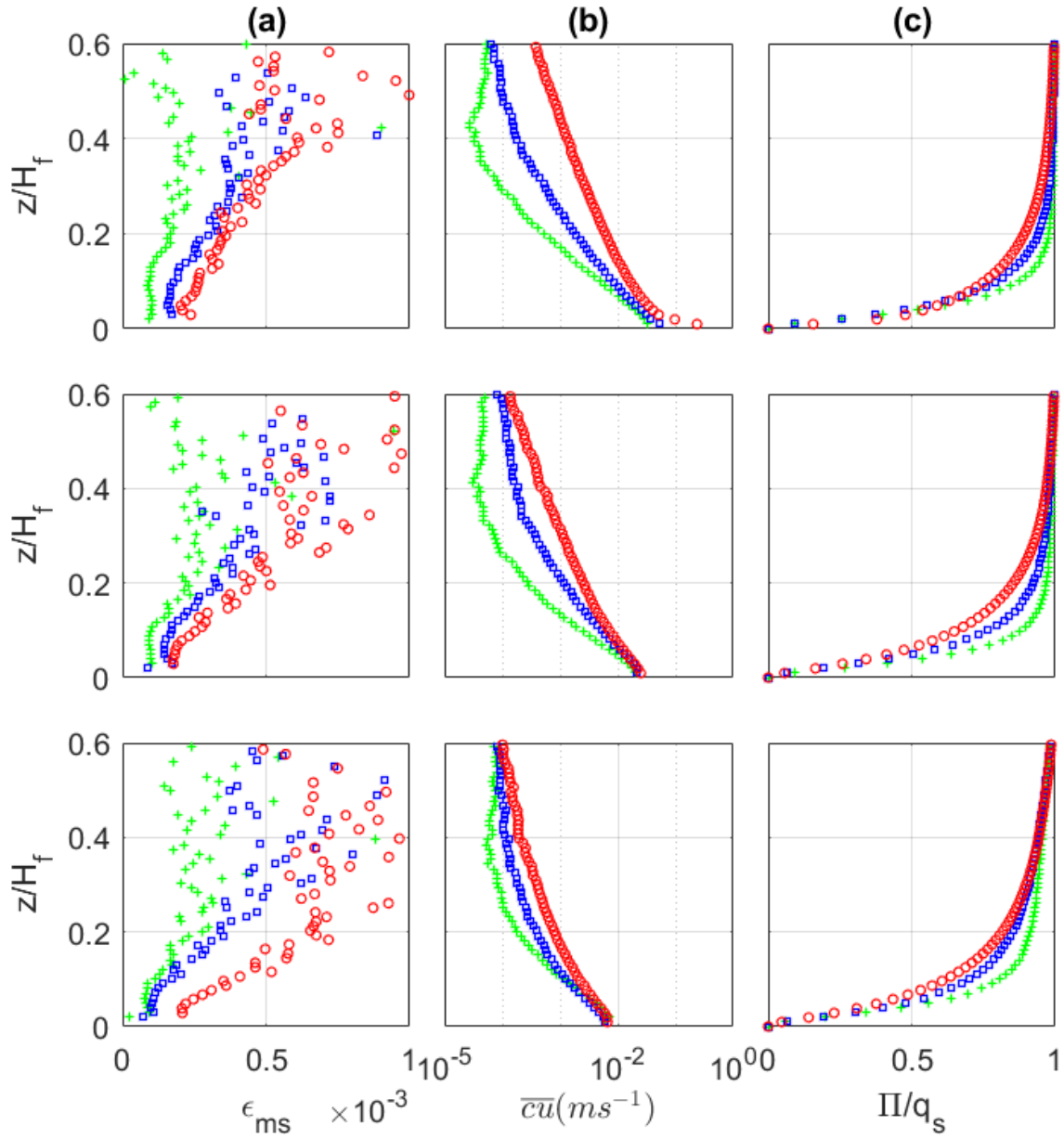


Figure 3-4. Mean profiles of eddy viscosity (a), sediment flux (b) and normalized cumulative sediment flux (c); for dp_3 ; with $\theta \approx 0.35$ (x, green), $\theta \approx 0.50$ (square, blue) and $\theta \approx 0.85$ (o, red); increasing concentration from low (bottom row) to near saturation (top row)

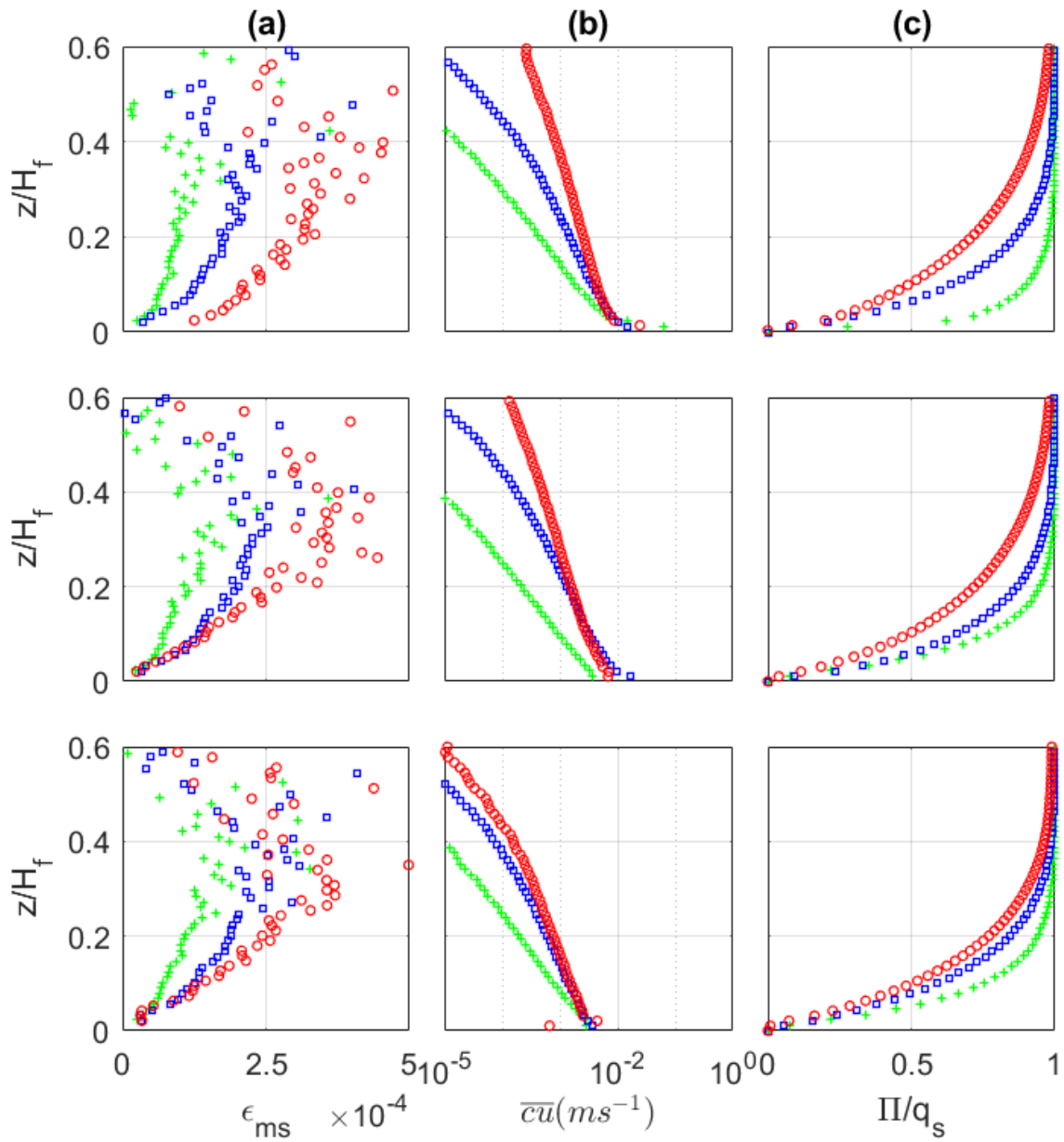


Figure 3-5. Mean profiles of eddy viscosity (a), sediment flux (b) and normalized cumulative sediment flux (c); for dp1; with $\theta \approx 0.4$ (x, green), $\theta \approx 0.90$ (square, blue) and $\theta \approx 1$ (o, red); increasing concentration from low (bottom row) to near saturation (top row)

3.3. Modelling parameters

3.3.1. von Karman parameter κ

The von Karman constant has been determined from a best fit of the mixing length profile with a linear function and from the best fit of the mean streamwise velocity profiles with the law of the wall. In this section, only the fitting based on the velocity profiles are shown. The fitting of the mixing length will be shown and discussed in chapter 4, only for dp3. Figure 3-6 and Figure 3-7 show the fitting of the SL runs and of their reference CW runs. The fitting were performed based on the log-formulation in the following form, applicable to hydraulically rough open-channel flows (Graf and Altinakar 1998):

$$\frac{u}{u_*} = \frac{1}{\kappa} \ln \left(\frac{z - z_d}{k_s} \right) + B_r \quad (3-4)$$

where B_r is the integration constant, z_d is the displacement height of the linear mixing length and k_s is the roughness height. The linear best fitting of the measured profile values of u/u_* on a log scale of $(z-z_d)$ values allows to evaluate the slope $1/\kappa$ and B_r , prescribing u_* , z_d , and k_s . As mentioned previously, the adopted shear velocity u_* is based on the linear extrapolation of the Reynolds shear stress at the bed level height $z=0$. The displacement height corresponds to the vertical level at the origin of the best fitted linear mixing length profile, as detailed in chapter in chapter 4. The roughness height k_s was estimated from the Colebrook and White formulation for rectangular open-channel flows. From Figure 3-6 and Figure 3-7, it can be seen that the deviation from the logarithmic distribution occurs in the lower flow region, due to both the roughness effects as well as the sediments constituting the surface canopy layer. The corresponding values of κ for SL and CW are also shown in the figures. Slight deviations from the universal value $\kappa = 0.41$ occur even in CW, but they remained generally within the range of measurement uncertainty of 15% in terms of relative difference.

The ratio between the values in SL and CW are reported in Figure 3-8. At LOW and MED solid-load conditions, the ratio remained generally close to unity ($\kappa_s/\kappa_{CW} \geq 0.85$). This result suggests that $\kappa_s \approx \kappa_{CW}$ up to moderately high concentrations, since the depth-averaged volumetric concentration at MED regime is roughly $\bar{C} \approx 3 \times 10^{-3}$. Despite some scatter in the results, from Figure 3-8, it seems that at higher concentrations (SAT), κ_s is slightly less affected at $w_s/u_* > 1$. At these regimes, there is a lower proportion of suspended sediments; hence, above the bed-load layer, the slope of the mixing length and the log velocity profiles converge to CW values. For $w_s/u_* < 1$, the local effects of the sediments are more pronounced. In these regimes, the sediments may affect the mixing length and velocity distribution even in the suspension layer. Hence, a quasi-linear mixing length and quasi-log distributions prevail over extended vertical ranges. The convergence towards the CW trends in the upper flow region is also observed. However, when they occur at high vertical levels, in the outer flow region, it is questionable if the log-layer is well justified. Similar observations were made by Lyn (1988), based on the velocity profiles. He reported that in the lower and outer flow regions, the velocity profiles were not strictly logarithmic in sediment-laden flows. He concluded that a log-layer occurred in the intermediate region, and that as the solid-load was increased, the log-layer became narrower and almost vanished in the highest concentrations conditions. He also concluded that the existence of a well-defined log-layer in his experiments is questionable for higher concentrations. Furthermore, at high concentrations,

he observed similar reduction in the values von Karman parameter, i.e., $\kappa_s \approx 0.3 - 0.32$. However, he also performed the fitting as suggested by Coleman (1981), including the wake effects. In this procedure, the von Karman parameter is taken as constant $\kappa = 0.4$, and the wake coefficient is fitted. He concluded that a reasonable good fitting was also obtained, although in the near-bed region, important deviations were observed. This procedure was also adopted by Cellino and Graf (1999) for fully dominated suspension flows, who observed a reasonably good fitting of the velocity-defect law taking $\kappa_s = 0.4$.

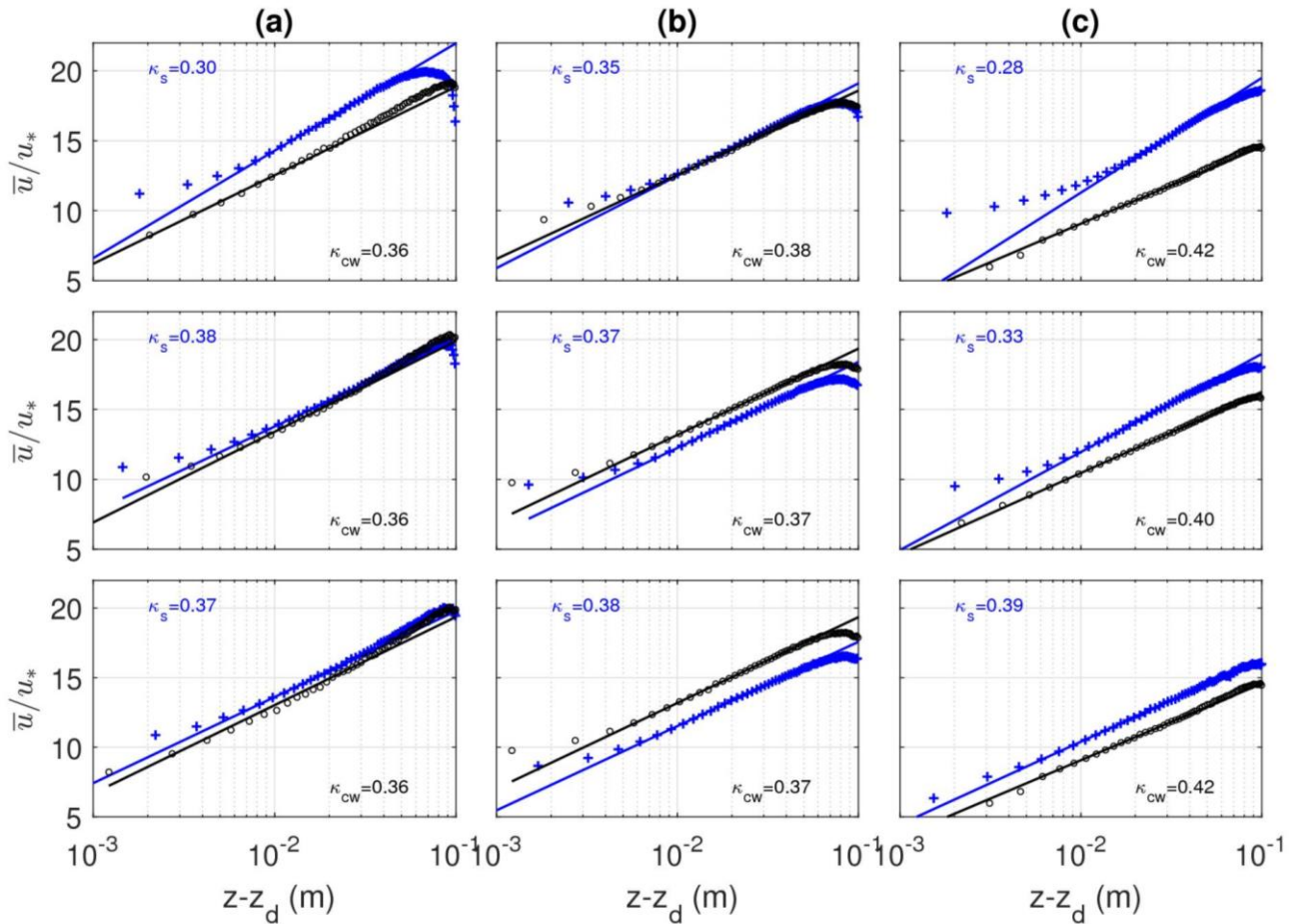


Figure 3-6. Values von Karman parameter in CW (κ_{cw}) and SL (κ_s) based on the fitting of the velocity profiles; for dp3; flow and solid transport regimes as described in Figure 3-4

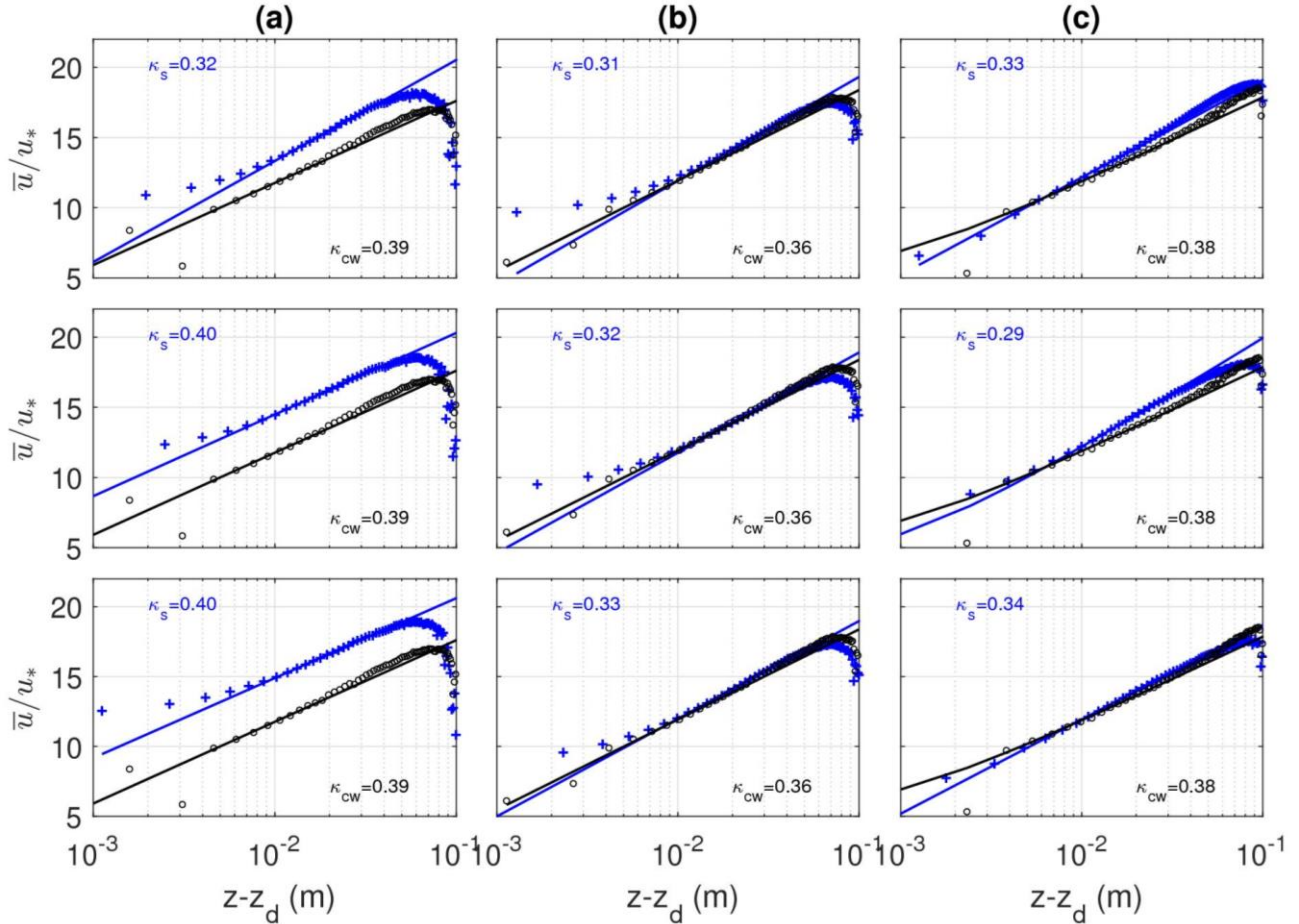


Figure 3-7. Values of von Karman parameter in CW (κ_{CW}) and SL (κ_S) based on the fitting of the velocity profiles; for dp1; flow and solid transport regimes as described in Figure 3-5

In summary, from the present results, and following the discussion above, it seems that the von Karman constant in SL flows with low to moderately high depth-averaged volumetric concentration $O(\bar{C} \approx 10^{-3})$ can be approximated by the CW value $\kappa_S \approx \kappa_{CW}$, since they seem to be only reduced by 15% maximum. At higher sediment concentrations, $O(\bar{C} \approx 10^{-2})$ a reduction of κ_S up to 25% was observed, notably at $w_s/u_* < 1$. It should be emphasized that in the near-bed region, the velocity profiles are not strictly logarithmic. There is generally a gradual convergence to the logarithmic distribution with slopes closer to CW, but in suspension flows with high concentration, the prevalence of a well-defined log-layer may not be always guaranteed. In such conditions, the adopted value of κ_S describes a general trend, rather than the evolving local flow conditions.

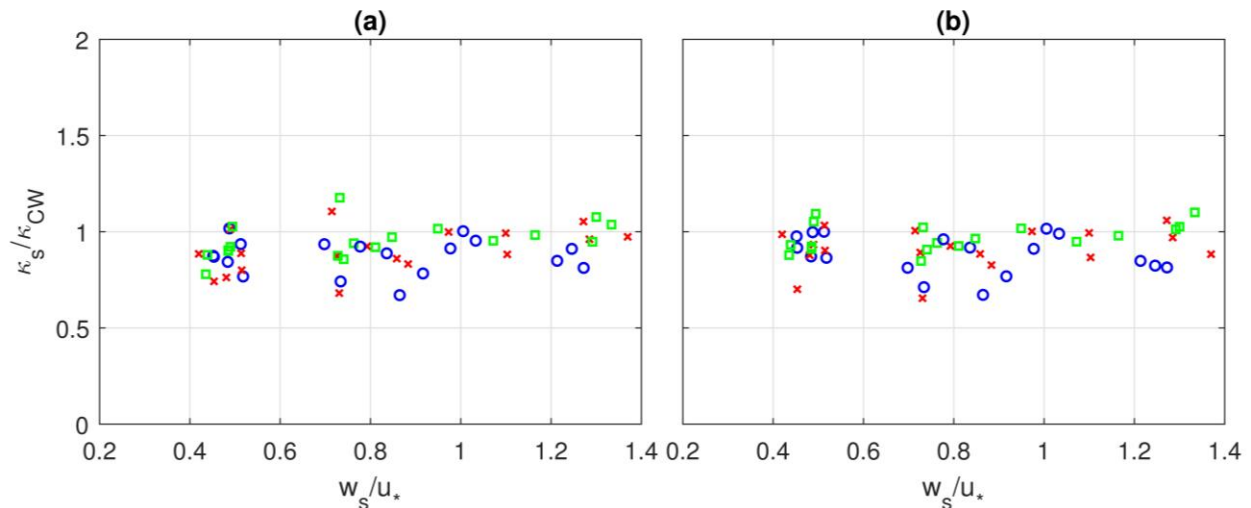


Figure 3-8. Ratio of von Karman parameter in SL and CW based on the linear fitting mixing length (a) and of logarithmic fitting of velocity profiles (b)

3.3.2. β -factor

The depth-averaged ratio between sediment and momentum diffusivity, the so called β -factor, enters into the analytical solution for the mean suspended concentration profile via the Rouse number as shown in section 1.3. In Figure 3-9 and Figure 3-10, profiles of eddy viscosity and sediment diffusivity are presented. Both quantities display a nearly parabolic distribution, at least from a given vertical elevation above the bed-load layer for dp3, and from the near-wall region for dp1. This supports that the bed-load layer significantly affects hydrodynamic properties in the experiments with larger particles. Figure 3-11 and Figure 3-12 show the ratio of sediment diffusivity and eddy viscosity, as well as the depth-averaged value over the quasi-constant vertical range, for dp3 and dp1, respectively. As can be seen, the assumption of proportionality between ϵ_s and ϵ_{ms} over the suspension layer is well justified. With dp3, for the less energetic hydraulic condition (Figure 3-11a) exhibiting a high variability in β -values, the larger discrepancies can be explained by the high suspension number $w_s/u_* = 1.3$ supporting a bed-load dominated transport regime. Furthermore, we can see that the variability in β -values is reduced for all other cases with increasing sediment load. This can be attributed to the increase of suspended particle concentration with loading whereas for the less energetic flow regime with a value of $w_s/u_* = 1.3$, the amount of suspended particles remains low even for the highest injected particle load due to the bed-load dominated transport. The β -factor values show a weak dependence on concentration for all flow conditions, which is in good agreement with previous direct measurements reported by Cellino and Graf (1999) for fully dominated suspension flows ($w_s/u_* < 0.6$).

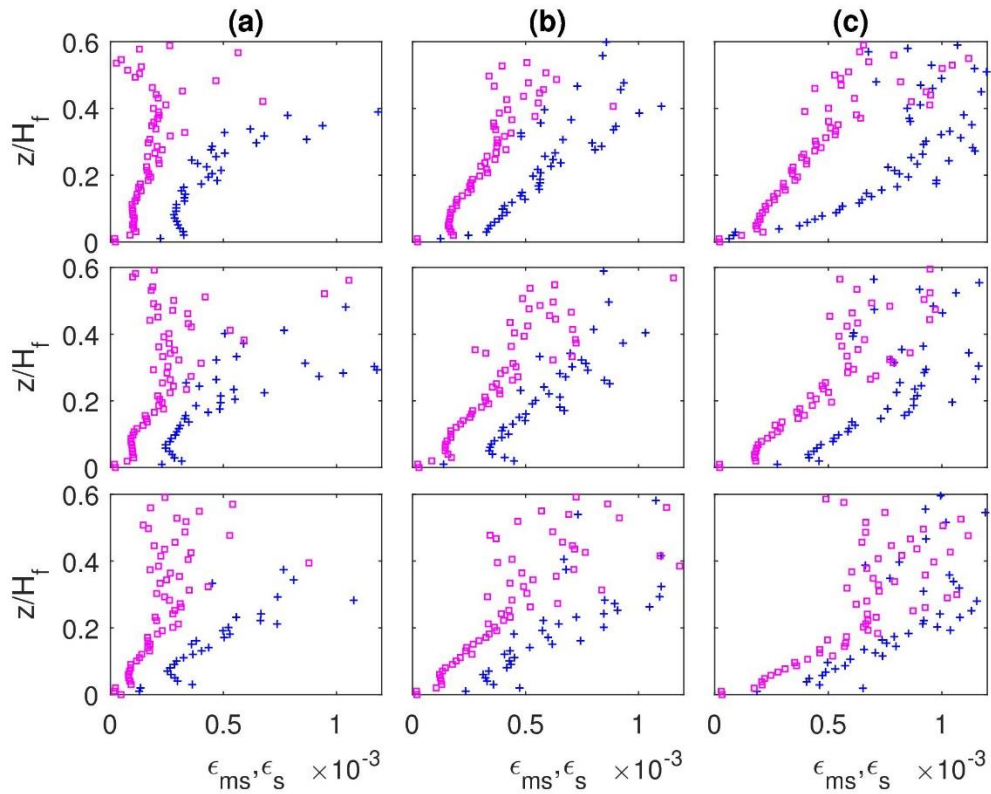


Figure 3-9. Eddy viscosity (ϵ_{ms} , \square) and sediment diffusivity (ϵ_s , $+$) for dp3; flow and solid transport regimes as described in Figure 3-4.

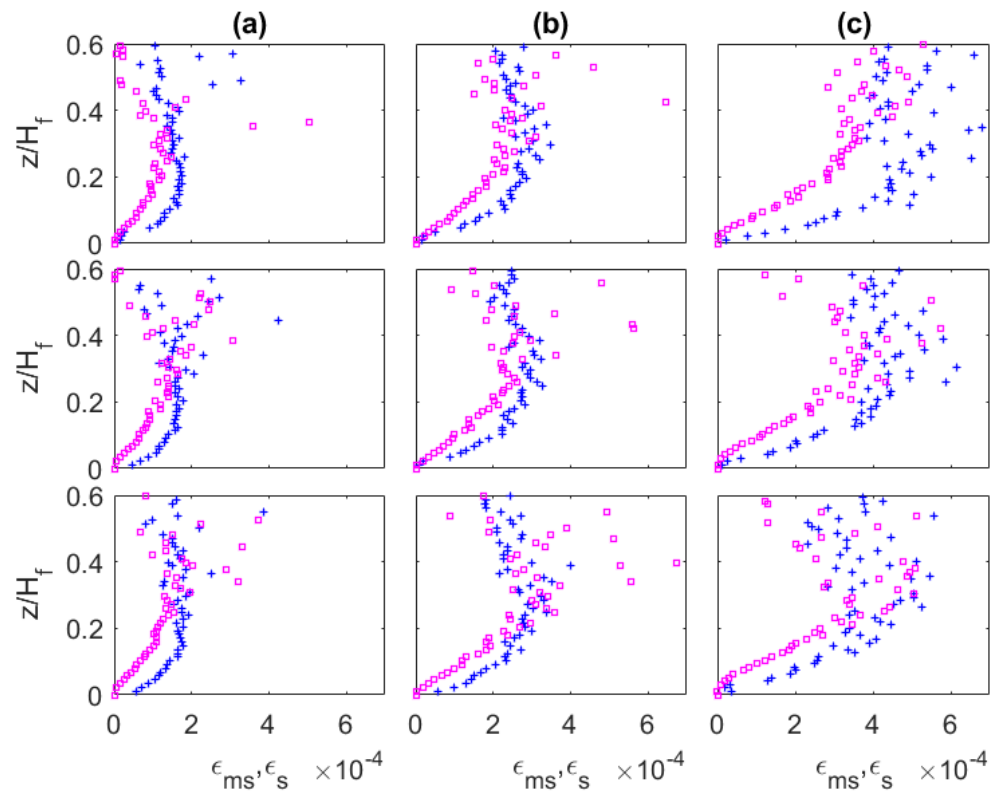


Figure 3-10. Eddy viscosity (ϵ_{ms} , \square) and sediment diffusivity (ϵ_s , $+$) for dp1; flow and solid transport regimes as described in Figure 3-5.

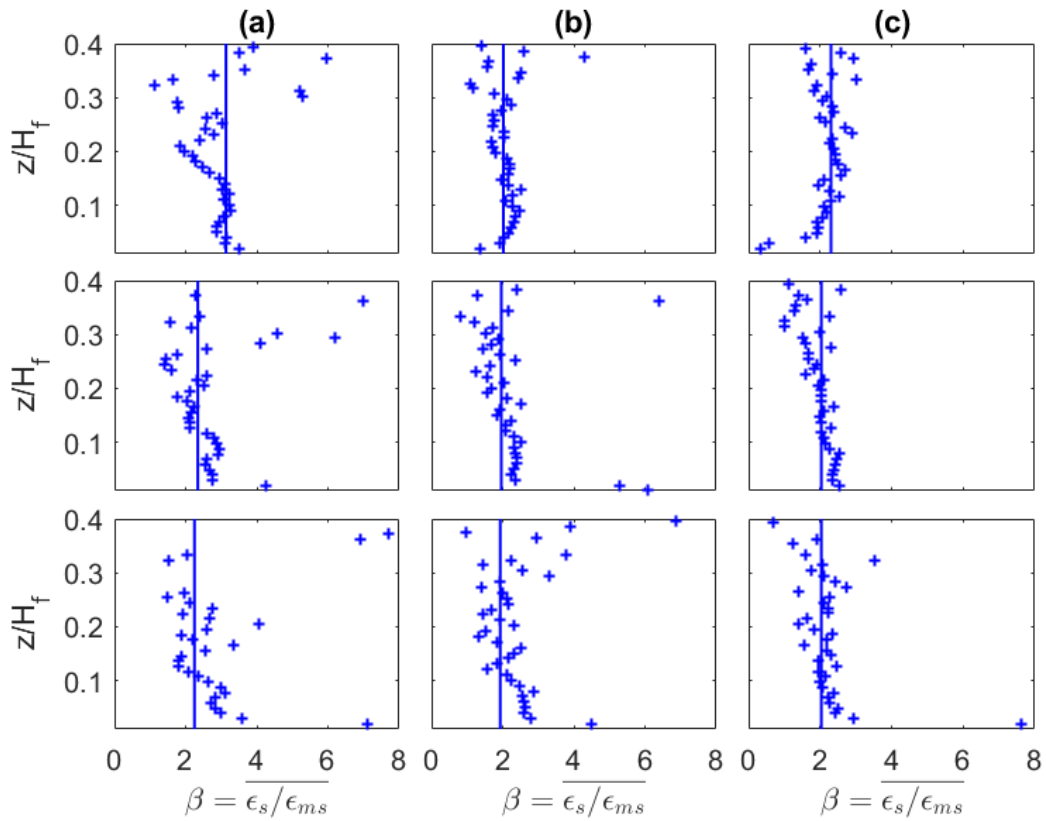


Figure 3-11. Ratio of sediment and momentum diffusivity and its depth-averaged value β ; with dp3; for $\theta \approx 0.35$ (a), $\theta \approx 0.55$ (b) and $\theta \approx 0.8$ (c); for LOW (bottom), MED (middle) and SAT (top).

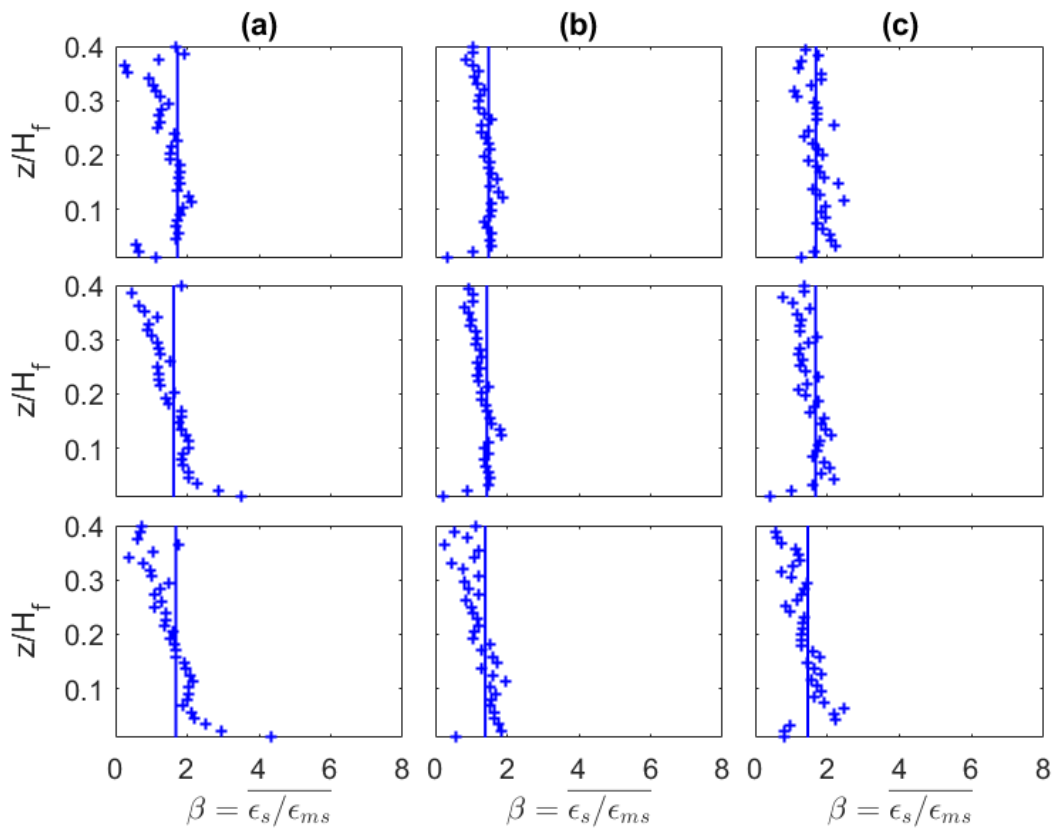


Figure 3-12. Ratio of sediment and momentum diffusivity and its depth-averaged value β ; with dp3; for $\theta \approx 0.4$ (a), $\theta \approx 0.9$ (b) and $\theta \approx 1.1$ (c); for LOW (bottom), MED (middle) and SAT (top).

The evolution of β -values with suspension number $S = w_s/u_*$ is shown in Figure 3-13 for all studied SL flows together with some existing literature data and the empirical model proposed by van Rijn (1984) given by Eq. (3-5) (solid line) as:

$$\beta = 1 + 2 \left(\frac{w_s}{u_*} \right)^2 \text{ for } 0.1 < w_s/u_* < 1 \quad (3-5)$$

A reasonable agreement with Eq. (3-5) is found for $w_s/u_* < 1$ which corresponds to the SL flow conditions used to derive the empirical model. The present data are in reasonable agreement with experimental results from Barton and Lin (1955), Coleman (1970) and Muste et al. (2005). Among the analysed data, measurements from Lyn (1988) are the only to display the opposite trend (β decreases with w_s/u_*), with values rather close to unity ($\beta \approx 0.83 - 1.16$). Graf and Cellino (2002) also observed increasing β -values with w_s/u_* , but with values systematically below unity ($\beta \approx 0.5$). This can be attributed to the methodology applied for the estimation of the β -factor based on direct measurement of $\overline{c'w'}$ rather than $\overline{c}w_s$ (applied herein and in most other studies). Nikora and Goring (2002) used the same method as Graf and Cellino (2002) to estimate β , and the authors obtained values close to unity or slightly above it. Their experiments had very low suspension numbers ($w_s/u_* < 0.1$) supporting the convergence of β towards unity for very small particles having very low inertia relative to the surrounding fluid parcels. An empirical modification of van Rijn (1984) model is proposed here (Eq. (3-6)) to extend the model over a wider range of suspension numbers:

$$\beta = 1 + 0.7 \left(\frac{w_s}{u_*} \right) + 0.7 \left(\frac{w_s}{u_*} \right)^2 \text{ for } 0 < w_s/u_* < 1.5 \quad (3-6)$$

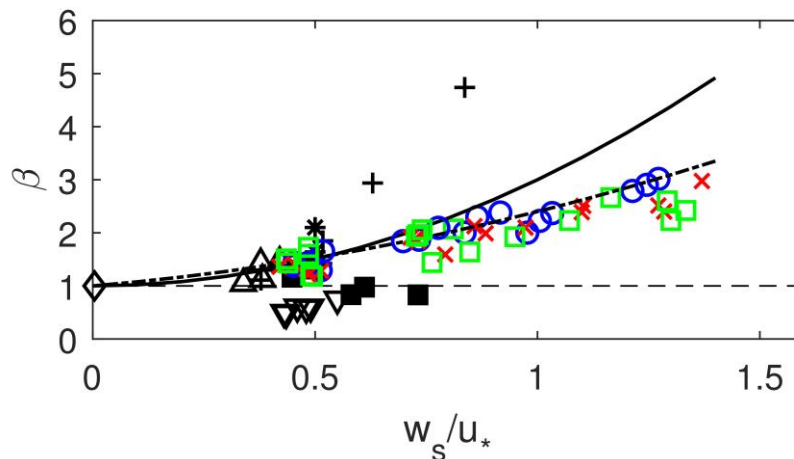


Figure 3-13. Values of depth averaged ratio of sediment and momentum diffusivity β as function of w_s/u_* ; For present results with different concentrations: (o) SAT, (x) MED and (□) LOW; (-) Eq. (3-5); (-.-) Eq. (3-6); (Δ) Barton and Li (1955), (+) Coleman (1970), (■) Lyn 1988, (▽) Graf and Cellino (2002), (◇) Nikora and Goring (2002), (*) Muste et al. (2005). Adapted from Lyn (2008).

3.3.3. Flow resistance: friction factor

In many practical hydraulic engineering applications, the input variables are the channel geometry (width B and slope S_0) and the flow discharge (Q), whilst the unknown are the hydrodynamic variables such as H and U . In both pipe flows and open-channel flows, the

estimations of the hydraulic variables is done by application of friction laws, such as the Darcy-Weisbach equation:

$$S_f = \frac{f}{2g} \frac{U^2}{D} \quad (3-7)$$

where S_f is the energy slope (head loss per meter of length), that equals the bed slope in uniform flow $S_f = S_0$, f is the friction factor, D is the hydraulic diameter, given by $D = 4R_h$ in open-channel, with $R_h = A/P$ as the hydraulic radius (A and P are the wet area and perimeter, respectively). In detailed 3D flow computations, the flow field is determined often using the Reynolds-Averaged-Navier-Stokes (RANS) equations, which requires the application of a turbulence model (mixing length, $k-\epsilon$, $k-\omega$, etc.), to close the momentum equations. However, if only Q and S_0 are known, as in many open-channel problems, the application of friction laws is necessary to estimate the flow depth, hence, the boundary layer thickness.

From the boundary layer theory, the drag force per unit area on the wall surface is given by (Schlichting and Gersten 1988):

$$\tau_0 = \frac{c_f}{2} \rho U^2 \quad (3-8)$$

where c_f is the skin-friction coefficient, related to the friction factor as $f = 4c_f$. This leads to the following equation:

$$\tau_0 = \frac{f}{8} \rho U^2 \quad (3-9)$$

In uniform open-channel, there is a balance between the driving gravity force in the direction of flow $\gamma A \sin\theta L$ (having a bed slope with an angle θ over its length L), and the resistive friction force $\tau_0 PL$, such that:

$$\tau_0 = \gamma R_h \sin\theta \quad (3-10)$$

For relatively small angles, $\sin\theta = \tan\theta = S_0$. In a more general case, in both for uniform and gradually varying free-surface flows, $\sin\theta = S_f$, where S_f is the friction slope or energy slope. The famous Chezy equation can be obtained by combining Eq. (3-9) to (3-10):

$$U = \sqrt{\frac{8g}{f}} \sqrt{R_h S_f} = C \sqrt{R_h S_f} \quad (3-11)$$

This equation has the exact same form as the Darcy-Weisbach equation, but it was developed many decades before (Henderson 1966). Despite its simplicity, it is based on two basic assumptions: the resistive force (shear stress) is proportional to the square of the velocity; and in uniform flows, there is a balance between the gravity force and the resistive force. As seen in the derivation of the equation, the first assumption is confirmed by the boundary layer theory that predicts Equation (3-7), and the second assumption is a direct result of the momentum balance in uniform flows.

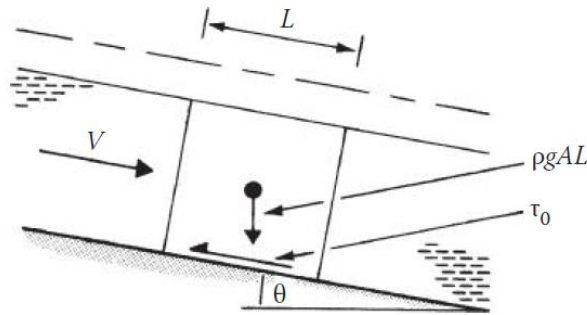


Figure 3-14. Sketch of the balance of forces in uniform open channel flows.

In the nineteenth century, extensive studies were carried out to determine the behaviour of the Chézy coefficient. Examples are the formulae of Ganguillet and Kutter (1869), Bazin (1865) and that of Keulegan (1938), which were all function of the hydraulic radius R_h and a constant dependent on the surface wall roughness. Nevertheless, the following simple formula that fitted well the data of Ganguillet and Kutter (1869) was independently proposed by Gauckler in 1868, Hagen in 1881, Manning in 1889 and Strickler in 1923:

$$C = R_h^{1/6} / n \quad (3-12)$$

where n is the Manning coefficient in $m^{-1/3}s$. Replacing (3-12) in the Chezy equation, it leads to the Manning-Strickler equation, first presented in the current form by Manning in 1889:

$$U = \frac{1}{n} R_h^{2/3} \sqrt{S_f} \quad (3-13)$$

The equation is valid for uniform and gradually varying flows in the hydraulically rough turbulent regime. It has been found to provide good results in both artificial and natural channels (Henderson 1966). Due to its simplicity and reliability in practical applications, it is virtually the most widely used equation for open channel flows (Chadwick et al. 2013). In the present study, the hydraulic quantities for the different forcing conditions were systematically predicted using the Manning-Strickler equation.

Although they may share many common features, turbulent open-channel flows have their own characteristics that differ from closed and open pipe flows. Hence, formulations derived for pipe flows should be applied with caution. Henderson (1966) refers that they are recommended only for small channels with very small roughness height. In field conditions, the surface roughness of rivers is generally very different from those in which the correlations for pipe flows were derived (Chanson 2004). Moreover, even with similar surface roughness, the free surface in open-channel flows has some specific effects on the velocity distribution (Chow 1959, Chadwick et al., 2013). The result is that calibrated uniform flow formulae derived from field observations remain nowadays, the most used approach for large-scale rivers and channels applications. This implies that in practical applications the Chezy and Manning coefficients do not only represent the friction associated to the size of the effective roughness, as the friction factor f . Instead, they include the global resistive effects over any condition of interest, such as regular and irregular surfaces, flood plains, vegetation, etc. The core difference with pipe flows is that f can be well determined for different existing pipe materials, while it is not feasible to represent all possible geometric features of natural rivers. Even in the same river reach, the friction coefficients may vary significantly.

The flow resistance coefficients for our studied flow conditions vary in the range of $f \approx 0.025 - 0.05$, $C \approx 40 - 50 \text{ m}^{0.5}\text{s}^{-1}$ and $n \approx 0.012 - 0.016 \text{ m}^{-1/3}\text{s}$. Figure 3-15 shows the evolution of the friction factor f with bulk Reynolds number and relative roughness for all studied CW runs. At the present range of values of Re and $k_s/4R_h$, the Moody diagram indicates that we are in the fully turbulent regime, therefore, f depends only on $k_s/4R_h$. The results show, however, that f values increase slightly with Re . In addition, f increases with the relative roughness, which is the opposite trend from that in the Moody diagram. One explanation may be that in the present conditions f is more sensitive to the dimensionless roughness height given as $Re_* = k_s u_* / \nu$. As seen in Table 2-1 and Table 2-2, Re_* in the most energetic flow regime is about twice that of the less energetic. These results suggest that the dimensionless roughness height is a better measure of the roughness effects on the flow resistance than the relative roughness $k_s/4R_h$. The former may nevertheless indicate a larger proportion of the roughness sublayer relative to the flow depth, which is the region where effects of the roughness elements on the flow may be pronounced (Raupach 1981).

An important result is that the injection of sediments did not affect the bulk flow resistance. Figure 3-16 shows the comparison between the friction factor in SL and their reference CW. A good agreement between their values is found over the entire range of flow conditions, in all solid-load conditions (LOW, MED and SAT). This is further supported by the practically unaltered flow depth with addition of sediments as seen in Table 2-1 and Table 2-2. From the obtained results, it seems that in absence of bed forms the bulk flow resistance remains rather constant even in under heavy solid-load conditions. This suggests that the typical increase of bulk resistance in mobile-bed flows are mostly due to form drag, induced by bed-forms, rather than turbulent suspension. Moreover, Revil-Baudard et al., (2016) have recently highlighted that the bed mobility has great impact on the flow turbulence near the bed. Therefore, the present starved-bed bulk flow resistance over a rigid bed may differ from the equilibrium-bed, in which the granular bed may indeed be intermittently mobile. Actually, Lyn (1991) reported higher friction factors f in equilibrium-bed, compared to starved-bed conditions. Nevertheless, given that she also reported an increase from CW to starved-bed flows, this evidence is not conclusive.

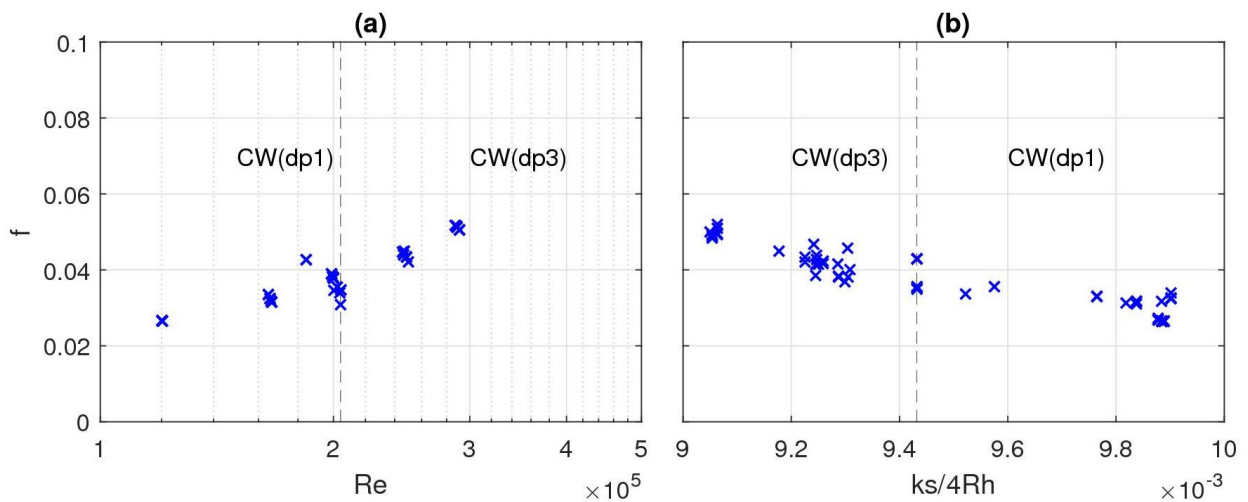


Figure 3-15. Evolution of friction factor with bulk Reynolds number (a) and the relative roughness (b); for the reference CW runs; with (o) SAT, (x) MED and (x) LOW; dashed line represents the transition between dp3 and dp1.

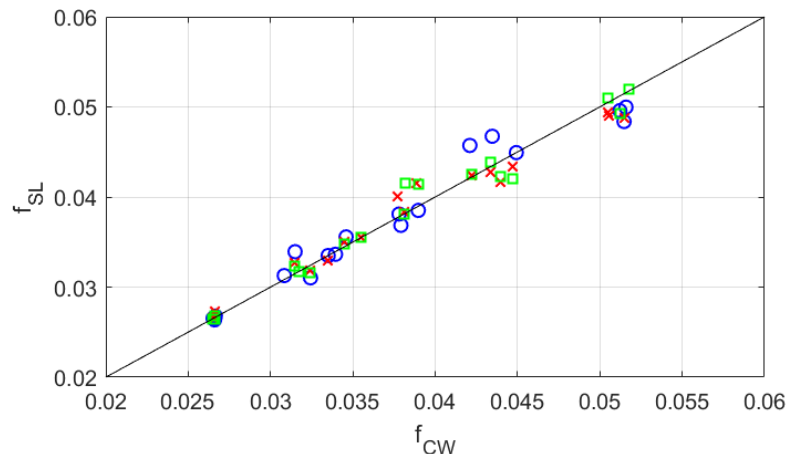


Figure 3-16. Comparison of friction factor in CW and SL; the symbols are the reference CW runs for: (o) SAT, (x) MED and (\square) LOW

3.4. Conclusions

In this chapter, mean profiles of velocity, concentration and Reynolds shear stress have first been presented. Their high degree of repeatability over the runs has been demonstrated. These fundamental hydrodynamic and solid particle transport profiles are used for the determination of profiles of turbulent mixing length, eddy viscosity, sediment diffusivity, and net solid particle fluxes. Key modelling parameters were determined from these profiles, namely, the von Karman parameter, the β -factor and the friction factor f .

It was shown that κ_s can be approximated by the CW values up to relatively high depth-averaged concentrations ($2-3 \times 10^{-3}$) since the maximum reduction was generally less than 15%. In general, at high concentrations the velocity profile is not logarithmic in the bed-load layer. Even outside the bed-load layer, it displays an evolving slope, suggesting that at high concentrations, the adopted values of κ_s represent a general trend, rather than the local flow features. Concerning the β -factor, the quasi-proportionality between momentum and sediment diffusivity was confirmed. The determined values of β agree with the model of van Rijn (1984) at low suspension numbers ($0.1 < w_s/u_* < 0.8$). For larger values of the suspension number, van Rijn's model deviates from the presented data. A modified parametrization was proposed, valid over a wider range of suspension numbers ($0 < w_s/u_* < 1.5$). Regarding the bulk flow resistance, it was seen that the friction factor f was similar in CW and SL flows. It should be stressed that in the present experimental conditions there is no sediment bed even in saturation, hence, the flow bed is a fixed rigid bed constituted of glued particles. Hence, the results should not be extrapolated to equivalent mobile bed conditions.

4. Bedload effects on turbulent suspension properties in large particle sediment-laden flows ($d_p=3\text{mm}$)

In the present chapter, the solid transport regimes with significant contribution of bedload are studied. Distinction between the bed-load and the suspension layer is discussed based on the linearity of turbulent mixing length profiles. It is shown that the bed-load layer has important impact on the vertical structure of the particle-laden flow. An upward shift of the logarithmic velocity layer is seen to be accompanied by a strong reduction of turbulent momentum mixing. The modification of the mixing length affects the theoretical formulation of both velocity and concentration profiles in the suspension layer. A modified analytical solution is derived for the suspended sediment concentration profile taking into account the presence of the bed-load layer for improved predictions compared with the classical Rouse equation.

The results discussed in this chapter are based on the following paper (accepted for publication) from Guta et al. (in press): Guta, H., Hurther D., Chauchat, J. (in press). “Bed-load and concentration effects on turbulent suspension properties in heavy particle sheet-flows”. *Journal of Hydraulic Engineering*, doi:10.1061/(ASCE)HY.1943-7900.0001988.

4.1. Introduction

When the Shields number θ exceeds a critical value of approximately 0.4 (Rickenmann 1991, García 2008), energetic bed-load occurs in a layer with thickness of several particle diameters d_p (Wilson 1987). In such conditions, bed-forms are washed out and the sediment bed becomes flat. This is known as sheet-flow (Sumer et al. 1996) or upper stage plane bed regime. In this regime, the hydraulic resistance and the relative bed roughness scale with the thickness of the bed-load layer rather than the skin roughness elements themselves (Wilson 1989, Sumer et al. 1996, Ribberink et al. 2008). Whether an intense bed-load carries a higher fraction of the transported sediment load as a turbulent suspension load or as bed load depends on the ratio w_s/u_* . Sumer et al. (1996) observed that the transition from the suspension mode to the no-suspension mode occurs around $w_s/u_* \approx 0.8 - 1$. By increasing importantly the range of suspension number value originally studied by Wilson (1989), he noticed that some properties of sheet-flows depend on whether it occurs in suspension ($S < 0.8$) or no-suspension mode ($w_s/u_* > 1$). Recently, Finn and Li (2016) represented all possible types of sediment-turbulence regimes in the Shields diagram. Their results suggest that the domain covering the range $0.8 < w_s/u_* < 1.3$ with $\theta > 0.8$, corresponds to sheet-flows of medium to large sand or gravel particles. This type of intense sediment-laden flows represents a frequently established flow case during river floods and coastal storms and therefore merits to be studied from a physical process-oriented point of view in order to improve our numerical prediction ability of sediment transport and bed morphology evolution.

In such sheet-flow conditions, the conventional bed-load formulae do not predict reliable sediment transport rates because complex turbulent particle mixing, turbulence-particle interactions as well as particle-particle interaction processes all play important different roles across the bottom boundary layer (Revil-Baudard et al. 2015, 2016). The modifications of the turbulent boundary layer in intense sediment-laden flow conditions implies greater efforts in

the parametrization of classical laws such as the log-law and Rouse profiles, for velocity and concentration distribution, respectively. For example, van Rijn (1984) concluded that more research effort was necessary to provide new parametrized velocity profile formulations valid for heavy sediment-laden flows. He stressed that the standard logarithmic velocity distribution was not able to predict the vertical velocity structure accurately enough to derive reliable sediment transport rates. Similar conclusions were drawn concerning the concentration distribution.

In the present chapter, we focus on the large particle experiments (dp3). They correspond to regimes having high Shields numbers ($\theta \geq 0.4$), with suspension number values of the order of $S \approx 0.8 - 1.3$. These challenging flow conditions have been rarely investigated in the literature despite their frequent occurrence in natural sediment-laden flows. We investigate the vertical flow structure with particular attention given to potential bed-load layer effects on the mean velocity and concentration profiles in the suspension layer.

4.2. Turbulent mixing length and eddy viscosity

The law of the wall is based on two basic assumptions: in the wall region of a fully turbulent wall-bounded flow, the turbulent mixing length is proportional to the distance z from the bed and the shear stress is nearly constant which can be approximated by the bed shear stress $\tau = \tau_0 = \rho u_*^2$. Measured profiles of Reynolds shear stress follow a nearly constant trend for $0.10 \leq z/H_f \leq 0.30$ around the maximum values and a nearly linear mixing length profile ($l_{ms} = u_*/(du/dz)$) for $z/H_f \geq 0.05 - 0.15$, as can be seen in Figure 3-1c and Figure 4-1, respectively. Please note that the nearly constant trend of the measured Reynolds stress profiles ($0.10 \leq z/H_f \leq 0.30$) herein refers to the region around its maximum value, where variations lower than 20% from the maximum are observed, hence, $\sqrt{|u'w'|}$ can be approximated as u_* following Prandtl assumption. In the near-bed region, corresponding to $z/H_f \leq 0.05 - 0.15$, Figure 4-1 reveals that the mixing length profiles for all SL flows deviates from the linear distribution.

The level δ below which the measured mixing length deviates by more than 15% from the linear fit is arbitrarily defined as the bed-load layer thickness. This threshold matches roughly the accuracy of the mixing length measurements (10-15%). The upper limit of the linear fit was limited such that the squared correlation coefficient between the fitted and measured data remained higher than 90% ($R^2 \approx 0.9$). Above the vertical level δ , the mixing length follows the linear relationship:

$$l_{ms} = \kappa_s(z - z_d) \quad (4-1)$$

where z_d is the origin of the linear mixing length and κ_s is the von Karman constant in SL flows. The level δ , illustrated with a horizontal dashed line in Figure 4-1, corresponds to the transition between the turbulence dominated region or suspension layer and the particle-particle interaction dominated region defined as the bed-load layer. Based on the considerations proposed by Bagnold (1956), Wilson (1987, 1989) reported that the thickness of this layer is approximately $\delta/d_p \approx 10\theta$. This should be taken as an indicative value, as Sumer et al. (1996) argued that the dynamics of sheet-flow processes depend on whether the sheet-flow is in suspension, transitional or no-suspension regime. Furthermore, Ribberink et al. (2008) showed that the proportionality constant 10 can also vary by more than 30% due to the different methods applied by authors for the bed-load layer thickness estimation. This is confirmed herein, with

the proportionality constant in capacity conditions, having values of 17, 12.5 and 9 for our three flow regimes (from lower to higher Shields number), based on the linear mixing length criteria. The corresponding bed-load thickness are $\delta \approx 6d_p$, $6.5d_p$ and $7d_p$, respectively. Note that the agreement with the proportionality constant of 10 is particularly good for the most energetic flow conditions, which are closer to the conditions in which this parametrization was obtained ($\theta \geq 1$). The result agrees well also with Sumer et al. (1996) for their larger particle experiments (designated sediment 1 and sediment 2 in their manuscript), with a range of bed-load thickness of $\delta/d_p \approx 5 - 15$. Due to the large size of the low-density particles used in the present work, the bed-load layer of all studied SL flows is considerably thick and can be well resolved by the ACVP measurement, since $\delta/z_d = 7$ corresponds roughly to $z/H_f \approx 0.14$. Recently, Blanckaert et al. (2017) estimated the bedload thickness based on ADV measurements, having obtained for their most intense flow conditions $\delta/d_p \approx 10$, consistent with the present results.

Applying the proposed criteria, the proportion of bed-load/suspended-load evolves from approximately 20/80, 40/60 and 70/30% to 70/30, 80/20 and 90/10% as the concentration is increased from low sediment load to capacity, for $w_s/u_* = 0.8$, 1.0 and 1.3, respectively. The only regime displaying persistently a greater proportion of bed-load is the one with $w_s/u_* \approx 1.3$, independently on the particle transport rate. This confirms that we are in presence of a bed-load dominated regime, and two transitional regimes in which greater proportions of suspended-load occur at lower concentration, while greater proportion of bed-load occurs in saturation.

Another relevant quantity is the displacement height z_d defined as the origin of the linear mixing length profile (Eq. (4-1)). Sumer et al. (1996) found that as the bed-load thickness, z_d also increases with Shields number θ , and its magnitude was approximately $0.5\delta < z_d < \delta$. This is in good agreement with the present experiments in capacity conditions for which $0.4\delta < z_d < 0.7\delta$.

For the highest sediment load experiments, the mixing length values are larger than the one measured in the corresponding CW flow inside the bed-load layer for $z/H_f \leq 0.05$ (black circle symbol curves in Figure 4-1). This supports the existence of additional shear stress due to particle-particle interactions. Nevertheless, since the mixing length remains nearly constant over the entire bed-load layer, the clear water value exceeds this constant value at a certain height inside the bed-load layer because its linear trend starts from a level much closer to the bed. The slope of the mixing length in SL flow gradually converges to CW values, above the bed-load layer. The obtained values of κ_s estimated from the linear fit of the mixing length are quite close to CW values for lower and intermediate concentrations, and moderately smaller for the highest sediment loads (see Table 4-1). It implies that in the present conditions, the absolute value of the mixing length at a given vertical level in the suspension layer may be significantly reduced, due principally to the large displacement height z_d induced by the presence of the bed-load layer rather than a strong reduction of mixing efficiency via a lower κ_s value. This is especially the case for moderate concentrations ($\bar{C} < 2 - 3 \times 10^{-3}$), as seen in Figure 4-1. Revil-Baudard et al. (2016) also found a strong upshift of the linear mixing length profile (see their Fig. 2b) due to a large displacement height associated with the bed-load layer in agreement with the present results. However, a much lower κ_s value was measured in the turbulent suspension layer which might be due to experiments conducted in fully developed capacity conditions over mobile granular beds.

The mixing length model is widely applied as a closure for velocity and concentration distribution through the eddy viscosity. Under the assumption of a constant Reynolds shear

stress in the logarithmic layer and a linear profile in the above outer flow region (confirmed from Fig. 1c), the well-known parabolic distribution of eddy viscosity (Lyn 2008) is given by:

$$\epsilon_{ms} = \kappa_s u_* (z - z_d) \left(1 - \frac{z}{H_f}\right), \text{ for } z > \delta \quad (4-2)$$

Equation (4-2) is valid in the flow region where the mean velocity distribution follows a logarithmic profile, usually called the log-layer. Above the log-layer, several researchers (Coleman 1981; Nezu and Rodi 1986) have shown that a better agreement is found when wake effects are included using the log-wake law. These effects are not considered here since the wake region is affected by the presence of the ACVP holding box placed at the water free-surface. For this reason no profile is analysed in this study for $z/H_f \geq 0.6$. In the following two subsections, the immediate implications of the modified turbulent mixing length and eddy viscosity on mean velocity and concentration will be presented.

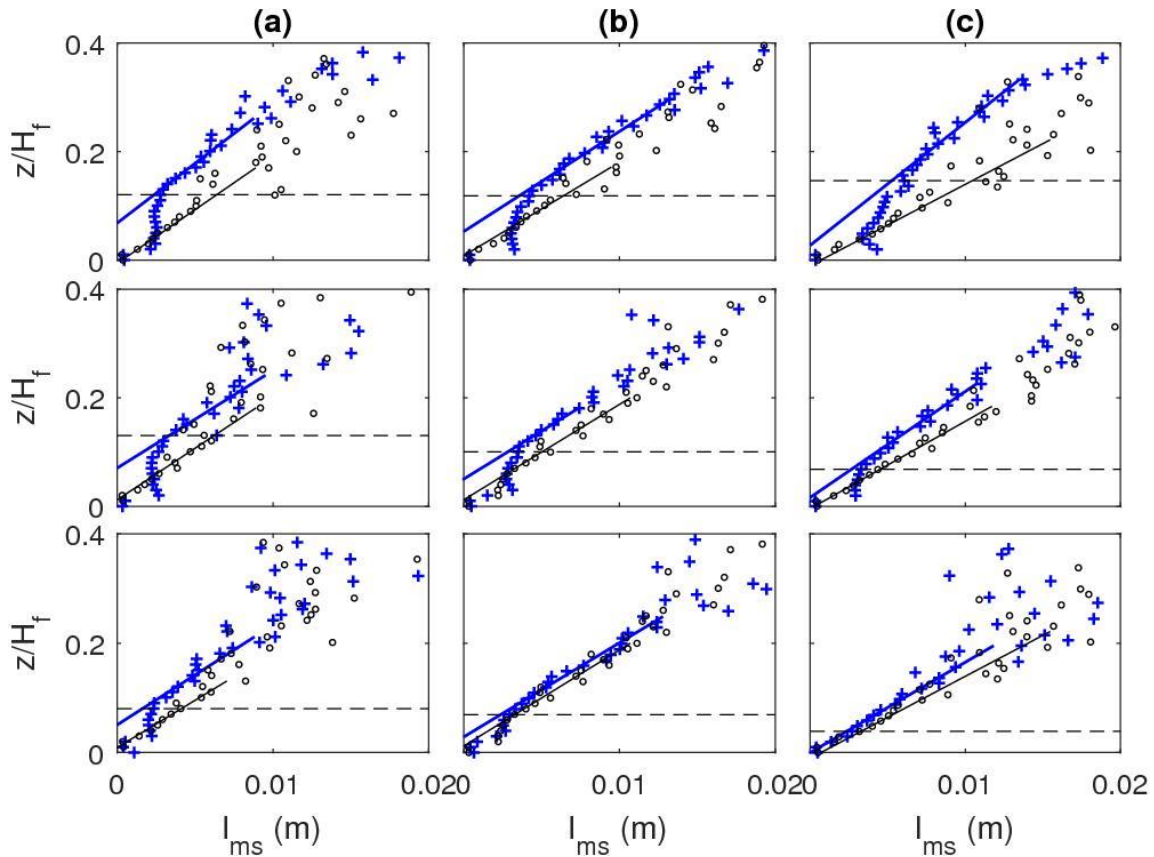


Figure 4-1. Mixing length $l_m = u_*^2 / (du/dz)$; for $\theta \approx 0.35$ (a), $\theta \approx 0.55$ (b) and $\theta \approx 0.8$ (c); for lower concentration (bottom), intermediate (middle) and saturated (top). Blue (+) is for sediment-laden and black (o) is for clear-water. Dashed line corresponds to bed-load thickness

4.3. Velocity distribution

The present section aims at proposing a revisited formulation of the mean velocity distribution valid in the suspension layer for SL flows of heavy particles. Integrating $du/dz = u_* / \kappa_s (z - z_d)$ in the suspension layer from the bed-load layer thickness δ to a given position z , the velocity profile can be written as:

$$u = \frac{u_*}{\kappa_s} \ln(z - z_d) + C \quad (4-3)$$

with $u = u_\delta$ at $z = \delta$, the integration constant is $C = u_\delta - u_*/\kappa_s \ln(\delta - z_d)$. Therefore, the law of the wall takes the following form:

$$u = \frac{u_*}{\kappa_s} \ln\left(\frac{z - z_d}{\delta - z_d}\right) + u_\delta \quad (4-4)$$

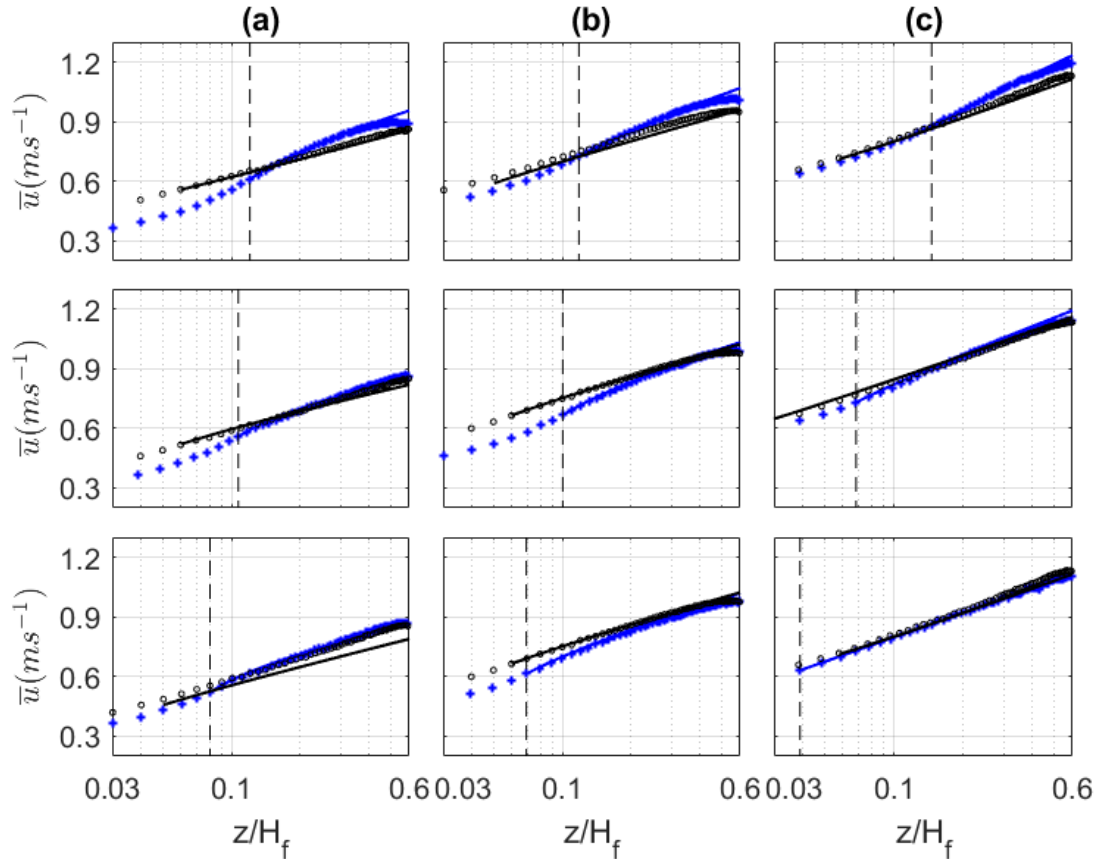


Figure 4-2. Velocity distribution; for SL (blue,+) and CW (black,o). Solid lines correspond to Eq. (4-4). Flow and solid transport regimes as described in Figure 4-1. Dashed line corresponds to bed-load thickness δ

In the literature the log-law in CW is often described with a similar equation, taking $u_\delta = Br u_*$, where Br is the integration constant valid for rough flows (García 2008) and $\delta - z_d = k_s$ is the roughness height. The displacement height z_d appears also in CW for hydraulically rough flows due to the presence of a roughness sublayer. Herein, the displacement height z_d of SL flows is larger than in the respective CW flows. The velocity profile can be fitted to determine κ_s and Br as the usual practice. The obtained values of κ_s are generally in very good agreement (as shown in section 3.3.1) with those determined from the slope of the mixing length distribution (see Figure 4-1). This is consistent with the good agreement between Eq. (4-4), represented as blue solid lines in Figure 4-2 with experimental data (blue cross symbols). The velocity profile is following closely the logarithmic distribution given by Eq. (4-4) over the entire suspension layer (above the vertical black dashed line). Compared with the logarithmic

layer in the corresponding CW flows (black cross symbol and solid curves), it can clearly be seen that the log-layer in the sheet-flow conditions are strongly shifted upwards due to the presence of the bed-load layer. Inside the bed-load layer, the velocity distribution approaches a quasi-linear shape in the vicinity of the fixed-bed. Similar trend has been reported by Sumer et al. (1996) who parametrized the velocity profile with a power law having an exponent close to unity (0.75). Regarding the overall shape of the observed velocity profiles, there is a good agreement with previous literature results (Einstein 1955, Coleman 1981, Lyn 1988). Typically, a significant reduction of the flow velocity in the bed-load layer followed by an increase in the outer layer is observed in the reported data when compared to the respective CW velocity profiles. A similar trend was recently found by Blanckaert et al. (2017).

4.4. Concentration distribution

The present section aims at proposing a revisited formulation of the mean sediment concentration distribution in the suspension layer of heavy SL flows. If the effect of displacement height in the eddy viscosity formulation is considered (Eq. (4-2)), the integration of the Eq. (1-31) of the vertical fluxes holds:

$$\frac{\bar{c}}{C_a} = e^{-z_r \left[\frac{2}{F} \operatorname{atan}\left(\frac{-2z/H_f+B}{F}\right) - \operatorname{atan}\left(\frac{-2a/H_f+B}{F}\right) \right]} \quad (4-5)$$

where

$$F = \sqrt{\frac{4z_d}{H} - \left(1 - \frac{z_d}{H}\right)^2} \quad (4-6)$$

and

$$B = \left(1 - \frac{z_d}{H}\right) \quad (4-7)$$

are two integration constants.

The β -factor ($\beta = \overline{\epsilon_s/\epsilon_{ms}}$) was determined experimentally taking ϵ_s estimated using Eq. (1-30) and $\epsilon_{ms} = -\overline{u'w'}/(du/dz)$, as discussed in chapter 3. The β value corresponds to the depth-averaged value of ϵ_s/ϵ_{ms} over the range of quasi-constant magnitude found in the suspension layer as it will be shown later. The behaviour of this crucial parameter and its prediction from a model will be addressed in the following subsection. The reference concentration is not taken at $a \approx 0.05H_f$ or $a \approx 2d_p$, as classically done, since the bed-load layer thickness varies considerably as a function of SL flow conditions (see subsection ‘‘Turbulent Mixing Length’’). The reference height here will be taken as the value of the bed-load thickness $a = \delta$. This will allow testing the validity of the new suspended sediment concentration formulation over the largest possible vertical range. The comparison between the measured and predicted concentration profiles from Eq. (4-5) and from the classical Rouse equation (Eq. (1-32)) are represented in Figure 4-3. The measured concentration distribution is well described by the revisited analytical solution. Note that the agreement is consistently better for the four panels on the upper right, where higher suspension load occurs. Although a relatively good agreement prevails, greater relative differences between the modelled and measured profiles are observed in the cases with the lowest concentrations or proportion of suspended load. This trend may indicate that high accuracy is required to model very low concentrations. One can observe that the Rouse equation overestimates the concentration

profile, consistent with the higher eddy viscosity model. Both equations provide good results when z_d is small. This is seen for the low concentration of the strongest flow regime (Figure 4-3c, bottom panel) for which most of the sediment load is carried in suspension. In this case the bed-load thickness δ is small, with a value of $z/H_f \approx 0.05$ very close to the reference height usually taken in open-channel suspension flows ($w_s/u_* < 0.8$). In cases where a thick bedload layer exists, the arbitrary height of 5% relative to the local flow depth might be located inside the bedload layer inducing significant errors in concentration prediction when using the classical Rouse formulation. In the present study, the new formulation of the suspended sediment concentration profile offers improved sediment transport prediction over the entire suspension layer in flows where both bedload and suspended load are significant (i.e. $0.6 < w_s/u_* < 1.5$).

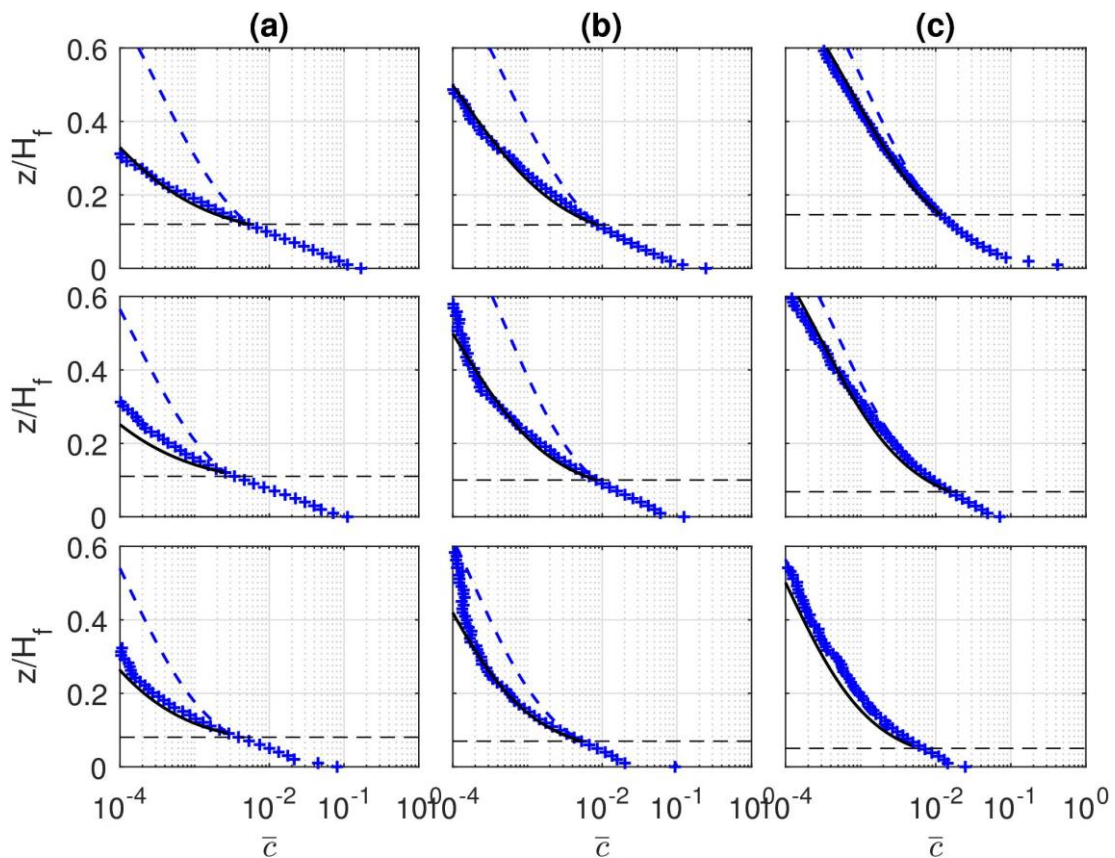


Figure 4-3. . Concentration distribution; measured + (blue), Rouse profile (- -, blue) as in Eq. (1-32) and Modified Rouse profile (--- black) as in Eq. (4-5). Flow and solid transport regimes as described in Figure 4-1.

Table 4-1. Summary of results, including range of variation over different experimental runs. κ_s is the von Karman in sediment-laden flows; δ is the bed-load thickness; z_d is the displacement height of the mixing length; β is the depth-averaged ratio between sediment and momentum diffusivity

u_* (m/s)	θ (-)	q_s ($\times 10^{-4}$) (m^2/s)	\bar{C} ($\times 10^{-3}$)	κ_s	δ/d_p	z_d/d_p
0.043	0.35	0.0	0.0	0.40 \pm 0.01	-	0.50 \pm 0.2
		0.67 \pm 0.04	1.20 \pm 0.07	0.38 \pm 0.01	4.70 \pm 0.58	2.79 \pm 0.26
		1.42 \pm 0.07	2.60 \pm 0.09	0.37 \pm 0.02	5.70 \pm 0.30	3.65 \pm 0.20
		2.42 \pm 0.16	4.10 \pm 0.26	0.31 \pm 0.04	6.03 \pm 0.40	3.28 \pm 0.23
0.055	0.55	0.0	0.0	0.4 \pm 0.01	-	0.30 \pm 0.2
		0.71 \pm 0.09	0.87 \pm 0.15	0.39 \pm 0.01	4.52 \pm 1.00	1.69 \pm 0.23
		2.17 \pm 0.11	2.80 \pm 0.14	0.38 \pm 0.01	5.70 \pm 0.58	2.68 \pm 0.23
		4.06 \pm 0.27	4.90 \pm 0.38	0.35 \pm 0.02	6.89 \pm 0.77	3.13 \pm 0.41
0.07	0.80	0.0	0.0	0.40 \pm 0.01	-	0.10 \pm 0.2
		0.96 \pm 0.09	0.81 \pm 0.10	0.40 \pm 0.03	2.17 \pm 0.29	0.12 \pm 0.27
		3.15 \pm 0.14	3.15 \pm 0.05	0.36 \pm 0.03	4.02 \pm 0.87	1.15 \pm 0.52
		9.76 \pm 0.51	9.40 \pm 0.80	0.32 \pm 0.04	7.21 \pm 0.58	2.21 \pm 0.72

4.5. Discussion

Bed-load layer effects on the velocity distribution in a SL flow involving heavy particles has been reported herein and a modified velocity distribution model has been proposed in Eq. (4-3) which takes these effects into account. As shown throughout its derivation, this modified logarithmic solution is valid only above a certain distance from the bed, herein corresponding to the top of the bed-load layer, where the linear mixing length assumption becomes valid. Sumer et al. (1996) noticed in their sheet-flow experiments with the larger particles, having similar particle diameters and density as in the present study, that the displacement height z_d may be much higher than the classical value for CW rough-bed flows. Furthermore, several researchers (Wilson 1989, Sumer et al. 1996; Ribberink et al. 2008) found that under sheet-flow conditions the relative roughness scale is neither that from smooth (viscous length related) or rough flows (related to size of elements constituting the bed skin friction). As seen in Eq. (4-3), the thickness of the bed-load layer δ and the displacement height z_d become relevant scales for defining k_s in SL flows involving heavy particles. This complex interaction between the bed-load and the flow resistance was also highlighted by Camenen et al. (2006) and Recking et al. (2008) over wide range of flow and transport conditions.

One important outcome of the bed-load layer induced upshift of the log-layer is the strong reduction of the mixing length in the near-wall region, and the classical analytical Rouse solution for the suspended sediment concentration profile becomes inaccurate with increasing displacement height z_d (scaling with the bed-load layer thickness). This seems to be due to the overestimation of the momentum diffusivity (and sediment diffusivity) in presence of a thick bed-load layer. An inspection of Eq. (1-32)) indicates that an overestimation of ϵ_{ms} leads to artificially reduced values of β , such that $\epsilon_s = \beta\epsilon_{ms}$ remains constant. It was indeed observed (not shown here) that the values of β obtained from a classical best fit method of the Rouse profile are systematically lower than those measured directly and represented in Figure 3-13. On the contrary, a good agreement was found between β values obtained from a best fit of the proposed modified Rouse solution (Eq. (4-5)) and the directly measured ratio $\beta = \epsilon_s/\epsilon_{ms}$. This confirms that in energetic SL flows and in presence of a thick bed-load layer, β cannot be determined from a best-fit of the classical Rouse equation as is usually done in laboratory and field studies.

In section 4.2, it was shown that even at the lowest concentration investigated herein, the hydraulic regime with higher values of w_s/u_* (higher proportion of bed-load) exhibited significant reduction of turbulent mixing length compared with the corresponding CW flows, although with similar values of κ_s . Since this reduction was due to larger displacement height z_d , it tends to indicate that the presence of a thick bed-load layer is the dominant effect on the reduction of momentum mixing at moderate concentrations ($\bar{C} < 2 - 3 \times 10^{-3}$). With a higher suspended load, additional effects dependent on local concentration may also play a role in the damping of momentum mixing. This reduction of momentum mixing has been studied in the literature (Smith & McLean, 1977; van Rijn, 1984; Hsu et al. 2004) and a damping factor ϕ corresponding to the ratio between the eddy viscosity or turbulent mixing length in SL flows and the corresponding CW quantity has been introduced $\phi = \overline{\epsilon_{ms}}/\overline{\epsilon_m}$. Figure 4-4 shows the mean values of ϕ as a function of suspension number w_s/u_* which have been depth-averaged over the suspension region in the same way as the β -factor. It can be seen that ϕ slightly increases before decreasing around the critical value of about $S = w_s/u_* \cong 1$, regardless of the injected sediment load. Note that the observed trend of lower values of ϕ for higher suspension numbers, $w_s/u_* = 1.2-1.3$ seems to be well established for all concentrations. This is not as well established for the lower values of $w_s/u_* \leq 1$, particularly for saturated cases. Nevertheless, the change in trends of ϕ at roughly $w_s/u_* \cong 1$, suggests that different transport mechanisms occur in suspension and no-suspension mode. Furthermore, the combination of global effects (roughness, thick bed-load layer) and local effects (stratification, drag modification, etc.) induces great challenges for two-phase flow modelling.

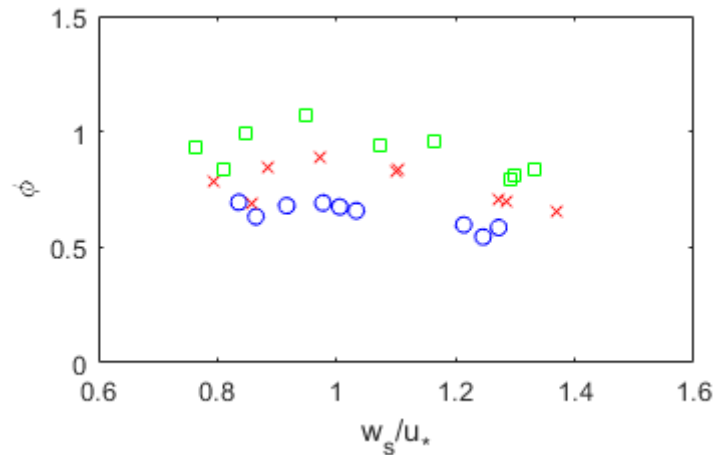


Figure 4-4. Values of ratio of eddy viscosity in SL and corresponding CW flow: $\phi = \overline{\epsilon_{ms}}/\overline{\epsilon_m}$. (o) SAT, (x) MED and (\square) LOW

4.6. Conclusions

Bed-load effects on turbulent suspension properties are investigated in SL flows involving heavy particles based on a new set of high-resolution experimental data. A new criterion for separating the bed-load layer from the suspension layer has been proposed based on the vertical distribution of turbulent mixing length. Inside the suspension layer, the mixing length follows a linear profile with a von Karman constant as the proportionality factor, of value close to its clear water flow value. Inside the bed-load layer, the mixing length exhibits a quasi-constant vertical distribution as previously observed in Revil-Baudard et al. (2015, 2016). This criterion

is found to be consistent with the signature of the other quantities such as the deviation of the velocity profile from the logarithmic distribution in the bed-load layer. The results agree with the parametrization of Wilson (1987, 1989) for the bed-load thickness δ in sheet-flow regime, only for the highest values of θ . The referred relationship seems to be adapted for high Shields number $\theta \geq 1$. For sheet-flow regime in the range $\theta < 1$ and $w_s/u_* > 1$, experimental results presented herein and previously in Sumer et al. (1996) may be indicative for the magnitudes of δ and z_d . Detailed analysis of bed-load processes are necessary in order to provide more insights concerning the behaviour of these parameters.

The logarithmic velocity profile layer occurs much higher in the water column due to the presence of the bed-load layer. Indeed, for low to moderate concentrations (below capacity), a reduction in momentum mixing can be explained mainly by a modified origin z_d (displacement height) of the linear mixing length, which was found to be approximately $z_d \approx 0.6\delta$. A reduction in the von Karman constant as the slope κ_s (up to 25%) of the mixing length profile was observed for the highest concentrations, only over a limited vertical range. Indeed, κ_s gradually converges to its clear water value with the gradual vanishing of turbulence damping induced by the presence of particles. The modified mixing length and eddy viscosity profiles were subsequently applied to model velocity and suspended particle concentration in heavy particle sheet-flows.

It was shown that the logarithmic velocity profile holds if applied above the bed-load layer. Additional parameters that describe the thickness of the bed-load layer δ and the origin z_d of the linear mixing length profile are taken into account in the law of the wall. Concerning the concentration distribution, it was shown that the classical Rouse equation becomes less accurate as the bed-load layer thickness increases. This is due to the poor description of the classical eddy viscosity profile. Using the modified eddy viscosity (that includes the bed-load layer induced upshift), a modified analytical solution for the profile of suspended particle concentration is proposed. It is shown that the new equation provides much better agreement than the classical Rouse formulation. When the bed-load layer becomes negligibly small (i.e. when $S < 0.8$) the new model is consistent with the Rouse profile.

Finally, it was seen that the damping in the momentum mixing relative to its corresponding clear-water ϕ is highly dependent on the turbulence level w_s/u_* and on the concentration. A transition in the evolution of the ϕ -factor is seen to occur at $w_s/u_* \approx 1$, supporting that different turbulent transport mechanisms occur in the suspension and no-suspension modes of heavy particle sheet-flows.

5. TKE Budget in Sediment-laden flows

In this chapter, the turbulent kinetic energy (TKE) budget in sediment-laden flows will be discussed. The aim is to analyse its characteristics in presence of sediments as a suspended load and/or a bed-load, from the point of view of turbulent processes. In addition, some considerations can be deduced related to the closures in the $k - \varepsilon$ model for improved numerical simulations of turbulent sediment-laden open-channel flows. In the continuity of the previous chapter, it will be verified whether the TKE balance is modified or not by the presence of a thick bed-load layer.

5.1. Introduction

One of the most important aspects in understanding and modelling sediment transport concerns the modification of turbulence in presence of particles (turbulence modulation). Experimentally, many phenomena are observed at different ranges of dimensionless numbers (Lumley 1976). The characteristics found in clear-water turbulent flows should also apply to turbulent suspensions transporting solid particles, as long as the suspension is sufficiently dilute. In very dilute suspensions ($c \leq 10^{-6}$), particles do not influence the flow dynamics, because the momentum transfer from the particles to turbulence is negligible (Elghobashi 1994). Therefore, like a dye, the particles act as a passive scalar. The interaction between turbulence and particles in these conditions is termed one-way coupling. For flows with modest concentrations ($10^{-6} < c < 10^{-3}$), particles can significantly modulate the turbulent kinetic energy spectrum (two-way coupling), and for dense suspensions, ($c > 10^{-3}$), particle-particle interactions (four-way coupling: e.g. collisions, drafting) further influence both the particle motion and turbulent spectra in complex ways (Finn and Li 2016). The limits between the different regimes are only approximatively known. The classification map from Elghobashi (1994), which summarizes the referred turbulence-particle regimes is shown in Figure 5-1. Comparisons with the measured turbulence quantities will be done later.

The difficulty in the description of sediment-laden flows stems also from the incomplete understanding of hydrodynamic turbulence itself as one of the seven unsolved mathematical problems of the millennium (Elghobashi 1994, Lyn 2008). Specifically, flows over different roughness surfaces exhibit different properties. For example, after observing important differences in the TKE budget over different type of roughness walls, Krogstad and Antonia (1999) concluded that boundary layers over different roughness characteristics pose a significant challenge for turbulence modelling. Similarly, Nezu and Nakagawa (1993) observed that turbulence production and transport mechanisms in hydraulically rough open-channel flows differ from those over smooth walls. Several turbulence measurements have been reported in clear-water open-channel flows (Nakagawa and Nezu, 1977, Nezu and Rodi 1986, Kironoto and Graf 1994, Blanckaert and de Vriend 2005) some of them including partial measurements of the TKE budget (Hurther et al., 2007 and Mignot et al., 2009). However, the TKE budget have rarely been investigated experimentally, surely due to difficulties in measuring all the important terms accurately, particularly in sediment-laden flows.

In this chapter, the results in terms of TKE budget are presented, in both clear-water (CW) and sediment-laden flows (SL). Each term of the TKE equation will be discussed, and main modifications in presence of particles will be highlighted. In addition, some considerations regarding turbulence modelling based on the presented measurements are made. In this chapter, only the lower and higher flow intensity profiles, for each particle diameter, will be presented. Hence, only the profiles from two out of the three hydraulic regimes will be presented.

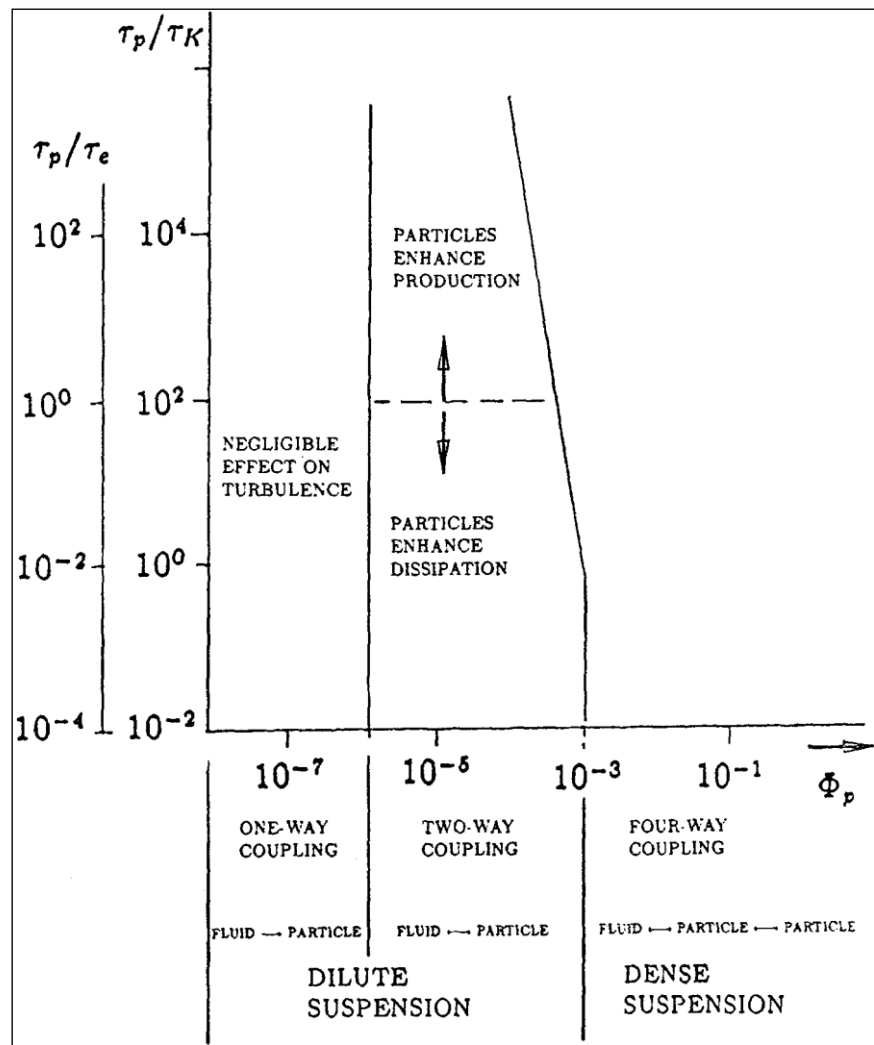


Figure 5-1. Regimes of interaction between turbulence and particles (Adapted from Elghobashi 1994); Φ_p is the volumetric concentration, τ_p , τ_K and τ_e are the time scales of particle response, Kolmogorov and turnover, respectively.

5.2. Second order moments and turbulence spectra

Although the extrapolated values of the Reynolds shear stress are rather similar to CW, in SL flows the Reynolds shear stress along the flow depth is reduced (see Figure 5-2). Furthermore, the Reynolds shear stress also is generally reduced in the near-bed, independently of particle size. One persistent signature of the second order moments in sediment-laden flows, specifically for dp_3 , is that the maximum values occur at higher vertical elevations. The trend is well noticed in quantities such as k (see Figure 5-3) and u_{rms} (see Figure 5-4). This may be

explained by significantly larger values of u' compared to other components (w' and v'). As mentioned previously, the streamwise component of k contains all the turbulence (shear) production, whereas the other components get turbulent energy via the non-linear pressure strain terms (Tennekes and Lumley 1972). Thus, the signature of u' (Figure 5-4) have great influence on k (Figure 5-3). This is more evident in the experiments with the larger particles dp3, but the overall trend is visible also for the smaller particles dp1. The wall-normal turbulence intensities (*see* Figure 5-4) are generally slightly reduced along the flow depth, in agreement with Cellino and Graf (1999).

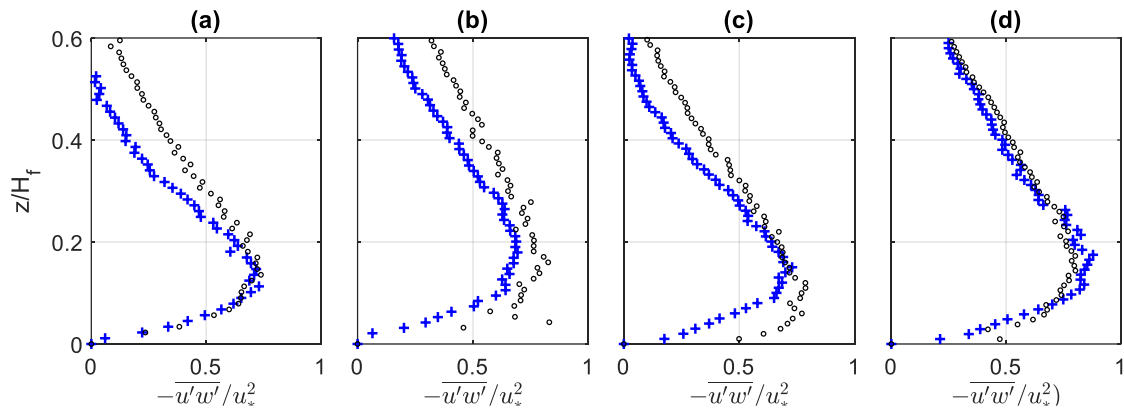


Figure 5-2. Normalized Reynolds shear stress for SL in capacity (+) and their respective CW runs (o); for dp1 ($\theta \approx 0.4$ (a), $\theta \approx 1.2$ (b)) and dp3 ($\theta \approx 0.35$ (c), $\theta \approx 0.8$ (d)).

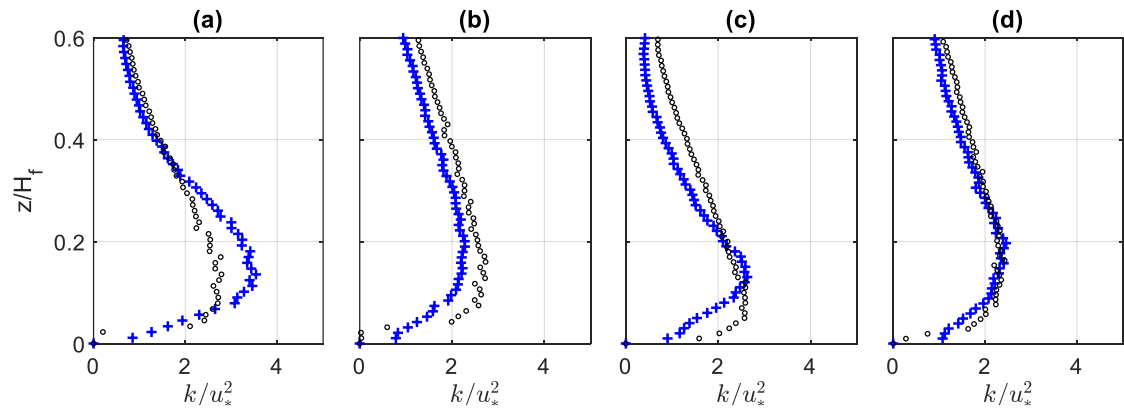


Figure 5-3. Normalized TKE; flow regimes and symbols as in Figure 5-2.

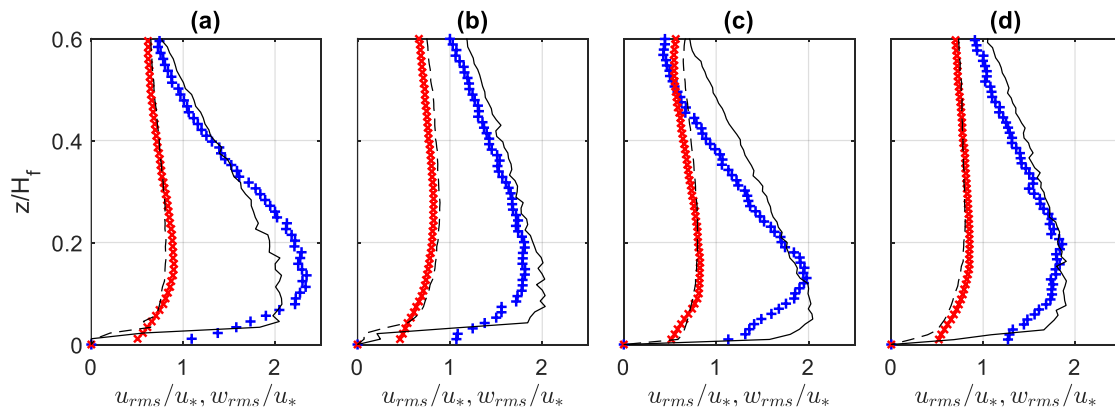


Figure 5-4. Normalized turbulent intensities in SL (u_{rms} (+), w_{rms} (x)) in capacity and CW (u_{rms} (-), w_{rms} (-)); flow regimes as in Figure 5-2.

The turbulence spectra of streamwise and vertical velocity fluctuations are shown in Figure 5-5, at a vertical elevation $z/H_f=0.5$. The spectra of longitudinal velocity fluctuations is $O(10^1)$ larger than the vertical at low frequencies for $f < 1$ Hz. The u' and w' spectra display closer values in the frequency range $f > 6$ Hz. This trend is observed for all hydrodynamic conditions but it is systematically established only for the flows of highest Reynolds numbers (column (d) in Fig. 5-4). These spectral trends confirm the anisotropy of the large-scale flow structures in a unidirectional open-channel flow as a 2D-mean shear-boundary layer flow, and the isotropy of the cascading small-scale turbulent flow structures in the inertial subrange, as proposed by Kolmogorov's first hypothesis (Bradshaw 1971, Tennekes and Lumley 1972). In addition, the well-known dependency of the inertial subrange on the Reynolds number is verified through the convergence of the slope spectra towards the universal $-5/3$ value observed almost systematically. This confirms the agreement with Kolmogorov's second hypothesis, except for the flows with the lowest Reynolds number (column a) that hardly converges towards a $-5/3$ slope value. Possibly, the convergence towards isotropy and Kolmogorov's slope at the lowest Reynolds number is not captured because of the limited spatio-temporal measurement resolution of the ACVP system for $f > 25$ Hz (as discussed in section 2.3.3.). Although not shown herein, it was observed that the tendency towards isotropy (and the $-5/3$ slope) is more pronounced at further distances from the wall because the turbulent integral scale (representative of large-scale turbulent flow structures) increases with distance from the wall in turbulent shear boundary layer flows. Laufer (1954) observed the same behaviour in his measurements of turbulence in fully developed pipe flows. These general trends prevail both in CW and SL flows.

In terms of the comparison between the CW and SL flows, particularly at maximum concentration, a reduction on the energy spectra is seen for the low-frequency subrange. This signature is particularly pronounced for the w' spectra, but it is observed also for u' . Cellino and Graf (1999) presented similar trends, only for the streamwise velocity spectra in u' . They increased the sediment load gradually up to saturation (in sediment-laden flows of suspension numbers below $w_s/u_* < 0.5$, i.e. purely suspension open-channel flows), and observed that the turbulence spectra at low frequencies was reduced compared to the equivalent CW flows, whereas at higher frequency similar energy levels were observed. These observations suggest that energy containing eddies may be less energetic in sediment-laden flows whereas small-scale isotropic flow structures have approximately the same intensity (as the integral over the corresponding spectral range). The systematic reduction of the w' spectra at low frequencies suggests that the integral scale (in particular the one associated with the vertical velocity

component w') is reduced by the presence of inertial sediments compared to the CW reference case.

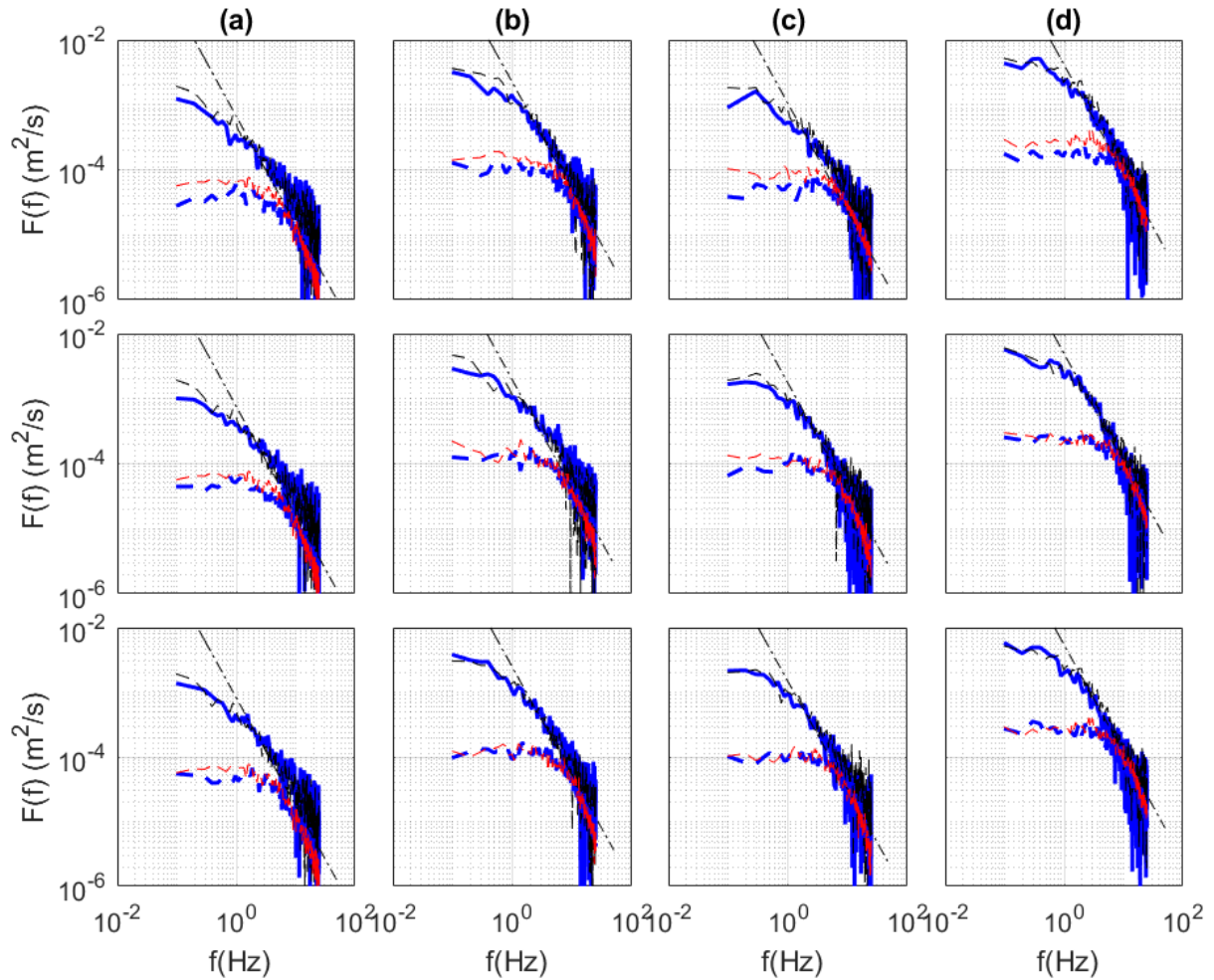


Figure 5-5. Spectra of streamwise (-) and vertical (--) velocity fluctuations at $z/H_f=0.50$; for $dp1$ ($\theta \approx 0.4$ (a), $\theta \approx 1.0$ (b)) and $dp3$ ($\theta \approx 0.35$ (c), $\theta \approx 0.8$ (d)) for lower concentration (bottom), intermediate (middle) and saturated (top). Blue (+) is for sediment-laden and black (o) is for clear-water

5.3. TKE budget

The TKE budget is shown in Figure 5-6, from clear-water in the bottom row to maximum concentration in the upper row. The imbalance term I represented by the solid line corresponds to:

$$I = -\overline{u'w'} \frac{\partial \bar{u}}{\partial z} - (s-1)w_s \bar{c}g - \frac{\partial}{\partial z} \left(\overline{kw'} - v_m \frac{\partial k}{\partial z} \right) - \varepsilon \quad (5-1)$$

The terms of Eq. (5-1) shown in Figure 5-6 are represented with a opposite sign, except for the production term. This is to facilitate the visual comparison between them. Then, in the referred figure, all positive terms except the production term will represent an energy loss. If one of them becomes negative, this means that they act as a source term.

It is seen that the balance is roughly closed generally for $z/H_f > 0.1 - 0.2$. The pressure diffusion term is not measured but in previous studies it was shown to have a small relative

contribution except very close to the flow bed and free-surface Nezu and Nakagawa (1993). The dissipation rate is not systematically well resolved below this level. Nevertheless, the small imbalance above the referred level indicates that Eq. (5-1) is a good approximation of the TKE budget. The production and the viscous dissipation are clearly the largest terms in the balance of TKE. However, other terms such as sediment suspension and turbulent diffusion become non-negligible in the near-bed and the outer flow regions. Discussion of each of the terms will be presented in the following points.

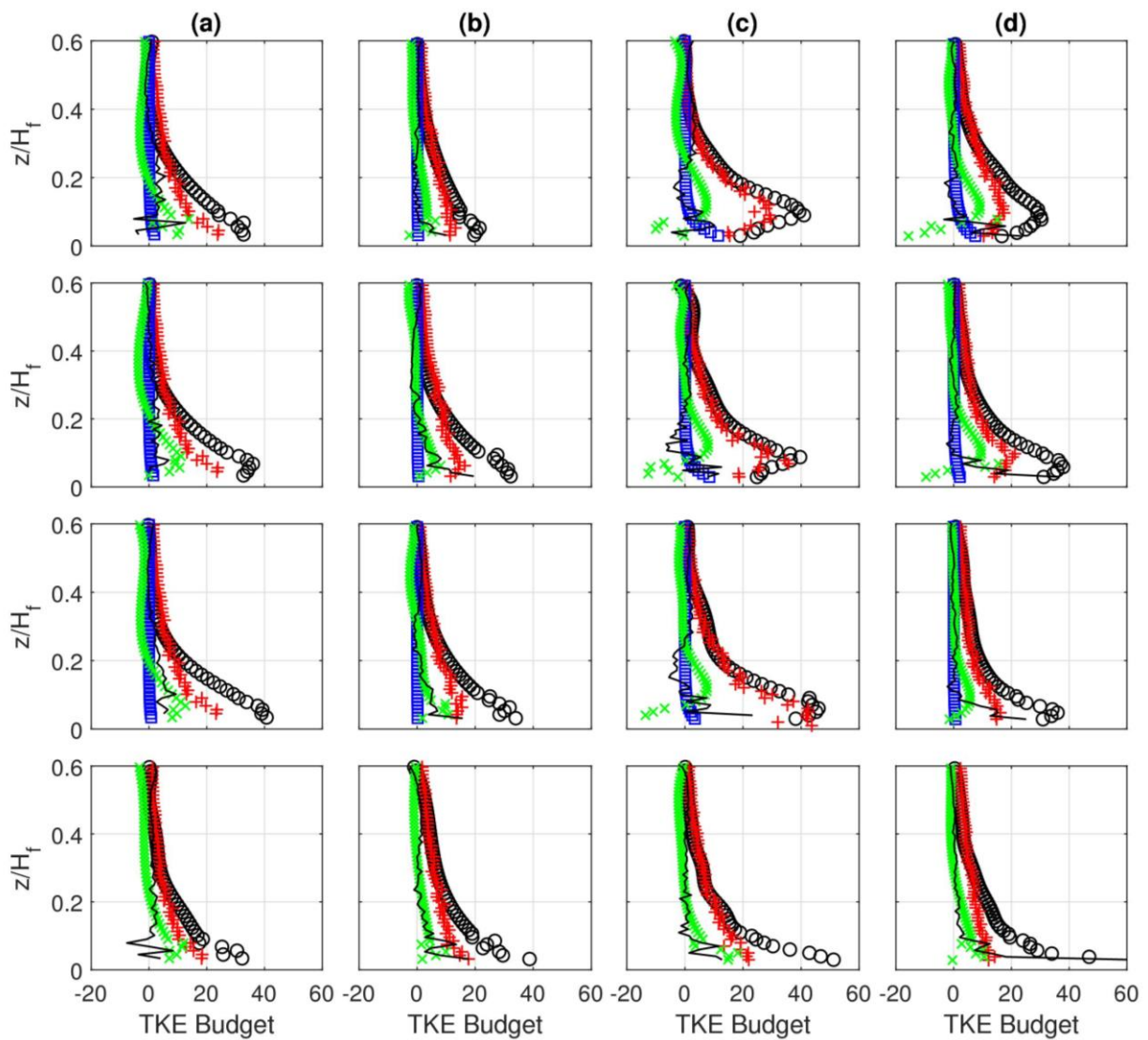


Figure 5-6. TKE budget normalized by H_f/u_*^3 ; Production (o), Dissipation (+), Turbulent diffusion (x), Stratification (□) and Imbalance (-); for dp1 ($\theta \approx 0.4$ (a), $\theta \approx 1.2$ (b)) and dp3 ($\theta \approx 0.35$ (c), $\theta \approx 0.8$ (d)); with increasing concentration from clear-water (bottom row) to saturation (top row).

In sediment-laden flows, production is reduced in the wall region, with the maximum value having smaller magnitude than in CW, regardless of particle diameter. Importantly, for dp3, it occurs at higher vertical position. Note that this seems consistent with the observed lower values of Reynolds shear stress in the near-bed region for $z/H_f < 0.10$. For the larger particles, the mean velocity gradients are also significantly reduced near the bed. Globally, the bulk production is

also reduced. This is verified by comparing the depth-integrated production in CW and SL (not shown here).

It is difficult to quantify precisely the modifications of the TKE dissipation rate since we do not resolve it in the bottom boundary layer. However, we can infer some features for $z/H_f > 0.10-0.15$, where the TKE budget is roughly closed. Above this vertical elevation, the equilibrium between turbulence production and dissipation rate is confirmed. Around the production peak level, production exceeds dissipation. The upshift of the production peak for the dp3 flows seems to be accompanied by a similar behaviour in the dissipation rate. Therefore, given that the near-wall region is not well resolved we cannot infer the trend of bulk dissipation for dp3. However, for dp1, where no discernible upshift of the production peak occurs, slightly enhanced dissipation in SL flows is observed.

As for CW, in sediment-laden flows the turbulent diffusion reaches the maximum values close to the vertical position of peak production. This energy excess region seems to be upshifted for dp3 experiments. The role of this term consists in redistributing the excess TKE from regions of high turbulence to lower ones. Therefore, with the decrease in turbulence production in the near-bed, the transport of TKE becomes more significant towards the wall. For the large particle S3 experiments, the transport term persistently reaches negative values in the near-wall region, indicating that it becomes a local source of TKE as the production term. The dependence of the diffusive TKE transport term on the roughness conditions has been discussed by several authors. Nezu and Nakagawa (1993) highlighted the modified signature of this term when analysing the TKE budget in open channel flows with different roughness surfaces. Similarly, Krogstad and Antonia (1999) observed different trends when comparing boundary layer flows with different roughness types. For the surface with most dense roughness, the transport downwards was increased. Therefore, it appears from previous clear water flow studies that this term is very sensitive to the modifications of the TKE production term profile.

The suspension term increases locally with mean concentration, hence it remains relatively small in the outer layer due its decay with z given by the Rouse formulation in Eq. (4-7) or its modified analytical expression in presence of a thick bedload layer, given by Eq. (4-8). However, it is observed that it becomes rather important in the near-bed flow region, particularly for dp3 experiments. Given the greater proportion of bed-load for dp3, higher concentrations occur in the near-bed flow region due to the presence of a thick bed-load layer, compared to dp1. In this region of higher concentration, the turbulent energy loss due to sediment suspension becomes pronounced as can be seen from Figure 5-8. Generally, the relative contribution of this term is measured by the flux Richardson number as:

$$Ri = g(s - 1) \frac{w_s \bar{c}}{-u'w'd\bar{u}/dz} = -g(s - 1) \frac{\epsilon_s}{\epsilon_{ms}} \frac{d\bar{c}/dz}{(d\bar{u}/dz)^2} \quad (5-2)$$

where ϵ_s and ϵ_{ms} are the sediment and momentum diffusivities, respectively. Note that for the same forcing condition, $w_s \bar{c}$ will be larger for higher values of w_s/u_* . Consequently, Ri will be higher and the stratification effects on turbulence will be more pronounced. This point will be further explored in the discussion section by comparing the SL flows with the same hydrodynamic conditions but with different particle diameters.

5.4. Discussion

5.4.1. Effect of bed-load on the TKE budget

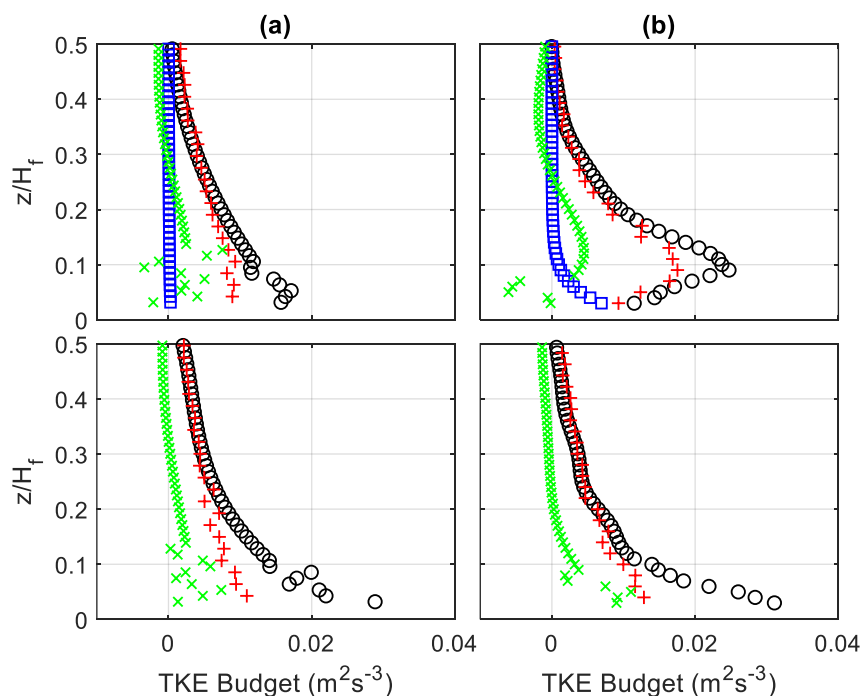


Figure 5-7. TKE budget for flows of same hydrodynamic conditions with dp1 (a) with S10 and dp3(b) with S03, for SAT (top) and CW (bottom);

One of the most remarkable observations concerns the persistent change in the signature of the TKE diffusive transport, from CW to SL flows in dp3 flows. This is highlighted in Figure 5-7, by comparing flows with same hydrodynamic conditions but with different particle diameters. Note that the production term converges towards a similar (absolute) value near the bed, supporting identical hydrodynamic forcing for both flows. For dp3, the energy loss associated with sediment suspension in the near bed is relatively high, reaching around 50% of the local production, indicating that the local flux Richardson number is $Ri \approx 0.5$ (see Figure 5-8). Since the dissipation rate in this region has similar magnitude as the production term, the energy loss through the sediment suspension term cannot be explained only by the local production. Apparently, the balance occurs through the transport terms, which becomes a local source of TKE. This is supported by the similar magnitude of the turbulent diffusion and the sediment suspension terms in Figure 5-7b upper panel. Hence, the diffusion term as an excess of TKE transported from the upshifted height of maximal TKE shear production towards the near-bed region could be responsible for the transport of particles as a bed-load. Given that for this flow condition, the suspension number for dp1 is rather low ($w_s/u_* = 0.4$), most particles are transported in suspension, even in saturation regime. It is seen from Figure 5-8, that Ri of dp1 is larger than dp3 in the suspension layer, but it remains generally well below the critical value of $Ri < 0.2$ excluding flow stratification effects (see the discussion in the next subsection). On the other hand, for dp3, $Ri > 0.2$ in the bedload layer which suggests strong stratification effects. Therefore, differently from dp3, the stratification term for dp1 does not represent a significant local energy loss even in the near-bed region. This strongly supports the observed almost unchanged behaviour of the production and diffusion terms for the small dp1

SL flows. Therefore, the energy excess region (where production exceeds dissipation) in saturated dp1 flows is seen to occur at the same very near-bed position as in the CW flow. Hence, TKE is only diffused upwards with no clear evidence of becoming a potential energy source for suspended sediment transport.

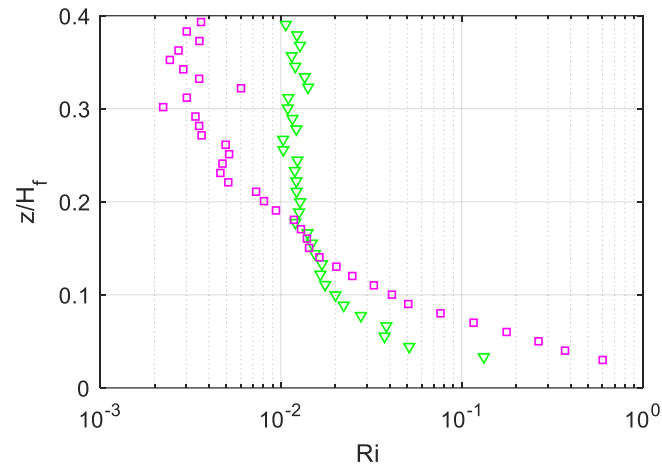


Figure 5-8. Comparison of flux Richardson number with the same hydrodynamic conditions with dp1 (∇) and dp3 (\square); both in capacity conditions (SAT).

Regarding the suspension region for $z/H_f > 0.3$, the unchanged signature of the turbulent diffusion term for both particle sizes seems to be correlated to the absence of the sharp increase of the sediment stratification term, as observed for dp3 in the bed-load layer. However, since a portion of the residual TKE is always transported by turbulent diffusion to the outer flow region, it can be postulated that part of this TKE may also act as a local energy source potentially entraining particles into suspension. Since local production becomes small in the outer flow region of open-channel flows, it is usually assumed in CW conditions that viscous dissipation in the region close to the free-surface is coming from the diffusive TKE transported from the near-bed turbulence generation region (Nezu and Nakagawa, 1993, Hurther et al., 2007). In SL flows, this upward transport of TKE may profit both viscous TKE dissipation and the sediment suspension. This suggested process is supported by the tendency towards negative values of the diffusion term (i.e. as a local energy source) for $z/H_f > 0.3$ in Figure 5-7, for both CW and SL conditions and both particle sizes which appears to be accompanied by a slight excess of TKE dissipation compared to its production (particularly in Figure 5-7 for the two top SL panels and the lower CW panel for dp3 on the right-hand side).

Since the influential study of Hsu et al. (2003), several two-phase flow models (Chauchat et al. 2017, Cheng et al. 2018, Mathieu et al. 2021) have reported the drag dissipation as the main mechanism of TKE dissipation in presence of particles, after the viscous dissipation. This differs from the single-phase mixture perspective discussed herein, in which the buoyancy flux (stratification) explains the TKE loss associated with the presence of particles. If the present TKE balance would be compared with the two-phase flow models, it should be in terms of the mixture equations, instead of the fluid TKE equation. At present, no detailed studies of the TKE budget of the mixture, based on the two-phase flow models are known by the author.

5.4.2. Energy repartition

An important aspect in stratified flow theory concerns the repartition of the TKE production, between buoyancy flux and dissipation. Since dissipation is always positive (as an energy sink), the vertically integrated buoyancy flux should necessarily be smaller than the production term, leading to $Ri < 1$. Actually, many arguments and experimental evidence support $Ri_{max} < 0.2$ (Tennekes and Lumley 1972). Since viscous dissipation at small scales occurs in all directional components of the TKE, while the buoyancy flux occurs only in the vertical direction, it is expected that viscous dissipation is significantly larger than the buoyancy flux (Osborn 1980). Herein, the bulk Richardson number Ri_{bulk} , defined as the depth-averaged flux Richardson number is shown in Figure 5-9a, only in capacity conditions. It is seen that $Ri_{bulk} \approx 0.07 - 0.1$, although there is some scattering mainly for the two most energetic regimes with dp1. This is explained by the higher variability in the solid-load conditions (discussed early in section 3.2.1). As the solid-load is decreased (LOW and MED regimes), Ri_{bulk} converges to lower values (not shown here). Nevertheless, a quasi-constant trend $Ri_{bulk} \approx 0.1$ describe reasonable well the presented saturated cases. A more detailed analysis in equilibrium bed experiments (with a bed of sediment at rest, having several particle diameter thick), which is the only condition in which full capacity is completed guaranteed, could confirm if Ri_{bulk} remains constant or evolves with w_s/u_* .

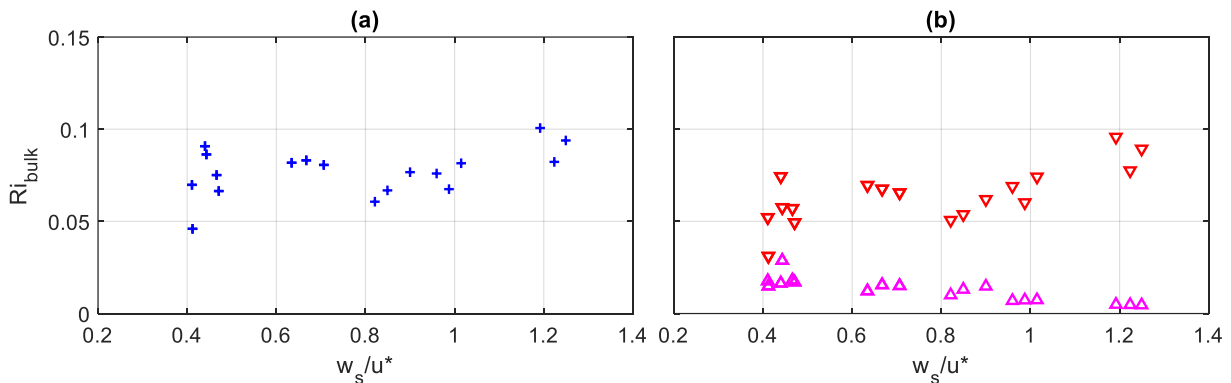


Figure 5-9. Bulk Richardson number Ri_{bulk} (a) and its repartition between bed-load (∇) and suspended-load (Δ); only in capacity conditions (SAT)

Osborn (1980) proposed that the maximum efficiency in the conversion of TKE to potential energy through the buoyancy flux is bounded by an upper limit $Ri_{bulk} \leq 0.15$, in stationary turbulence, under equilibrium conditions. Recent DNS simulations have supported this classical argument (Caulfield 2020). In analogy, the almost constant range $Ri_{bulk} \approx 0.1$ found herein (in capacity conditions) is appealing. It would imply that the TKE spent by the flow to transport solid particles in saturation is bounded by an upper value around 10% of the mean stream power ($SP = \tau_0 U$). This solid transport efficiency appears to be independent of the suspension number value, i.e. independent of the repartition into suspension and bedload transport modes, varying around $Ri_{bulk} \approx 0.07 - 0.1$, as shown previously. This value is in agreement with the energetic approach model proposed by Bagnold (1966) for sediment transport modelling in river flows. Indeed, he proposed a model resulting in a 15% total (bedload and suspended-load) transport efficiency (in capacity conditions). This solid transport efficiency was defined as the ratio between the flow energy associated with each transport mode and the stream power. The latter quantity corresponds closely to the depth-averaged TKE production term, i.e. to the denominator of the bulk Richardson number, such that Ri_{bulk} is closely related to Bagnold's transport efficiency. The estimation of the repartition between the energy associated with both transport modes is presented in Figure 5-9b. It is observed that the bulk Richardson numbers

associated with bed-load Ri_B remained generally higher than the suspended-load Ri_S as proposed by Bagnold (1966). For regimes with important proportion of suspended-load ($w_s/u_* < 1$), $Ri_S \geq 0.01$. Generally, the value evolves from $Ri_S \approx 0.01$ to about $Ri_S \approx 0.03$ with decreasing values of w_s/u_* . The ratio between the bulk Richardson number associated with suspension and bed-load Ri_S / Ri_B is presented in Figure 5-10. It is observed that the energy proportion associated with suspended-load decreases with w_s/u_* , as expected. The bed-load transport efficiency increases slightly over the full range of w_s/u_* values but with much larger values compared to suspension values (which explains the almost constant total transport efficiency found in Figure 5-9a). An important result is that even in flow regimes dominated by suspension, bed-load explains a significant proportion of the energy loss due to stratification effects. Note that whilst the energy loss due to suspension will be spread along the flow depth, the occurrence of bed-load transport imply a significant energy loss concentrated over a thin near-bed flow region. This further supports the arguments discussed in the previous subsection.

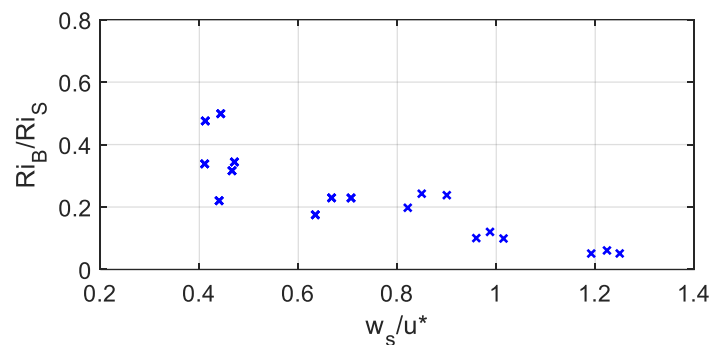


Figure 5-10. Ratio of between bulk Richardson numbers associated with bed-load (Ri_B) and suspended-load (Ri_S); only for capacity conditions (SAT)

It was seen that the present results follow the sediment transport predictions obtained with the energetic approach model of Bagnold (1966). However, some of his assumptions seem too crude. He reported an evolving bed-load efficiency with mean velocity and particle diameter ($dp \approx 0.01-0.3$ mm), as well as a constant suspended-load efficiency. The scaling of the former lacks of generality. The constant assumption for the later requires further detailed turbulence analysis, in particular of the vertical turbulent velocity asymmetry. As seen from the present measurements, although the bed-load seems to have a higher transport efficiency (as proposed in Bagnold 1966) evolving slightly with w_s/u_* , the bulk Richardson number associated with suspension Ri_S is found to decrease with w_s/u_* , and represent about 50% of the bed-load efficiency. More generally, the present discussion inspires revisiting the mechanisms and their validity behind the energetic solid transport model of Bagnold (1966).

5.4.3. Turbulence-particle interactions

In two-phase flow simulations, predicting the turbulence-particle interaction regime is crucial for defining the appropriate method of choice. The level of complexity increases from the case in which the particles are smaller than the smallest turbulence scales (the Kolmogorov length scale η_K), to the regimes in which they scale with the inertial subrange eddies. Fully resolving the flow-particle interactions in the regime with $d_p/n_K > 1$, termed finite-size in the two-phase literature (Balachandar 2009), very common in sediment transport applications, would require to apply Direct Numerical Simulations (DNS). This is unfeasible for the typical sediment transport problem; with high Reynolds numbers and large number of particles to be resolved (even in low concentration configurations). The Eulerian two-fluid methodology,

which does not resolve the individual trajectories of the particles, a priori is ideal for simple flow regimes, with $d_p < \eta_K$. However, due to its lower computational cost, Eulerian modelling strategies are developed and employed in a wide range of turbulence-particle regimes.

The measurement of the mean TKE dissipation rate permits the estimation of the turbulent flow microscales as:

$$\tau_\lambda = \sqrt{\frac{15\nu}{\varepsilon}} \quad (5-3)$$

$$\tau_K = \left(\frac{\nu}{\varepsilon}\right)^{1/2} \quad (5-4)$$

where τ_λ and τ_K are the Taylor and Kolmogorov time scales, respectively. Based on these time scales, two Stokes numbers $St_\lambda = \tau_p/\tau_\lambda$ and $St_K = \tau_p/\tau_K$ were determined, taking $\tau_p \approx w_s/[g(s-1)/s]$. It results that $St_K < 1$ for dp1 and $St_K > 1$ for dp3, as shown in Figure 5-11, only for saturated SL flow conditions. In this Figure, the increasing values of the Stokes number with hydrodynamic forcing is clear. This is explained by the higher TKE dissipation rates at larger Reynolds number values. According to Finn and Li (2016), who recast and developed scaling arguments from Elghobashi (1994) and (Balachandar 2009), negligible effects of the flow turbulence are expected for $St_K < 1$, whilst a dissipative regime (i.e. as a fluid turbulence damping) occurs with $St_K > 1$, so long as particles Reynolds number Re_p does not exceed the critical value $Re_p \approx 400$ (Elghobashi 1994). This seems consistent with the present observations. Since we do not measure the relative velocity $u_p - u_f$, Re_p can be estimated based on the particle settling velocity leading as $Re_p = d_p w_s/\nu = 168$ and 19, for $dp=3$ mm and 1 mm, respectively. Although the values for the larger particles are one order greater than the smaller, they remain below the assumed threshold for enhancement of fluid turbulence ($Re_p < 400$). The present results agree well also with Elghobashi (1994) classification map that predicts a transition between dissipative and productive regimes at much larger Stokes number $St_K \approx 100$ or $St_e \approx 1$, where $St_e \approx$ is the Stokes number based on the turnover time of large eddies. It seems that the transition threshold $St \approx 1$ may be better suited with the Stokes number based on the Taylor microscale rather than the Kolmogorov scale. In addition, he had already suggested that for $Re_p < 400$, the dissipative regime prevails. In terms of length scales, it is found that $d_p/\eta_K \approx 10 - 40$ and $d_p/\lambda \approx 0.3 - 1$. For each of the ratios, the lower and higher values correspond to dp1 and dp3, respectively. Hence, it is observed that the particle diameters are of the same order as the Taylor microscale. In the turbulence productive regime, it can be expected that the particle diameter scales with a larger flow scale, the energy containing eddies (much larger than the Taylor microscale), as referred by Muste et al. (2005). In two-phase flows, classical fluid-particle interactions are modelled based on the drag law, employing a drag coefficient that is derived for $d_p < \eta_K$. Recently, Mathieu et al. (2021) have shown that in typical sediment transport applications, it is necessary to include finite-size effects. They have found that by modifying the drag law in order to include the finite size effects, predictions of turbulent suspension were greatly improved, without any empirical tuning coefficients.

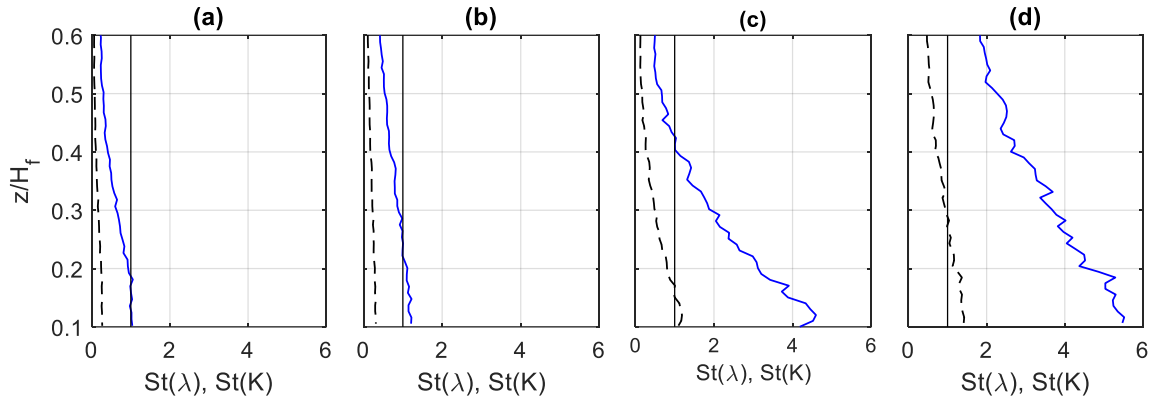


Figure 5-11. Taylor (--) and Kolmogorov (-) Stokes numbers; for dp1 ($\theta \approx 0.4$ (a), $\theta \approx 1.2$ (b)) and dp3 ($\theta \approx 0.35$ (c), $\theta \approx 0.8$ (d)). The vertical solid line corresponds to the value $St=1$.

It is necessary to be aware of the simplifications made in the scaling arguments discussed above. One of the most important is to ignore the effects of particle-particle interactions on the general turbulent flow structure. Finn and Li (2016) stressed that the role of four way coupling in the overall turbulence modulation were not taken into account in their regime map, and that they should be included as their features are better understood. Hence, these arguments may probably be more justified for small values of w_s/u_* , where the bed-load and its effects are less important. More generally, although they may provide some guidance, they should be viewed with caution as several factors may affect the turbulence in sediment-laden open-channel flows. For example, Mathieu et al. (2021) have found large disparities when applying their finite-size correction to model our flow configuration corresponding to $w_s/u_* \approx 1.3$, where large bed-load effects on the overall flow structure were reported herein.

5.4.4. Turbulence modelling: $k - \varepsilon$ model closures

In RANS models, the goal is to close the momentum budget through the prescription of the eddy viscosity for the determination of the Reynolds stresses. It was shown previously that in 2D mean flows, the only quantity to be addressed in the closure problem is the Reynolds shear stress $-\overline{u'w'} = \epsilon_m du/dz$. The TKE equation analysed in the precedent section is very important in understanding turbulent processes across the boundary layer, but has no immediate application for the closure problem, since new unknowns appear in the equation. Therefore, when applying turbulence models, closures for the terms in the k -equation should be developed. Since the $k - \varepsilon$ model is one of the most widely applied for hydraulic engineering problems (Rodi 2017), some considerations regarding the closures of the model equations will be made, based on the present measurements. The model equations for k and ε in uniform flow conditions can then be written as:

$$\frac{\partial k}{\partial t} = \epsilon_m \left(\frac{\partial \bar{u}}{\partial z} \right)^2 - g(s-1) \frac{\epsilon_m}{\sigma_t} \frac{d\bar{c}}{dz} - \frac{\partial}{\partial z} \left(\frac{\epsilon_m}{\sigma_k} \frac{\partial k}{\partial z} \right) - \varepsilon \quad (5-5)$$

$$\frac{\partial \varepsilon}{\partial t} = c_{1\varepsilon} \frac{\varepsilon}{k} \epsilon_m \left(\frac{\partial \bar{u}}{\partial z} \right)^2 - c_{1\varepsilon} c_{3\varepsilon} \frac{\varepsilon}{k} g(s-1) \frac{\epsilon_m}{\sigma_t} \frac{d\bar{c}}{dz} - \frac{\partial}{\partial z} \left(\frac{\epsilon_m}{\sigma_\varepsilon} \frac{\partial \varepsilon}{\partial z} \right) - c_{2\varepsilon} \frac{\varepsilon}{k} \varepsilon \quad (5-6)$$

Whereas Eq. (5-5) is an approximation of the exact TKE equation, through the application of some closures, Eq. (5-6) does not result from the exact equation for ε . The terms in the latter, for the mean dissipation rate are analogous to those in the TKE equation. In both equations, the first term on the right-hand side is the production of k and ε , respectively. The second term reflects the effects of buoyancy, the third term corresponds to the turbulent diffusion and the

last term is a destruction term. The terms in the dissipation equation are modelled based on the corresponding TKE terms. The Schmidt number $\sigma_t = 1/\beta$ was introduced instead of the β –factor discussed in section 3.3.2, as commonly used in fluid mechanics literature. This shows that the prescription of this parameter is fundamental both in the simple mixing length model, as well as in more advanced models. The constant σ_k is a Schmidt number, associated with TKE diffusion by turbulent transport $\overline{k'w'}$. Without the buoyancy term, the standard $k - \varepsilon$ model involves five empirical constants: $c_\mu \approx 0.09$ (see Eq. (5-7)), $c_{1\varepsilon} \approx 1.44$, $c_{2\varepsilon} \approx 1.92$, $\sigma_k \approx 1.0$ and $\sigma_\varepsilon \approx 1.3$. In stratified flows, there is one additional model constant $c_{3\varepsilon}$. Because the main terms of the TKE equation were measured in the present study, the values of some model constants can be verified based on the experimental data.

For equilibrium shear layers ($P \approx \varepsilon$), the constant c_μ corresponds to the square of the ratio between the Reynolds shear stress and the TKE:

$$c_\mu = (\overline{-u'w'}/k)^2 \quad (5-7)$$

A constant value as it is assumed often in model applications implies that the ratio remains roughly constant with z . This is confirmed Figure 5-12 particularly in the intermediate flow region. The ratio remains around $\overline{-u'w'}/k \approx 0.3$, in agreement with Nezu and Nakagawa (1993), who concluded that $\overline{-u'w'} = 0.3k$. This confirms the value of this model constant as $c_\mu = 0.3^2 = 0.09$. Furthermore, the measured eddy viscosity $\varepsilon_m = -u'w'/(du/dz)$ is compared to the formulation employed in the $k - \varepsilon$ model:

$$\varepsilon_m = c_\mu k^2 / \varepsilon \quad (5-8)$$

The good agreement between the directly measured eddy viscosity and the Eq. (5-8) shown in Figure 5-13, supports the good measurements of k and ε . Moreover, it further confirms the universality of c_μ over the wide range of hydrodynamic and solid transport conditions. Note that in the near-bed region for $z/H_f < 0.1-0.15$, the eddy viscosity of the saturation regimes is quasi-constant, only for dp3. This aspect has been discussed in detail in the previous chapter (see section 4). This strong effect of the bed-load in the momentum diffusion may be challenging to model even with the two-equation models. However, it should be stressed that the mean TKE dissipation rate ε is not fully resolved in the near-flow region, hence, it is not expected that Eq. (5-8) provides a good agreement below $z/H_f \approx 0.1-0.15$.

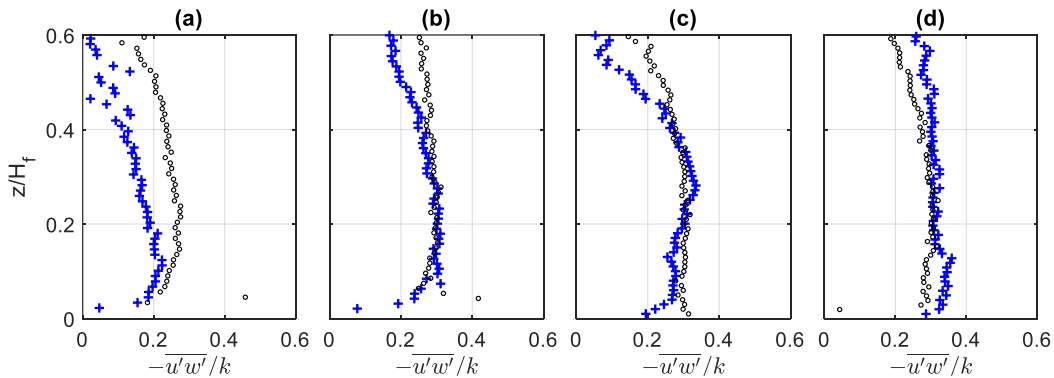


Figure 5-12. Ratio $\overline{-u'w'}/k$ for SL in capacity (+) and their respective CW runs (o) that lead to values of c_μ as in Eq. (5-7); for dp1 ($\theta \approx 0.4$ (a), $\theta \approx 1.2$ (b)) and dp3 ($\theta \approx 0.35$ (c), $\theta \approx 0.8$ (d))

As for σ_t , the values of σ_k can be obtained by the following relationship:

$$\sigma_k = \varepsilon_m / \nu_k \quad (5-9)$$

where

$$v_k = \frac{\overline{k w'}}{\partial k / \partial z} \quad (5-10)$$

The experimental results indicate that σ_k remains fairly constant in the outer flow region $0.15 < z/H_f < 0.6$, hence, the assumption of a constant value is justified. Moreover, the depth-averaged values over the vertical range of fairly constant value is about $\sigma_k \approx 0.5 - 0.7$, hence, remaining systematically below unity. These values were obtained in both CW and SL (see Appendix). This suggests that TKE is diffused slightly faster than momentum. In the modified version of the $k - \varepsilon$, the Renormalization Group (RNG) $k - \varepsilon$ model, $\sigma_k \approx 0.7$ (Wilcox 2006). In addition to the adopted von Karman value of $\kappa \approx 0.39$ in the log-law, instead of $\kappa \approx 0.43$ prescribed in the standard $k - \varepsilon$ model, it seems that the RNG $k - \varepsilon$ model display better agreement with the present measurements.

To investigate the behaviour of the remaining model constants, the assumption $c_{1\varepsilon} \approx 1.44$ was considered, based on the observation that two-equation models agree fairly well on its value, and that scaling arguments supporting $c_{1\varepsilon} \approx 1.5$ have been presented by Tennekes (1989) (cited by Lyn 2008). If we restrict the analysis to CW, and taking the equilibrium assumption, only two terms are non-zero in the equation of ε (the first and the last on the right-hand side). With these assumptions, it was found that $c_{2\varepsilon}$ decreases from values slightly larger than 2 in the near-bed see (Figure E-2 in Appendix E), and remains quasi-constant in the intermediate flow region $0.2 < z/H_f < 0.6$. In this quasi-constant vertical range, the depth-averaged values are approximately $c_{2\varepsilon} \approx 1.5 - 1.7$. Same range of values were observed in sediment-laden flows.

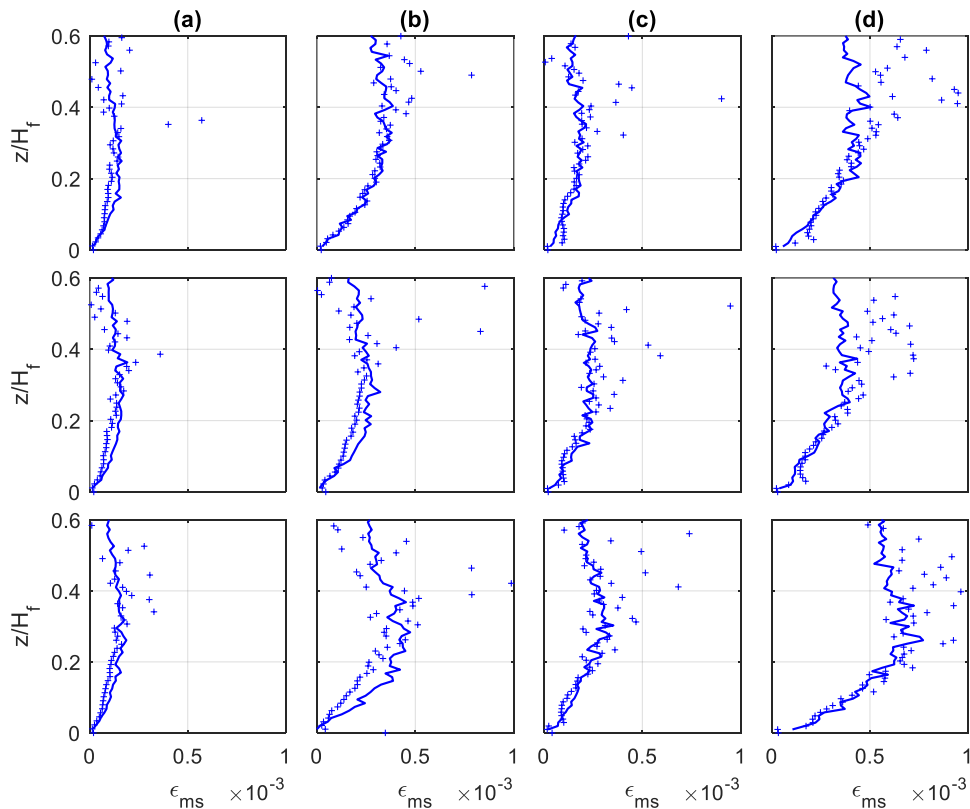


Figure 5-13. Comparison of measured eddy viscosity (+) and Eq. (5-8) in sediment-laden flows; flow solid-load regimes as in Figure 5-5.

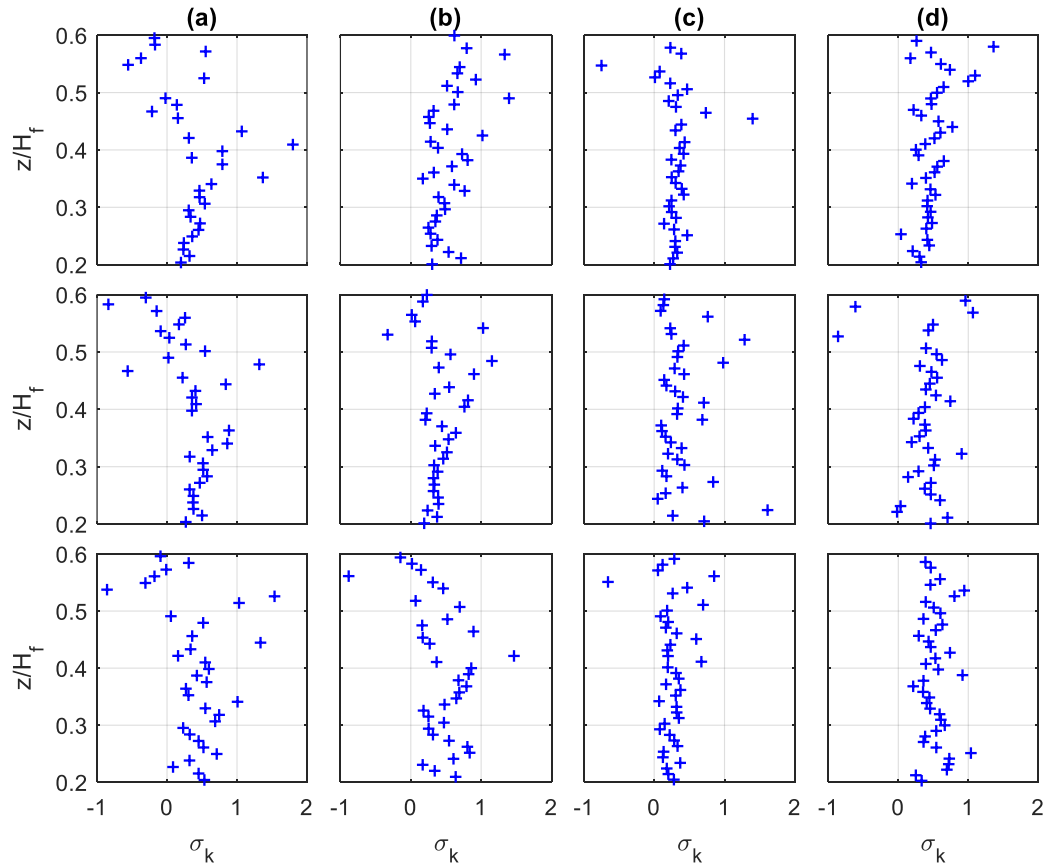


Figure 5-14. Values of the ratio $\sigma_K = \overline{k'w'}/(dk/dz)$ in sediment-laden flows; flow solid-load regimes as in Figure 5-5

The two remaining constants, $c_{3\varepsilon}$ and σ_ε , are not reported herein because their evaluation should include the vertical range where the dissipation rate is not well-resolved. Since in the intermediate flow region, production and dissipation are the most important terms, and they are in equilibrium, the terms depending on $c_{3\varepsilon}$ and σ_ε , will be significantly smaller there (they are non-negligible mostly in the near-wall region). Hence, these constants should be less influential than as $c_{1\varepsilon}$ and $c_{2\varepsilon}$, associated with the production and destruction of the dissipation rate. Indeed, Rodi (1993) reported that calculations are much more sensitive to $c_{1\varepsilon}$ and $c_{2\varepsilon}$. A common practice is to ignore the stratification effect in the ε equation, but to account for it in the k equation, such that $c_{3\varepsilon} \approx 0$. Concerning σ_ε , the consensus is that it should not differ significantly from unity. Assuming that it is close to σ_k , the recommended value based on the present measurements would be $\sigma_\varepsilon \approx 0.7$, as proposed in the RNG $k - \varepsilon$ model.

From the discussion above, it seems that the model constants are not very sensitive to the presence of sediments, except the Schmidt number, which evolution has been described previously in terms of β -factor ($\sigma_t = 1/\beta$). This is true specifically under the assumption that they are determined in the intermediate flow region, where production and dissipation are approximately in equilibrium. It was also observed that the estimated constants seem to agree better with the RNG $k - \varepsilon$ model, compared to the standard version of the model. It should be recalled that the ε -equation stems mainly from analogy with the k -equation. This explains that efforts in improving the performance of two-equation models generally lead to keep the k -equation and replace the equation for ε , such as $k - \omega$ or $k - kL$ models. Actually, this exercise of evaluating the model constants can be performed also with other popular models, such as $k - \omega$, knowing that $\omega = \varepsilon/(c_{kw}k)$, with $c_{kw} \approx 0.09$. Given that several of the model constants discussed herein are obtained in equilibrium conditions (negligible transport by

turbulent diffusion), it can be anticipated that the presence of the thick bed-load layer as seen for dp_3 will require particular modelling efforts. In such conditions, all the terms in the equations for k and ε are important, including the turbulent diffusion. Furthermore, the change in signature of the transport term observed only for dp_3 flows represents undoubtedly an important challenge both in the physical interpretation and in modelling.

5.5. Conclusions

The primary result in this chapter is that the effects of sediments on the TKE budget are very pronounced in the experiments with large particles ($dp=3\text{mm}$), in which a thick bed-load layer is developed. The production term is heavily reduced in the bed-load layer, consistent with a sharp increase in the local flux Richardson number. A strong signature in these experiments is that the peak of turbulence production seems to occur around the edge of the bedload layer. This vertical upshift of the production region leads to an increased diffusion of TKE towards the bed, and this term becomes negative in the lower flow region, acting as a potential TKE source term for dissipation and/or particle transport. Importantly, these features are not observed in the experiments with smaller ($dp=1\text{mm}$) particles. It was suggested herein that the TKE inside the bed-load layer is mostly transported by diffusion from the production region at the edge of the bed-load layer, rather than local production. For the saturated dp_3 flow cases, this term is found to be locally in good balance with the particle transport term. The mechanism of this TKE energy balance will be further analysed in the next chapter, considering the dynamics of turbulent coherent flow structures.

6. Coherent Flow Structures Dynamics

In this chapter, the dynamics of turbulent coherent flow structures will be investigated in the studied sediment-laden flows. This possibility is offered by the time-resolved vertical profiles of the 2C velocity field, concentration and particle fluxes provided by the ACVP technology. Previous literature results have shown that coherent flow structures are dominant contributors to the dynamics of Reynolds shear stress $u'w'$ and particle fluxes in suspension dominated sediment-laden flows ($w_s/u_* < 0.6$). Fewer studies have examined their link to particle suspension dynamics and the mean TKE budget (because of the lack of simultaneous and co-located measurements of velocity and particle concentration) for sediment-laden flows with higher suspension numbers $0.8 < w_s/u_* < 1.3$. It is the main motivation of the present chapter to address these issues based on the quadrant threshold technique.

6.1. Introduction

Coherent structures in rivers are classified into two categories, namely, bursting phenomena and large-scale vortical motions (Nezu and Nakagawa 1993). The former include different types of vortical motions, which are not all associated with turbulence. In this chapter, we are interested in the features of bursting phenomena, known to be responsible for the generation of near-wall Reynolds shear stress (Nakagawa and Nezu 1977, Raupach 1981) and turbulence production (Tardu 2002). Because we have seen in the previous chapter that $\overline{c'w'}$ appears in the TKE equation (rather than the mean energy equations), it can be expected, from a theoretical point of view, that the structures that produce turbulence, should also be important in generating sediment suspension.

Bursting phenomena are characterised by the occurrence of a quasi-cyclic process consisting of ejections and sweeps (Grass 1971). More precisely, it refers to the complete sequence of lift-up of low-speed (elongated) streaks from the wall, followed by oscillation in three dimensions and collapse, ejecting a substantial portion of the low-speed-streak fluid into the outer flow. This is followed by an inrush of high-speed streaks that sweep the remaining low fluid parcels in the lower flow region. They are called coherent structures because they correspond to organized motions of fluid parcels, in time and space.

Two important features of coherent structures in open-channel flows should be outlined. The first is their dependence on the wall-roughness and the second is the strong link to the TKE budget. Nakagawa and Nezu (1977) have shown that the ratio of the relative contributions to $-\overline{u'w'}$, from sweeps over ejections $RS4/RS2$ (defined in section 6.3) increase with roughness size, and that it is associated with variations in (turbulent) velocity skewness and diffusion factors from smooth to rough flows. In addition, they found that the vertical range of negative values of TKE flux also increases with roughness and that this trend is equally associated to the same diffusion and skewness factors governing $RS4/RS2$. These observations lead them to conclude that the bursting motions associated with ejections and sweeps are directly related to the TKE budget in the form of turbulent diffusion. Raupach (1981) proposed a linear relationship between the mean vertical TKE flux (F_k) and another sweep/ejection parameter defined as $\Delta RS = RS4 - RS2$, corresponding to the difference in relative contributions between

sweeps and ejections. The proposed relationship has several implications. In sweeps dominated layer, called roughness sublayer by Raupach (1981), the TKE flux is negative (downwards), whereas in the ejections dominated region is positive (upwards). Note that the effect of roughness size is to increase the roughness sublayer size, hence, it should simultaneously affect the vertical distribution of $RS4/RS2$ and F_K . From these literature considerations, we can expect to observe modifications in the TKE budget from smooth to rough flows, since the turbulent transport of TKE is defined as $\partial F_K / \partial z$.

A particular interest in the analysis of coherent structures dynamics in open-channel flows is their role on sediment entrainment (also called pick-up) and the maintaining of sediments in suspension as a mean turbulent erosion flux. Sumer and Deigaard (1981) were among the first to perform detailed analysis on the correlation between particle motion and bursting phenomena. By following the paths of single particles, they concluded that in both smooth and rough flows, the particle motion is in good agreement with the bursting motions of ejection and sweep types. They found that the mean life period between the terminations of the downward path are close to the bursting motions, although the life period of individual bursting motion evaluated from Lagrangian observation differs from the Eulerian. Sechet and Guennec (1999) combined measurements of instantaneous velocity and particle trajectory to study bed-load over a smooth bed. They reported that the period between two consecutive jumps are commensurable with the corresponding ejection periods. Hence, it supports the results from Sumer and Deigaard (1981). Based on acoustic measurements, Hurther and Lemmin (2003) highlighted the high intermittency of $\overline{c'w'}$, with 50% being generated by structures that persist only 30% of the time, whilst Cellino and Lemmin (2004) referred that ejections contributions to $\overline{c'w'}$ are always larger than sweeps. Some investigators have included the bursting motion scales in the description of some solid transport phenomena (Gyr 1983, Ashida and Fujita 1986, Cao 1999). Recently, Raus et al. (2019) have presented experimental evidence that in flows with immobile cobbles and boulders, fine sediments at the bed can be disturbed mainly by sweeps events.

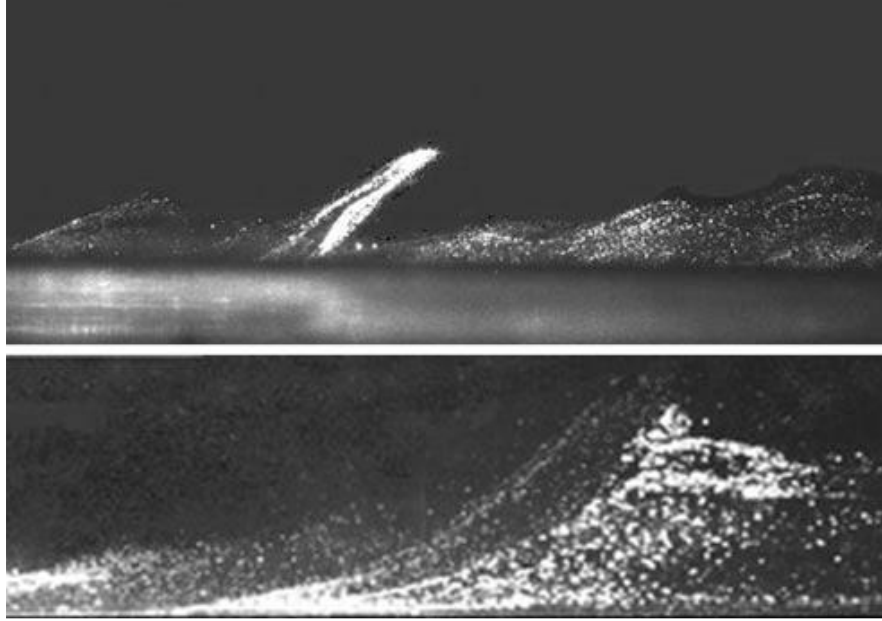


Figure 6-1. Ejection (top) and Sweep event (bottom) (adapted from Dey 2014; reported by Mao 2003)

Although numerous studies investigated the role of coherent structure on particle motion, only few reported on quantitative analysis of coherent structure dynamics over a wide range of solid-load transport conditions, especially in terms of suspension number values. Even fewer included simultaneous velocity and concentration measurements. Therefore, in the present chapter, the quadrant threshold method is applied and revisited to investigate the dynamics of coherent flow structures in sediment-laden flows. One goal is to provide further insights on the TKE budget features observed in the previous chapter. Another objective is to investigate their importance on turbulent suspension. Only the lower and higher flow intensity profiles, for each particle diameter, will be presented.

6.2. Quadrant Threshold Method

The Quadrant Method allows to evaluate the total Reynolds shear stress at a given vertical position as a sum of contributions from different bursting events, which are distinguished according to their instantaneous orientation in the (u', w') plane (Lu and Willmarth 1973), shown in Figure 6-2, and their respective threshold level H . The four quadrants (bursting events) are: outward interactions $Q_1 (u' > 0, w' > 0)$, ejections $Q_2 (u' < 0, w' > 0)$, the inward interactions $Q_3 (u' < 0, w' < 0)$ and sweeps $Q_4 (u' > 0, w' < 0)$. The Hole is denoted as the $Q=5$ (see Figure 6-2). The relative contribution of the events in a given quadrant Q to the mean Reynolds shear stress $\overline{u'w'}$ is determined according to the following expression:

$$RS_Q = \frac{\overline{u'w'}_{Q,H}}{\overline{u'w'}} = \frac{1}{\overline{u'w'}} \lim_{T \rightarrow \infty} \frac{1}{T} \int_0^T u'w' I_{Q,H}(t) dt \quad (6-1)$$

where the subscript Q and H refer to the quadrant and threshold level H , respectively. The detection function is given by:

$$I_{Q,H}(t) = \begin{cases} 1 & \text{if } u'w' \text{ is in quadrant } Q \text{ and } |u'w'| > H u_{rms} w_{rms} \\ 0 & \text{otherwise} \end{cases} \quad (6-2)$$

where u_{rms} and w_{rms} are the streamwise and vertical turbulence intensities, respectively. The relative contribution of the Hole events to $\overline{u'w'}$ is obtained as follows:

$$RS_5 = \frac{\overline{u'w'}_{5,H}}{\overline{u'w'}} = \frac{1}{\overline{u'w'}} \lim_{T \rightarrow \infty} \frac{1}{T} \int_0^T u'w' I_{5,H}(t) dt \quad (6-3)$$

where

$$I_{5,H}(t) = \begin{cases} 1 & \text{if } u'w' \text{ is in quadrant } Q \text{ and } |u'w'| \leq H u_{rms} w_{rms} \\ 0 & \text{otherwise} \end{cases} \quad (6-4)$$

It should be stressed that when $H=1$ we have $|u'w'_{H=1}| \geq H u_{rms} w_{rms} \approx 2.5 |\overline{u'w'}|$. This stems from the property $-\overline{u'w'}/u_{rms}w_{rms} = 0.4$, observed generally in turbulent open-channel flows. It should be referred that Nakagawa and Nezu (1977) adopted a slightly modified criterion, in which the detection function in Eq. (6-2) is taken as $|u'w'| > H u'w'$. In this modified procedure, when $H=1$, we have $|u'w'_{H=1}| > |\overline{u'w'}|$. Accordingly, one should keep in mind that according to the adopted criterion, the intensity of the selected events would differ. From the considerations above, it can be inferred that in the original procedure from Lu and Willmarth (1973) adopted herein, the intensity of events with a given threshold H corresponds to about 2.5 times the intensity based on the modified criterion. Note that the sum of the relative contributions of the four quadrants and the Hole events equals unity. It is noteworthy that only quadrants Q_2 and Q_4 produce positive shear stress. When the two quadrants are summed up at low values of H , their relative contributions may surpass unity. This implies that this excess is balanced by the sum of the negative Reynolds shear stress events Q_1 and Q_3 .

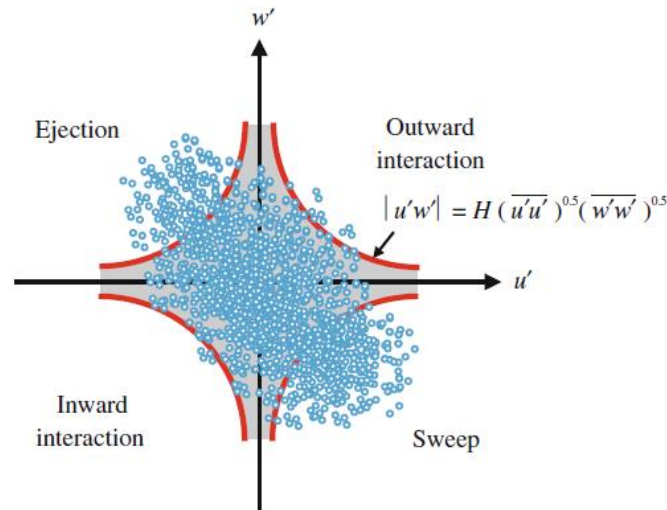


Figure 6-2. Sketch of the four quadrants and the delineation of the Hole region as originally defined by Lu and Willmarth (1973) (Adapted from Dey 2014).

The duration over which the conditionally sampled $u'w'_H$ is averaged (time T in Eqs. (6-1) and (6-3)) can be the total duration of the experimental run or the time of the detected events. The former is applied to investigate the fractional contributions of the selected events $u'w'_H$ to the mean Reynolds shear stress $-\overline{u'w'}$, whilst the latter provides information about the intensity of these events. In addition, in the present study, the quadrant analysis is not applied only to understand the dynamics of $u'w'$. It is extended to the turbulent flux kw' as in Hurther et al., 2007 and Mignot et al., 2009) and $c'w'$ as in Hurther and Lemmin (2003). For this purpose, the

detection function in Eq. (6-2) is not modified since we are interested in observing how shear stress selected events contribute to TKE flux kw' and particle flux $c'w'$.

6.3. Ejections and sweeps: fractional contributions, time fractions and periods

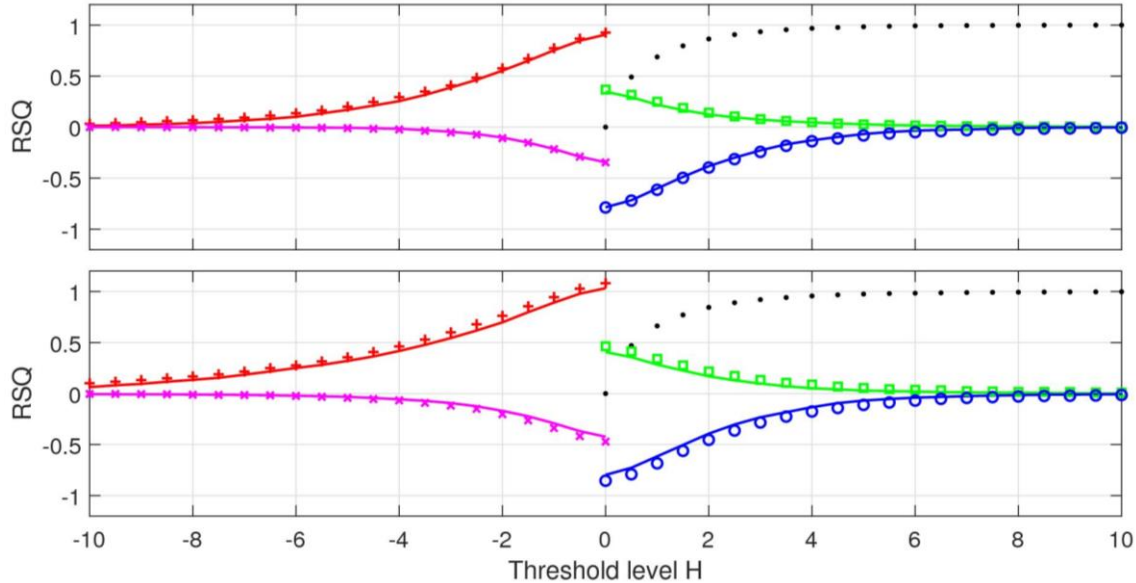


Figure 6-3 shows the fractional contributions from the four quadrants for the sediment-laden runs in saturation having the same hydrodynamic forcing, for dp1 (upper panel) and dp3 (lower panel), at position $z/H_f = 0.3$. It also includes the time fraction of the Hole events (dotted line). For all quadrants, the fractional contributions to $-\overline{u'w'}$ decreases with the threshold level. It is clearly seen that contributions from ejections and sweeps are significantly larger than the outward and inward interactions. At $H \approx 5$, the fractional contributions from sweeps reach 10% whilst ejections reach these fractional contributions at about $H \approx 7 - 9$. This suggests that in the outer flow region ($z/H_f > 0.15-0.20$) ejections are the main contributors to $-\overline{u'w'}$. As will be shown in the following figure, the trend is reversed in the inner flow region. The time fraction of the Hole events is equal to zero for $H=0$, and reaches about 85-90% and 93-96% for $H=2.5$ and $H=4$, respectively. This indicates that the latter two thresholds values select strong and rare events that means intense shear stress events. The result is further supported by the relatively small contributions of the Hole events for low values of H . For example, although the time fraction occupied by the Hole events delineated by $H < 2.5$ is about 85-90% of the total time, the respective fractional contribution to $-\overline{u'w'}$ is only about 30-40%. It implies that the events with $H > 2.5$ occur only 10-15% of the time, but they contribute to 60-70% of the production of $-\overline{u'w'}$. This proportion decreases to about 30-50% at $H=4$. The time fractions of ejections and sweeps for $H=0$ are fairly similar, and correspond roughly to 30% each (not shown here). For higher threshold values ($H=2.5$) it drops significantly to about 3-6%.

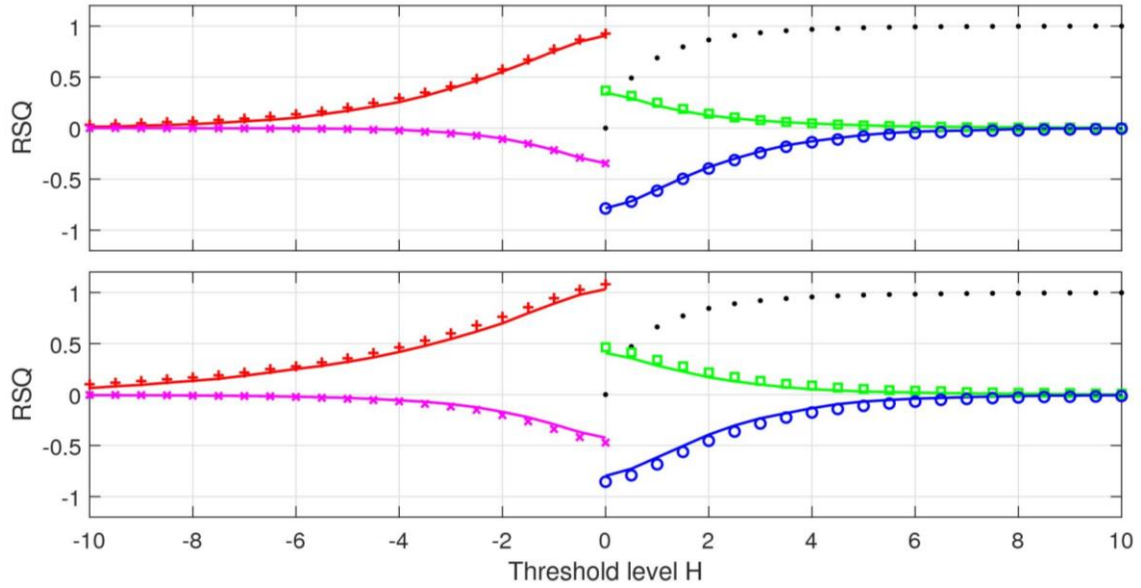


Figure 6-3. Relative contribution from ejections (+), sweeps (o), outward interactions (\square), inward interactions (x) and time fraction of the Hole events (.) for SL, as function of threshold level H ; solid lines are their reference CW; with the same hydrodynamic condition, for dp1 (upper panel) and dp3 (lower panel) at vertical level $z/H_f=0.3$.

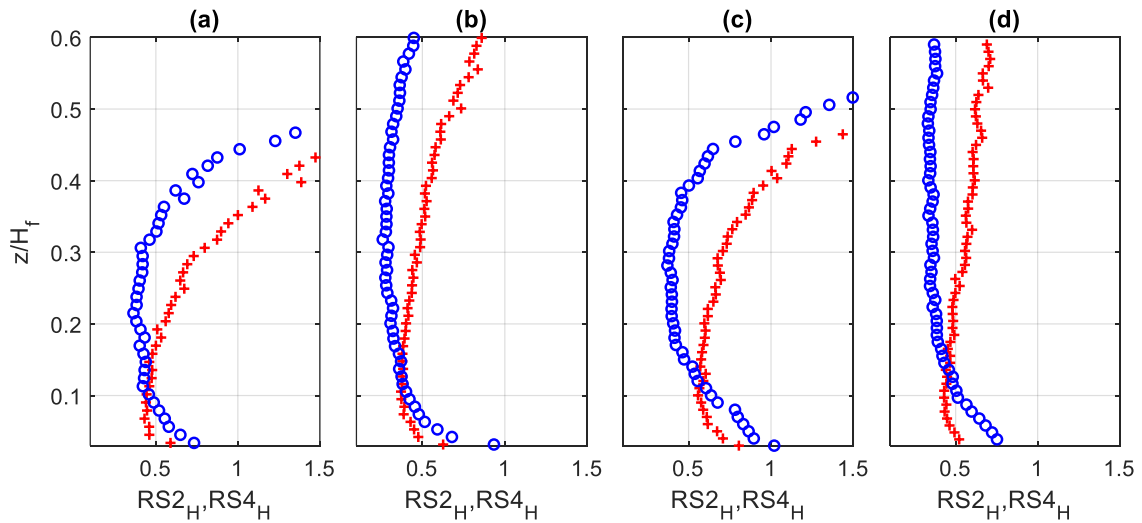


Figure 6-4. Fractional contributions from sweeps $RS4$ (o) and ejections $RS2$ (+), with $H=2.5$; for dp1 ($\theta \approx 0.4$ (a), $\theta \approx 1.2$ (b)) and dp3 ($\theta \approx 0.35$ (c), $\theta \approx 0.8$ (d)).

The fractional contributions discussed in the last paragraph are shown as vertical profiles in Figure 6-4, for a fixed value $H=2.5$, only for ejections (+) and sweeps (o). It includes only four hydrodynamic regimes, all in capacity conditions. As seen also in the previous figure, it is seen that at $H=2.5$, the fractional contributions in the outer flow region remain slightly above 50% of the mean Reynolds shear stress, whilst sweep contributions are slightly below it. Another important feature is observed for the larger particle experiments in Figure 6-6. It is seen that only for dp3, the region where the fractional contributions from sweeps is larger than ejections (*i.e.* where $RS4/RS2 > 1$) is systematically extended vertically as the concentration is increased up to saturation. This can be attributed to the presence of the bed-load layer, in which turbulence

production is reduced as shown in chapter 5. For dp1, it seems that the roughness sublayer extension is not affected by the presence of the particles, since the bed-load thickness is considerably smaller than for dp3. This aspect will be further discussed later.

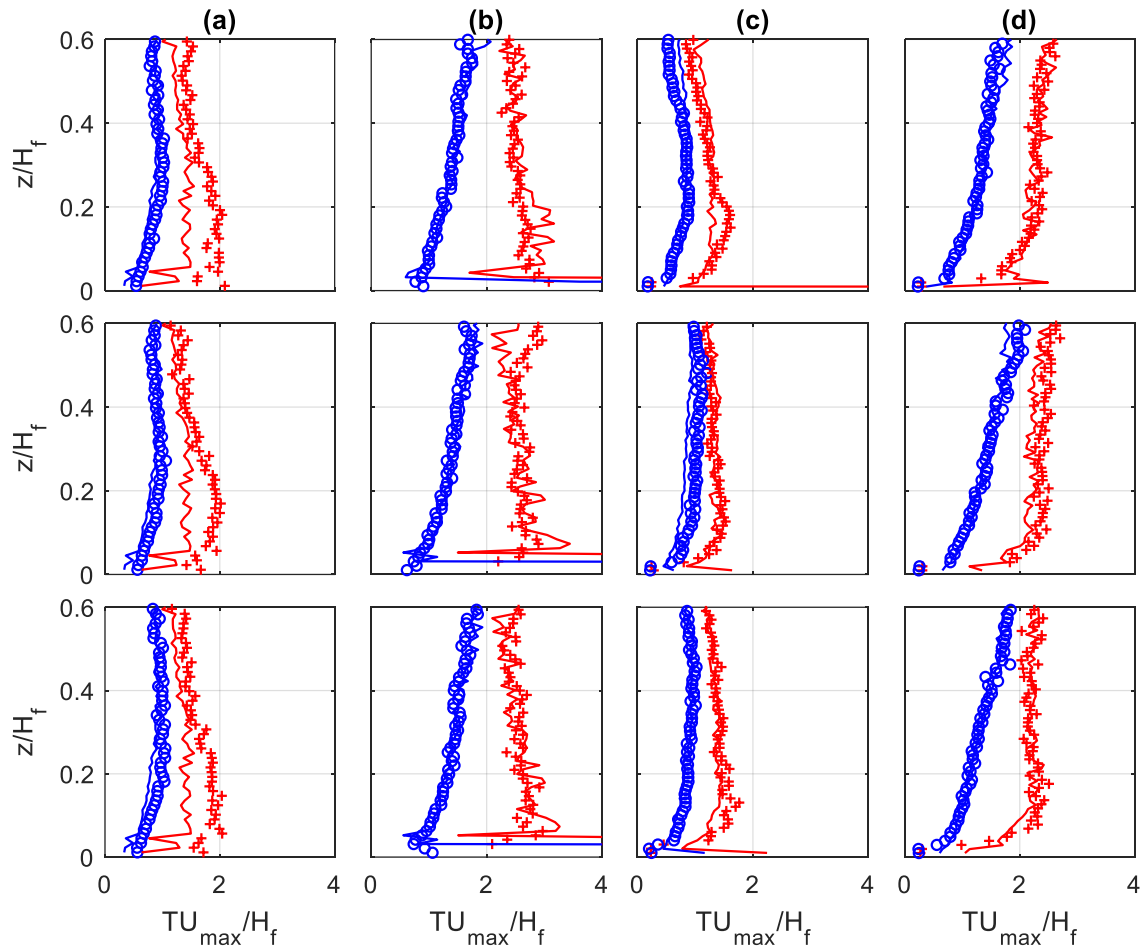


Figure 6-5. Bursting period of ejections (+) and sweeps (o) in sediment-laden flows; Solid lines correspond to the reference CW. For dp1 ($\theta \approx 0.4$) (a), $\theta \approx 1.0$ (b) and dp3 ($\theta \approx 0.35$) (c), $\theta \approx 0.8$ (d) for lower concentration (bottom), intermediate (middle) and saturated (top).

To estimate the mean periods of ejections and sweeps, Lu and Willmarth (1973) proposed to count the number of times that ejections or sweep events are detected, as a function of the threshold level H , and divide it by the total duration of the experimental run. This basically corresponds to the mean occurrence frequency of ejection and sweep events. Note that this is equivalent to counting the number of zero crossing in the time series of $u'w'_{Q2}$ or $u'w'_{Q4}$. Because the intensity of ejections and sweeps are different, the thresholds values for determining the occurrence frequency of the events are different for ejections (He) and sweeps (Hs). The cited authors defined Hs as the level H for which the contributions of interactions Q1 and Q3 to the shear stress disappear, whereas He is the level for which Q1, Q3 and Q4 become negligible, leaving only ejections as the contributor to the shear stress. The measured periods of sweeps and ejections, with $Hs=2.5$ and $He=4$ as proposed by Lu and Willmarth (1973) are shown in Figure 6-5. Negligible effects are seen in presence of sediments, for both particle diameters. Furthermore, the values are in good agreement with previous literature results. Based on the literature results, Nezu and Nakagawa (1993) concluded that in open-channel flows, the mean period of ejections T_e and sweeps T_s can be approximated to the mean bursting periods T_B , as follows:

$$\frac{T_B U_{max}}{H_f} \approx 1.5 - 3.0 \quad (6-5)$$

Raupach (1981) obtained for $He=4$, $TU_{max}/h = 3.6$ for smooth surface, and $TU_{max}/h = 2.4$ for intermediate rough surface and $TU_{max}/h = 2.1$ for the surface with larger roughness height. The values coincide well with Nakagawa and Nezu (1977) and more recently Krogstad and Antonia (1999). Like herein, a more constant vertical distribution of T_e , compared to T_s was also identified in the cited studies.

6.4. Connection between Bursting motions and TKE transport

Figure 6-6 shows the profiles of vertical TKE flux $Fk = \overline{k w'}$ and the profiles of the parameter RS_4/RS_2 . An almost perfect match can be found between the positions of $Fk=0$ and $RS_4/RS_2=1$, both in CW and SL flows for dp1 and dp3. This strongly supports that the same bursting motions govern the transport of momentum and the vertical transport of TKE. The dominance of sweep events is associated with a downward transport of TKE ($Fk < 0$), whereas ejections transport TKE upwards ($Fk > 0$). Raupach (1981) provided quantitative evidence for this result. Given that the turbulent diffusion in the TKE budget is simply $\partial Fk / \partial z$, this experimental result confirms a direct link between coherent structures dynamics and the TKE budget.

It can further be seen in Figure 6-6 that only for dp3, the level corresponding to the upper limit of the sweep dominated region, is systematically upshifted with increasing concentration, while maintaining a good agreement between the positions where $Fk=0$ and $RS_4/RS_2=1$. This result is consistent with the significant upshift of the energy excess region observed in chapter 4 for the large particle experiments dp3. Hence, in presence of a thick bed-load layer, there is an increased dominance of sweep events, which transports TKE downwards into the bedload layer. Interestingly, the change of signature in presence of sediment is barely noticeable for dp1. This supports that the presence of a bed-load layer larger than the sweep-dominated layer in the same clear-water condition is the cause of the modified signature, for dp3. This suggests that for dp1, the sweep-dominated layer has the same extension as in CW because the thickness of the bedload layer remains smaller than the (bed roughness induced) sweep-dominated layer.

The dependence and sensitivity of the production and turbulent diffusion terms to the bed roughness conditions is documented in the literature. Nakagawa and Nezu (1977) have shown that the ratio of the magnitude of sweep over ejections RS_4/RS_2 increase with roughness, and they associated it to variations in velocity skewness and diffusion factors that change from smooth to rough flows. In addition, they found that the vertical range of negative values of Fk also increases with roughness and that this trend is equally associated to the same diffusion and skewness factors governing RS_4/RS_2 . Later, Raupach (1981) presented an explicit relationship between Fk and the bursting parameter $\Delta RS = RS_4 - RS_2$. One major difference between the present SL flow results with dp3 and the typical CW rough flows is that in the latter the increased downwards TKE transport in absence of sediments is balanced by viscous dissipation, whereas in presence of a thick bed-load layer, the transported TKE becomes locally a TKE source term, which could potentially support the (bedload) sediment transport term (as discussed in chapter 5) and/or the viscous dissipation.

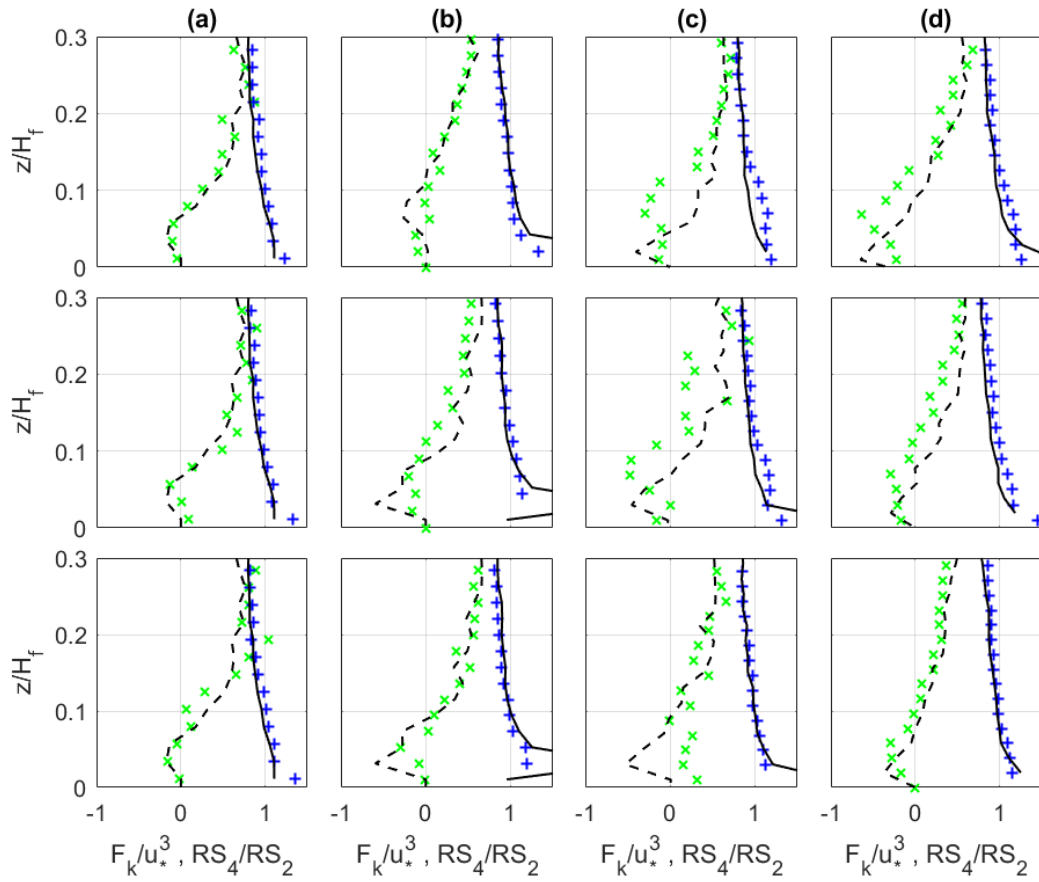


Figure 6-6. Turbulence transport Fk (x for SL and -- for CW) and $RS4/RS2$ (+ for SL and – for CW); panels as in Figure 6-5.

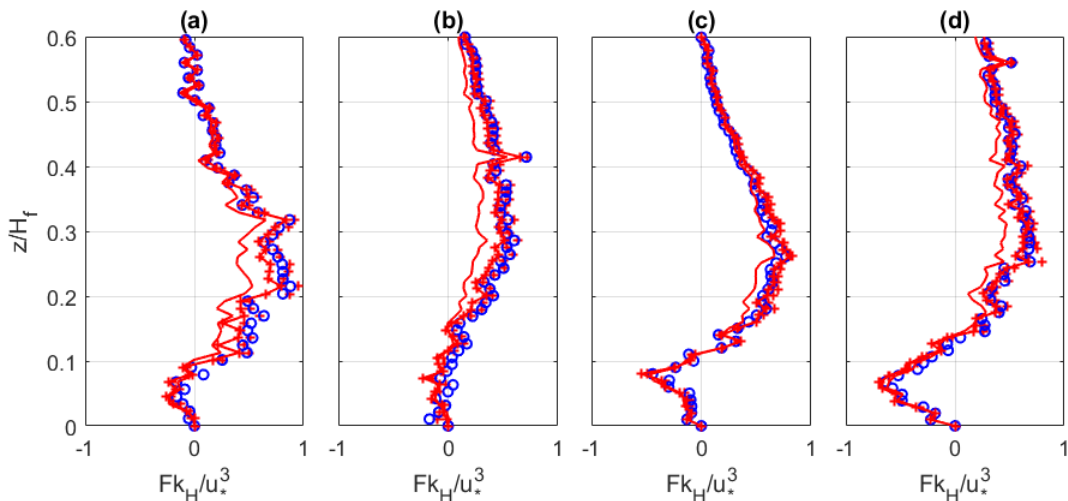


Figure 6-7. Mean Fk (bo) and conditionally sampled Fk_H (all four quadrants), for $H=2.5$ (+), $H=4$ (-+) and $H=6$ (-); for dp1 ($\theta \approx 0.4$ (a), $\theta \approx 1.0$ (b)) and dp3 ($\theta \approx 0.35$ (c), $\theta \approx 0.8$ (d)) only runs in saturation.

To have further insights into the transport of TKE by coherent flow structures, Fk was conditionally sampled (considering all 4 quadrants), with different values of threshold level H , as shown in Figure 6-7, only for the SL flows under capacity condition. As stated in section 6.2, this is performed by applying the detection function $I_{Q,H}$ on the time-series of Fk . It is seen that up to about $H=4$, the signature and magnitude of conditionally sampled Fk_H is almost unchanged compared to the mean Fk which means that shear stress events of level below $H=4$ have a negligible contribution to Fk . Only for $H=6$, Fk starts to decrease noticeably, although

the conditionally sample Fk_H still represents a large fraction of Fk . This observation suggests that TKE flux Fk is almost entirely generated by strong shear stress events. This result was previously highlighted by Hurther et al., (2007) and Mignot et al., 2009), based on ADV measurements in turbulent rough clear-water open-channel flows. A similar analysis was performed by taking only $Q2$ and $Q4$ events into account. It was seen that Fk_H is even larger than Fk , indicating that $Q2$ and $Q4$ shear stress events are responsible for the diffusive TKE transport. Hence, it can be inferred that the transport of TKE into the bed-load layer is due to occurrence of very intense and intermittent coherent structures. This is supported by the low time fraction of the events with the selected threshold levels, corresponding approximately to $T = 12, 6$ and 2% , for $H=2.5, 4.0$ and 6.0 , respectively.

6.5. Correlation between turbulent suspension and coherent structures

In the precedent sections, it was shown that ejections and sweeps are highly correlated with the transport of momentum ($\overline{u'w'}$) and of turbulent energy ($\overline{kw'}$). In this section, their role in the transport of mass ($\overline{c'w'}$) will be highlighted, taking only the runs with maximum concentration (in saturation). The accuracy of measured vertical turbulent sediment fluxes $\overline{c'w'}$ in the present highly inertial conditions seems questionable. The solid transport regime herein is different from previous studies (Nikora and Goring, 2002, Hurther and Lemmin, 2003, Cellino and Lemmin, 2004) with acoustic measurements. In these studies, the assumption of similar velocity fluctuations for the solid and fluid phases were taken, hence the estimations of $\overline{c'w'}$ could be justified. Despite the referred limitations, we can assert some properties at least for $H>0$, corresponding to bursting motions where the lag between phases may be reduced. Furthermore, we are interested mostly in the relative contributions and general trends, rather than absolute values of $\overline{c'w'}$.

In Figure 6-8, the ratio between the conditionally sampled $\overline{c'w'_H}$ (taking all 4 quadrants) and its mean value $\overline{c'w'}$ is represented, for different values of shear stress threshold level H . It is seen that for events selected with $H=1.0, 2.5$ and 4.0 , the relative contributions to the mean vertical solid flux are approximately $\overline{c'w'_H} / \overline{c'w'} = 0.70 - 0.8, 0.35 - 0.5$, and $0.2 - 0.28$, respectively. This confirms the strong correlation between the bursting motions and the vertical particle fluxes for all SL conditions, irrespective of particle size and of suspension number value. These referred events occur at fractions of time $T_f = 33 - 36, 10 - 15$ and $3 - 7\%$, respectively, supporting the high intermittency of $\overline{c'w'}$ originating from the high intermittency of ejection and sweeps. One important feature is the higher particle entraining efficiency of the stronger events, for $dp3$. Note that in columns (c) and (d), the referred ratio is systematically larger than in (a) and (b), indicating greater correlation between $\overline{c'w'}$ and $\overline{u'w'}$ events. This result supports the argument of Gyr (1983) that large particles can only be entrained by intense coherent flow structures. To verify the importance of ejections and sweeps for this case, the same ratio was estimated taking only $Q2$ and $Q4$ events. Very similar magnitudes as in the case of the four quadrants (Figure 6-8c and Figure 6-8d) were found confirming the leading role in $\overline{c'w'}$ dynamics played by ejection and sweep type events. Similar dynamics was found by Hurther and Lemmin, 2003, for sediment laden flows in the suspension regime ($w_s/u_* < 0.6$). The same dominant role played by ejection and sweep type events is observed here for sediment-laden flows with much higher suspension number value.

Figure 6-9 shows $\overline{c'w'}$ associated with different quadrants, for a level $H=2.5$. It is seen that sweeps contributions to $\overline{c'w'}$ remain systematically dominant in the near-bed region. Contributions from inward and outward interactions are negligible. The larger contributions from sweeps in the near-bed, suggests that although they consist of downward movement of

fluid parcels, they are more efficient to dislodging particles from the bed. Because the intensity of ejections become more important away from the bed, they may be the dominant mechanism in maintaining particles in suspension. Summarizing, sweeps seem to be the dominant entrainment mechanism, whilst ejection are the most important for maintaining particle suspension.

Experimental evidence indicates that ejections are associated with the occurrence of clouds of suspended sediments, ejected from the near-bed. On the other hand, sweeps transport high momentum fluid parcels and particles from the upper flow region to the bed. From this description, it can be deduced that ejections are likely to increase local concentration along the water column, whereas sweeps have probably the opposite effect by bringing a more dilute mixture into the lower flow region and hence generating local negative values of c' . This hypothesis was confirmed by conditionally sampling the signal of concentration fluctuation, based on ejections and sweeps for different threshold levels. It is seen in Figure 6-10 that the averaged concentration fluctuations associated with sweeps and ejections are negative and positive, respectively. The observed signature explains the generation of positive $c'w'$ by sweeps as the product of negative concentration with negative vertical velocity fluctuations. Another interesting feature is that larger concentration fluctuations are obtained for larger H values, i.e. for larger shear stress events. This further supports that ejection and sweeps are very important in the suspension dynamics. Such observations are permitted thanks to the simultaneous and co-located measurements (within the same sample volume) of bedload, suspended sediment concentration and velocity at a spatio-temporal rate resolving small turbulent flow scales.

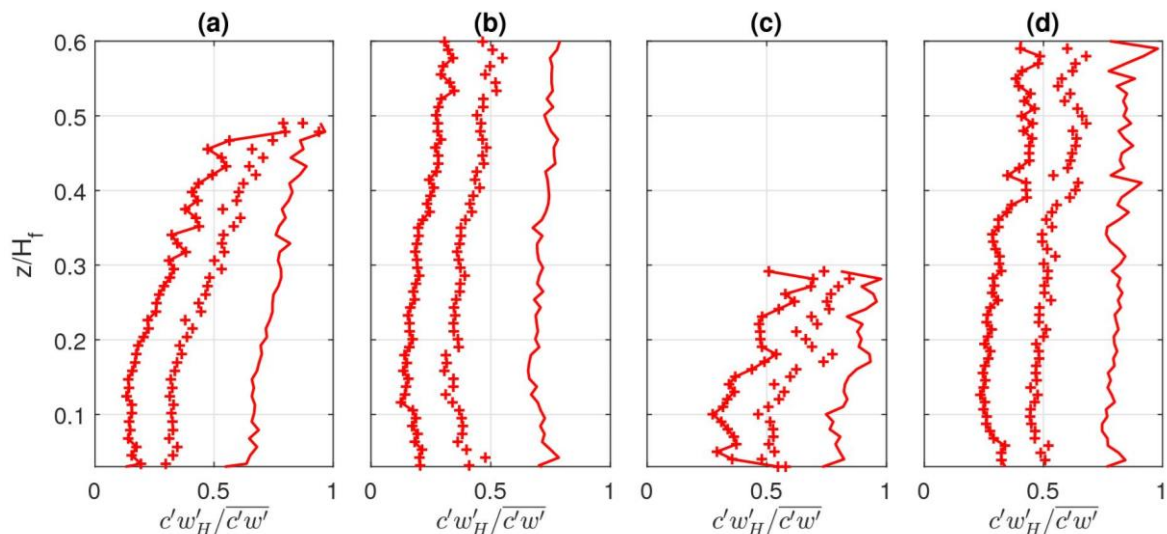


Figure 6-8. Fractional contribution of selected events (taking all four quadrants) to the mean vertical turbulent sediment flux; with $H=1$ (-), $H=2.5$ (+) and $H=4$ (+-); for maximum sediment concentration regime (SAT).

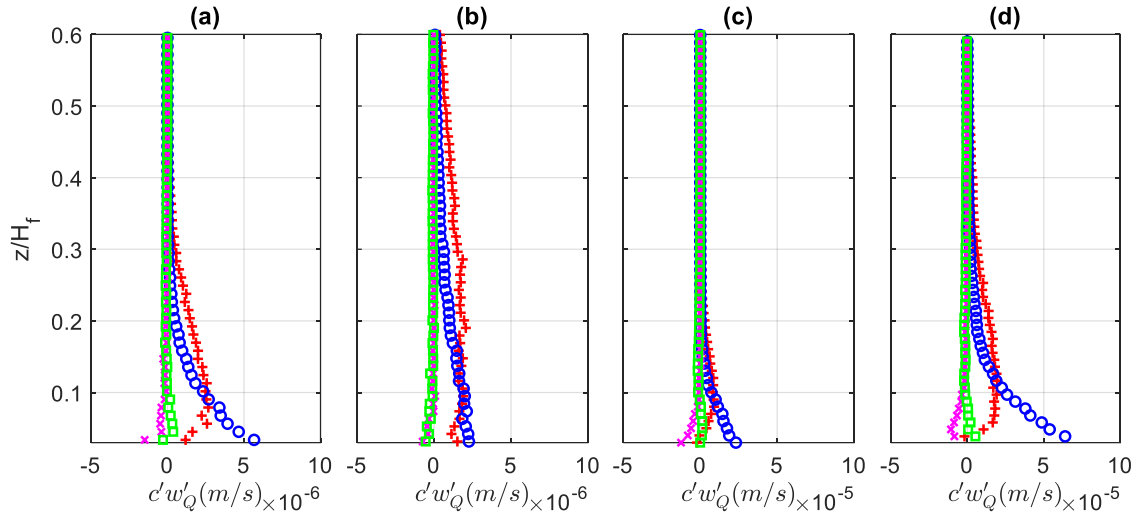


Figure 6-9. Vertical turbulent sediment flux for ejections (+), sweeps (o), outward interactions (x) and inward interactions (□), for $H=2.5$.

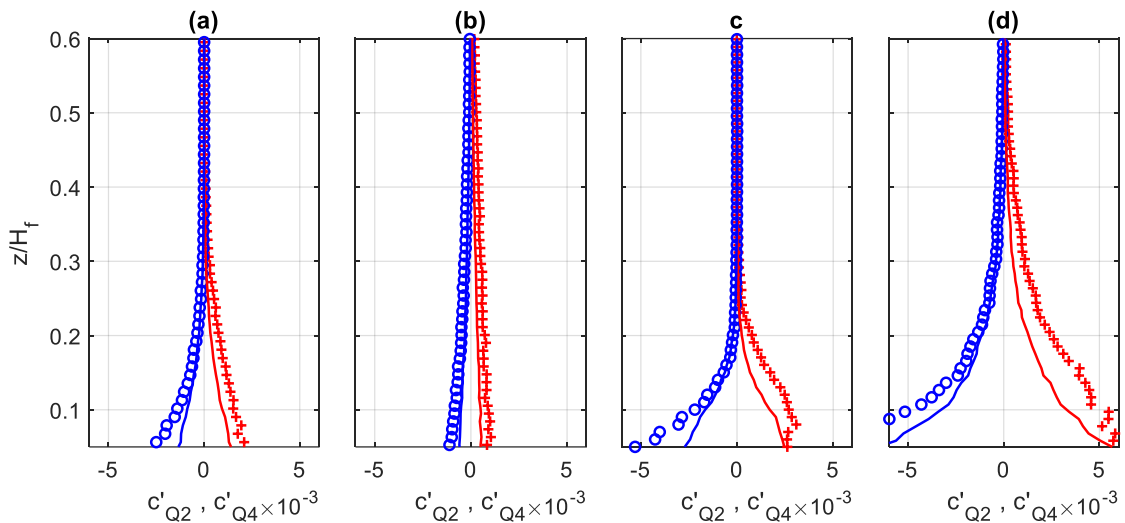


Figure 6-10. Conditionally sampled concentration fluctuations associated with ejections c'_{Q2} (cross corresponds to $H=2.5$ and solid line to $H=0$) and sweeps c'_{Q2} (circle correspond to $H=2.5$ and solid line to $H=0$); for maximum sediment concentration regime (SAT).

The conditionally sampled ratio w'_H/w_s is shown Figure 6-11, in which the conditionally sampled w'_H is an intrinsic average (in contrast to a superficial average), *i.e.* an average only over the time of the selected events. Please also note that the mean vertical velocity is close to zero because the open-channel flow is unidirectional. Away from the wall, the characteristic (vertical) velocity ratio increases with the threshold H and exceeds unity at different levels of H , depending on the particle diameter and flow conditions. It implies that during intense shear stress events, the upward velocity exceeds the downward settling velocity w_s . Furthermore, it confirms that the suspension capacity of coherent structures depends on the shear stress magnitude as well as the particle weight. Taking a ratio value equal to unity for selecting the flow structures carrying particles, we find threshold levels of approximately $H = 4$ and $H = 2.5$ in Figures 6-11a and 6-11b, and $H = 8$ (not shown) and $H = 6$ in Figures 6-11c and 6-11d, respectively. The observed trend in H values is expected, as suggested by the suspension

number (w_s/u_*) values, often used to characterize the suspension regime. Indeed, the high threshold of the particle carrying structures in column (c) confirms that it corresponds to a transport condition with very low suspension capacity, hence, dominated by bed-load transport. For SL flows in the same turbulence level (Figures 6-11b and 6-11c), the carrying structures display a much lower value of H , due to the lower immersed particle weight for dp1.

Figure 6-12 illustrates the estimated critical value of the H level selecting the particle carrying structures (in the suspension layer) over the entire range of suspension number w_s/u_* studied herein. It can be seen that this critical H level increases linearly with w_s/u_* , with a slope of about 6.5. The higher threshold H associated with the larger particles indicates that more energetic coherent structures are required to carry particles in suspension. The definition of a critical H value offers new perspectives for burst dependent modelling of sediment pick up functions (Cao, 1999) or identification of the different modes of sediment transport as rolling/saltating bedload or suspension load (Gyr 1983).

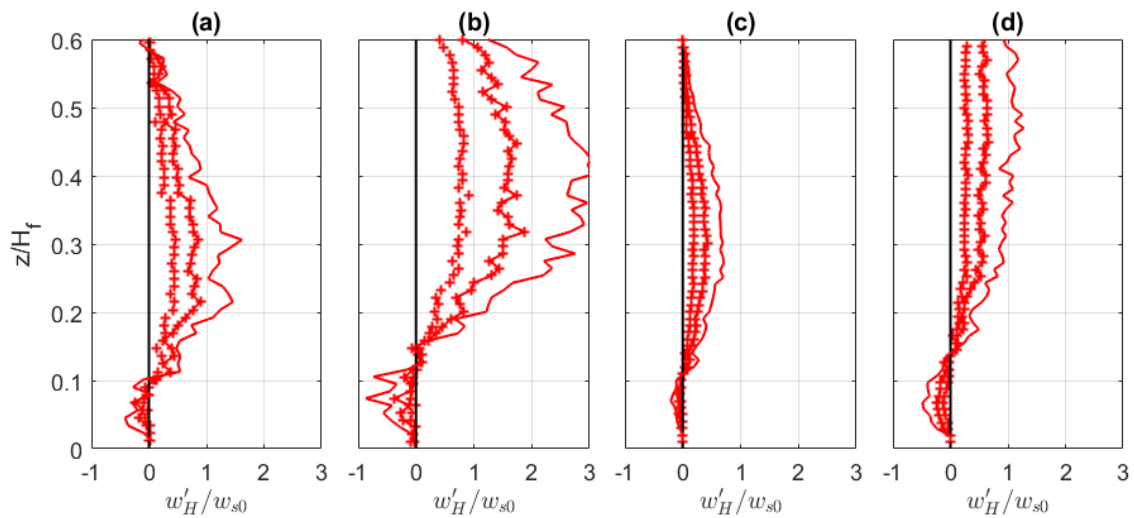


Figure 6-11. Ratio w'_H/w_{s0} (w'_H time averaged over the duration of the selected events) corresponding to all four quadrants with $H=2.5$ (+), $H=4.0$ (+-) and $H=6.0$ (-); for dp1 ($\theta \approx 0.4$ (a), $\theta \approx 1.0$ (b)) and dp3 ($\theta \approx 0.35$ (c), $\theta \approx 0.8$ (d)) only runs in saturation.

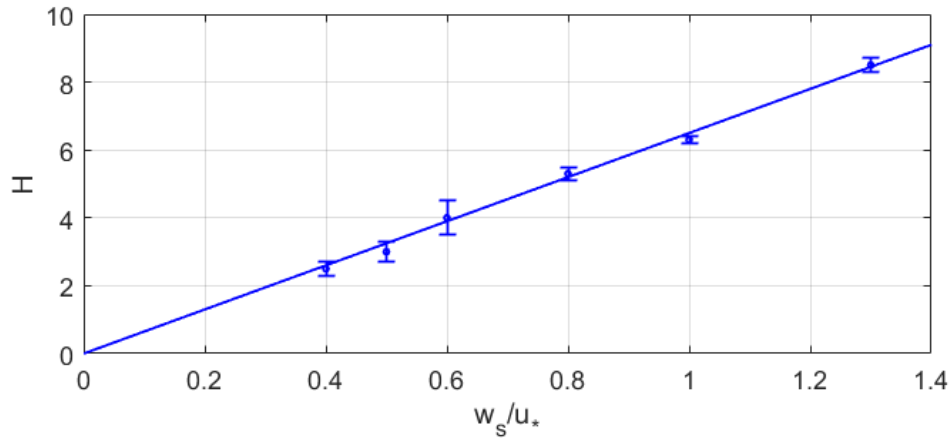


Figure 6-12. Evolution of H corresponding to $w'_H/w_{s0} = 1$ for the six hydrodynamic regimes in saturation; the error bars represent the variability over the three repeated runs; The linear fit corresponds to $H = 6.5w_s/u_*$.

6.6. Discussion and conclusions

In the present chapter, it was shown that turbulent coherent structures play a dominant role in the TKE budget via the shear production term of TKE but also the TKE flux. This was demonstrated by the good agreement between the transition level where TKE flux $Fk = 0$ and the level at which $RS4/RS2 = 1$, in both CW and SL. This result confirms that the same turbulent structures govern the transport of momentum $u'w'$ and of turbulent energy kw' , given that the dominance of ejections and sweeps are directly correlated to net upward and downwards fluxes of TKE, respectively (Nakagawa and Nezu 1977, Raupach, 1981). In addition, only for larger particles dp3, the transition level was significantly upshifted by the presence of a thick bedload layer, while retaining the good agreement previously mentioned. This appears to be consistent with the strong upshift of the TKE production peak, which leads to increased downward diffusion of TKE into the bedload layer. Analysis of coherent structures based on the quadrant threshold technique, confirmed that TKE flux is generated mainly by strong and intermittent coherent shear stress flow structures, with threshold levels $H \geq 4$.

The correlation between vertical turbulent sediment flux $c'w'$ and $u'w'$ was put into quantitative evidence. This correlation is stronger for heavier (*i.e.* the large) particles, suggesting that intense bursts are important to the suspension of heavy particles. A criterion for identifying the sediments carrying structures was tested. It was observed that the sediment carrying flow structures were characterized by different critical threshold levels H depending on the suspension number value w_s/u_* as a ratio between the particle settling velocity scale (particle inertia) and the bed friction velocity (turbulent velocity scale).

A criterion for identifying the sediments carrying structures was tested. It was observed that the carrying structures were characterized by different threshold levels H depending on the ratio of particle inertia and turbulence level and (w_s/u_*). A visual representation of the carrying structures is provided in Figure 6-13 and Figure 6-14, for run P3S03D10_SAT. They correspond to contours of shear events sampled using the critical threshold levels $H=2.5$ (for dp1) and $H=8.0$ (for dp3), in the former and latter figures, respectively. It is clear that the carrying structures with $H=8$ are detected much more intermittently than with $H=2.5$. However, given that $|u'w'_{H=8}| > 20|u'w'|$ and $|u'w'_{H=2.5}| > 6.25|u'w'|$ (see section 6.2), the former events are significantly more intense than the latter. It implies that the efficiency of coherent structures in generating turbulent suspension $\overline{c'w'}$ decreases with w_s/u_* . The figures in

reference also confirm that the regime with the higher values of w_s/u_* is strongly dominated by bed-load transport, with very intermittent particle suspension events due to the strong ejection events. On the other hand, the regime with the lower ratio w_s/u_* , which corresponds to the same hydrodynamic condition, particles are efficiently suspended more regularly, by structures that are less intense.

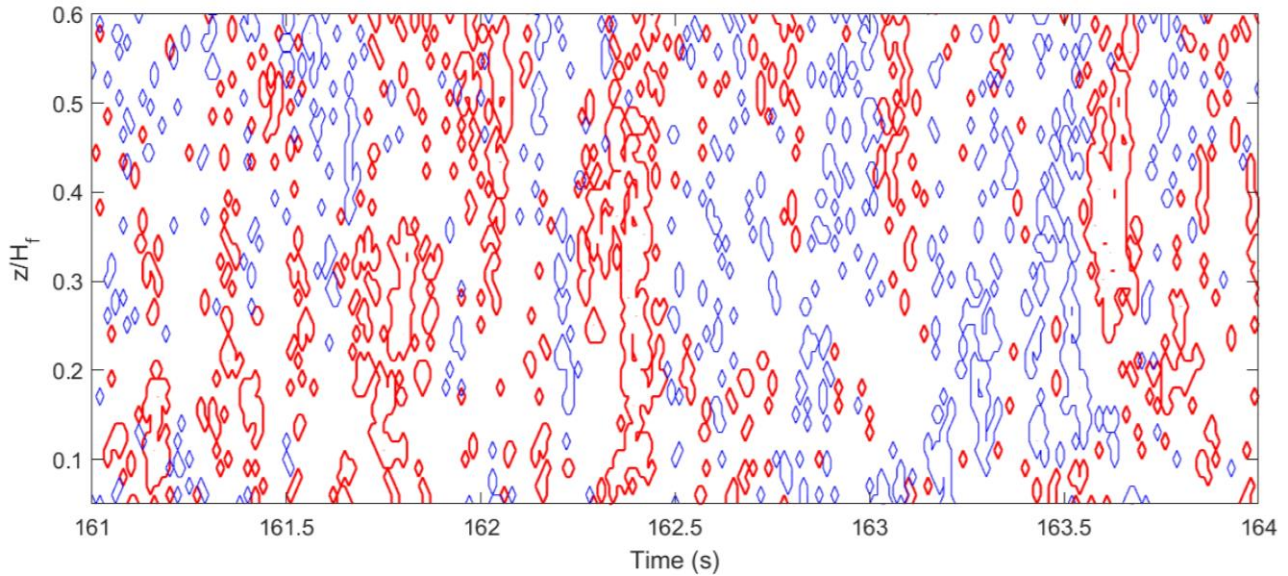


Figure 6-13. Contours of ejections (red ant thicker line) and sweeps (blue and thinner line) at the threshold $H=2.5$; run P3S03D10_SAT

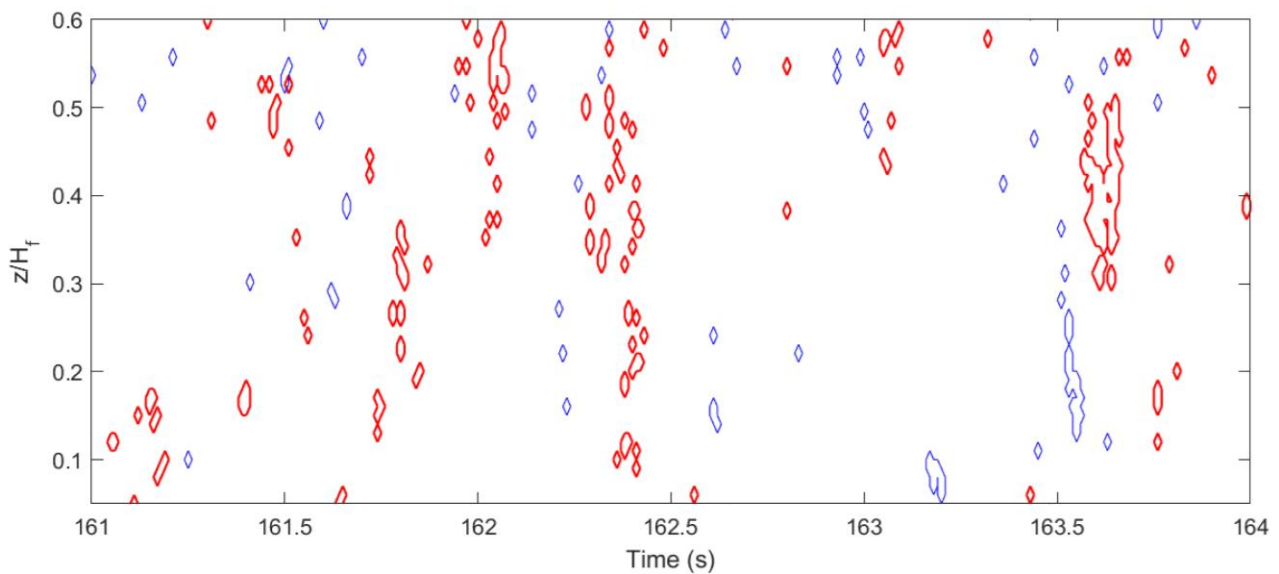


Figure 6-14. Contours of ejections (red ant thicker line) and sweeps (blue and thinner line) at the threshold $H=8$; P3S03D10_SAT

7. Conclusions and perspectives

In this Ph.D Thesis, two major measurement campaigns with PMMA particles of diameter $dp=3\text{mm}$ and $dp=1\text{mm}$ were carried out, covering a range of Shields numbers of $0.4 < \theta < 1.2$ and suspension numbers of $0.4 < w_s/u_* < 1.3$. The first goal was to produce a dataset suitable for process-based study of solid transport phenomena. The second objective was to investigate turbulent processes in sediment-laden flows. The particle interactions were not studied, but their effects on the turbulent flow characteristics were discussed in detail. The main conclusions are summarized in the following section, followed by perspectives for future work.

7.1. Conclusions

In chapter 3, mean profiles and modelling parameters were presented. The mean profiles concerned velocity, concentration and Reynolds shear stress, that allow the estimation of most hydrodynamic and solid-transport quantities, as well as important modelling parameters. The main conclusions of the chapter are:

- The von Karman parameter in sediment-laden flows κ_s can be approximated to the CW value up to relatively high depth-averaged (volumetric) concentrations ($2\text{-}3 \times 10^{-3}$). Furthermore, at high values of $w_s/u_* \geq 1$, κ_s remains similar to CW values even at higher concentrations (SAT) because the solid transport occurs mostly in the bed-load layer. In general, with high suspension the velocity profile is not logarithmic in the bed-load layer. Even above this layer, it displays an evolving slope, suggesting that at high concentrations, the adopted values of κ_s represent a general trend, rather than the local flow features.
- The quasi-proportionality between momentum ϵ_{ms} and sediment diffusivity ϵ_s was confirmed. The depth-averaged ratio $\beta = \epsilon_s/\epsilon_{ms}$ agree with the model of van Rijn (1984) at low suspension numbers ($0.1 < w_s/u_* < 0.8$). For larger values of the suspension number, van Rijn's model deviates from the presented data. A modified parametrization was proposed, such that it is applicable over a wider range of suspension numbers ($0 < w_s/u_* < 1.5$).
- The friction factor f remained rather unchanged between equivalent CW and SL conditions. This supports the argument in Hydraulics literature (Henderson 1966; Raudkivi 1998), that in absence of bed-forms, the bulk flow resistance in sediment-laden flows remains practically unaltered.

In chapter 4, the effects of the presence of a thick bed-load layer ($dp=3\text{mm}$) on velocity and concentration profiles were investigated, based on the mixing length theory. The main conclusions of the chapter are the following:

- The linear mixing length profile was applied as a criterion for separating bed-load and suspended-load layers. The method is based on the principle that in the suspension layer, the mixing length displays the typical quasi-linear distribution, and that strong deviation from this trend in the near-bed region of turbulent boundary layers is due to the presence of a bed-load layer.

- The logarithmic velocity distribution in sediment-laden flows with thick bed-load layers occurs at vertical elevation much higher than in the reference clear-water flow, consistent with the region of linear mixing length observed at higher elevations $z/H_f > 0.1$, compared to their reference clear-water flows. This normalized height is well above the typically used reference height of 5% in the standard Rouse formulation for the prediction of the mean suspended sediment concentration profile.
- The application of the modified mixing length and eddy viscosity profiles to model velocity and suspended particle concentration in large particle sheet-flows, confirmed that the logarithmic velocity profile holds if applied above the bed-load layer. Regarding the concentration model, the classical Rouse equation becomes less accurate as the bed-load layer thickness δ increases. This is due to the poor description of the eddy viscosity profile in such SL flows. Using a modified eddy viscosity (that includes the bed-load layer induced upshift), a modified analytical solution for the profile of mean suspended particle concentration was proposed. This relationship is recommended when the bed-load thickness $\delta \geq 0.05H_f$.

Chapter 5 presented the results in terms of measurements of Turbulent Kinetic Energy (TKE) Budget. The main findings of the chapter are:

- Consistent with the observations reported in chapter 4, the presence of a thick bed-load layer significantly alters the structure of the energy balance. Only with the large particles ($dp=3\text{mm}$), the production term is heavily reduced in the bed-load layer, consistent with a sharp increase in the local flux Richardson number, that exceeds the critical value $Ri = 0.2$.
- Accordingly, for the large particle experiments ($dp3$), the peak of turbulence production is significantly upshifted, compared to the reference clear-water flow, leading to an increased diffusive transport of TKE towards the bed, *i.e.* into the bed-load layer. This term is found to act as a potential TKE source for particle transport as bed-load and/or viscous dissipation. This is supported by the findings that the diffusive TKE transport term is locally in good balance with the particle transport term, inside the bed-load layer, only for $dp=3\text{mm}$.
- The TKE inside the bed-load layer might be mostly transported by diffusion from the production region at the edge of the bed-load layer, rather than local TKE production generated by the work of turbulent shear stress against the mean flow deformation.
- Based on the depth-averaged repartition of the energy terms, it was concluded that the sediment suspension term represents about 7-10% of the available produced TKE, in capacity conditions, for all solid-load regimes.

In chapter 6, features of turbulent coherent flow structures were reported. Their importance in the transport of momentum, turbulent energy and mass was demonstrated. The main conclusions of this chapter are:

- A very good agreement between the transition level where TKE flux is zero ($Fk = 0$) and the ratio between sweeps and ejections intensities is in equilibrium ($RS4/RS2 = 1$), prevails in both clear-water and sediment-laden flows, regardless of particle diameter and sediment concentration. This strongly supports that the

same turbulent structures govern the transport of momentum $u'w'$ and of turbulent energy kw' .

- Only for dp3, the transition level was significantly upshifted, consistent with the strong upshift of the production peak, which leads to increased downward diffusion of TKE.
- Based on the quadrant threshold technique, it was confirmed that TKE flux is generated mainly by strong and intermittent structures, with threshold levels $H \geq 4$.
- Applying a simple criterion $w'_H/w_s \approx 1$ for identifying the carrying coherent flow structures, it was found that they are characterized by threshold levels H that increase linearly with w_s/u_* , implying that the efficiency of coherent structures in generating turbulent suspension decreases with w_s/u_* .

Note that in chapters 3 and 4, aspects that have direct implication on velocity and concentration prediction were presented, whilst on chapters 5 and 6 important turbulence processes in sediment-laden flows were discussed in detail. Therefore, efforts were made to target the basic problem of prescribing the solid-load as result of the product of velocity and concentration, with direct implication in modelling of large-scale morphological evolution, as well as in improving our understanding of the turbulent transport processes in sediment-laden flows.

7.2. Perspectives

Since the present measurements are performed under starved-bed conditions (absence of an erodible bed constituted by sediments at rest), caution should be taken in the extrapolation of some results to equilibrium beds condition. Given that Lyn (1986) seems to be the only to have performed detailed measurements of equilibrium-bed and starved-bed near transport capacity, under similar flow and solid-transport conditions, his results could provide some insights about the potential applicability and limitations of the starved-bed experiments. He concluded that, generally, at higher sediment concentration, the starved-bed (near-capacity) experiments displayed similar qualitative behaviour in the velocity and concentration profiles. Nevertheless, it seems that the degree of saturation could explain at least part of the observed quantitative differences between the two conditions. Furthermore, Revil-Baudard et al. (2016) suggested that bed mobility may have some important impacts on the turbulence structure in the near-bed region. Therefore, although the results in near-capacity conditions provide general trends valid under equilibrium beds, experiments in non starved-bed conditions should be considered to confirm the results obtained herein.

In addition to the referred effects of bed mobility on the turbulence near-bed properties, the depth-averaged energy repartition discussed in chapter 5 also deserves special attention in future equilibrium bed experiments. The prevalence of a quasi-constant upper limit for the energy ratio of the stratification term should be further explored. If not constant, its evolution with w_s/u_* should be determined. This approach is appealing because it targets a basic sediment transport question: if we gradually feed a given turbulent flow with denser particles, what will be the energy proportion associated to $\overline{c'w'}$, when the flow can no longer transport more sediments (starts to deposit additional particles fed to the flow). Hence, it corresponds to the transport capacity problem. As discussed in chapter 5, this is the basis of the energetic approach explored by Bagnold (1966), that provides an efficiency of the energy spent by the flow to transport sediments as bed-load and suspended-load. The determination of such energy efficiencies and their parametrization over a wide range of suspension number values is left for future work,

particularly for SL flows under equilibrium bed conditions. A preliminary analysis of a potential parametrization of solid-transport based on these considerations is shown in Appendix Figure C-1.

The sediment entrainment process also merits special attention in future experiments under equilibrium beds. The pick-up function introduced by Einstein (1950) can be effectively applied to investigate the near-bed boundary conditions, specifically, the near-bed concentration. The deposition rate at the interface of the bed-load layer is $D = w_s \bar{c}_b$ (with \bar{c}_b as the mean concentration at the edge of the bed-load layer), while the entrainment rate (as an upward erosion flux) at the same level is $E = \overline{c'w'}$. Introducing a dimensionless entrainment rate $E_s = E/w_s$, the pick-up rate from bed-load towards the suspension layer can be given as $E = E_s w_s$, such that the net vertical sediment flux at the edge of the bed-load layer can be written as:

$$J_b = w_s(E_s - \bar{c}_b) \quad (7-1)$$

In equilibrium conditions, the relationship becomes:

$$E_s = \bar{c}_b \quad (7-2)$$

Eq. (7-2) states that under equilibrium conditions, the dimensionless pick-up rate function defines the reference concentration. The available relationships for the pick-up functions (Garcia and Parker 1991, van Rijn 1993) can be revisited and tested against this type of dataset. The analysis should be performed in equilibrium beds, because the near-bed concentration is highly dependent on the degree of saturation. The efforts of Cao (1999), whose parametrization of the near-bed concentration involves the description of the bursting periods can be supported by the future experiments in equilibrium beds. Although the data from Lyn (1986) in equilibrium beds provide some information on the bursting phenomena and on concentration, the near-bed ($z/H_f < 0.1$) measurements are not reported.

The knowledge gathered herein should be useful to the improvement of the next generation of process based sediment transport models in particular for those based on two-phase fluid-particle approach (Chauchat et al. 2017, Mathieu et al. 2021). The advantage of these models is that they consider all possible interaction process between the dispersed phase as particles, and the carrying fluid phase. Since they incorporate the interactions between phases, conceptually, they are more justified than the classical single-phase models developed under restrictive hypothesis. Nevertheless, they require more closures to model the new terms, namely the interaction between fluid and particle, and the stresses related to the solid phase. In addition, the fluid turbulence still has to be modelled, including the eventual turbulence modulation, due to the presence of particles. The TKE budget measurements discussed herein, should be compared with simulation results for the mixture TKE balance, based on two-phase flow models, instead of the usually reported fluid-phase equation (Hsu et al. 2004, Cheng et al. 2018). In spite of all these challenges, the high-resolution measurements reported herein are instrumental in advancing the development of such models.

A. Additional experimental considerations

A.1. Repeatability of the experiments

In chapter 2, the repeatability has been shown for only two flow conditions with particle diameter. In this section, the results for the remaining flow conditions are shown.

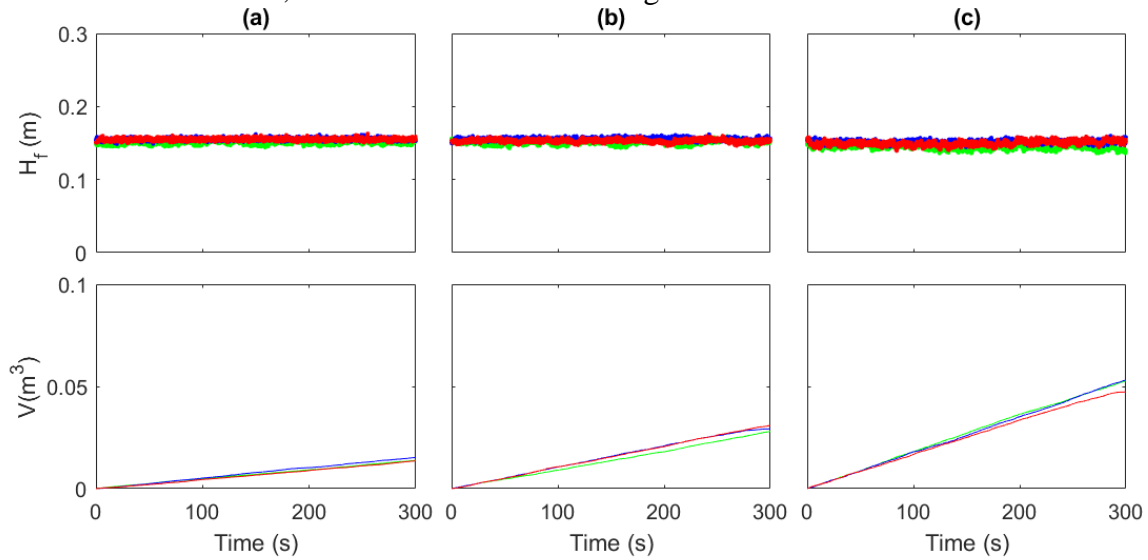


Figure A-1. Time evolution of flow depth and cumulative volume of transported sediments for dp3 (S03); for lower (LOW), intermediate (MED) and saturation (SAT) conditions.

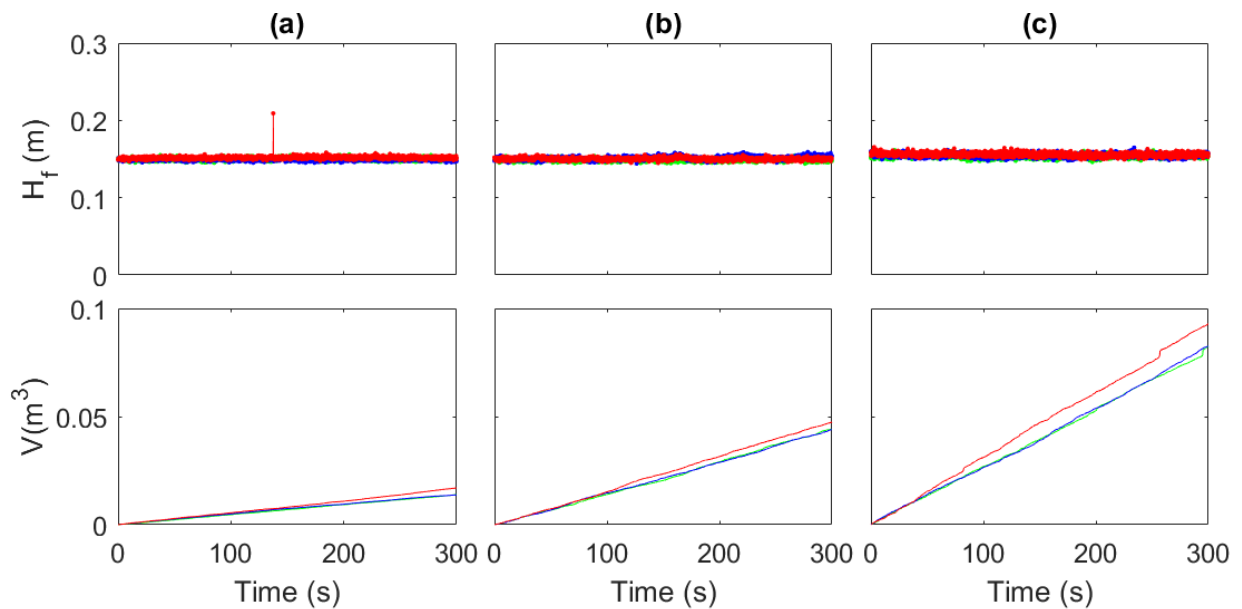


Figure A-2. Time evolution of flow depth and cumulative volume of transported sediments for dp3 (S05); for lower (LOW), intermediate (MED) and saturation (SAT) conditions.

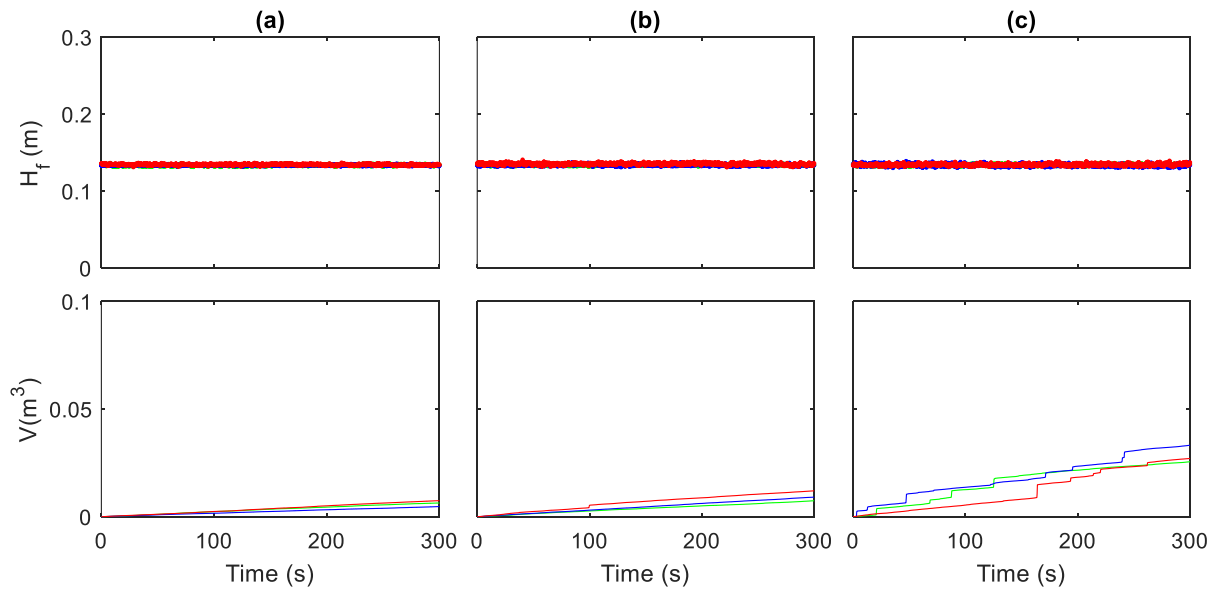


Figure A-3. Time evolution of flow depth and cumulative volume of transported sediments for dp1 (S04); for lower (LOW), intermediate (MED) and saturation (SAT) conditions.

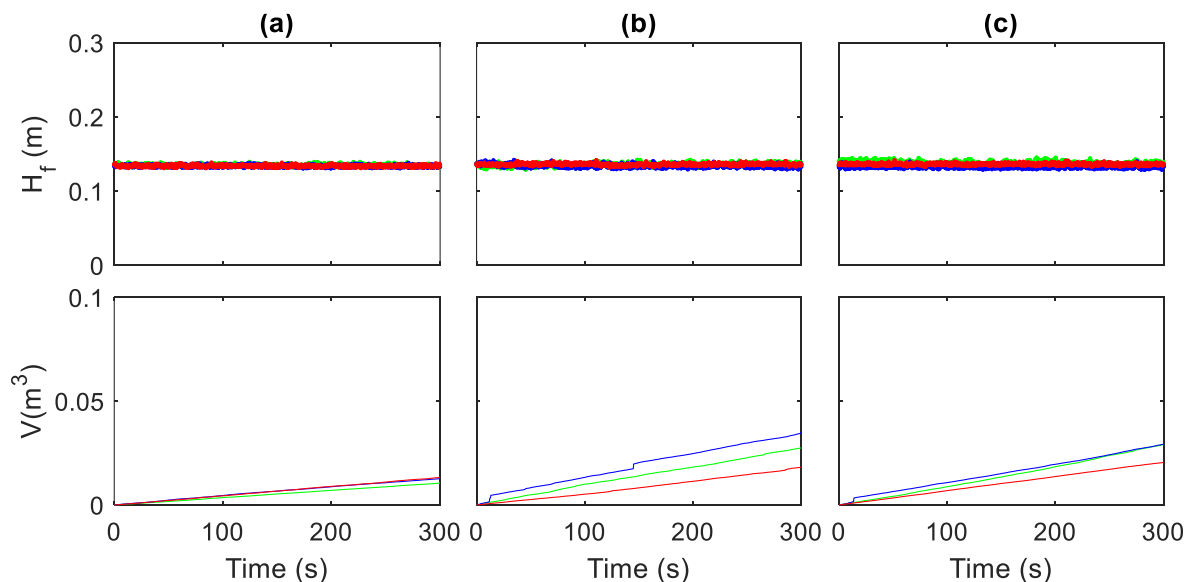


Figure A-4. Time evolution of flow depth and cumulative volume of transported sediments for dp1 (S06); for lower (LOW), intermediate (MED) and saturation (SAT) conditions.

A.2. Additional experimental runs

Two sets of runs were not presented in the detailed analysis, although they have been studied as well. It correspond to additional runs in capacity regimes for S03 and S05, presented in Table A-1 with superscript a. These runs have higher injected solid-loads compared to the selected ones. They were performed as an effort to ensure the approach to full capacity conditions. It seems that flow uniformity was slightly less established compared to the selected set of runs, particularly for S03. Nevertheless, the overall data quality is the same and may be important for studies concerning the bed-load processes. In both cases, the injected solid-load are about 30% higher than the selected runs. For S03, the selected runs have an injected solid-load $q_{\text{injected}} \approx 3.3 \times 10^{-4} \text{ m}^2/\text{s}$, whereas the additional runs P3S03D1_SAT, P3S03D2_SAT and

P3S03D3_SAT have $q_{s\text{injected}} \approx 4.4 \times 10^{-4} \text{ m}^2/\text{s}$. For S05, the selected runs have an injected solid-load $q_{s\text{injected}} = 4.7 \times 10^{-4} \text{ m}^2/\text{s}$, whereas the additional runs P3S05D6_SAT, P3S05D7_SAT and P3S05D9_SAT have $q_{s\text{injected}} = 6.2 \times 10^{-4} \text{ m}^2/\text{s}$. However, in terms of turbulent suspension properties, the information from these data is somehow redundant. This is confirmed by comparing the 6 runs (3 presented and 3 additional), in terms of mean profiles of velocity, concentration and Reynolds shear stress in Figure A-5. The presented runs and the referred additional experiments are represented in green and red, respectively. The mean profiles are rather similar, with some minor deviations from the linear trend of Reynolds shear stress with the higher solid-load. Additionally, the water levels variations (not shown here) were slightly more pronounced, although it remained generally stable indicating steady flow conditions.

To summarize, there are 6 additional runs for dp_3 , with $\theta = 0.35$ and $\theta = 0.5$ saturated regimes, with solid-loads 30% higher compared to the presented runs. These seems to have slightly less stable and uniform conditions, but they have similar quality as the presented runs. They were used to confirm all trends of the main processes evaluated but they are not presented in the main results because it would be redundant. For detail analysis of bed-load processes however, it may be interesting to have greater focus in these runs, since they have greater solid-loads and concentration in the near-bed region.

Table A-1. Flow conditions including the addition experimental runs. Symbols as in *Table 2-1*.

u_* (m/s)	θ (-)	S (-)	Q (m^3/s)	S_0 (-)	U (m/s)	H_f (m)	q_s (m^2/s)	Runs
0.043	0.35	1.3	0.032	0.0023	0.60	0.15	0.0	8 CW runs
							6×10^{-5}	P3S03D4_LOW, P3S03D5_LOW, P3S03D6_LOW
							2×10^{-4}	P3S03D4_MED, P3S03D7_MED, P3S03D8_MED
							3.3×10^{-4}	P3S03D9_SAT, P3S03D10_SAT, P3S03D11_SAT
							4.4×10^{-4}	P3S03D1_SAT ^a , P3S03D2_SAT ^a , P3S03D3_SAT ^a
0.056	0.55	1.0	0.041	0.0040	0.79	0.15	0.0	6 CW runs
							7×10^{-5}	P3S05D1_LOW, P3S05D2_LOW, P3S05D8_LOW
							2×10^{-4}	P3S05D1_MED, P3S05D2_MED, P3S05D8_MED
							4.5×10^{-4}	P3S05D6_SAT, P3S05D7_SAT, P3S05D9_SAT
							6.2×10^{-4}	P3S05D3_SAT ^a , P3S05D3_SAT ^a , P3S05D3_SAT ^a

^a indicates the additional experimental runs that were also studied but not presented in the detailed discussions of turbulent transport processes.

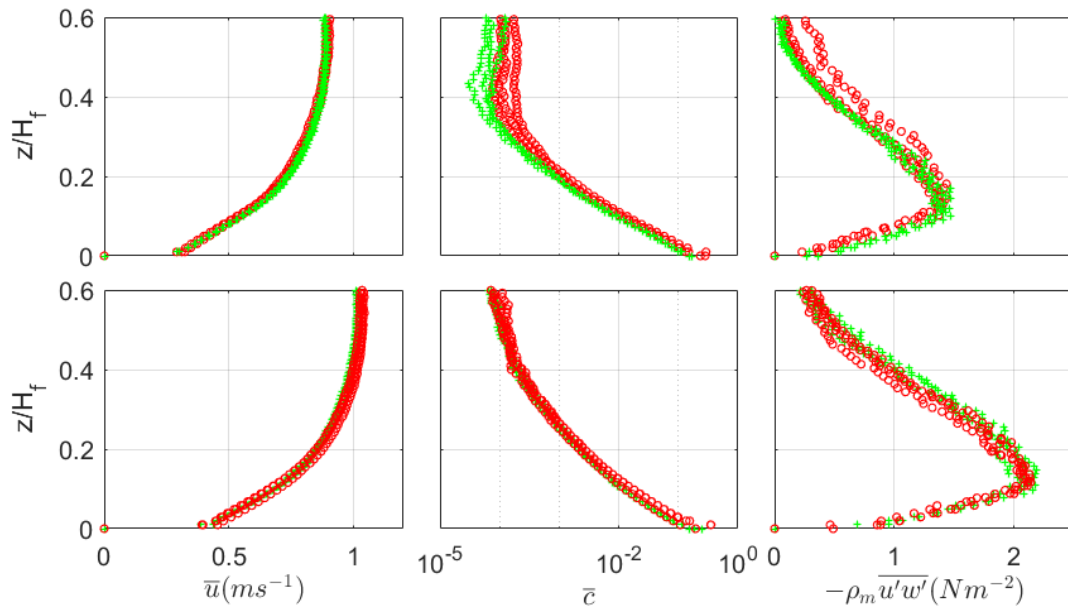


Figure A-5. Comparison between the selected runs in saturation and the addition runs for S03 (top) and S05 (bottom).

Finally, some additional runs in lower transport capacity were not considered for the analysis, simply because it was considered that three runs per solid regime is enough for comprehensive analysis.

B. Mixing length for dp1

A strong result observed for dp3, in chapter 4, was that momentum mixing was significantly reduced due to the bed-load layer. In the near-bed region, the mixing length was quasi-constant and it increased linearly with z in the upper flow region $z/H_f > 0.1$. It can be seen in Figure B-1 that the turbulent mixing length estimated in the same way as that discussed in chapter 4 does not show the same feature, for dp1. It generally increases linearly with z from lower vertical elevations $z/H_f > 0.04 - 0.05$, even in saturation. This further confirms the bed-load effects discussed in chapters 4.

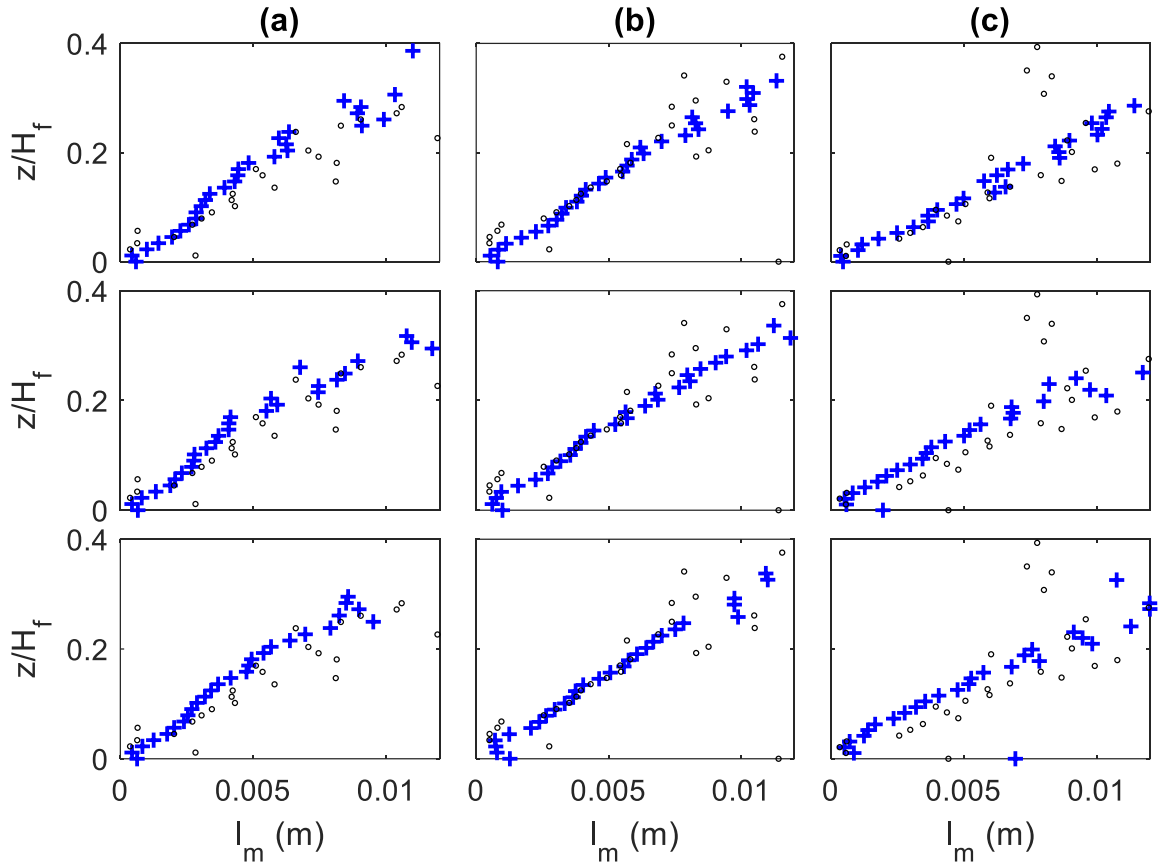


Figure B-1. Mixing length $l_m = u_*^2/(du/dz)$; for $\theta \approx 0.4$ (a), $\theta \approx 0.9$ (b) and $\theta \approx 1.2$ (c); for lower concentration (bottom), intermediate (middle) and saturated (top). Blue (+) is for sediment-laden and black (o) is for clear-water.

C. Pick-up functions and reference concentration

Several relations for the pick-up function and reference concentration have been proposed in the literature. Herein, some of them have been tested against the present dataset, only in saturation conditions. Fenandez Luque (1974) presented the following relationship:

$$E = \alpha[(s-1)gd_{50}]^{0.5}(\theta - \theta_{cr})^{1.5} \quad (C.3)$$

with $\alpha = 0.02$. Another relationship based on the Shields number θ is that of Nakagawa and Tsujimoto (1980):

$$E = \alpha[(s-1)gd_{50}]^{0.5} \left(1 - \frac{0.035}{\theta}\right)^3 \theta \quad (C.4)$$

where $\alpha = 0.02$. Based on his own experiments, van Rijn (1984a) obtained the following formula:

$$E = 0.00033\rho_s[(s-1)gd_{50}]^{0.5}D_*^{0.3}T^{1.5} \quad (C.5)$$

where

$$T = \left(\frac{\theta}{\theta_c} - 1\right) \text{ and } D_* = d_{50} \left[\frac{(s-1)g}{v^2}\right]^{1/3}$$

van Rijn (1993) mentioned the functions of Fenandez Luque (1974) and Nakagawa and Tsujimoto (1980) as those that provided, overall, the best results. In addition to the pick-up

functions mentioned above, the following equation from Smith et al. (1977) for the reference concentration is cited by García (2008) as one of the most accurate formulae:

$$Ca = 0.65 \frac{\gamma_0 T}{1 + \gamma_0 T} \quad (\text{C.6})$$

where $\gamma_0 = 2.4 \times 10^{-3}$. Figure C-1 shows the measured reference concentration Ca and the predicted by the methods of Fenandez Luque (1974), Smith et al. (1977) and Nakagawa and Tsujimoto (1980). They are evaluated at the edge of the bed-load layer.

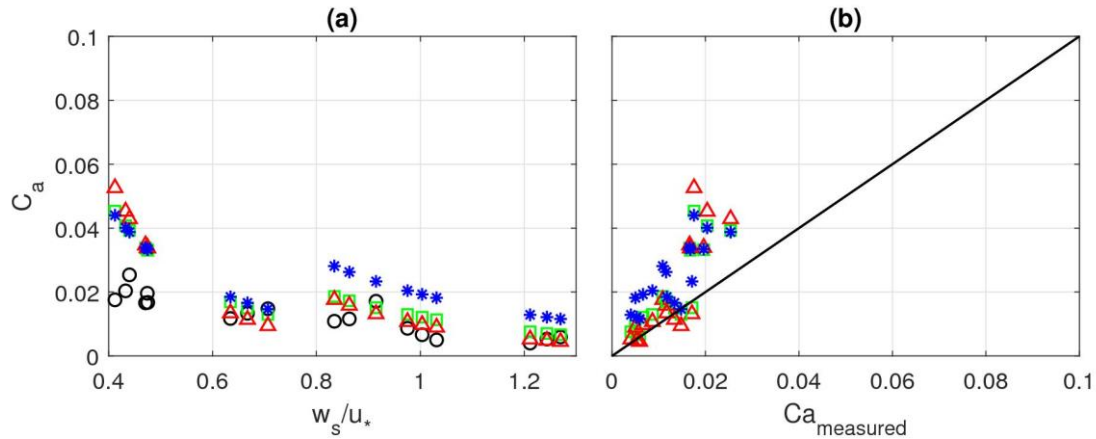


Figure C-1. Reference concentration Ca evolution with w_s/u_* (a); (o) measured in saturation, (Δ) Fenandez Luque (1974), (\square) Nakagawa and Tsujimoto (1980) and (*) Smith et al. (1977); In panel (b) the measured and calculated pick-up functions are compared

A good agreement between the measured reference concentration and the predictions from Fenandez Luque (1974) and Nakagawa and Tsujimoto (1980) is persistent, particularly in the range $0.6 < w_s/u_* < 1.3$. One possible explanation for the discrepancies at the range $w_s/u_* < 0.6$ may be that we are not at full capacity, even at maximum concentration. It is observed that the pick-up function from van Rijn (1984a) displays better results (see Figure C-2) when prescribed closer to $z/Hf \leq 2.5d_p$, and not necessarily at the edge of the bed-load layer. This seems consistent with the experimental determination of the pick-up function by this author. Note that similar discrepancy at $w_s/u_* < 0.6$ is observed, supporting that at these conditions the flow may not be in saturation. It must be noted that the visual verification of near capacity conditions for the small particle diameter experiments is much more difficult than for the large particle experiments particularly when the bed roughness is larger than the size of the injected particles.

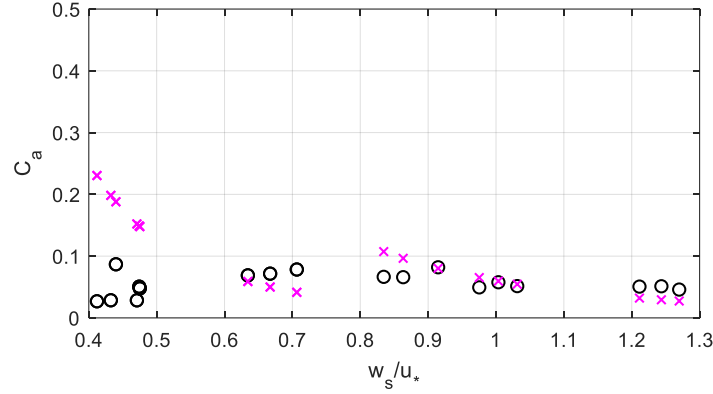


Figure C-2. Reference concentration based on (x) van Rijn (1984a)

D. A simple total solid flux based on the TKE budget results

We can derive a solid-transport equation based on the findings on the TKE budget. Specifically, the relationship between the depth-integrated stratification and turbulence production terms, respectively.

$$(s - 1)gw_s \int_0^{H_f} \bar{c} dz \approx 0.1 \int_0^{H_f} -\overline{u'w'} \frac{\partial \bar{u}}{\partial z} dz \quad (\text{D.7})$$

We can introduce some simplifications to the production term, such that

$$(s - 1)gw_s \int_0^{H_f} \bar{c} dz \approx 0.1K_1u_*^2 \int_0^{H_f} \bar{u} dz \quad (\text{D.8})$$

where $K_1 \approx 2.5$ is an empirical constant to account for the simplifications on the turbulence production term, as well as the shape effects on the velocity and concentration profiles. The relationship then becomes:

$$C_{TKE} = 0.1 \frac{K_1u_*^2U}{(s - 1)gw_s} \quad (\text{D.9})$$

where C_{TKE} and U are the depth-averaged concentration based on the TKE budget considerations and streamwise velocities, respectively. By multiplying the equation above to UH_f , we can give the equation for the total solid-load per meter of width:

$$q_{sTKE} = 0.1 \frac{K_1K_2u_*^2U^2H_f}{(s - 1)gw_s} \quad (\text{D.10})$$

The constant $K_2 \approx 1$ should account for shape effects of the velocity profile. Figure D-1 shows the application of Eq. (D.9) and Eq. (D.10) based on the present dataset and on measurements from Graf and Cellino (2002), Revil-Baudard et al. (2016) and Guta et al. (2019). It is seen that the relative error remains below $E < 75\%$ for most of the tested data. For the present experiments in the range $0.4 < w_s/u_* < 0.6$, this method largely overestimate the solid-load and depth-averaged concentration. It is believed that it may be explained by the fact that these experiments did not reach full transport capacity. This relationship should be further tested and eventually calibrated based on a large dataset. This is left for future work.

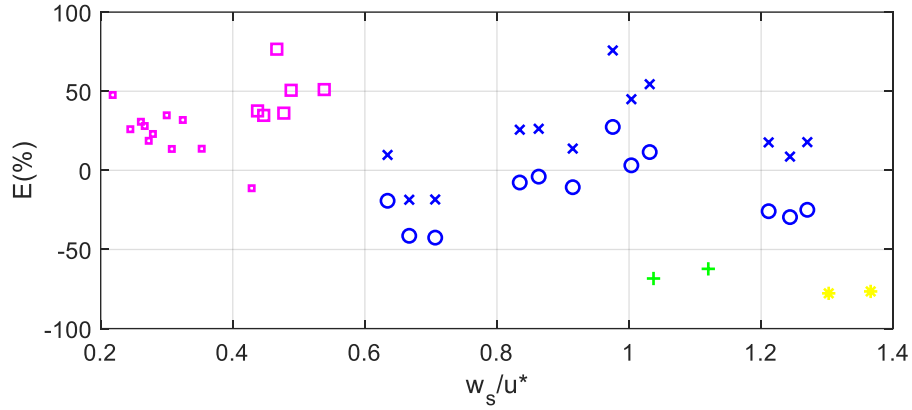


Figure D-1. Relative error of the estimated depth-averaged concentration based on the dataset from Graf and Cellino (2002) (\square) and total solid-load per meter of width, based on the present dataset (\times), Revil-Baudard et al. (2016) ($+$) and Guta et al. (2019) ($*$).

E. Constants of $k - \varepsilon$ model

This Appendix section presents some of the quantities that were discussed in section 5.4.4. These are the σ_K and $c_{2\varepsilon}$, in the equations for k and ε , respectively.

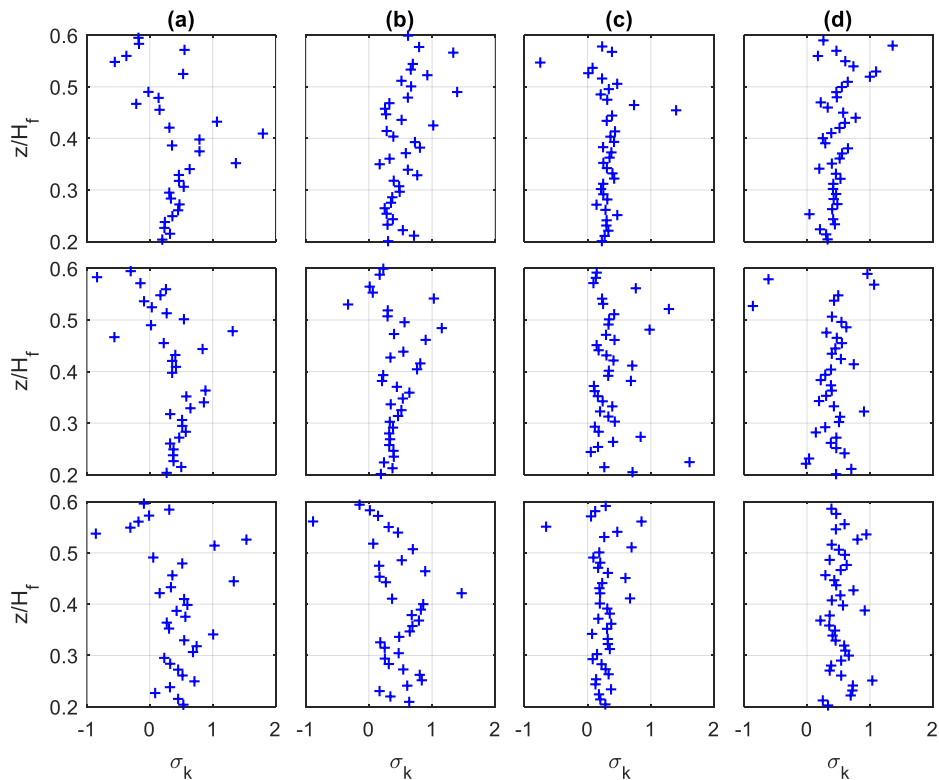


Figure E-1. Values of the ratio $\sigma_K = \overline{k'w'}/(dk/dz)$; For dp1 ($\theta \approx 0.4$ (a)), $\theta \approx 1.2$ (b)) and dp3 ($\theta \approx 0.35$ (c), $\theta \approx 0.8$ (d)) for lower concentration (bottom), intermediate (middle) and saturated (top).

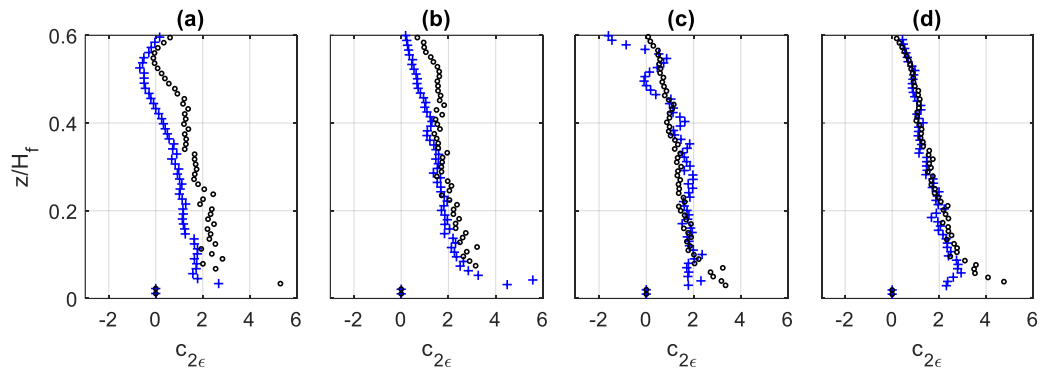


Figure E-2. Values of the constant $c_{2\varepsilon}$; for SL in capacity (+) and their respective CW runs (o) that lead to values of c_μ as in Eq. (5-7); for dp1 ($\theta \approx 0.4$ (a), $\theta \approx 1.2$ (b)) and dp3 ($\theta \approx 0.35$ (c), $\theta \approx 0.8$ (d))

References

- van der A, Dominic A., Joep van der Zanden, Tom O'Donoghue, David Hurther, Iván Cáceres, Stuart J. McLelland, and Jan S. Ribberink. 2017. "Large-Scale Laboratory Study of Breaking Wave Hydrodynamics over a Fixed Bar." *J. Geophys. Res. Ocean.* 122(4):3287–3310. doi: 10.1002/2016JC012072.
- Ackers, P., and WR. White. 1973. "Sediment Transport: New Approach and Analysis." *J. Hydraul. Div.* 99(11):2041–60.
- Antoine, G., B. Camenen, M. Jodeau, J. Némery, and M. Esteves. 2020. "Downstream Erosion and Deposition Dynamics of Fine Suspended Sediments Due to Dam Flushing." *J. Hydrol.* 585:1–35. doi: 10.1016/j.jhydrol.2020.124763.
- Ashida, A., and M. Fujita. 1986. *Mechanism of Particle Suspension in an Open Channel.*
- Bagnold, A. .. 1966. *An Approach to the Sediment Transport Problem From General Physics.* Washington, DC.
- Bagnold, R. A. 1956. "The Flow of Cohesionless Grains in Fluids." *Philos. Trans. R. Soc. London. Ser. A, Math. Phys. Sci.* 249(964):235–97. doi: 10.1098/rsta.1956.0020.
- Balachandar, S. 2009. "A Scaling Analysis for Point-Particle Approaches to Turbulent Multiphase Flows." *Int. J. Multiph. Flow* 35(9):801–10. doi: 10.1016/j.ijmultiphaseflow.2009.02.013.
- Barton, J., and N. Lin. 1955. *A Study of the Sediment Transport in Alluvial Streams.*
- Barton, J. R., and P. NA study of the sed Lin. 1955. "iment Transport in Alluvial Streams." *Color. A&M Coll. Fort Colins, USA, CO, Rep. 55JRB2.*
- Blanckaert, Koen, Joris Heyman, and Colin D. Rennie. 2017. "Measuring Bedload Sediment Transport with an Acoustic Doppler Velocity Profiler." *J. Hydraul. Eng.* 143(6):04017008. doi: 10.1061/(asce)hy.1943-7900.0001293.
- Blanckaert, Koen, and Ulrich Lemmin. 2006. "Means of Noise Reduction in Acoustic Turbulence Measurements." *J. Hydraul. Res.* 44(1):3–17. doi: 10.1080/00221686.2006.9521657.
- Blanckaert, Koen, and H. J. de Vriend. 2005. "Turbulence Characteristics in Sharp Open-Channel Bends." *Phys. Fluids* 17(5):1–15. doi: 10.1063/1.1886726.
- Boujia, Nissrine. 2018. "Vulnérabilité Des Ouvrages d ' Art Au Risque d ' Affouillement Des Fondations." l'Université Paris-Est.
- Bradshaw, P. 1971. "An Introduction to Turbulence and Its Measurement: Thermodynamics and Fluid Mechanics Series." 238.
- Brooks, H. 1954. "Laboratory Studies of the Mechanics of Streams Flowing over a Movable Bed of Fine Sand." California Institute of Technology.
- Camenen, Benoît. 2007. "Simple and General Formula for the Settling Velocity of Particles." *J. Hydraul. Eng.* 133(2):229–33. doi: 10.1061/(ASCE)0733-9429(2007)133:2(229).
- Camenen, Benoît, Atilla Bayram, and Magnus Larson. 2006. "Equivalent Roughness Height for Plane Bed under Steady Flow." *J. Hydraul. Eng.* 132(11). doi: 10.1061/(asce)0733-9429(2006)132:11(1146).
- Cao, Zhixian. 1999. "Equilibrium Near-Bed Concentration of Suspended Sediment."

(December):1270–78.

- Caulfield, Colm Cille P. 2020. “Open Questions in Turbulent Stratified Mixing: Do We Even Know What We Do Not Know.” *Phys. Rev. Fluids* 5(11):110518. doi: 10.1103/PhysRevFluids.5.110518.
- Cellino, M., and W. H. Graf. 1999. “Sediment-Laden Flow in Open-Channels under Noncapacity and Capacity Conditions.” *J. Hydraul. Eng.* 125(5):455–62.
- Cellino, M., and U. Lemmin. 2004. “Influence of Coherent Flow Structures on the Dynamics of Suspended Sediment Transport in Open-Channel Flow.” *J. Hydraul. Eng.* 130(11):1077–88. doi: 10.1061/(asce)0733-9429(2004)130:11(1077).
- Cerema. 2019. *Analyse de Risque Des Ponts En Site Affouillable*.
- Chadwick, Andrew, John Morfett, and Martin Borthwick. 2013. *Hydraulics in Civil and Environmental Engineering*.
- Chanson, Hubert. 2004. *Hydraulics of Open Channel Flow: An Introduction*. Elsevier.
- Chassagneux, François Xavier, and David Hurther. 2014. “Wave Bottom Boundary Layer Processes below Irregular Surfzone Breaking Waves with Light-Weight Sheet Flow Particle Transport.” *J. Geophys. Res. Ocean.* 119(3):1668–90. doi: 10.1002/2013JC009338.
- Chauchat, J., D. Hurther, T. Revil-Baudard, Z. Cheng, and T. J. Hsu. 2022. “Controversial Turbulent Schmidt Number Value in Particle-Laden Boundary Layer Flows.” *Phys. Rev. Fluids* 7(1):1–16. doi: 10.1103/PhysRevFluids.7.014307.
- Chauchat, Julien, Zhen Cheng, Tim Nagel, Cyrille Bonamy, and Tian Jian Hsu. 2017. “SedFoam-2.0: A 3-D Two-Phase Flow Numerical Model for Sediment Transport.” *Geosci. Model Dev.* 10(12):4367–92. doi: 10.5194/gmd-10-4367-2017.
- Cheng, Zhen, Tian Jian Hsu, and Julien Chauchat. 2018. “An Eulerian Two-Phase Model for Steady Sheet Flow Using Large-Eddy Simulation Methodology.” *Adv. Water Resour.* 111. doi: 10.1016/j.advwatres.2017.11.016.
- Chow, V. T. 1959. *Open Channel Hydraulics*.
- Coleman, N. L. 1970. “Flume Studies of the Sediment Translet Coefficient.” *Water Resour. Res.* 6(3):801–9.
- Coleman, N. L. 1981. “Velocity Profiles With Suspended Sediment.” *J. Hydraul. Res.* 22(4):263–89. doi: 10.1080/00221688409499383.
- Cunge, J. .., F. .. Holly, and A. .. Verwey. 1980. *Practical Aspects of Computational River Hydraulics*. London: Pitman.
- Dey, Subhasisch. 2014. *Fluvial Hydrodynamics*. Springer.
- Dey, Subhasisch, and Ratul Das. 2012. “Gravel-Bed Hydrodynamics: Double-Averaging Approach.” *J. Hydraul. Eng.* 138(8):707–25. doi: 10.1061/(asce)hy.1943-7900.0000554.
- Egiazaroff, J. 1965. “Calculation of Non-Uniform Sediment Concentrations.” *J. Hydraul. Div.* 91(4):225–47.
- Einstein, H. A. 1950. *The Bed-Load Function for Sediment Transportation in Open Channel Flows*.
- Einstein, H. A., and N. Chien. 1955. *Effects of Heavy Sediment Concentration near the Bed on the Velocity and Sediment Distribution*. Berkeley, California.

- Einstein, Hans Albert. 1955. "Effect of Heavy Sediment Concentration near the Bed on Velocity and Sediment Distribution." *Univ. California, Berkeley, Calif.* 33:2.
- Elghobashi, S. 1994. "On Predicting Particle-Laden Turbulent Flows." *Appl. Sci. Res.* 52(4):309–29. doi: 10.1007/BF00936835.
- Engelund, F., and E. Hansen. 1967. *A Monograph on Sediment Transport in Alluvial Streams*. Copenhagen: Teknisk Forlag.
- Fenandez Luque, R. 1974. "Erosion and Transport of Bed-Load Sediment." TU Delft.
- Finn, Justin R., and Ming Li. 2016. "Regimes of Sediment-Turbulence Interaction and Guidelines for Simulating the Multiphase Bottom Boundary Layer." *Int. J. Multiph. Flow* 85:278–83. doi: 10.1016/j.ijmultiphaseflow.2016.06.007.
- Fromant, G., R. S. Mieras, T. Revil-Baudard, J. A. Puleo, D. Hurther, and J. Chauchat. 2018. "On Bedload and Suspended Load Measurement Performances in Sheet Flows Using Acoustic and Conductivity Profilers." *J. Geophys. Res. Earth Surf.* 123(10):2546–62. doi: 10.1029/2017JF004560.
- Fromant, Guillaume, David Hurther, Joep Van der Zanden, D. A. Van Der A, I. Caceres, Tom O'Donoghue, and J. S. Ribberink. 2019. "Wave Boundary Layer Hydrodynamics and Sheet Flow Properties under Large-scale Plunging-type Breaking Waves." *J. Geophys. Res. Ocean.* 124(1):75–98.
- Garbini, Joseph L., Fred K. Forster, and Jens E. Jorgensen. 1982. "Measurement of Fluid Turbulence Based on Pulsed Ultrasound Techniques. Part 1. Analysis." *J. Fluid Mech.* 118. doi: 10.1017/S0022112082001153.
- García, Marcelo H. 2008. "Sediment Transport and Morphodynamics." Pp. 21–163 in *ASCE Manuals and Reports on Engineering Practice*. Vol. 110.
- Garcia, Marcelo, and Gary Parker. 1991. "Entrainment of Bed Sediment into Suspension." *J. Hydraul. Eng.* 117(4):414–35. doi: 10.1061/(ASCE)0733-9429(1991)117:4(414).
- Graf, W., and M. Altinakar. 1998. *Fluvial Hydraulics Flow and Transport Processes in Channels of Simple Geometry*.
- Graf, W. H. 1984. *Hydraulics of Sediment Transport*. Water Resources Publications, Fort Collins, CO.
- Graf, W. H., and M. Cellino. 2002. "Suspension Flows in Open Channels; Experimental Study." *J. Hydraul. Res.* 40(4):435–48. doi: 10.1080/00221680209499886.
- Grass, A. J. 1971. "Structural Features of Turbulent Flow over Smooth and Rough Boundaries." *J. Fluid Mech.* 50(2):233–55. doi: 10.1017/S0022112071002556.
- Guo, Junke, and Pierre Y. Julien. 2001. "Turbulent Velocity Profiles in Sediment-Laden Flows." *J. Hydraul. Res.* 39(1):11–23. doi: 10.1080/00221680109499798.
- Guta, H., M. Burckbuchler, S. Fischer, and D. Dufour. 2019. "Suspended Sediment Concentration and Sediment Transport Measurements with a New Two Components Ultrasonic Profiler." in *15 th International Conference on Fluid Control, Measurements and Visualization*. Naples, Italy.
- Guta, H., D. Hurther, and J. Chauchat. 2022. "Bed-Load and Concentration Effects on Turbulent Suspension Properties in Heavy Particle Sheet-Flows." *J. Hydraul. Eng.* doi: 10.1061/(ASCE)HY.1943-7900.0001988.
- Gyr, A. 1983. "Discussion: Towards a Better Definition of the Three Types of Sediment

- Transport.” *J. Hydraul. Res.* 21(5):389. doi: 10.1080/00221688309499460.
- Hager, Willi H., Anton J. Schleiss, Robert M. Boes, and Michael Pfister. 2020. “Hydraulic Engineering of Dams.” *Hydraul. Eng. Dams.* doi: 10.1201/9780203771433.
- Henderson, F. M. 1966. *Open Channel Flow*. edited by U. MacMillan Company: New York.
- Hsu, T., J. Jenkins, and P. Liu. 2004. “On Two-Phase Sediment Transport: Sheet Flow of Massive Particles.” *Proc. R. Soc. A Math. Phys. Eng. Sci.* 460(2048):2223–50. doi: 10.1098/rspa.2003.1273.
- Hsu, Tian Jian, James T. Jenkins, and Philip L. F. Liu. 2003. “On Two-Phase Sediment Transport: Dilute Flow.” *J. Geophys. Res. Ocean.* 108(3). doi: 10.1029/2001jc001276.
- Hurther, D., and U. Lemmin. 2001. “A Correction Method for Turbulence Measurements with a 3D Acoustic Doppler Velocity Profiler.” *J. Atmos. Ocean. Technol.* 18(3):446–58. doi: 10.1175/1520-0426(2001)018<0446:ACMFTM>2.0.CO;2.
- Hurther, D., and U. Lemmin. 2003. “Turbulent Particle Flux and Momentum Flux Statistics in Suspension Flow.” *Water Resour. Res.* 39(5):1–11. doi: 10.1029/2001WR001113.
- Hurther, D., U. Lemmin, and E. A. Terray. 2007. “Turbulent Transport in the Outer Region of Rough-Wall Open-Channel Flows: The Contribution of Large Coherent Shear Stress Structures (LC3S).” *J. Fluid Mech.* 574:465–93. doi: 10.1017/S0022112006004216.
- Hurther, D., P. Thorne, M. Bricault, U. Lemmin, and J. Barnoud. 2011. “A Multi-Frequency Acoustic Concentration and Velocity Profiler (ACVP) for Boundary Layer Measurements of Fine-Scale Flow and Sediment Transport Processes.” *Coast. Eng.* 58(7):594–605. doi: 10.1016/j.coastaleng.2011.01.006.
- Hurther, D., and Peter D. Thorne. 2011. “Suspension and Near-Bed Load Sediment Transport Processes above a Migrating, Sand-Rippled Bed under Shoaling Waves.” *J. Geophys. Res. Ocean.* 116(C7):7001. doi: 10.1029/2010JC006774.
- Jodeau, Magali, Sabine Chamoun, Jiawei Feng, Giovanni De Cesare, and Anton J. Schleiss. 2018. “Numerical Modeling of Turbidity Currents with Ansys CFX and Telemac 3D.” *E3S Web Conf.* 40:1–8. doi: 10.1051/e3sconf/20184003014.
- Julien, Pierre Y. 2018. *River Mechanics*. Cambridge University Press.
- Kironoto, B., and W. H. Graf. 1994. “Turbulence Characteristics in Rough Uniform Open-Channel.” *Proc. Inst. Civ. Eng. Water, Marit. Energy* 106(Dec):333–44.
- Krogstad, P. Å., and R. A. Antonia. 1999. “Surface Roughness Effects in Turbulent Boundary Layers.” *Exp. Fluids* 27(5):450–60. doi: 10.1007/s003480050370.
- Kundu, Pijush K., and Ira M. Cohen. 1990. *Fluid Mechanics*. Fourth Edi. Elsevier.
- Laufer, John. 1954. “The Structure of Turbulence in Fully Developed Pipe Flow.” *Naca Tr 1174* 417–34.
- Lemmin, Ulrich, and Thierry Rolland. 1997. “Acoustic Velocity Profiler for Laboratory and Field Studies.” *J. Hydraul. Eng.* 123(12):1089–98. doi: 10.1061/(ASCE)0733-9429(1997)123:12(1089).
- Lu, S. S., and W. W. Willmarth. 1973. “Measurements of the Structure of the Reynolds Stress in a Turbulent Boundary Layer.” *J. Fluid Mech.* 60(3):481–511. doi: 10.1017/S0022112073000315.
- Lumley, J. L. 1976. “Two-Phase and Non-Newtonian Flows.” *Turbul. Bradshaw, P. (Ed.), Fed.*

- Rep. Ger. Springer-Verlag Berlin Heidelberg, 1976* 12):289–324. doi: 10.1007/978-3-662-22568-4_7.
- Lyn, D. A. 1986. “Turbulence and Turbulent Transport in Sediment-Laden Open-Channel Flows.” (Report No. KH-R-49):1–264.
- Lyn, D. A. 1988. “A Similarity Approach to Turbulent Sediment-Laden Flows in Open Channels.” *J. Fluid Mech.* 193:1–26. doi: 10.1017/S0022112088002034.
- Lyn, D. A. 1991. “Resistance in Flat-Bed Sediment-Laden Flows.” *J. Hydraul. Eng.* 117(1):94–115. doi: 10.1061/(ASCE)0733-9429(1992)118:4(663.2).
- Lyn, D. A. 2008. “Turbulence Models for Sediment Transport Engineering.” *Sediment. Eng.* 763–825. doi: 10.1061/9780784408148.ch16.
- Mathieu, Antoine, Julien Chauchat, Cyrille Bonamy, Guillaume Balarac, and Tian Jian Hsu. 2021. “A Finite-Size Correction Model for Two-Fluid Large-Eddy Simulation of Particle-Laden Boundary Layer Flow.” *J. Fluid Mech.* 913:1–31. doi: 10.1017/jfm.2021.4.
- Mignot, Emmanuel, D. Hurther, and E. Barthelemy. 2009. “On the Structure of Shear Stress and Turbulent Kinetic Energy Flux across the Roughness Layer of a Gravel-Bed Channel Flow.” *J. Fluid Mech.* 638:423–52. doi: 10.1017/S0022112009990772.
- Monin, A. S., and A. M. Yaglom. 1971. *Monin A. S. & A. M. Yaglom : Statistical Fluid Mechanics : Mechanics of Turbulence – Vol 1* ». Vol. Volume 1. edited by T. M. Press.
- Monin, A. S., and A. M. Yaglom. 1975. “Statistical Fluid Mechanics: Mechanics of Turbulence, Vol. 2, 874 Pp.”
- Muste, M., K. Yu, I. Fujita, and R. Ettema. 2005. “Two-Phase versus Mixed-Flow Perspective on Suspended Sediment Transport in Turbulent Channel Flows.” *Water Resour. Res.* 41(10). doi: 10.1029/2004WR003595.
- Nakagawa, H., and T. Tsujimoto. 1980. “Sand Bed Instability Due to Bed Load Motion.” *J. Hydraul. Div.* 106(12):2029–51.
- Nakagawa, Hiroji, and Iehisa Nezu. 1977. “Prediction of the Contributions to the Reynolds Stress from Bursting Events in Open-Channel Flows.” *J. Fluid Mech.* 80(1):99–128. doi: 10.1017/S0022112077001554.
- Naqshband, S., J. S. Ribberink, D. Hurther, P. A. Barraud, and S. J. M. H. Hulscher. 2014. “Experimental Evidence for Turbulent Sediment Flux Constituting a Large Portion of the Total Sediment Flux along Migrating Sand Dunes.” *Geophys. Res. Lett.* 41(24):8870–78. doi: 10.1002/2014GL062322.
- Nezu, I., and H. Nakagawa. 1993. *Turbulence in Open Channel Flows*. A. A. Balkema, Rotterdam.
- Nezu, Iehisa, and Wolfgang Rodi. 1986. “Open-channel Flow Measurements with a Laser Doppler Anemometer.” *J. Hydraul. Eng.* 112(5):335–55. doi: 10.1061/(asce)0733-9429(1986)112:5(335).
- Nikora, Vladimir I., and Derek G. Goring. 2002. “Fluctuations of Suspended Sediment Concentration and Turbulent Sediment Fluxes in an Open-Channel Flow.” *J. Hydraul. Eng.* 128(2):214–24. doi: 10.1061/(asce)0733-9429(2002)128:2(214).
- Nnadi, F., and K. Wilson. 1997. “Nnadi & Wilson Bed1997 -Bed-Load Motion at High Shear Stress.Pdf.” *J. Hydraul. Eng.* 123(4).
- Osborn, T. 1980. “Estimates of the Local Rate of Vertical Diffusion from Dissipation

- Measurements.” *J. Phys. Oceanogr.* 10:83–89.
- Parker, G., P. .. Kilington, and D. .. McLean. 1982. “Bed Load and Size Distribution in Paved Gravel Bed Streams.” *J. Hydraul. Div.* 108(4):544–71.
- Parker, Gary. 2008. “Transport of Gravel and Sediment Mixtures.” *Sediment. Eng.* 165–251. doi: 10.1061/9780784408148.ch03.
- Pope, Stephen B. 2000. *Turbulent Flows*. Vol. 13. Cambridge University Press.
- Raudkivi, A. J. 1998. *Loose Boundary Hydraulics*. 4th Ed. Rotterdam: Balkema.
- Raupach, M. R. 1981. “Conditional Statistics of Reynolds Stress in Rough-Wall and Smooth-Wall Turbulent Boundary Layers.” *J. Fluid Mech.* 108:363–82. doi: 10.1017/S0022112081002164.
- Raus, David, Frédéric Yann Moulin, and Olivier Eiff. 2019. “The Impact of Coarse-Grain Protrusion on Near-Bed Hydrodynamics.” *J. Geophys. Res. Earth Surf.* 124(7):1854–77. doi: 10.1029/2018JF004751.
- Recking, A., P. Frey, A. Paquier, P. Belleudy, and J. Y. Champagne. 2008. “Feedback between Bed Load Transport and Flow Resistance in Gravel and Cobble Bed Rivers.” *Water Resour. Res.* 44(5). doi: 10.1029/2007WR006219.
- Revil-Baudard, T., J. Chauchat, D. Hurther, and P. Barraud. 2015. “Investigation of Sheet-Flow Processes Based on Novel Acoustic High-Resolution Velocity and Concentration Measurements.” *J. Fluid Mech.* 767:1–30. doi: 10.1017/jfm.2015.23.
- Revil-Baudard, T., J. Chauchat, D. Hurther, and O. Eiff. 2016. “Turbulence Modifications Induced by the Bed Mobility in Intense Sediment-Laden Flows.” *J. Fluid Mech.* 808:469–84. doi: 10.1017/jfm.2016.671.
- Revil-baudard, Thibaud. 2015. “Experimental Study and Modelling of the Sediment Transport in Sheet-Flow Regime.”
- Ribberink, Jan, Jebbe van der Werf, Thomas O’Donoghue, and Wael Hassan. 2008. “Sand Motion Induced by Oscillatory Flows: Sheet Flow and Vortex Ripples.” *J. Turbul.* 9:20. doi: 10.1080/14685240802220009.
- Rickenmann, Dieter. 1991. “Hyperconcentrated Flow and Sediment Transport at Steep Slopes.” *J. Hydraul. Eng.* 117(11):1419–39.
- van Rijn, L. 1984a. “Sediment Pick-Up Functions.” *J. Hydraul. Eng.* 110(10):1494–1502.
- van Rijn, L. 1984b. “Sediment Transport, Part I: Bed Load Transport.” *J. Hydraul. Eng.* 110(10):1431–56.
- van Rijn, L. 1984c. “Sediment Transport: Part II.” *J. Hydraul. Eng.* 110(11):8–9.
- van Rijn, L. 1993. *Principles of Sediment Transport in Rivers, Estuaries and Coastal Seas*. Vol. 1006. Aqua publications Amsterdam.
- Rodi, Wolfgang. 1993. *Turbulence Models and Their Application in Hydraulics: A State of the Art Review*.
- Rodi, Wolfgang. 2017. “Turbulence Modeling and Simulation in Hydraulics: A Historical Review.” *J. Hydraul. Eng.* 143(5):03117001. doi: 10.1061/(asce)hy.1943-7900.0001288.
- Ronco, Paolo, Giacomo Fasolato, Michael Nones, and Giampaolo Di Silvio. 2010. “Morphological Effects of Damming on Lower Zambezi River.” *Geomorphology* 115(1–2):43–55. doi: 10.1016/J.GEOMORPH.2009.09.029.

- Rouse, Hunter. 1938. "Experiments on the Mechanics of Sediment Suspension." Pp. 550–54 in *5th Int. Congress of Applied Mech.*
- Schleiss, Anton J., Mário J. Franca, Carmelo Juez, and Giovanni De Cesare. 2016. "Reservoir Sedimentation." <https://doi.org/10.1080/00221686.2016.1225320> 54(6):595–614. doi: 10.1080/00221686.2016.1225320.
- Schlichting, Hermann, and Klaus Gersten. 1988. *Boundary-Layer Theory*.
- Sechet, P., and B. Le Guennec. 1999. "Bursting Phenomenon and Incipient Motion of Solid Particles in Bed-Load Transport Bursting Phenomenon and Incipient Motion of Solid Particles in Bed-Load Transport." *J. Hydraul. Res.* 37.
- Smith, J. Dungan, and S. R. McLean. 1977. "Spatially Averaged Flow over a Wavy Surface." *J. Geophys. Res.* 82(12):1735–46. doi: 10.1029/1999jc900116.
- Sumer, B. M., A. Kozakiewicz, J. Fredsøe, and R. Deigaard. 1996. "Velocity and Concentration Profiles in Sheet-Flow Layer of Movable Bed." *J. Hydraul. Eng.* 122(10):549–58. doi: 10.1061/(asce)0733-9429(1996)122:10(549).
- Sumer, B. Mutlu, and Rolf Deigaard. 1981. "Particle Motions near the Bottom in Turbulent Flow in an Open Channel. Part 2." *J. Fluid Mech.* 109(4):311–37. doi: 10.1017/S0022112081001092.
- Tardu, Sedat F. 2002. "Characteristics of Single and Multiple Bursting Events in the Inner Layer. Part 2. Level-Crossing Events." *Exp. Fluids* 33(5):640–52. doi: 10.1007/s00348-002-0482-z.
- Taricska, M. 2014. "An Analysis of Recent Bridge Failures (2000-2012)." Ohio State University.
- Tennekes, Henk, and John L. Lumley. 1972. *A First Course in Turbulence*.
- Thorne, Peter D., and Daniel M. Hanes. 2002. "A Review of Acoustic Measurement of Small-Scale Sediment Processes." *Cont. Shelf Res.* 22(4):603–32. doi: 10.1016/S0278-4343(01)00101-7.
- Thorne, Peter D., and David Hurther. 2014. "An Overview on the Use of Backscattered Sound for Measuring Suspended Particle Size and Concentration Profiles in Non-Cohesive Inorganic Sediment Transport Studies." *Cont. Shelf Res.* 73:97–118. doi: 10.1016/j.csr.2013.10.017.
- Townsend, A. A. 1976. *The Structure of Turbulent Shear Flow*.
- Vanoni, Vito A. 1946. "Transportation of Suspended Sediment by Water." *Trans. Am. Soc. Civ. Eng.* 111(1):67–102. doi: 10.1061/TACEAT.0005975.
- Vanoni, Vito A. 2006. "Sedimentation Engineering." *Sediment. Eng.* 1–418. doi: 10.1061/9780784408230.
- Voulgaris, George, and John Trowbridge. 1998. "Evaluation of the Acoustic Doppler Velocimeter (ADV) for Turbulence Measurements." *J. Atmos. Ocean. Technol.* 15:272–89. doi: 10.1175/1520-0426(1998).
- Wilcox, David C. 2006. "Turbulence Modeling for CFD (Third Edition)." *DCW Ind.* (1):2006.
- Wilson, K. 1987. "Analysis of Bed-Load Motion at High Shear Stress." *J. Hydraul. Eng.* 113(1):97–103.
- Wilson, K. 1989. "Mobile-Bed Friction at High Shear Stress." *J. Hydraul. Eng.* 115(6):825–

- Wu, W. ..., S. .. Wang, and Y. .. Jia. 2000. "Nonuniform Sediment Transport in Alluvial Rivers." *J. Hydraul. Res.* 38(6):427–34.
- Wu, Weiming, and Sam S. Y. Wang. 2006. "Formulas for Sediment Porosity and Settling Velocity." *J. Hydraul. Eng.* 132(8):858–62. doi: 10.1061/(ASCE)0733-9429(2006)132:8(858).
- van der Zanden, Joep, Dominic A. van der A, Iván Cáceres, David Hurther, Stuart J. McLelland, Jan S. Ribberink, and Tom O'Donoghue. 2018. "Near-Bed Turbulent Kinetic Energy Budget Under a Large-Scale Plunging Breaking Wave Over a Fixed Bar." *J. Geophys. Res. Ocean.* 123(2):1429–56. doi: 10.1002/2017JC013411.

List of Figures

Figure 1-1. Collapse of Wilson Bridge (Tours, France) in 1978 due to general scour; source: Cerema (2019).....	2
Figure 1-2. Proportion of suspended-load on the total solid-load versus the ratio u^*/ws (adapted from Julien 2018).....	11
Figure 1-3. Scheme of turbulent flow over smooth (a) and rough (b) beds (from Nezu and Nakagawa 1993).....	13
Figure 2-1. Sketch of experimental set up.....	19
Figure 2-2. Photo of the flume during a sediment-laden experimental run ($dp=3mm$)	20
Figure 2-3. Calibration of solid-load (with $dp=3mm$) as function of voltage on the conveyor belt system. The uncertainties in each measured are represented independently, with a minimum of 5% (for Voltage = 0.4 V) and a maximum of 9% (for Voltage = 1.5 V).....	21
Figure 2-4. Configuration of typical ADV systems. Adapted from Blanckaert and Lemmin (2006)	26
Figure 2-5. Example of bed detection based on mean profile echo intensity I (a) and mean streamwise velocity (b); for P1S08D5_CW. The convergence to zero velocity coincides with the sudden increase of the backscattered intensity at gate number 86, identified by the vertical solid line.	27
Figure 2-6. Comparison q_{SACVP} versus $q_{S_{injected}}$ Solid line is $X=Y$; for d_{p3} (blue, circle) and for d_{p1} (black, square).	29
Figure 2-7. Relative error of the solid-load measurements (in percentage); for $dp3$ (blue, circle) and $dp1$ (black, square) solid line is the mean value; dashed lines are the standard deviations.....	29
Figure 2-8. Time evolution of flow depth and cumulative volume of transported sediments for $dp3$ (S08); for lower (LOW), intermediate (MED) and saturation (SAT) conditions.....	30
Figure 2-9. Time evolution of flow depth and cumulative volume of transported sediments for $dp1$ (S10); for lower (LOW), intermediate (MED) and saturation (SAT) conditions.....	30
Figure 2-10. Comparison of noise correction methods applied for the signal of u' ; uncorrected(.), spectra based noise (-), Garbini method (--); for P3S08D5_CW. Black line represents the $-5/3$ slope; the white noise level was determined at $f \approx 25$ Hz.	33
Figure 2-11. Normalized turbulence intensities; uncorrected (u' (-) and w' (--)), spectra based correction (u' (\square) and w' (+)) Garbini method (u' (o) and w' (x)); for P3S08D5_CW	33
Figure 3-1. Mean velocity (a), concentration (b) and Reynolds shear stress (c) profiles for $dp3$; for the three repeated sediment-laden runs (o, \square and +); with increasing concentration from clear-water (bottom row) to saturation (top row); the three hydrodynamic forcing are distinguished by the magnitude of the measured profiles.	37
Figure 3-2. Mean velocity (a), concentration (b) and Reynolds shear stress (c) profiles for $dp1$; with increasing concentration from clear-water (bottom row) to saturation (top row); for the three repeated sediment-laden runs (o, \square and +); with increasing concentration from clear-	

water (bottom row) to saturation (top row); the three hydrodynamic forcing are distinguished by the magnitude of the measured profiles. 38

Figure 3-3. Ratio of bed-shear stress with sidewall correction and the measured one (extrapolation of the Reynolds shear stress to the bed) for dp1 (a) and dp3 (b); (o) SAT, (x) MED and (□) LOW; including all 27 SL runs for each particle diameter. 40

Figure 3-4. Mean profiles of eddy viscosity (a), sediment flux (b) and normalized cumulative sediment flux (c); for dp3; with $\theta \approx 0.35$ (x, green), $\theta \approx 0.50$ (square, blue) and $\theta \approx 0.85$ (o, red); increasing concentration from low (bottom row) to near saturation (top row)..... 42

Figure 3-5. Mean profiles of eddy viscosity (a), sediment flux (b) and normalized cumulative sediment flux (c); for dp1; with $\theta \approx 0.4$ (x, green), $\theta \approx 0.90$ (square, blue) and $\theta \approx 1$ (o, red); increasing concentration from low (bottom row) to near saturation (top row)..... 43

Figure 3-6. Values von Karman parameter in CW (κ_{CW}) and SL (κ_S) based on the fitting of the velocity profiles; for dp3; flow and solid transport regimes as described in Figure 3-4.... 45

Figure 3-7. Values of von Karman parameter in CW (κ_{CW}) and SL (κ_S) based on the fitting of the velocity profiles; for dp1; flow and solid transport regimes as described in Figure 3-5 46

Figure 3-8. Ratio of von Karman parameter in SL and CW based on the linear fitting mixing length (a) and of logarithmic fitting of velocity profiles (b) 47

Figure 3-9. Eddy viscosity (ϵ_{ms} , □) and sediment diffusivity (ϵ_s , +) for dp3; flow and solid transport regimes as described in Figure 3-4..... 48

Figure 3-10. Eddy viscosity (ϵ_{ms} , □) and sediment diffusivity (ϵ_s , +) for dp1; flow and solid transport regimes as described in Figure 3-5..... 48

Figure 3-11. Ratio of sediment and momentum diffusivity and its depth-averaged value β ; with dp3; for $\theta \approx 0.35$ (a), $\theta \approx 0.55$ (b) and $\theta \approx 0.8$ (c); for LOW (bottom), MED (middle) and SAT (top). 49

Figure 3-12. Ratio of sediment and momentum diffusivity and its depth-averaged value β ; with dp3; for $\theta \approx 0.4$ (a), $\theta \approx 0.9$ (b) and $\theta \approx 1.1$ (c); for LOW (bottom), MED (middle) and SAT (top). 49

Figure 3-13. Values of depth averaged ratio of sediment and momentum diffusivity β as function of ws/u^* ; For present results with different concentrations: (o) SAT, (x) MED and (□) LOW; (-) Eq. (3-5); (-.-) Eq. (3-6); (Δ) Barton and Li (1955), (+) Coleman (1970), (■) Lyn 1988, (▽) Graf and Cellino (2002), (◇) Nikora and Goring (2002), (*) Muste et al. (2005). Adapted from Lyn (2008)..... 50

Figure 3-14. Sketch of the balance of forces in uniform open channel flows..... 52

Figure 3-15. Evolution of friction factor with bulk Reynolds number (a) and the relative roughness (b); for the reference CW runs; with (o) SAT, (x) MED and (x) LOW; dashed line represents the transition between dp3 and dp1..... 53

Figure 3-16. Comparison of friction factor in CW and SL; the symbols are the reference CW runs for: (o) SAT, (x) MED and (□) LOW 54

Figure 4-1. Mixing length $l_m = u^* 2dudz$; for $\theta \approx 0.35$ (a), $\theta \approx 0.55$ (b) and $\theta \approx 0.8$ (c); for lower concentration (bottom), intermediate (middle) and saturated (top). Blue (+) is for sediment-laden and black (o) is for clear-water. Dashed line corresponds to bed-load thickness 59

Figure 4-2. Velocity distribution; for SL (blue,+) and CW (black,o). Solid lines correspond to Eq. (4-4). Flow and solid transport regimes as described in Figure 4-1. Dashed line corresponds to bed-load thickness δ	60
Figure 4-3. . Concentration distribution; measured + (blue), Rouse profile (- -, blue) as in Eq. (1-32) and Modified Rouse profile (--- black) as in Eq. (4-5). Flow and solid transport regimes as described in Figure 4-1.....	62
Figure 4-4. Values of ratio of eddy viscosity in SL and corresponding CW flow: $\phi = \epsilon_{ms}/\epsilon_m$. (o) SAT, (x) MED and (\square) LOW	64
Figure 5-1. Regimes of interaction between turbulence and particles (Adapted from Elghobashi 1994); Φp is the volumetric concentration, τp , τK and τe are the time scales of particle response, Kolmogorov and turnover, respectively.....	68
Figure 5-2. Normalized Reynolds shear stress for SL in capacity (+) and their respective CW runs (o); for dp1 ($\theta \approx 0.4$ (a), $\theta \approx 1.2$ (b)) and dp3 ($\theta \approx 0.35$ (c), $\theta \approx 0.8$ (d)).	69
Figure 5-3. Normalized TKE; flow regimes and symbols as in Figure 5-2.	69
Figure 5-4. Normalized turbulent intensities in SL (u_{rms} (+), w_{rms} (x)) in capacity and CW (u_{rms} (-), w_{rms} (--)); flow regimes as in Figure 5-2.	70
Figure 5-5. Spectra of streamwise (-) and vertical (--) velocity fluctuations at $z/H_f=0.50$; for dp1 ($\theta \approx 0.4$ (a), $\theta \approx 1.0$ (b)) and dp3 ($\theta \approx 0.35$ (c), $\theta \approx 0.8$ (d)) for lower concentration (bottom), intermediate (middle) and saturated (top). Blue (+) is for sediment-laden and black (o) is for clear-water	71
Figure 5-6. TKE budget normalized by $H_f/u * 3$; Production (o), Dissipation (+), Turbulent diffusion (x), Stratification (\square) and Imbalance (-); for dp1 ($\theta \approx 0.4$ (a), $\theta \approx 1.2$ (b)) and dp3 ($\theta \approx 0.35$ (c), $\theta \approx 0.8$ (d)); with increasing concentration from clear-water (bottom row) to saturation (top row).	72
Figure 5-7. TKE budget for flows of same hydrodynamic conditions with dp1 (a) with S10 and dp3(b) with S03, for SAT (top) and CW (bottom);.....	74
Figure 5-8. Comparison of flux Richardson number with the same hydrodynamic conditions with dp1 (∇) and dp3 (\square); both in capacity conditions (SAT).....	75
Figure 5-9. Bulk Richardson number Ri_{bulk} (a) and its repartition between bed-load (∇) and suspended-load (Δ); only in capacity conditions (SAT).....	76
Figure 5-10. Ratio of between bulk Richardson numbers associated with bed-load (Ri_B) and suspended-load (Ri_S); only for capacity conditions (SAT)	77
Figure 5-11. Taylor (--) and Kolmogorov (-) Stokes numbers; for dp1 ($\theta \approx 0.4$ (a), $\theta \approx 1.2$ (b)) and dp3 ($\theta \approx 0.35$ (c), $\theta \approx 0.8$ (d)). The vertical solid line corresponds to the value $St=1$	79
Figure 5-12. Ratio $-u'w'/k$ for SL in capacity (+) and their respective CW runs (o) that lead to values of $c\mu$ as in Eq. (5-7); for dp1 ($\theta \approx 0.4$ (a), $\theta \approx 1.2$ (b)) and dp3 ($\theta \approx 0.35$ (c), $\theta \approx 0.8$ (d))	80
Figure 5-13. Comparison of measured eddy viscosity (+) and Eq. (5-8) in sediment-laden flows; flow solid-load regimes as in Figure 5-5.....	81
Figure 5-14. Values of the ratio $\sigma K = k'w'/(dk/dz)$ in sediment-laden flows; flow solid-load regimes as in Figure 5-5	82

Figure 6-1. Ejection (top) and Sweep event (bottom) (adapted from Dey 2014; reported by Mao 2003)	87
Figure 6-2. Sketch of the four quadrants and the delineation of the Hole region as originally defined by Lu and Willmarth (1973) (Adapted from Dey 2014).	88
Figure 6-3. Relative contribution from ejections (+), sweeps (o), outward interactions (\square), inward interactions (x) and time fraction of the Hole events (.) for SL, as function of threshold level H ; solid lines are their reference CW; with the same hydrodynamic condition, for dp1 (upper panel) and dp3 (lower panel) at vertical level $z/H_f=0.3$	90
Figure 6-4. Fractional contributions from sweeps RS4 (o) and ejections RS2 (+), with $H=2.5$; for dp1 ($\theta\approx 0.4$ (a), $\theta\approx 1.2$ (b)) and dp3 ($\theta\approx 0.35$ (c), $\theta\approx 0.8$ (d)).	90
Figure 6-5. Bursting period of ejections (+) and sweeps (o) in sediment-laden flows; Solid lines correspond to the reference CW. For dp1 ($\theta\approx 0.4$ (a), $\theta\approx 1.0$ (b)) and dp3 ($\theta\approx 0.35$ (c), $\theta\approx 0.8$ (d)) for lower concentration (bottom), intermediate (middle) and saturated (top).	91
Figure 6-6. Turbulence transport Fk (x for SL and -- for CW) and RS4/RS2 (+ for SL and – for CW); panels as in Figure 6-5.	93
Figure 6-7. Mean Fk (bo) and conditionally sampled Fk_H (all four quadrants), for $H=2.5$ (+), $H=4$ (-+) and $H=6$ (-); for dp1 ($\theta\approx 0.4$ (a), $\theta\approx 1.0$ (b)) and dp3 ($\theta\approx 0.35$ (c), $\theta\approx 0.8$ (d)) only runs in saturation.	93
Figure 6-8. Fractional contribution of selected events (taking all four quadrants) to the mean vertical turbulent sediment flux; with $H=1$ (-), $H=2.5$ (+) and $H=4$ (-+); for maximum sediment concentration regime (SAT).	95
Figure 6-9. Vertical turbulent sediment flux for ejections (+), sweeps (o), outward interactions (x) and inward interactions (\square), for $H=2.5$	96
Figure 6-10. Conditionally sampled concentration fluctuations associated with ejections $cQ2'$ (cross corresponds to $H=2.5$ and solid line to $H=0$) and sweeps $cQ2'$ (circle correspond to $H=2.5$ and solid line to $H=0$); for maximum sediment concentration regime (SAT).	96
Figure 6-11. Ratio wH'/ws_0 (wH' time averaged over the duration of the selected events) corresponding to all four quadrants with $H=2.5$ (+), $H=4.0$ (-+) and $H=6.0$ (-); for dp1 ($\theta\approx 0.4$ (a), $\theta\approx 1.0$ (b)) and dp3 ($\theta\approx 0.35$ (c), $\theta\approx 0.8$ (d)) only runs in saturation.	97
Figure 6-12. Evolution of H corresponding to $wH'/ws_0 = 1$ for the six hydrodynamic regimes in saturation; the error bars represent the variability over the three repeated runs; The linear fit corresponds to $H = 6.5ws/u *$	98
Figure 6-13. Contours of ejections (red ant thicker line) and sweeps (blue and thinner line) at the threshold $H=2.5$; run P3S03D10_SAT	99
Figure 6-14. Contours of ejections (red ant thicker line) and sweeps (blue and thinner line) at the threshold $H=8$; P3S03D10_SAT	99
Figure A-1. Time evolution of flow depth and cumulative volume of transported sediments for dp3 (S03); for lower (LOW), intermediate (MED) and saturation (SAT) conditions.	106
Figure A-2. Time evolution of flow depth and cumulative volume of transported sediments for dp3 (S05); for lower (LOW), intermediate (MED) and saturation (SAT) conditions.	106
Figure A-3. Time evolution of flow depth and cumulative volume of transported sediments for dp1 (S04); for lower (LOW), intermediate (MED) and saturation (SAT) conditions.	107

Figure A-4. Time evolution of flow depth and cumulative volume of transported sediments for dp1 (S06); for lower (LOW), intermediate (MED) and saturation (SAT) conditions.....	107
Figure A-5. Comparison between the selected runs in saturation and the addition runs for S03 (top) and S05 (bottom).....	109
Figure B-1. Mixing length $lm = u * 2dudz$; for $\theta \approx 0.4$ (a), $\theta \approx 0.9$ (b) and $\theta \approx 1.2$ (c); for lower concentration (bottom), intermediate (middle) and saturated (top). Blue (+) is for sediment-laden and black (o) is for clear-water.....	110
Figure C-1. Reference concentration Ca evolution with $ws/u *$ (a); (o) measured in saturation, (Δ) Fenandez Luque (1974), (\square) Nakagawa and Tsujimoto (1980) and (*) Smith et al. (1977); In panel (b) the measured and calculated pick-up functions are compared.....	111
Figure C-2. Reference concentration based on (x) van Rijn (1984a).....	112
Figure D-1. Relative error of the estimated depth-averaged concentration based on the dataset from Graf and Cellino (2002) (\square) and total solid-load per meter of width, based on the present dataset (x), Revil-Baudard et al. (2016) (+) and Guta et al. (2019) (*).	113
Figure E-1. Values of the ratio $\sigma K = k'w'/(dk/dz)$; For dp1 ($\theta \approx 0.4$ (a), $\theta \approx 1.2$ (b)) and dp3 ($\theta \approx 0.35$ (c), $\theta \approx 0.8$ (d)) for lower concentration (bottom), intermediate (middle) and saturated (top).	113
Figure E-2. Values of the constant $c2\varepsilon$; for SL in capacity (+) and their respective CW runs (o) that lead to values of $c\mu$ as in Eq. (5-7); for dp1 ($\theta \approx 0.4$ (a), $\theta \approx 1.2$ (b)) and dp3 ($\theta \approx 0.35$ (c), $\theta \approx 0.8$ (d)).....	114

